



TECHNISCHE  
UNIVERSITÄT  
WIEN

DISSERTATION

# Quantum Cascade Intersubband Devices for Mid-Infrared Sensing

ausgeführt zum Zwecke der Erlangung des akademischen Grades  
eines Doktors der technischen Wissenschaften

unter der Leitung von

Univ.-Prof. Dr. Gottfried Strasser  
Institut für Festkörperelektronik

eingereicht an der

TECHNISCHEN UNIVERSITÄT WIEN  
FAKULTÄT FÜR ELEKTROTECHNIK UND INFORMATIONSTECHNIK

von

**Dipl.-Ing. Andreas Harrer**

Mat.Nr. 0625378

Gumpendorferstraße 92/15

A-1060 Wien

Wien, im Mai 2017

1. Gutachter: Prof. Dr. Sven Höfling
2. Gutachter: a.Univ.-Prof. Dr. Thomas Fromherz

Tag der mündlichen Prüfung: 31.05.2017

”The piano ain’t got no wrong notes.”

Thelonious Monk





## Kurzfassung

Quantenkaskadendetektoren (QCDs) und Quantenkaskadenlaser (QCLs) bieten eine leistungsfähige Plattform für miniaturisierte, integrierte optische Sensorsysteme. Die Kombination dieser beiden Technologien zu bi-funktionalen Quantenkaskaden-Materialien, welche sowohl als Detektor als auch als Laser betrieben werden können, macht die Entwicklung von kompakten, optischen, chemischen Sensoren möglich. Die Leistungsfähigkeit der Emission und die Empfindlichkeit der Detektion von Licht im mittleren Infrarot-Bereich ist dabei maßgebend für die erreichbare Messauflösung bei Spektroskopieanwendungen. Im Zuge der vorliegenden Dissertation wurden verschiedene Methoden der Lichtkopplung für QCDs und bi-funktionale Materialien untersucht.

QCDs können nahezu dunkelstromfrei im Photovoltaik-Modus betrieben werden, wodurch Betriebstemperaturen bis zur Raumtemperatur erreicht werden. Zur Erhöhung der Absorptionseffizienz dieser Detektoren, wurde eine alternative Kopplungsmethode basierend auf Plasmonenlinsen konzipiert, simuliert und gefertigt. Diese Plasmonenlinsen ermöglichen dabei die Kopplung einer größeren Menge auftreffender Strahlungsenergie, ohne die elektrisch aktive Fläche des Detektors zu vergrößern. Die vorgestellte Geometrie ermöglicht eine bis zu 6-fache Erhöhung des Photostroms der Detektoren bei Raumtemperatur bei einer gleichzeitigen Verbesserung des Signal-Rausch-Verhältnisses (SNR).

Die Integrierbarkeit von QCDs zu Pixelsensoren wurde anhand eines im Bereich der starken  $\text{CO}_2$ -Absorption empfindlichen Detektormaterials untersucht. Im Zuge dessen wurde die Lichtkopplung durch Simulationen optimiert und ein Demonstrator mit  $8 \times 8$  Pixeln gefertigt und charakterisiert. Ein Ansprechvermögen von  $R_p = 16 \text{ mA/W}$  und eine spezifische Detektivität von  $D^* = 5 \cdot 10^7 \text{ cm}\sqrt{\text{Hz}}/\text{W}$  konnte dabei in der Pixelgeometrie erreicht werden.

Basierend auf einem bi-funktionalen Quantenkaskaden-Laser-Detektor (QCLD) Material wurde die Lichtkopplung für monochromatische Emission und Detektion in oberflächennormaler Richtung untersucht und ein Sensorprototyp entwickelt, welcher die Analyse von Gaskonzentrationen mittels Absorptionsmessung ermöglicht. Dabei wurde die Laser- und die Detektorstruktur auf dem selben Chip monolithisch integriert. Das vom Sensor emittierte Licht wird nach der Kollimation mittels einer Linse und der Interaktion mit dem zu messenden Gas an einem Spiegel reflektiert und durch die Linse auf den Sensor zurück fokussiert. Das so gemessene Detektorsignal ist ein Maß für die Konzentration des Testgases im vorliegenden Fall, in einer Stickstoffmatrix.

Dieses Konzept wurde durch geometrische Anpassungen und verbesserte elektri-

sche Kontakte dahingehend weiter entwickelt, dass Messungen bei Raumtemperatur bis zu einer Detektierbarkeitsgrenze von 400 ppm möglich sind. Darüber hinaus konnte die Realisierbarkeit mehrerer Emissionswellenlängen entlang der selben optischen Achse gezeigt werden. Die demonstrierte Methode kann einfach auf weitere Emissionswellenlängen erweitert werden. Dadurch können potentiell externe optische Komponenten, wie Spiegel und Linsen, eingespart werden und die Lichtkopplung gegenüber äußeren Einflüssen, wie zum Beispiel Vibrationen, unempfindlicher gemacht werden.

## Abstract

Quantum cascade lasers (QCLs) and quantum cascade detectors (QCDs) have shown remarkable progress in their performance, availability and their use in different applications over the past years. Recently, the demonstration of their combination to a high performance bi-functional quantum cascade laser detector (QCLD) material enabled for novel integrated sensing devices in the mid-infrared (MIR) region. Light coupling for infrared light emission and detection is essential for integrated sensing device design and has a major impact on the sensing performance. Device integration based on these bi-functional materials shows an efficient way towards portable, light weight and compact in field sensing solutions.

In this thesis MIR light coupling to QCDs and bi-functional QCLD materials has been investigated and different schemes have been applied to various sensing device designs. Plasmonic lens based on chip light focusing to extended the optical area and coupling efficiency of QCDs is shown. The plasmonic coupling and focusing structure is sensitive to surface normal MIR light. The coupled light is focused and guided by surface plasmon polariton (SPP) waves to the active zone (AZ) of the detector element centered in the lens structure.

Quantum cascade detectors (QCDs) operated in photovoltaic mode allow for room temperature operation which makes them a promising narrow bandwidth high speed alternative to quantum well infrared photodetector (QWIP) cameras. QCD integration to array devices has been investigated for a device design which is sensitive to the strong CO<sub>2</sub> absorption at 4.3  $\mu\text{m}$  wavelength. A  $8 \times 8$  pixel demonstrator has been designed, fabricated and characterized. A single pixel responsivity of  $R_p = 16 \text{ mA/W}$  with a specific detectivity of  $D^* = 5 \cdot 10^7 \text{ cm}\sqrt{\text{Hz}}/\text{W}$  could be realized at room temperature.

A bi-functional surface emitting and detecting integrated gas-sensor has been designed, fabricated and evaluated by proof of concept gas measurements. The surface operation mode allows for long interaction lengths as required for low absorption analytes e.g. gases. The device is based on a single mode distributed feedback (DFB) ring cavity quantum cascade laser (QCL) and a centered detector element. The emitted light is collimated to pass a gas-cell, reflected at a flat mirror and re-focused to the on-chip detector element. Gas measurements in a wide range of concentrations are shown with an on-chip detector signal corresponding to a test gas concentration. A design is presented with lower electrical crosstalk, an improved contact design and an enhanced coupling geometry. This design features two distinct emission wavelengths to demonstrate multi-wavelength integration on one chip. A limit of detection of 400 parts-per-million is achieved at room temperature operation.



# CONTENTS

<b>1</b>	<b>Introduction</b>	<b>1</b>
1.1	Infrared radiation . . . . .	2
1.2	Infrared detection and imaging - an overview . . . . .	2
1.2.1	Thermal detectors . . . . .	3
1.2.2	Quantum detectors . . . . .	4
1.3	Mid-infrared emitter and laser . . . . .	7
1.3.1	Quantum emitter . . . . .	7
1.4	Chemical sensing . . . . .	9
1.5	Motivation of this thesis . . . . .	11
<b>2</b>	<b>Heterostructures and Optical Transitions in Quantum Wells</b>	<b>13</b>
2.1	Heterostructures and growth . . . . .	13
2.2	Heterostructure calculation . . . . .	17
2.2.1	Crystals . . . . .	17
2.2.2	Bloch theorem . . . . .	17
2.2.3	Band structure . . . . .	18
2.2.4	Envelope function approximation . . . . .	21
2.2.5	Potential wells . . . . .	23
2.3	Optical transitions . . . . .	25
2.3.1	Interband and intersubband transitions . . . . .	25
<b>3</b>	<b>Quantum Cascade Detectors</b>	<b>31</b>
3.1	Figures of merit . . . . .	31
3.1.1	Comparability . . . . .	32
3.1.2	Responsivity . . . . .	32
3.1.3	Detectivity . . . . .	32
3.1.4	Noise equivalent temperature difference . . . . .	34
3.1.5	Spectral width and coupling properties . . . . .	35

3.2	Device principles . . . . .	35
3.2.1	Responsivity . . . . .	37
3.2.2	Extraction efficiency . . . . .	37
3.2.3	Absorption efficiency . . . . .	38
3.2.4	Noise . . . . .	39
3.2.5	Resistance . . . . .	40
3.2.6	Non radiative scattering mechanisms . . . . .	40
3.2.7	Doping concentration . . . . .	42
3.2.8	Design trade-off . . . . .	42
3.3	Design and optimization . . . . .	47
3.3.1	Wavelength matching . . . . .	47
3.3.2	Example design for CO <sub>2</sub> sensing and array integration . . . . .	47
3.4	Characterization . . . . .	50
3.4.1	Fourier transform infrared spectroscopy . . . . .	50
3.4.2	Current voltage characterization . . . . .	52
3.4.3	Resistance limitations . . . . .	53
3.4.4	Responsivity . . . . .	54
3.4.5	Absolute photocurrent . . . . .	55
3.4.6	Sample preparation . . . . .	56
<b>4</b>	<b>Enhanced Light Coupling</b>	<b>57</b>
4.1	Mesa devices . . . . .	58
4.2	Facet based absorption geometries . . . . .	59
4.3	Grating coupling . . . . .	60
4.4	Plasmonic lens quantum cascade detectors . . . . .	62
4.4.1	Fundamentals . . . . .	63
4.4.2	Plasmonic lens detector design . . . . .	75
4.4.3	Coupling and propagation . . . . .	76
4.4.4	Simulations . . . . .	77
4.4.5	Fabrication . . . . .	81
4.4.6	Results . . . . .	83
4.5	Alternative coupling methods . . . . .	92
4.5.1	Meta material coupling . . . . .	92
4.5.2	Surface normal coupling . . . . .	93
<b>5</b>	<b>Quantum Cascade Detector Arrays</b>	<b>95</b>
5.1	Basic considerations . . . . .	96
5.1.1	Radiation power . . . . .	97

5.1.2	Focal plane arrays . . . . .	98
5.2	Quantum cascade detector array integration . . . . .	100
5.2.1	Motivation . . . . .	100
5.2.2	Detector design . . . . .	100
5.2.3	Single pixel test structures . . . . .	101
5.2.4	Light coupling simulations . . . . .	104
5.2.5	Pixel array . . . . .	106
5.2.6	Integration and packaging . . . . .	111
<b>6</b>	<b>Bi-functional Quantum Cascade Sensing</b>	<b>115</b>
6.1	Direct absorption gas sensing . . . . .	115
6.2	Quantum cascade laser basics . . . . .	117
6.3	Bi-functional quantum cascade material . . . . .	119
6.4	Bi-functional gas-sensing device . . . . .	119
6.4.1	Characterization . . . . .	122
6.4.2	Gas sensing . . . . .	124
6.4.3	Light coupling . . . . .	126
6.5	Revised bi-functional gas sensing device . . . . .	128
6.5.1	Device design . . . . .	129
6.5.2	Gas sensing . . . . .	132
6.5.3	Light coupling . . . . .	133
<b>7</b>	<b>Summary and Outlook</b>	<b>135</b>
7.1	Summary . . . . .	135
7.2	Outlook . . . . .	137
<b>A</b>	<b>Growth Sheets</b>	<b>141</b>
A.1	H853 . . . . .	142
A.2	C0120/C0280 . . . . .	145
A.3	K086 . . . . .	149
A.4	C0115 . . . . .	151
A.5	C0119 . . . . .	152
A.6	C0321 . . . . .	155
A.7	C0323/C0342 . . . . .	156
<b>B</b>	<b>Devices</b>	<b>157</b>
B.1	Cleanroom devices . . . . .	157
B.2	Measurement devices . . . . .	157

<b>Bibliography</b>	<b>159</b>
<b>List of Publications</b>	<b>185</b>
<b>Curriculum Vitae</b>	<b>191</b>



## INTRODUCTION

Isaac Newton's investigations on light, colors, refraction and reflections presented in 1672 to the Royal Society in London was the first methodical scientific work on mid-infrared (MIR) radiation. Newton reported on light refraction in a prism, decomposing it to red, orange yellow, green, blue and violet components. He disproved the common theory that colors are a mixture of white light and amounts of darkness, as proposed previously [1]. Several investigations on the temperature distribution in the solar spectrum were left without broad attention in the late 18th century [2]. It took more than a hundred years until infrared radiation was discovered by Sir

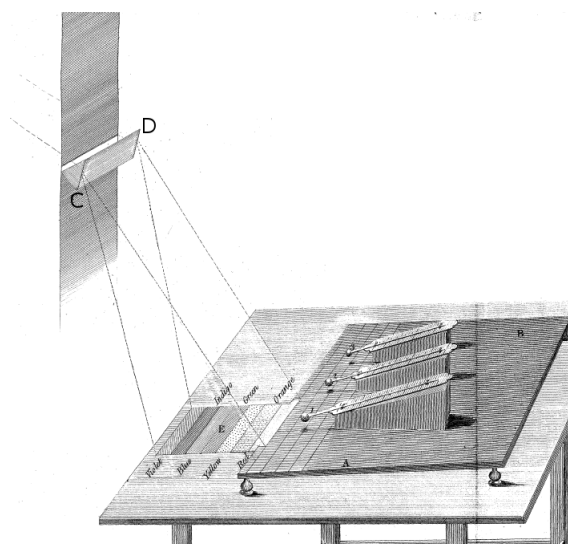


**Figure 1.1:** The prism experiment conducted by W. Herschel in 1800, which led to the discovery of infrared radiation using three thermometers. The prism is at C and D in front of a slit. Image taken from [3].

William Herschel, a German musician and astronomer [3]. Herschel used a prism to diffract light into its spectral components and three thermometers to measure the temperature of different spots in the refracted beam. The distribution of radiation power over the visible and into non-visible spectral regions was conducted with a simple setup depicted in figure 1.1. Herschel reported on increased temperatures

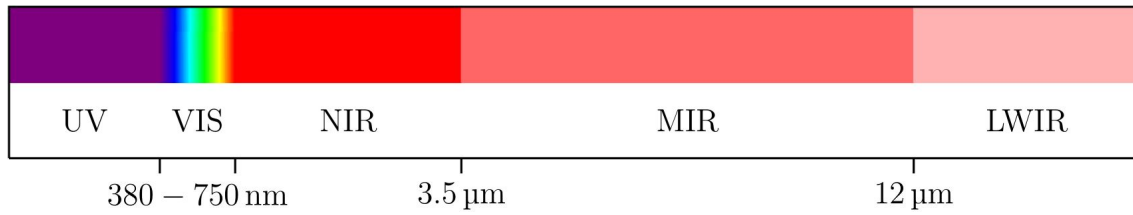


**Figure 1.2:** Electromagnetic spectrum from short to long wavelengths starting with the ultra violet, visible, NIR, MIR, LWIR and microwave region.

in the region below the last visible red spectral line. He concluded that it is inappropriate to distinguish between visible light and radiant heat if they are from the same origin.

## 1.1 Infrared radiation

Infrared light - 'infra', from the Latin for 'below' - is the spectral region of electromagnetic waves below red, spanning to the microwave region. It is divided into three sub-spectral regions with loosely defined borders depending on the source. The mid-infrared (MIR) region this work is focused on, is located in the electromagnetic spectrum with wavelengths  $\lambda$  between  $3.5\text{ }\mu\text{m}$  and  $12\text{ }\mu\text{m}$ . At the short wavelength side the MIR regime is bounded by the near-infrared (NIR) ( $750\text{ nm} - 3.5\text{ }\mu\text{m}$ ) followed by the visible spectrum. Towards long wavelengths it neighbors the long-wave infrared (LWIR) regime starting around  $12\text{ }\mu\text{m}$  followed by microwaves (figure 1.2).

A wide range of consumer and medical products operating in the infrared (IR) spectral region are available which utilize infrared radiation, such as infrared radiators for heating, infrared cabins and medical devices for musculoskeletal system treatment. Besides residual light amplifiers, IR radiation detection attracted attention for imaging applications and night vision systems, environmental sensing, military countermeasure and identification systems. Infrared detection is widespread in the production and construction industries for temperature monitoring. Thermal leaks in building insulation are identified by IR imaging devices.

## 1.2 Infrared detection and imaging - an overview

Since infrared (IR) radiation was discovered its detection methods have been investigated. In the first experimental setups thermometers were used. Thermal detection is one of two methods of IR detection used since the discovery of the IR spectrum. Later in the 20<sup>th</sup> century quantum detectors were introduced, which define the sec-

ond group of detector types. This section gives a brief overview of the key inventions and technologies of both groups.

### 1.2.1 Thermal detectors

Bulk thermometers need a couple of minutes to show stable temperatures, when exposed to radiation. Due to their heat capacity they exhibit slow response times and long stabilization times. The research on [IR](#) radiation soon required more elaborate detectors.

**Bolometric effect** S. P. Langley, an American astronomer, showed a device he named the 'bolometer' in 1878, which made sensitive measurements with shorter response times possible. His design was based on a Wheatstone bridge formed by two arms of meandering thin metal conductors made of steel, platinum or palladium. The reference arm is shielded from any radiation but kept near to the measurement arm exposed to [IR](#) radiation. The temperature change of the measurement arm results in a change of its resistance  $R$ . A galvanometer indicated the change in the current ratio in the two bridge arms [4].

**Thermoelectric effect** T. J. Seebeck, a German doctor and physicist, discovered the thermoelectric effect. A voltage of several  $\mu\text{V}/\text{K}$  can be observed between two conducting wires of different materials if one pair of ends is kept at a different temperature than the other while they are electrically connected at one of the ends. A major advance was a serial connection of several of such thermocouples to generate higher output voltages [5]. In 1947 M.J.E. Golay introduced a pneumatic radiation detector with an absorber in a thermal expanding gas volume which moves a membrane with high sensitivity [6]. Most of these principles are still in use today after years of research and improvement.

Thermoelectric [IR](#) detection evolved to very sensitive devices used in astronomy. Golay cells are nowadays used for THz radiation detectors, whereas the bolometric effect is still utilized in state-of-the-art infrared detectors and imaging devices. Their combination with micro-fabrication technology led to the so-called micro-bolometer arrays for industrial and personal use. They are mostly made of amorphous Si or  $\text{VO}_x$  and commercially available as uncooled focal plane arrays (FPAs) with different pixel counts and price ranges [7]. Thermal [IR](#) detection in general is sensitive to a broad spectral range. Their response times and sensitivity strongly depend on their thermal capacity (size) and temperature coefficient (i.e.  $R(T)$  or Seebeck coefficient).

### 1.2.2 Quantum detectors

Besides thermal infrared detection, quantum detectors define the second group of detector devices discovered and developed in the more recent past. Quantum **IR** detectors are based on optical excitation of charge carriers and can be further separated in interband and intersubband (**ISB**) detector devices. In general, they are operating at very fast response times in comparison to thermal detectors. Two exceptions have to be mentioned for thermal detection, which are graphene based detectors [8] and superconducting hot electron bolometers [9].

Photoconductivity of selenium was discovered by W. Smith in 1873 during the search for a wire insulator [10, 11]. Photoconductivity of different crystals was reported 1917 by T. W. Case, who investigated the resistance change of crystals when exposed to light [12]. Lead salt photoconductors such as PbS and PbSe were investigated for military purposes after T. W. Case's reports. Photocathode **NIR** converters with Ag/O/Cs coatings for imaging were investigated by L.R. Kohler around 1929 [13] for night vision applications.

A wide spread interband detector type is the photodiode used e.g. in optical data storage devices such as compact disc readers and optical data transmission interfaces from the mid 1980s on. Since the ternary alloy HgCdTe was discovered for infrared detection it was developed to one of the most common intraband **IR** detector materials. It is often referred to as mercury cadmium telluride (**MCT**). Since the detection wavelength is material dependent high uniformity in material composition and spatial growth uniformity is needed. Even if **MCT FPA**s show excellent performance they suffer from several drawbacks like substrate compatibility, price and availability. Recently **MCT FPA**s could be grown on Si substrates [14, 15] which potentially improves cost efficiency. **MCT** detectors are used as single detector elements and are commercially available as **FPA**s with relatively high pixel counts.

A common III-V compound used for **NIR** detection is indium antimonide (InSb). Its low bandgap of 0.23 eV at 80 K and extraordinary high electron mobility [16, 17] enables the design of high performance detectors limited towards longer wavelengths at  $\lambda \approx 5 \mu\text{m}$ . Recently, similar to **MCT**, InSb growth on Si substrate could be shown utilizing a GaAs pre-deposition layer [18]. InSb detectors are operated at cryogenic temperatures and are available as single elements or as **FPA**s with large pixel counts for imaging [19]. Their major drawback is the required operation temperature and cutoff wavelength.

In the **NIR** spectral region InGaAs photodiodes are operated in the 1.55  $\mu\text{m}$  wavelength range with the best efficiency. Their growth is based on the work of Pearsall

and Hopson in 1978 [20] who reported on lattice matched growth on InP. InGaAs photodiodes in linear array and megapixel imager configurations are today widely available and provided by e.g. Hamamatsu Photonics or Sofradir.

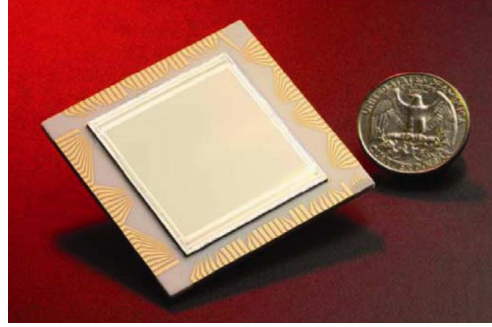
**Superlattice devices** require more elaborate material growth technology to provide the needed quantum confinement and layer thicknesses in the nano meter range. The invention of molecular beam epitaxy (MBE) by A. Y. Cho and J. R Arthur at AT&T Bell labs paved the way for realization of the resonant tunneling diode proposed by Tsu and Esaki in 1973 [21] and the quantum cascade laser (QCL) proposed by Kazarinov and Suris [22]. After these proposals and investigations on GaAs/AlGaAs growth [23] resonant tunneling in double barriers was shown [24]. The development of metal-organic chemical vapor deposition (MOCVD) in 1968 by H. M. Manasevit led to a cost efficient way of large scale heterostructure manufacturing for optoelectronics [25]. MOCVD is a complex variant of chemical vapor deposition (CVD) with metal-organic precursors which made the mass production of double heterostructure light emitting diodes (LEDs) possible. These pioneering works set the basis for the realization of a large variety of superlattice (SL) based interband and intersubband devices.

A state of the art interband FPA detector is the type II SL detector proposed in 1987 [26] and investigated towards long wave detection capabilities in 1988 [27]. The SLs are based on III-V material systems where the valence band edge of one material is higher than the conduction band edge of the second. Various designs have been shown demonstrating operation wavelengths up to 25  $\mu\text{m}$  [28], optimization for low dark currents by utilizing a barrier layer [29] and W shaped barriers [30]. Imaging up to 150 K with high detectivity was reported [31] including megapixel devices [32].

**QWIPs** are the most prominent example of MIR intersubband detector devices. Developed in the late 1980s [33], extensive research resulted in mega-pixel FPAs for astronomy and defense applications. Figure 1.3 shows such a QWIP FPA for dual-band imaging.

The quantum well infrared photodetector (QWIP) is mostly based on GaAs/AlGaAs or InGaAs/InAlAs semiconductor heterostructures. They are based on a simple heterostructure design as an arrangement of quantum wells (QWs). The QWs are designed to exhibit a bound ground state and an excited upper quasi-bound state. The device is then operated in biased mode, hence an electric field is applied to it. Impinging IR photons of suitable polarization and energy, excite the electrons in the ground states of the well to the excited quasi-bound state. From there they escape to the continuum and are extracted by the electric field. A major drawback

**Figure 1.3:** Megapixel ( $1024 \times 1024$ ) focal plane array (FPA) of a quantum well infrared photodetector demonstrated by Gunapala et al. in 2010. Image from [49]. ©2009 IEEE.



of this detector type is its dark current and therefore the operation limitation to cryogenic temperatures. In the past years several efforts had been made to achieve elevated operation temperatures. In our group surface normal detection, doping concentration [34, 35], resonance tuning [36, 37, 38], higher order modes [39] and critical coupling [40] has been investigated to increase the QWIP operation temperature. Recently a QWIP based on the  $\text{Si}_x\text{Ge}_{1-x}$  material system was demonstrated based on ISB transitions in the valence band [41].

**Quantum cascade detectors** (QCDs) evolved from photovoltaic QWIPs [42] and were first shown as detecting quantum cascade laser (QCL) structures in 2002 [43]. The term quantum cascade detector (QCD) was introduced since their operation principle is very similar to QCLs. Since then they have improved in performance and operation temperature in various material systems. Important contributions to the field were made by M. Graf [44] and F. Giorgghetta [45] at Université de Neuchâtel and by A. Delga [46] and L. Gendron [47]. QCDs are operated in unbiased (photovoltaic) or low bias mode by design. Photovoltaic operation allows for detection at room temperature. QCDs are compatible with well-established material and growth systems such as MBE and MOCVD while they share all the advantages of intersubband detectors such as a photocurrent response defined by the QW dimensions rather than material composition, compatibility to mature well-established material systems and high performance. Recently their flexibility in design and speed was applied to a combination with an emitting QCL structure to a lab-on-a-chip, which showed them perfectly suitable for integrated spectroscopy devices [48]. The operation principle, design parameters and optimization of QCDs is described in detail in chapter 3.

**Hybrid detector** schemes have been shown in the past years, with higher quantum confinement utilizing quantum dots [50, 51] and quantum dot-in-a-well structures. They are sensitive to normal incident radiation and show promising results in performance and light coupling. Hybrid QCDs with quantum dots in the active well

have been demonstrated [52] with similar performance to standard designs without dots.

Thermal emission characteristics are essential for IR imaging devices without active scene illumination and their noise behavior. The spectral width and position of the detectors peak response determines the incident power per pixel. These imaging related aspects of thermal background and scene illumination are discussed in chapter 5.

A good overview of the history of IR detectors is given by A. Rogalski in [53] including an overview of commercially available imaging FPAs.

## 1.3 Mid-infrared emitter and laser

Mid-infrared light can be generated by thermal sources or quantum sources. Thermal electric driven SiC glowing sources are commonly used in Fourier transformation infrared spectrometers (FTIRs) and referred to as global source.

### 1.3.1 Quantum emitter

In the IR spectral region depending on the wavelength range IR LEDs, laser diodes, interband cascade lasers (ICLs) and QCLs are available. Infrared light emission in GaAs, GaSb and InP by carrier injection was shown in 1955 with their emission peaks close to the bandgap energy [54]. Since the LED emission wavelength is dependent on the bandgap energy, the emission wavelength is dependent on the materials used and their composition. Until QCLs matured, lead salt laser diodes were the main source used in the field of laser spectroscopy [55, 56].

Vertical cavity surface emitting lasers (VCSELs) are a high power emitter option restricted to the NIR regime with devices ranging from high power arrays [57] to single mode emission [58]. VCSELs have two strong constraints in their design. First, surface normal light coupling to the optic transition has to be possible - which is fulfilled by interband transitions - and second the Bragg reflectors have to be grown with a sufficient number of periods. For long wavelengths, the second restriction would lead to too thick Bragg mirrors or an insufficient number of periods for the needed mirror reflectivity.

**Interband cascade lasers** (ICLs) are based on type II heterostructures and combine the interband operation method of diode lasers with the cascading of QCLs. A major advantage is their low threshold current while they provide sufficient output power for spectroscopy applications. First realized in 1997 by Lin et al. [59],



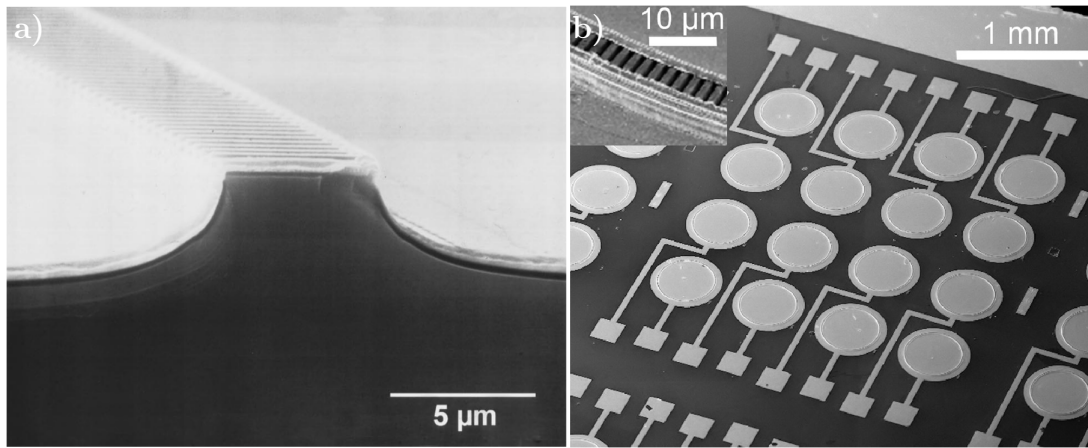


**Figure 1.4:** Scanning electron microscope (SEM) image of a) a DFB QCL shown in 1997 by Faist et al. [69] and b) SEM image of an  $4 \times 4$  ring quantum cascade laser (ring-QCL) array [70]. Taken from [69] and [70].

room temperature operation in pulsed mode was shown in 2002 [60]. State of the art devices, show depending on the operation wavelength, threshold currents below  $500 \text{ A/cm}^2$  in continuous wave (CW) operation with mW output power [61, 62]. Single mode two-section ICLs with 160 nm total tunability around  $3.7 \mu\text{m}$  wavelength was shown recently [63]. An up to date review on ICLs was given by Vurgaftman et al. in [64].

**Quantum cascade laser** In 1994 at AT&T Bell Laboratories the first working QCL was demonstrated by J. Faist et al. [65]. About a year later CW operation could be shown at a wavelength of  $4.6 \mu\text{m}$  [66], at that time up to 85 K. The next important step was to realize single mode emission [67] which is needed for many spectroscopy applications. A common way to achieve single mode emission is the fabrication of distributed feedback (DFB) gratings (figure 1.4). It took several years of research until the QCL was published as the first room temperature CW operating mid-infrared semiconductor laser [68]. At this point one of the most important requirements for compact spectroscopy applicable sources was met.

The emission wavelength of QCLs is determined by the heterostructure design. Hence, with a stable material and growth system the quantum well thicknesses determine the laser emission wavelength and QCLs are able to cover a wide spectral range without gaps. The continuous research effort led to room temperature operation, single mode emission, high power devices up several Watt output power [71] and a wide variety of applications including direct absorption spectroscopy, trace gas sensing [72] and frequency combs [73]. QCLs cover a wide wavelength range from the NIR [74] down to the THz [75] region. Recently the total THz output



power per facet could be enhanced up to 0.47 W by a symmetric active zone (AZ) design with a two stack waver-bonded active region [76].

Spectroscopy applications often require the used MIR laser sources to cover a wide wavelength range. For tunable QCLs a broadband gain active zone is an essential building block. As QCLs have 20 to  $\approx 100$  periods stacked in their AZ different period designs can be combined to achieve broad spectral gain [77]. A second approach has been demonstrated which uses identical periods which are optimized for broad gain based on multiple upper laser levels [78]. Combined with external cavities, MIR sources with a wide tuning range can be realized [79, 80]. Another approach for fine tuning the emission wavelength is based on thermal wavelength shifts. Tuning within a laser pulse or by substrate mount temperature control can be applied [81].

For many applications efficient light coupling from a laser facet or surface to an analyte interaction region is desired without using external optics such as mirrors and lenses. Distributed feedback lasers (DFB) with 2<sup>nd</sup> order grating coupling enable surface emission [82]. This concept has been extended to ring quantum cascade lasers (ring-QCLs) in 2007 introducing a ring shaped laser resonator for QCLs [83]. Surface emitting QCLs can be designed to exhibit a large emitting surface in comparison to facet emitters, which results in a lower beam divergence. Surface emission allows for two dimensional array integration of several emitters with a low divergence angle [70]. Such a two dimensional ring-QCL array is illustrated in the scanning electron microscope (SEM) picture in figure 1.4 b.

Active mode locking in a 8  $\mu\text{m}$  wavelength QCL was shown in 2000 by R. Paiella et al. with a 3.75 mm long device which results in a longer cavity round trip time than for other semiconductor laser types [84].

Since Fabry-Pérot (FP) laser cavities exhibit a relatively divergent emission beam several works on beam shaping were published including plasmonic structures on the laser facet for beam collimation [85, 86] or grating modifications for ring-QCLs [87].

## 1.4 Chemical sensing

The MIR region is frequently referred to as the chemical fingerprinting region. The rotational vibrational absorption resonances of most chemical compounds can be found in the MIR region (figure 1.5) where they are orders of magnitude stronger and have usually a lower full width at half maximum (FWHM) than in the NIR regime [88]. These distinct sharp absorption lines being accessible by optical spectroscopy

allow the identification of molecules and their concentration. A major advantage of MIR spectroscopy is the possibility of substance identification without direct analyte contact and its speed which enables for remote sensing and realtime monitoring of substance concentrations.

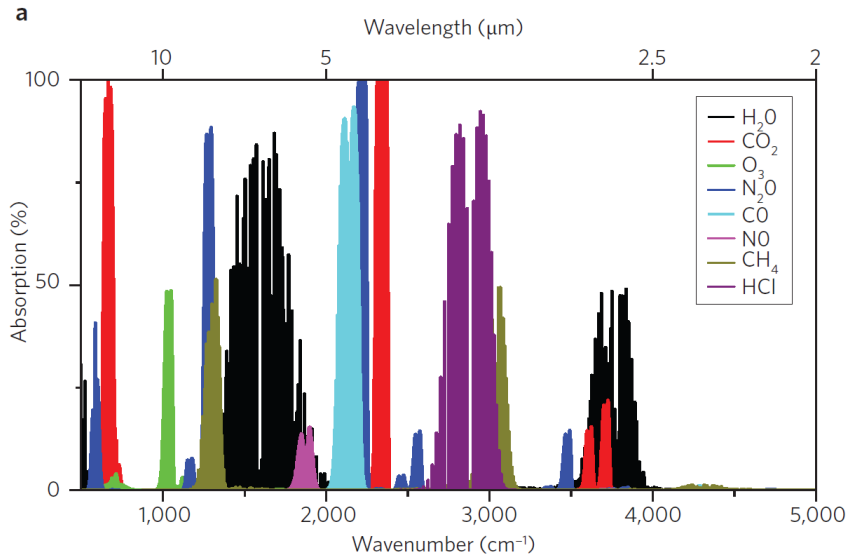


**Figure 1.5:** Part of the MIR absorption spectrum containing the absorption features of several substances. Image taken from [89].

A well established method for chemical fingerprinting is direct absorption spectroscopy with a thermal broadband source and a Fourier transformation infrared spectrometer (FTIR). In general FTIRs are laboratory devices which are large, heavy and stationary, which require the substance under test to be analyzed in a laboratory. The extensive research on QCLs briefly described in section 1.3 provided a reliable tailorable source for optical spectroscopy covering the MIR spectral region with high output power at room temperature and multi-wavelength configurations. In combination with the manifold of optical spectroscopy methods investigated up to now, these compact sources and detectors enable device designs which address specific applications such as remote trace gas sensing, realtime liquid analyte concentration measurements, realtime exhaust gas monitoring [90] and fast compact medical applicable sensing devices. A common miniaturization strategy is direct absorption spectroscopy as used in FTIR spectroscopy, but based on compact QCL or ICL sources. A MIR source emits light which is passed through the material to be analyzed. After passing the material the beam is re-collected at a detector sensitive to the wavelength region of interest. The detector signal is then determined by the absorption signature of the analyte and its concentration. Single mode lasers offer light emission at a distinct wavelength which is chosen to coincide with significant

absorption features in order to identify a substance. Commonly multiple narrow or single mode lasers are used with spectrally broad detectors. The first demonstration with [DFB QCLs](#) was by S.W. Sharpe et al. in 1998 probing NO and NH<sub>3</sub> in combination with InSb and [MCT](#) detectors [91].

An indirect spectroscopy method based on the photoacoustic effect first described by A. G. Bell in 1881 [92] is so called photoacoustic spectroscopy ([PAS](#)) [93]. The analyte is periodically exposed to [IR](#) radiation with a wavelength matching the absorption pattern of the substance to be detected. The excited rotational vibrational resonances introduce heat and thereby periodic expansion. This expansion oscillation can be measured as an acoustic wave. The more recently shown [QCL](#) based [PAS](#) and quartz enhanced photoacoustic spectroscopy ([QPAS](#)) provide high sensitivity measurement of gases in low concentrations [94, 95, 96].

Recently [QCL](#) frequency combs were [73], paving the way for [QCL](#) based dual comb spectroscopy demonstrated in 2014 [97]. Frequency combs exhibit many laser modes which have an exact and constant spectral spacing. Depending on the cavity length this spacing can be altered. The analyte can be probed at the spectral positions of the comb lines discretely. Hence the spectroscopic resolution is determined by the comb spacing. [QCL](#) frequency combs can be shifted between these discrete comb lines by electrical current or heating. [QCL](#) dual comb spectroscopy takes advantage of the speed of quantum detectors, lasers and the simultaneous interaction of the comb lines with the analyte and is therefore a very fast method.

Other promising methods shown recently are based on plasmonic interaction regions based on quantum cascade structures, where the light source and the detector is fabricated from a bi-functional quantum cascade laser detector ([QCLD](#)) material [98, 99]. An unique advantage of these materials is their integration onto a single chip in one fabrication run with no need for wafer bonding and aligning of optical structures.

## 1.5 Motivation of this thesis

Sensing based on [MIR](#) photonics has shown huge progress in the past years. Source and detector performance was improved while the technology became stable and commercially applicable. A manifold of quantum cascade lasers ([QCLs](#)) is commercially available from numerous suppliers with different emission wavelengths and output power ready to be operated in a plug and play fashion. Complete units with power sources and thermal stabilization can be obtained. A similar situation can be seen for [IR](#) detectors which are available in a broad product range as well as imag-

ing devices for various applications. The requirements on the next generation of MIR chemical sensors, detectors and imagers are demanding and give rise to several challenges to focus on. These can be summarized as:

- Room temperature operation
- Energy efficiency
- Compactness and portability
- Fast response times / realtime operation

These challenges have to be met when novel sensing systems are developed. A possible solution is the integration of the IR source and the detector on the same device. In that way compact and potentially robust devices are possible. Room temperature operation is in tight connection with the system size. Room temperature operable devices do not need bulky, heavy and energy consuming cooling devices to allow for sensitive measurements. Temperature stabilization around 20 °C can be achieved in very compact and lightweight designs by thermoelectric cooler (TEC) devices.

In the scope of this thesis light coupling, focusing and integration of quantum cascade detectors (QCDs) and bi-functional quantum cascade laser detector (QCLD) sensing devices is investigated to advance towards these goals. The focus has been set to room temperature operation materials and their application to novel compact integrated device designs. Performance and coupling efficiency of plasmonic light coupling and guiding structures for QCDs is investigated by simulation and demonstrated by measurements on various device designs. A bi-functional gas sensing device with high integration potential based on a high performance QCLD material is presented with proof of concept gas sensing measurements. Further, the integration of QCDs to pixel array devices has been investigated to show their potential for compact, narrow peak wavelength and portable imaging applications.

# HETEROSTRUCTURES AND OPTICAL TRANSITIONS IN QUANTUM WELLS

The basic building block of quantum cascade (QC) devices is a semiconductor heterostructure which includes its design and growth. In this chapter the fundamentals of heterostructures and their growth are summarized. Then the theoretical background will be introduced which is involved in quantum cascade detector (QCD), quantum cascade laser (QCL) and so called bi-functional quantum cascade laser detector (QCLD) material design. The fundamentals of semiconductor physics and heterostructure calculation presented in this chapter are based on the more detailed literature [100, 101, 102, 103].

## 2.1 Heterostructures and growth

Quantum devices require material growth and fabrication in the sub nanometer range to provide the needed quantum confinement for the charge carriers. The de Broglie wavelength  $\lambda = \frac{h}{p}$  determines these dimensions which enable the design of energy bands and optical transitions between them. The required potential wells to confine carriers, allow to engineer their lifetime, concentration and transport. These potential wells are formed by semiconductor heterostructures which consist in general of two or more different materials grown onto each other in crystalline form. For QC devices mostly group III-V materials are used which are i.e. GaAs/AlGaAs, InGaAs/InAlAs, InAs/AlAsSb or the aluminum free system InGaAs/GaAsSb [104, 105]. As illustrated in figure 2.1, depending on the semiconductor band scheme three different types of heterostructures can be grown. The GaAs/AlGaAs and InGaAs/InAlAs material system form a type I heterostructure where the barrier

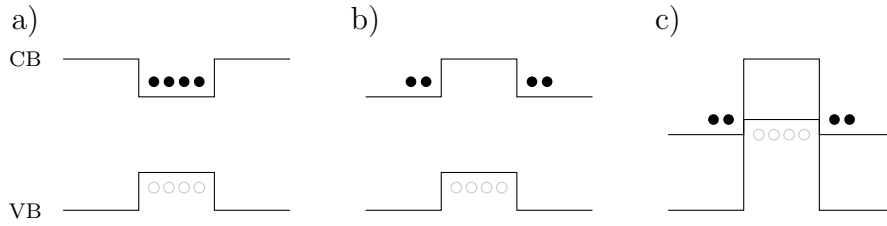


**Figure 2.1:** The three types of heterostructures depending on the band parameters of the used compounds a) type I - straddling gap b) type II - staggered and c) type III - broken gap heterostructure based on alternating materials with different band parameters.

material with the higher bandgap is the Al containing compound (figure 2.1 a). Depending on the Al content the bandgap of the barrier material can be tuned. For other material combinations such as InAs/GaSb or InAs/AlSb depending on their band parameters type II (figure 2.1 b) or type III heterostructures are formed (figure 2.1 c). An essential band parameter is, besides the bandgap, the conduction band offset (CBO) which is the energy difference between the conduction band edge of material one and the conduction band edge of material two. For intersubband devices such as QCLs and QCDs the CBO limits the devices towards shorter wavelengths, hence higher optical transition energies. Type II structures are used for superlattice interband infrared detectors and ICLs.

Heterostructure growth of these materials is usually done by molecular beam epitaxy (MBE) or metal-organic chemical vapor deposition (MOCVD) on single crystalline substrates. The devices investigated in the scope of this thesis were grown from the InGaAs/InAlAs III-V material system lattice matched on InP substrate. Crystalline growth on single crystal substrates is subjected to constraints given by the lattice mismatch of the involved materials and their layer thicknesses.

Different lattice constants result in strained layers and may lead when the so called critical thickness is exceeded to growth modes which favor material nucleation in form of islands or strain relaxation dislocations. Figure 2.2 shows a map of common materials with their lattice constant and corresponding bandgap energy. Heterostructure growth is limited to material combinations in the close vicinity of vertical lines in the diagram. As illustrated GaAs and  $\text{Al}_x\text{Ga}_{1-x}\text{As}$  exhibit nearly the same lattice constant for all compositions and are therefore lattice matched. In the case of  $\text{In}_x\text{Ga}_{1-x}\text{As}$  and  $\text{In}_x\text{Al}_{1-x}\text{As}$  lattice matching or strain compensation is necessary to maintain layer by layer crystal growth, while the individual layer thickness has to stay below the critical layer thickness. Lattice matching is done by adjusting the composition of the alloy accordingly. Linear interpolation between the components following Vegard's law allows to adjust the lattice constant of a

ternary or quaternary alloy [106]. In case of strain compensation the layer strain has to be compensated before the critical thickness is reached, which results in layer relaxation and a change of the growth mode. By strain compensated growth the band parameters such as the conduction band edge  $E_c$ , the valence band edge  $E_v$  and the split off energy  $E_{SO}$  of the compounds can be altered. Thereby, the CBO can be increased to allow for short wavelength device designs [107]. A model for strained heterostructure growth is introduced in detail in [108].

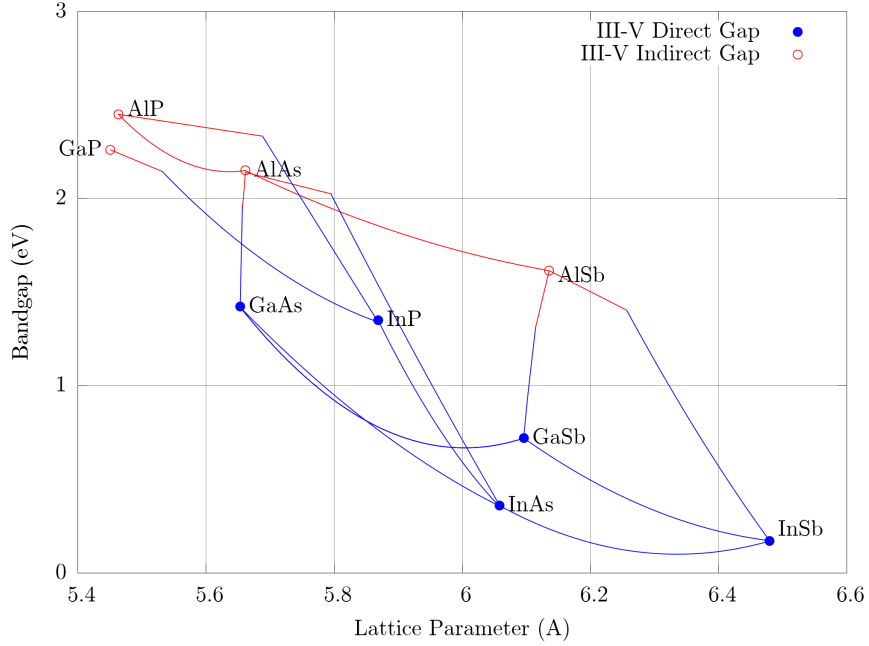


**Figure 2.2:** Common III-V materials, their lattice constants and bandgap energy. Materials with the same lattice constant are on a vertical line and lattice matched. The GaAs/AlAs system is lattice matched for alloy compositions of  $\text{Al}_x\text{Ga}_{1-x}\text{As}$  with various Al concentrations. The  $\text{In}_x\text{Ga}_{1-x}\text{As}/\text{In}_x\text{Al}_{1-x}\text{As}$  ternary alloys require a composition which is lattice matched to InP substrates. Reprinted with permission from A.M. Andrews.

**Molecular beam epitaxy** growth requires an ultra high vacuum (UHV) chamber and very pure single element material sources. The low pressure increases the mean free path of the atoms in the molecular beam, which minimizes their collisions on their way from the source to substrate to ideally zero. The different source materials are located in evaporation cells arranged hemispherically in the chamber facing the substrate. Cell types commonly used are the Knudsen effusion cell and so called thermal cracker cells for the As source. One key aspect of MBE growth is the precise control of the layer thickness of a grown material. Monolayers of atoms can be grown which corresponds to layer thicknesses of several Å up to nm. Vacuum

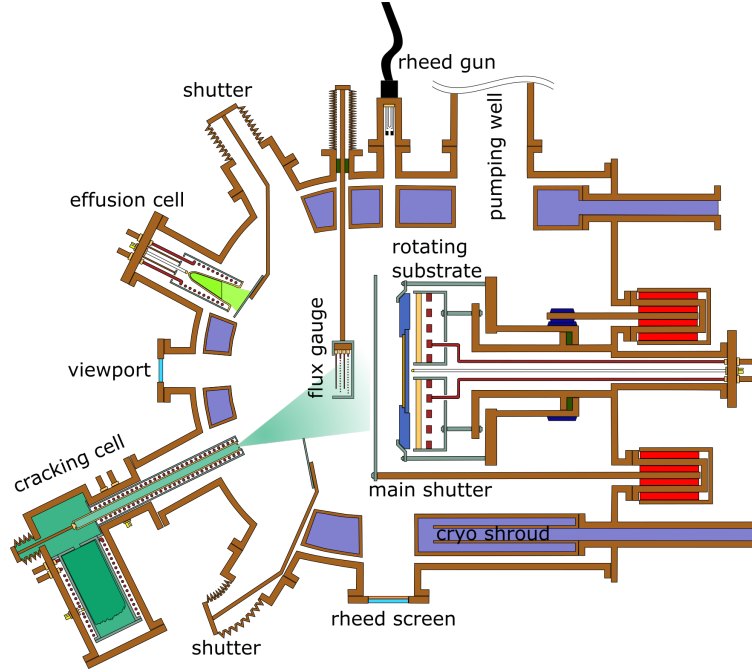


**Figure 2.3:** Schematic drawing of a MBE chamber with the effusion cell beam sources and the corresponding shutters. The sample is mounted on a heated constantly rotating mount facing the sources. A LN<sub>2</sub> cooled cryo shroud surrounds the chamber. The RHEED gun and the RHEED screen allow for monitoring reconstruction patterns. Figure printed with permission from T. Zederbauer [109].

quality, hence low pressures is a key aspect to ensure low background doping. The intentional doping concentration is controlled by the Si cell temperature which is calibrated by a hall measurement of the doping concentration in the calibration samples. Besides the vacuum level other key parameters for MBE growth include substrate temperature, shutter timing, beam flux and doping calibration. Due to the geometry of the growth chamber the sources are in different position relative to the substrate. As a result the grown heterostructure is not perfectly uniform at the wafer edges. Characterization of samples from different positions on a wafer thereby may lead to slightly varying results. The grown structures are characterized by X-ray diffraction and Hall carrier mobility and density measurements.

A schematic MBE chamber is sketched in figure 2.3 with the effusion cells containing the high purity materials, the heated rotated substrate holder and the shutters in front of the cells. Additionally to the shutters in front of the cells, a main shutter can cover the substrate from all source beams. The beam flux is controlled by the cell temperature and the opening times of the corresponding shutter. A reflection high energy electron diffraction (RHEED) gun and a monitor allow for surface reconstruction pattern monitoring. The cryo shroud is LN<sub>2</sub> filled and ensures the required vacuum quality by condensing remaining molecules in the chamber in combination



with other vacuum pumps. Typical growth rates are  $\mu\text{m/h}$  or monolayer/s.

## 2.2 Heterostructure calculation

Heterostructures for intersubband (ISB) devices consist of many coupled quantum wells to control electron confinement, electron wave functions and optical, tunneling- and scattering transitions. The device characteristics are designed and by simulations of these transitions based on manipulating the well and barrier geometrical dimensions in a given material system. Fundamental for the optical and charge carrier behavior in the crystal is the band structure of the semiconductor compound. This section introduces the essential basics of band structure and QW calculation.

### 2.2.1 Crystals

Crystals show distinct symmetry properties dependent on their crystal lattice. The primitive basis vectors  $\vec{a}$ ,  $\vec{b}$  and  $\vec{c}$  define the structure and the direct lattice vector  $\vec{R}$ . The lattice is invariant under any linear combination

$$\vec{R} = m\vec{a} + n\vec{b} + o\vec{c} \quad (2.1)$$

$$\vec{G} = j\vec{a}^* + k\vec{b}^* + l\vec{c}^* \quad (2.2)$$

with  $m$ ,  $n$  and  $o$  and  $j$ ,  $k$ ,  $l$ , being integers. The reciprocal lattice can be defined in a very similar way with the reciprocal basis vectors  $\vec{a}^*$ ,  $\vec{b}^*$  and  $\vec{c}^*$  defining the reciprocal lattice vector  $\vec{G}$ . The reciprocal lattice vectors are normal on the lattice planes in the direct lattice [101].

Many III-V semiconductors crystallize in a zincblende lattice structure, which is formed by two face centered cubic (fcc) primitive cells from two different materials. The two fcc primitive cells are shifted and intersect each other. Figure 2.4 depicts such a zincblende lattice which is also the crystal lattice of GaAs/AlGaAs and InGaAs/InAlAs.

### 2.2.2 Bloch theorem

Since single crystals are highly periodic structures, according to Bloch's theorem the wave functions and electronic potentials in the solid crystal reflect the periodicity of the lattice. The potential distribution in the crystal lattice is periodic with the same periodicity as the lattice. Considering a lattice vector  $\vec{R}$  the potential can be

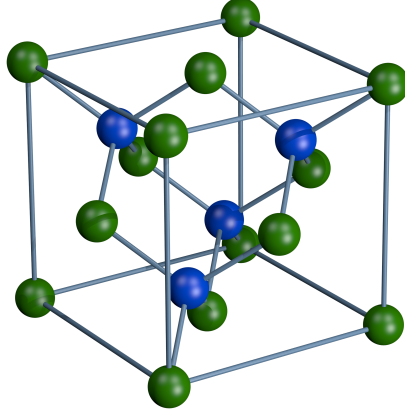


**Figure 2.4:** Zincblende lattice formed by two face centered cubic (fcc) primitive cells shifted and intersecting each other. Picture taken from [110].

written as

$$V(\vec{r}) = V(\vec{r} + \vec{R}) = T_R V(\vec{r}) \quad (2.3)$$

where  $\vec{R}$  is the periodicity of the lattice. This translation symmetry is equivalent to the application of a translational operator  $T_R = e^{i\vec{k} \cdot \vec{R}}$ , where  $\vec{k}$  is the wave vector, a point in the reciprocal space. Similarly we can expect wave functions, the solutions of Schrödinger's equation to be periodic as well

$$\Psi(\vec{r}) = \Psi(\vec{r} + \vec{R}) = T_R \Psi(\vec{r}) \quad (2.4)$$

having the same periodicity  $\vec{R}$ . Therefore, according to Bloch's theorem the solution of the Schrödinger equation for the periodic structure is of the form

$$\Psi(\vec{k}) = e^{i\vec{k} \cdot \vec{r}} u(\vec{r}) \quad (2.5)$$

with the plane wave  $e^{i\vec{k} \cdot \vec{r}}$  and a function  $u(\vec{r})$  with the periodicity of the potential. Wave functions of the form of equation (2.5) are called Bloch functions.

### 2.2.3 Band structure

Band structure computations can be complex and time consuming to an extent that simplified models are necessary or even not avoidable. A variety of models have been introduced in literature with different approximations. Dependent on the device type and energy range a choice has to be made. One common method is the tight binding model (TBM) which considers the outer shell orbitals of an atom of a 1-atom problem expanded to a many atom problem [111]. It considers  $N$  atoms and is based on an atomic Hamiltonian with a perturbation term. An example for

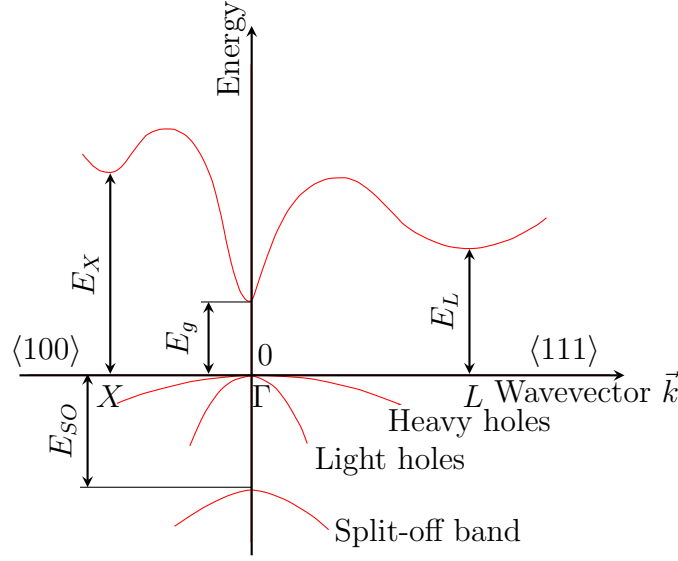


**Figure 2.5:** Band structure of InGaAs, a direct gap semiconductor with the conduction band and valence bands. The symmetry points  $\Gamma$ ,  $X$  and  $L$  denote crystal directions in the lattice. Image modified from [17].

a band structure is illustrated for InGaAs in figure 2.5. Essential parameters are the bandgap  $E_g$ , the valley energies  $E_x$ ,  $E_L$  the split-off band energy  $E_{SO}$  and the band shapes, where the valleys are at distinct high symmetry points ( $X, L$ ) of the first Brillouin zone.

**The pseudo potential method** approximates the atomic core influence on the valence electrons with an effective 'pseudo potential'. The effect of the neighboring atoms in the lattice on the strongly localized core electrons of the atoms is small, which makes the approximation valid. The filled core orbitals shield the outer valence electrons from the nucleus. This allows to overcome the computation of fast valence electron oscillations in the vicinity of the core. These would require a high spatial resolution when computing the atomistic model. Using the pseudo potential method the valence and conduction band can be modeled. A detailed source for this method including model parameters for various materials is [112].

**The  $\mathbf{k} \cdot \mathbf{p}$  method** relies on the expansion of known solutions of Schrödinger's equation at  $\vec{k} = \vec{k}_0$  for other values of  $\vec{k}$ . Thus an expansion of a known solution at the  $\Gamma$  point. This solution includes several bands  $n$  at different energies. The Schrödinger equation for a crystal including spin-orbit coupling reads

$$\left( \frac{p^2}{2m_0} + V(\vec{r}) + \frac{\hbar}{4m_0^2c^2}(\sigma \times \vec{\nabla}V) \cdot \vec{p} \right) \Psi_n(\vec{k}, \vec{r}) = E_n(\vec{k}, \vec{r}) \Psi_n(\vec{k}, \vec{r}) \quad (2.6)$$

with the wave function  $\Psi(\vec{k}, \vec{r})$ , the potential  $V(\vec{r})$ , the reduced Planck constant  $\hbar$ , the speed of light  $c$ , the Pauli matrix  $\sigma$  and the Hamiltonian including spin-orbit coupling.

The momentum operator  $\vec{p} = -i\hbar\vec{\nabla}$  applied to a Bloch function for a solution  $n$  gives

$$-i\hbar\vec{\nabla} \cdot (e^{i\vec{k} \cdot \vec{r}} u_{n,k}(\vec{r})) = e^{i\vec{k} \cdot \vec{r}} (\vec{p} + \hbar\vec{k}) u_{n,k}(\vec{r}) \quad (2.7)$$

Using the Bloch function Ansatz for a solution  $\Psi_n(\vec{k}, \vec{r})$  the equation reads

$$\left( \frac{p^2}{2m_0} + V(\vec{r}) + \frac{\hbar}{m_0} \vec{k} \cdot \vec{p} + \frac{\hbar}{4m_0 c^2} (\sigma \times \vec{\nabla} V) \right) u_{n,k}(\vec{r}) = \left( E_{n,k} - \frac{\hbar^2 k^2}{2m_0} \right) u_{n,k}(\vec{r}) \quad (2.8)$$

The Hamiltonian can now be grouped to the following components with spin-orbit coupling neglected

$$H = H_1 + H_2 \quad (2.9)$$

$$H_1 = \frac{p^2}{2m_0} + V(\vec{r}) \quad (2.10)$$

$$H_2 = \frac{\hbar}{m_0} \vec{k} \cdot \vec{p} + \frac{\hbar}{4m_0 c^2} (\sigma \times \vec{\nabla} V) \quad (2.11)$$

Here  $H_1$  is  $\vec{k}$  independent and  $H_2$  the  $\vec{k}$  dependent part of the Hamiltonian. The Kane model defines a space spanned by known solutions  $u_{n,0}(\vec{r})$ , at  $\vec{k} = \vec{k}_0$  for the basis functions  $u_{n,k}$  of equation (2.8).

$$u_{n,k}(\vec{r}) = \sum_{n'} b_{n'}(\vec{k}, \vec{k}_0) u_{n',0}(\vec{r}) e^{i(\vec{k} - \vec{k}_0) \cdot \vec{r}} \quad (2.12)$$

where  $b_{n'}$  are the expansion coefficients for the known solutions at the  $\Gamma$  point. The expansion is done for  $n'$  bands. The  $\vec{k}$  dependent part of the Hamiltonian  $H_2$  from equation (2.11) and the term  $\frac{\hbar^2 k^2}{2m_0}$  from equation (2.8) can be handled as perturbations.

The perturbation approach works in general very well for small values of  $k$ , hence near to the  $\Gamma$ -point. With a number  $n$  of  $u_n$  which defines a complete set of basis functions the band structure for all  $\vec{k}$  can be calculated. Spin-orbit coupling has to be considered for accurate band structure results.

An introduction to the method is given in [102] and detailed explanations of the  $k \cdot p$  theory including spin-orbit coupling can be found in [113].

**Effective mass approximation** Following the  $k \cdot p$  approximation as introduced before, for small values of  $\vec{k}$  where the perturbation expansion around  $k_0$  is valid an effective mass  $m^*$  can be introduced. The second order perturbation without

spin-orbit coupling is

$$u_{n,k} = u_{n,0} + \frac{\hbar}{m_0} \sum_{n' \neq n} \frac{\langle u_{n,0} | \vec{k} \cdot \vec{p} | u_{n',0} \rangle}{E_{n,0} - E_{n',0}} u_{n',0} \quad (2.13)$$

and for the energy it reads

$$E_n(\vec{k}) = E_n(0) + \frac{\hbar^2 k^2}{2m_0} + \frac{\hbar^2}{m_0^2} \sum_{n' \neq n} \frac{\langle u_{n,0} | \vec{k} \cdot \vec{p} | u_{n',0} \rangle}{E_{n,0} - E_{n',0}} \quad (2.14)$$

For small values of  $\vec{k}$  the energy can be expressed as

$$E_n(\vec{k}) = E_n(0) + \frac{\hbar^2 k^2}{2m^*} \quad (2.15)$$

where  $m^*$  is defined as the effective mass for the energy band  $E_n$ . The effective mass is then defined as

$$\frac{1}{m^*} = \frac{1}{m} + \frac{2}{m^2 k^2} \sum_{n' \neq n} \frac{\langle u_{n,0} | \vec{k} \cdot \vec{p} | u_{n',0} \rangle}{E_{n,0} - E_{n',0}}. \quad (2.16)$$

For the conduction band  $E_c(\vec{k})$ , when the valence band is approximated by a single band with the Kane energy defined as

$$E_P = \frac{2}{m_0} |\langle u_{n,0} | p | u_{n',0} \rangle|^2 \quad (2.17)$$

and  $E_g = E_{n,0} - E_{n',0}$ , equation (2.14) can be rewritten to

$$E_n(\vec{k}) = E_n(0) + \frac{\hbar^2 k^2}{2m_0} \left( 1 + \frac{E_P}{E_g} \right) \quad (2.18)$$

which results in the effective mass for the one band model

$$\frac{1}{m^*} = \frac{1}{m} \left( 1 + \frac{E_P}{E_g} \right) \quad (2.19)$$

### 2.2.4 Envelope function approximation

Since quantum wells are heterostructures consisting of two materials the band structures and effective masses for the barriers and the wells in a superlattice are different. The envelope function approximation [103] is a method to calculate the confined energies in heterostructures without computations at an atomic level. It allows the

calculation of energy states using position dependent effective parameters for the different regions. The results are accurate for small values of  $\vec{k}$  around the band extrema in the Brillouin zone  $\Gamma, X, L$ . The wave functions in the two materials can be expressed as

$$\Psi_B(\vec{r}) = \sum_n F_n^B(\vec{r}) u_{n,0}^B(\vec{r}) \quad (2.20)$$

$$\Psi_W(\vec{r}) = \sum_n F_n^W(\vec{r}) u_{n,0}^W(\vec{r}) \quad (2.21)$$

with the Bloch functions  $u_n^B$  and  $u_n^W$ . The expansion is around  $\vec{k} = \vec{k}_0$  and states the sum over all considered band edge states  $n$ .

The transitions between the well and the barrier material are assumed to be ideal. Further, both regions are assumed to be crystalline in the same lattice type without lattice mismatch. The Bloch functions for the barriers and the wells are assumed to be equal, hence  $u_{n,0}^B(\vec{r}) = u_{n,0}^W(\vec{r})$ . In both cases the sum over  $n$  considered band edges is done in both the wells and barriers. The Bloch functions represent the local barrier/well periodicity, while the envelope functions show the heterostructure variation. The slowly varying envelope functions  $F_n^{B,W}(\vec{r})$  are to be determined. These functions  $F_n$  can be written as plane waves in the  $x, y$  - in plane direction

$$F_n^{B,W}(r_{\parallel}, z) = \frac{1}{\sqrt{S}} e^{(i\vec{k}_{\parallel} \cdot \vec{r}_{\parallel})} X_n^{B,W}(z) \quad (2.22)$$

with the in plane direction  $\vec{r}_{\parallel}$  and the in plane wave vector  $\vec{k}_{\parallel}$ . The growth axis is then in  $z$  direction with the interface between the barrier and the well at  $z = z_0$  and the boundary condition  $F_n^B(\vec{r}_{\parallel}, z_0) = F_n^W(\vec{r}_{\parallel}, z_0)$ . The wave functions have to be continuous at the interface. The Hamiltonian can then be written as

$$H = \frac{p^2}{2m_0} + \epsilon_B(z) V_B(\vec{r}) + \epsilon_W(z) V_W(\vec{r}) \quad (2.23)$$

with the potentials  $V_B(\vec{r})$  in the barrier and  $V_W(\vec{r})$  in the well multiplied by a Heaviside functions  $\epsilon_{B,W}(z)$  to switch the valid potentials. With the envelope function approximation band offsets for the barriers and the wells are obtained and effective masses for the heterostructure. With these the confined energy states for a heterostructure can be calculated. The envelope function approximation is described in more detail in [103].

### 2.2.5 Potential wells

With the envelope function approximation which provides the effective band parameters in a heterostructure the energy levels can be calculated. The barriers and quantum wells are the basic building block of heterostructure devices (figure 2.6 a). Ensembles of multiple coupled quantum wells define optical transition regions, superlattices, tunneling and scattering transitions and i.e. the charge transport in the device. A relatively simple way to illustrate the electronic states in a potential well or in a semiconductor heterostructure is the single uncoupled and undoped quantum well (QW). Figure 2.7 shows a schematic band diagram of the conduction band of two separated quantum wells with different well width. The wells are formed by alternating layers of materials (M1 and M2) with different bandgaps leading to the CBO. The discrete energy levels and electron wave functions can be calculated from Schrödinger's equation. In its general form (time dependent) it reads

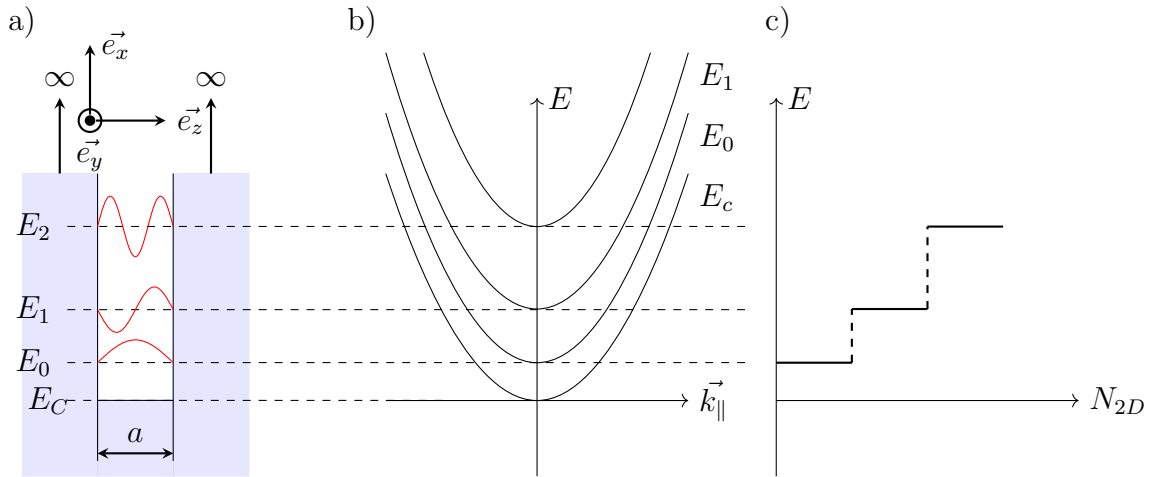


**Figure 2.6:** Ideal quantum well (QW) a) with infinitely high potential barriers and a well width of  $a$ . Inside the barriers the wave functions are zero  $\Psi_n(\vec{k}, \vec{r}) = 0$ . The in-plane wave vector  $\vec{k}_{\parallel}$  is normal to the growth direction (hence in the  $\vec{e}_x \vec{e}_y$  plane). The schematic in-plane conduction band structure b) over the in-plane wave vector. The density of states c) for the QW, hence a two dimensional system, with the electrons confined in  $\vec{e}_z$  direction over the energy showing the characteristic steps.

$$i\hbar \frac{\partial}{\partial t} |\Psi(\vec{r}, t)\rangle = H |\Psi(\vec{r}, t)\rangle \quad (2.24)$$

with the time and position dependent wave function  $\Psi$ , the reduced Planck's constant  $\hbar$  and the Hamiltonian  $H$ . For time independent and position dependent

potentials  $V(\vec{r})$  the separation ansatz

$$\Psi(\vec{r}, t) = f(t)\Psi(\vec{r}) \quad (2.25)$$

is justified. Thereby the time independent form can be deduced. In this case the QW can be calculated from

$$\left[ -\frac{\hbar^2}{2m_0} \vec{\nabla}^2 + V(\vec{r}) \right] \Psi(\vec{r}, \vec{k}) = E(\vec{k}) \Psi(\vec{r}, \vec{k}) \quad (2.26)$$

with mass  $m_0$ , the lattice dependent electric potential  $V(\vec{r})$  and the electron wave function  $\Psi(\vec{r}, \vec{k})$ . The solution of equation (2.26) with appropriate boundary conditions gives the electron wave functions in the well. For idealization of the infinitely high QW there are no evanescent penetrations of the wave function into the barrier, they are 0 at the interface and in the barrier. This requirement defines the boundary conditions at the interfaces. The potential in the ideal well with the interfaces at  $z = 0$  and  $z = a$  is defined as

$$\begin{aligned} z < 0, z > a : V(z) &= \infty \\ 0 \leq z \leq a : V(z) &= 0 \end{aligned} \quad (2.27)$$

With this idealization the energy levels in the well can be calculated as

$$E_n = \frac{\hbar^2 \pi^2}{2m^* a} n^2 \quad (2.28)$$

with the integer  $n$  denoting the energy level. The wave functions as solutions of equation (2.26) with the boundary conditions from equation (2.27) are then

$$\begin{aligned} z < 0, z > a : 0 \\ 0 \leq z \leq a : \Psi_n(z) &= A \cdot \cos\left(\frac{n\pi z}{a}\right) \end{aligned} \quad (2.29)$$

as illustrated in figure 2.6 for the ideal infinitely high barrier QW. In the barriers of a real structure the wave functions exponentially decay into the barrier material. Figure 2.7 shows the simulation result for two QWs with different width. The narrow well is 5 nm thick and the broader well 18 nm. The energy levels are numbered from the lowest level in a well  $E_0$  up to the higher levels. These energy levels  $E_n$  correspond to the  $\Gamma$ -point in  $\vec{k}$ -space. The functions plotted at the energy level positions in the wells are the absolute square of the electron wave functions.

$$\left| \Psi_n(\vec{r}, \vec{k}) \right|^2 = \Psi_n^*(\vec{r}, \vec{k}) \Psi_n(\vec{r}, \vec{k}) \quad (2.30)$$



where  $\Psi_n^*(\vec{r}, \vec{k})$  is the complex conjugate of the wave function. The example from figure 2.7 is calculated for the lattice matched grown InGaAs/InAlAs material system. The well material with the lower bandgap is InGaAs followed by the barrier layers grown from InAlAs with a higher bandgap energy  $E_g$ . The depth of the well is limited by the conduction band offset  $E_{\text{CBO}}$  between the two materials.

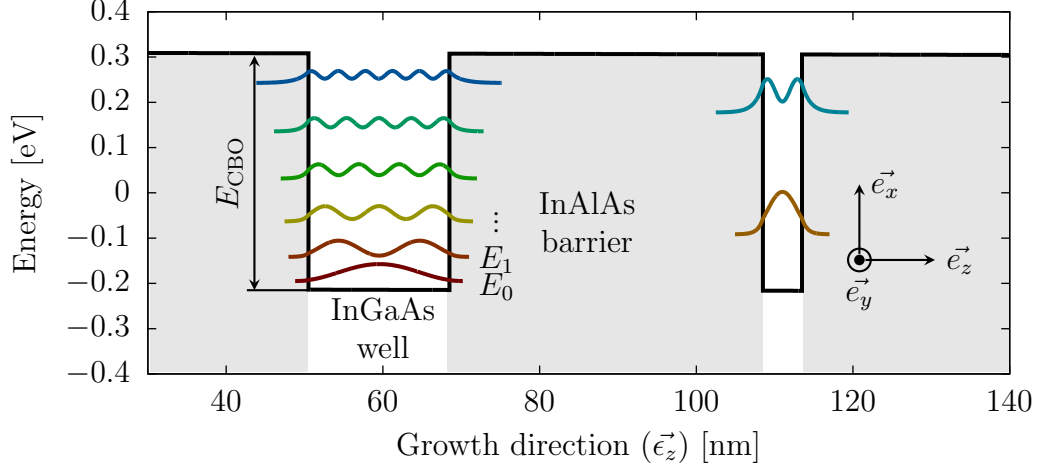


**Figure 2.7:** Two uncoupled quantum wells (QWs) consisting of two different materials which lead to the shown conduction band offset. For the narrow 5 nm wide QW the discrete energy levels have larger spacing as for the 18 nm broad well. Hence less bound states are in the well. The energy levels are numbered starting from the ground level  $E_0$  to higher energies. The gray shaded parts illustrate the barrier material.

## 2.3 Optical transitions

Optoelectronic semiconductor devices can be categorized depending on the optical transitions they are based on. Two different types of transitions are distinguished and lead to different characteristics in optical and charge transport design.

### 2.3.1 Interband and intersubband transitions

**Interband** Devices based either on interband (IB) or intersubband (ISB) transitions show different characteristics. Optical IB transitions elevate an electron from the valence band to the conduction band of the semiconductor or vice versa, in case that sufficient energy is provided to overcome the bandgap  $E_g$ . Figure 2.8 shows IB transitions for different  $\vec{k}$  values. For photon emitting devices such as LEDs and laser diodes, electrons in the conduction band recombine with holes in the valence

band and emit a photon at the wavelength

$$\lambda = \frac{ch}{E_g} \quad (2.31)$$

with the speed of light  $c$  and Planck's constant  $h$ .

Photon emission is either spontaneous or stimulated by another photon. Both, emission and recombination of a photon, requires a free final state for the electron involved in the transition. The optical transition is only possible if the momentum  $\vec{p} = \hbar\vec{k}$  matches or a scattering mechanism is provided to change the momentum of the electron to match the provided final state. This momentum requirement is illustrated in figure 2.8 by the vertical arrows showing possible transitions without momentum exchange. This type of transition is called a direct transition. The schematic band diagram in figure 2.8 (a) shows a direct bandgap semiconductor which is characterized by a conduction band minimum vertically aligned with the valence band maximum in the band structure. In indirect semiconductors the optical transitions between the valence band and the conduction band always need a scattering process to match the electron momentum. Interband devices with the transition energy determined by the bandgap energy  $E_g$  require a different bandgap for different operation wavelengths. Hence for bandgap detectors the photocurrent spectrum is material parameter dependent.

Interband absorption, i.e. optical electron - hole pair generation, is utilized by type-II superlattice detectors, photodiodes and photovoltaic cells. LEDs and Interband lasers such as laser diodes and ICLs are based on spontaneous and stimulated IB emission respectively.

**Intersubband transitions** are transitions between sub levels within the valence band or between sub levels in the conduction band of a semiconductor. Intersubband transitions in the conduction band are in general relevant for device applications because of the lower effective mass of the related electrons. Figure 2.8 b) illustrates the conduction band of a semiconductor with several allowed optical absorption transitions for different wave vectors  $\vec{k}$ .

For an optical transition the initial state wave function can be written as

$$\Psi^i = (\vec{r}) = F^i(\vec{r})u^m(\vec{r}) \quad (2.32)$$

and the final state of the optical transition

$$\Psi^f = (\vec{r}) = F^f(\vec{r})u^n(\vec{r}) \quad (2.33)$$

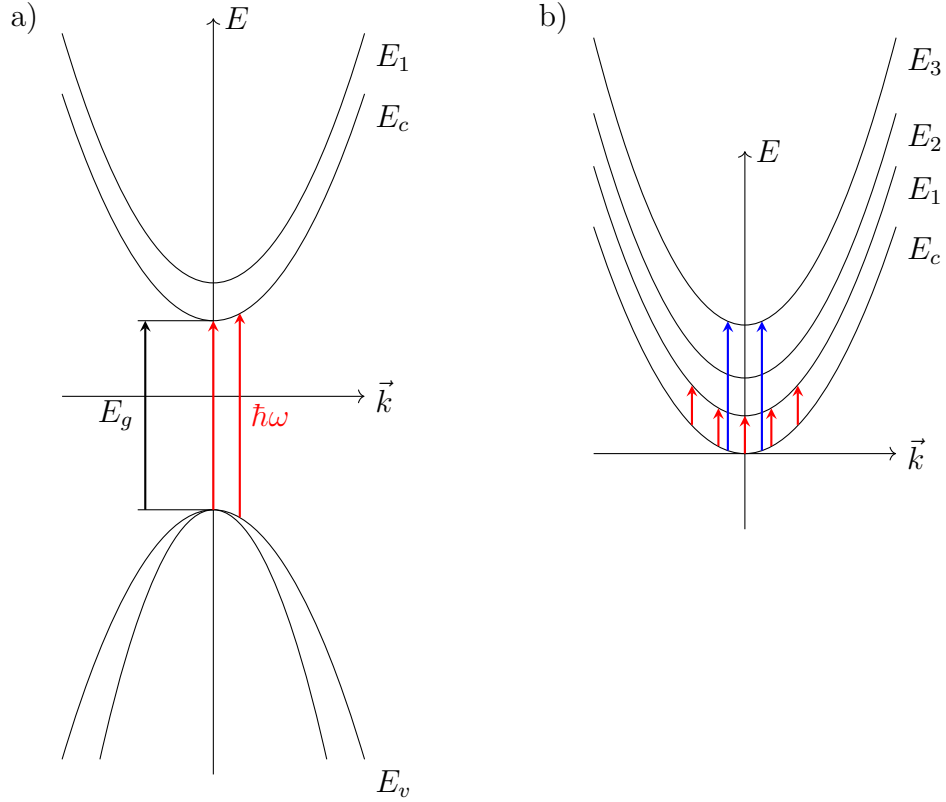


**Figure 2.8:** Optical a) interband transitions between valence band ( $E_v$ ) and conduction band ( $E_c$ ) states and b) intersubband transitions between states in the conduction band of a semiconductor.

with the envelope functions  $F^{i,f}(\vec{r})$  and the Bloch functions  $u^{m,n}(\vec{r})$ .

The Hamiltonian for the optical transition can be approximated as a perturbation of the heterostructure Hamiltonian  $H_0$  without the action of the light. The perturbation by the electromagnetic wave on the electron state is time dependent. According to Bastard [103] the total Hamiltonian reads

$$H = H_0 + V_p = H_0 + \frac{q}{2m_0c} [\vec{p} \cdot A_{\text{light}} + A_{\text{light}} \cdot \vec{p}] \quad (2.34)$$

with the elementary charge  $q$ , the electron mass  $m_0$ , the electron momentum  $\vec{p}$  and the vector potential of the light wave  $A_{\text{light}}$ . The transition probability  $P_{i,f}$  per unit time is expressed by Fermi's golden rule

$$\tilde{P}_{i,f} = \frac{2\pi}{\hbar} |\langle f | V_p | i \rangle|^2 \delta[E_f - E_i - \hbar\omega] \quad (2.35)$$

with the final state  $f$ , the initial state  $i$  and the corresponding energies of the states  $E_f$  and  $E_i$ . The perturbation Hamiltonian as consequence of the electromagnetic light wave is given by  $V_p$ . For heterostructure dimensions much smaller than the

photon wavelength the wave vector of the light can be neglected in equation (2.34) for the perturbation part  $V_p$ , which results in

$$V_p = \frac{qE_0}{2m^*\omega} \vec{\epsilon} \cdot \vec{p} \quad (2.36)$$

with the electromagnetic field polarization vector  $\vec{\epsilon}$  and the electric field amplitude  $E_0$  [114]. Inserting the perturbation term into equation (2.35) yields

$$\tilde{P}_{i,f} = \frac{2\pi}{\hbar} \frac{q^2 E_0^2}{4m^{*2}\omega^2} |\langle f | \vec{\epsilon} \cdot \vec{p} | i \rangle|^2 \delta[E_f - E_i - \hbar\omega] \quad (2.37)$$

with the matrix element  $|\langle f | \vec{\epsilon} \cdot \vec{p} | i \rangle|$ . If the expressions for the wave functions from equations (2.32) and (2.33) are included in the matrix element it reads

$$|\langle i | \vec{\epsilon} \cdot \vec{p} | f \rangle| = |\langle \Psi^i(\vec{r}) | \vec{\epsilon} \cdot \vec{p} | \Psi^f(\vec{r}) \rangle| = |\langle F^i(\vec{r}) u^m(\vec{r}) | \vec{\epsilon} \cdot \vec{p} | F^f(\vec{r}) u^n(\vec{r}) \rangle| \quad (2.38)$$

and further

$$\begin{aligned} \langle i | \vec{\epsilon} \cdot \vec{p} | f \rangle &= \langle F^i(\vec{r}) | \vec{\epsilon} \cdot \vec{p} | F^f(\vec{r}) \rangle \langle u^m(\vec{r}) | u^n(\vec{r}) \rangle + \langle F^i(\vec{r}) | F^f(\vec{r}) \rangle \langle u^i(\vec{r}) | \vec{\epsilon} \cdot \vec{p} | u^f(\vec{r}) \rangle \\ &= \langle F^i(\vec{r}) | \vec{\epsilon} \cdot \vec{p} | F^f(\vec{r}) \rangle \delta_{if} + \langle F^i(\vec{r}) | F^f(\vec{r}) \rangle \langle u^i(\vec{r}) | \vec{\epsilon} \cdot \vec{p} | u^f(\vec{r}) \rangle \end{aligned} \quad (2.39)$$

For the one band approximation the last expression in equation (2.39) can be split into an **ISB** and an **IB** part.

Note that the band occupations for the initial and final state have not yet been taken into account. For a photon absorption or emission an electron has to be present in the initial state and a free state available at the final state. The unit time probability for an electron to be absorbed is given by

$$P_{i,f} = \tilde{P}_{i,f} f(E_i) [1 - f(E_f)] \quad (2.40)$$

with the occupancy  $f(E)$  defined as the Fermi-Dirac distribution

$$f(E) = \frac{1}{1 + e^{\left(\frac{E_v - \mu}{k_B T}\right)}} \quad (2.41)$$

where  $k_B$  is the Boltzmann constant,  $T$  the temperature and  $\mu$  the chemical potential of the electrons.

**The intersubband selection rules** describe the allowed optical transitions between subbands. They impose significant light coupling restrictions on applicable optoelec-

tronic intersubband devices. For the one band case they can be deduced straight forward based on equation (2.39). For ISB transitions (figure 2.8 b) the Bloch function parts of the wave functions  $\Psi^{i,f}(\vec{r})$  are identical, hence  $u_m(\vec{r}) = u_n(\vec{r})$ . Equation (2.39) consists of two terms which in the one band model can be assigned to intersubband (ISB) and interband (IB) transitions.

$$\langle i | \vec{\epsilon} \cdot \vec{p} | f \rangle = \underbrace{\langle F^i(\vec{r}) | \vec{\epsilon} \cdot \vec{p} | F^f(\vec{r}) \rangle}_{ISB} \delta_{if} + \underbrace{\langle F^i(\vec{r}) | F^f(\vec{r}) \rangle \langle u^i(\vec{r}) | \vec{\epsilon} \cdot \vec{p} | u^f(\vec{r}) \rangle}_{IB} \quad (2.42)$$

For ISB devices the first term is relevant. According to equation (2.33) and (2.32) the wave functions can be split into a Bloch function and an envelope function  $F^{i,f}(\vec{r})$ . This envelope part can be expressed similar to equation 2.22 as

$$F^{i,f} = \frac{1}{\sqrt{S}} e^{i\vec{k}_{\parallel} \vec{r}_{\parallel}} \chi^{i,f}(z) \quad (2.43)$$

with the in plane wave vector  $\vec{k}_{\parallel}$  and the position vector  $\vec{r}_{\parallel}$ . The envelope function  $\chi^{i,f}(z)$  describes the electron motion in  $z$  direction. In the ISB case for the one band approximation the matrix from equation (2.42) element reads, again following Bastard

$$\begin{aligned} \langle i | \vec{\epsilon} \cdot \vec{p} | f \rangle &= \frac{1}{S} \int \chi_{n_i}^*(z) e^{-i\vec{k}_{\parallel} \cdot \vec{r}_{\parallel}} [\epsilon_x \vec{p}_x + \epsilon_y \vec{p}_y + \epsilon_z \vec{p}_z] \times \chi_{n_f}(z) e^{i\vec{k}_{\parallel} \cdot \vec{r}_{\parallel}} d^3r \\ &= \underbrace{(\epsilon_x \hbar k_x + \epsilon_y \hbar k_y) \delta_{n_i, n_f} \delta_{k'_{\parallel}, k_{\parallel}}}_{\gamma} + \epsilon_z \delta_{k'_{\parallel}, k_{\parallel}} \times \int \chi_{n_i}^*(z) \vec{p}_z \chi_{n_f}(z) dz \end{aligned} \quad (2.44)$$

with the conjugate complex envelope function  $\chi_{n_i}^*$  and the polarization vectors  $\epsilon_{x,y,z}$ . The first part in the second line of equation (2.44) (term  $\gamma$ ) is zero for transitions between two different bands. Hence light polarized in  $\epsilon_{x,y}$  direction does not couple to ISB transitions according to the one band model. The second part is dependent on light polarization in growth direction  $\epsilon_z$ . The expression  $\delta_{k'_{\parallel}, k_{\parallel}}$  is the requirement for momentum conservation. For light polarized in  $\vec{\epsilon}_x$  direction, hence in plane with  $\vec{\epsilon}_x \cdot \vec{p}$ , i.e. equation (2.44), leads to

$$\langle i | \vec{\epsilon}_x \cdot \vec{p} | f \rangle = \frac{1}{S} \langle \chi_i | \chi_f \rangle \hbar k_x \epsilon_x \delta_{k'_{\parallel}, k_{\parallel}} \quad (2.45)$$

which is zero for transitions between different states due to  $\langle \chi_i | \chi_f \rangle$ . A similar expression as equation (2.45) for light polarized in  $\vec{\epsilon}_y$  direction leads to zero as well.

With the **ISB** selection, hence the coupling to  $\vec{\epsilon}_z$  polarized light, the dipole matrix element for the optical transition can be expressed using equation (2.37) and (2.44) as

$$\tilde{P}_{i,f} = \frac{2\pi}{\hbar} \frac{q^2 E_0^2}{4} \epsilon_z^2 |\langle i | \vec{p}_z | f \rangle|^2 \times \delta_{k'_\parallel, k_\parallel} \delta(E_f - E_i - \hbar\omega) \quad (2.46)$$

In conclusion optical intersubband (**ISB**) transitions are sensitive only to light polarized in growth direction. For light detection photons from light polarized in  $\epsilon_z$  direction only, can excite electrons to a higher subband. Consequently **ISB** lasers emit light polarized in growth direction (so called transverse-magnetic (**TM**) polarized light). Since the calculations presented are based on the one band approximation, they do not account for relatively weak interactions with  $\epsilon_{x,y}$  polarized light which can be observed in specific measurements. H.C. Liu conducted comparative measurements to evaluate these **ISB** selection rules in practice with suitable sample geometries presented in [115].

## QUANTUM CASCADE DETECTORS

Mid-infrared detection has been under investigation for many years. The applicability of infrared light in a wide variety of fields promoted research on imaging and non-imaging detectors. A variety of detection technologies has been shown with diverse properties as discussed in more detail in the introduction. The quantum well infrared photodetector (QWIP) introduced in the 90s is up to now the most prominent example of an ISB detector. Based on the photovoltaic QWIP [42] and the four-zone model for photovoltaic QWIPs [116] both H. Schneider et al. and D. Hofstetter's report on the photoresponse of QCLs [43], the path for the quantum cascade detector (QCD) was set. Important milestones of QCD research were the design of room temperature detectors in various wavelength ranges [117, 118], the demonstration of high speed devices [119, 120, 121], broadband designs [122] and detectors fabricated from various material systems such as InGaAs/InAlAs [123], InAs/AlAsSb [124] and ZnCdSe/ZnCdMgSe [125].

This chapter starts with an introduction to the figures of merit, followed by the basic operation principle of a QCD the parameters and effects to consider for detector design are introduced. The trade-offs to be made are described and an example design optimized for the detector array presented in chapter 5 is discussed.

### 3.1 Figures of merit

The following section covers the basic figures of merit for infrared detection in general and are not limited to ISB detectors. Their application to QCD devices is then covered in the design section. These definitions are further used in the last section of the chapter where the device characterization methods are presented.

### 3.1.1 Comparability

For detector performance evaluation comparable figures of merit are necessary. They enable for comparison of devices designed for different device geometries, coupling methods and detector dimensions. Performance evaluation is commonly done based on the responsivity measured in A/W for detectors in current amplification/measurement mode or V/W for devices in voltage amplification/measurement mode. The second figure of merit is referred to as detectivity and related to the signal to noise ratio (SNR) of the detector commonly given in Jones = cm $\sqrt{\text{Hz}}$ /W.

### 3.1.2 Responsivity

The responsivity  $R$  of a detector is defined as the output photocurrent or output photovoltage per incident radiation power in W. In current operation mode it is expressed as

$$R = \frac{I_{\text{ph}}}{P_i} \quad (3.1)$$

with the photocurrent  $I_{\text{ph}}$  and the incident radiation power  $P_i$ . For detectors in voltage operation mode it is defined in a similar way. In general the responsivity  $R(\lambda)$  is wavelength dependent, with the spectral response around the peak responsivity  $R_P$ . Hence, the peak responsivity  $R_P$  is the maximum of  $R(\lambda)$ .

### 3.1.3 Detectivity

The detectivity  $D$  of a photodetector gives information about the noise performance of the device, hence the signal to noise ratio (SNR). It complements the responsivity and is commonly plotted over the operation temperature range of the device. The detectivity  $D$  can be expressed as

$$D = \frac{R_P}{i_n} \quad (3.2)$$

with the peak responsivity  $R_P$  and the root mean square noise current  $i_n$ . This is essentially the SNR for 1 W optical power incident on the detector. The specific detectivity  $D^*$  is then introduced as

$$D^* = D\sqrt{A\Delta f} = \frac{R_P}{i_n}\sqrt{A\Delta f} \quad (3.3)$$

with the measurement bandwidth  $\Delta f$  and the total detector area  $A$ . The specific detectivity normalizes the detectivity with respect to the device area and the measurement bandwidth and is used for comparison between devices with different



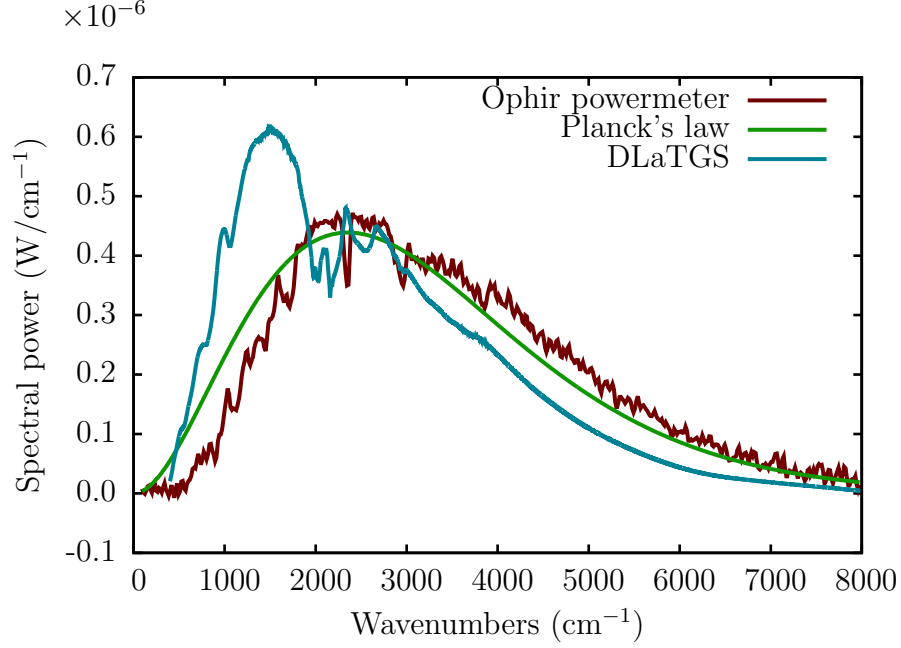


**Figure 3.1:** Spectral power density spectrum of the global source measured with the internal deuterated triglycine sulfate (DTGS) detector of the FTIR and the external Ophir power meter in comparison to Planck's radiation law. External measurements include the characteristics of the beamsplitter.

geometries. The measurement bandwidth can be related to the integration time  $\tau_{\text{int}}$  by

$$\Delta f = \frac{1}{2\tau_{\text{int}}} \quad (3.4)$$

Quantum cascade detector (QCD) detectivity is strongly related to the operation temperature of the device. In general with lower temperature the specific detectivity  $D^*$  increases, hence  $D^* \propto \sqrt{R_0(T)}$ , with the differential resistance  $R_0$  at zero bias. This increase towards lower temperatures is limited at  $T_{\text{BLIP}}$ . For operation temperatures over  $T_{\text{BLIP}}$  the detector noise limits the SNR. This regime is referred to as detector limited detection. At temperatures below  $T_{\text{BLIP}}$  the background radiation impinging the device is the dominating noise contribution which limits the detectivity at  $D_{\text{BLIP}}^*$ . The temperature  $T_{\text{BLIP}}$  is defined as the temperature, where the background limited detectivity equals the detector limited detectivity. The background limited detectivity for QCDs can be expressed as

$$D_{\text{BLIP}}^* = \frac{R_P}{\sqrt{2q^2 g_p \int g_p \eta_{\text{abs}}(v') \frac{d\Phi(v')}{dv'} dv'}} \quad (3.5)$$

with the peak responsivity  $R_P$ , the elementary charge  $q$ , the absorption efficiency  $\eta_{\text{abs}}$  and the spectral background photon flux density  $\frac{d\Phi(v')}{dv'}$  and the photodetector

gain  $g_p$  [126]. The photodetector gain is known from QWIPs where it is referred to as photoconductive gain

$$g_p = \frac{p_e}{N_{\text{Per}} p_c} \quad (3.6)$$

with the extraction efficiency  $p_e$  and the capture probability  $p_c$ . For the photodetector gain for QCDs a capture probability of  $p_c \approx 1$  can be assumed. This assumes a unity probability for an electron scattered down the LO-phonon staircase to make the transition to the ground level of the next active well. This corresponds to the transition from F to A' in figure 3.2.

For QCDs in photovoltaic operation, Johnson noise is the dominant noise contribution in detector limited operation. The specific detectivity which accounts for this noise type is denoted

$$D_J^* = R_P \sqrt{\frac{AR_0}{4k_B T}} \quad (3.7)$$

with the Boltzmann constant  $k_B$  and the device temperature  $T$ . It can be seen that the detectivity is directly proportional to the peak responsivity and proportional to the square root of the differential resistance detector area product. Among other aspects introduced in section 3.2 a main design challenge for QCDs is to achieve a high  $R_P$  while the resistance stays comparable high.

### 3.1.4 Noise equivalent temperature difference

The noise equivalent temperature difference (NETD) is a SNR based figure of merit mostly used in imaging applications. The NETD is based on the noise equivalent power (NEP)

$$\text{NEP} = \frac{i_n}{R} \quad (3.8)$$

with the responsivity  $R$ . The NEP gives the detector input radiation power which is equivalent to the noise power. The NETD is the required change in temperature of the input signal radiation source which equals the NEP [127, 128]. It is defined by

$$\text{NETD} = \frac{\text{NEP}}{dP/dT} = \frac{k_B T^2}{h\nu} \frac{N_N}{N_S} \quad (3.9)$$

with the number of noise electrons  $N_N$ , the number of signal electrons  $N_S$  and the frequency  $\nu$ . For an ideal photoconductor according to [127] this can be expressed as

$$\text{NETD} = \frac{k_B T^2}{h\nu} \sqrt{\frac{2g_p}{N_S}}. \quad (3.10)$$

### 3.1.5 Spectral width and coupling properties

The detectivity or [NETD](#) and the responsivity gives comparison data to evaluate the detector performance for an application. In addition to these figures of merit the performance data should be complemented by the spectral width of the response. For chemical sensing and absolute temperature measurements, multiple narrowband detectors or a single multicolor narrowband detector is favorable. For pure temperature difference imaging commonly commercially available single color broadband thermal detectors are used. A standard way to express the width of the spectral response for relatively narrow band detectors is the full width at half maximum ([FWHM](#)). For broadband detectors with a non flat response, a plot of the spectral responsivity is needed.

Light coupling properties range from incidence angle to polarization selectivity. Imaging devices require surface normal incident radiation to be detected due to their orientation towards the scene and the involved objective and pixel array. In case of [ISB](#) detectors such as [QWIPs](#) and [QCDs](#) additional light coupling structures are required to allow radiation coupling to [ISB](#) transitions. A selection of applicable methods for that purpose is presented in chapter 4. The polarization selectivity of a detector device has to be considered in setups which involve the detection of linearly polarized light e.g. emitted from [QCLs](#).

## 3.2 Device principles

In this section, first, the basic operation principle is introduced with a generic device. Then, the effects and parameters that have to be considered during design are introduced. Consequently, design trade-offs and optimization strategies are presented with an example design.

**The quantum cascade detector (QCD)** is a photovoltaic intersubband detector for unbiased or near zero bias operation. It consists of 20 up to 30 periods of the same heterostructure segment called a period. One period consists of an active well in which the optical intersubband ([ISB](#)) transition takes place and an extractor region for charge carrier transport. The [QCDs](#) fabricated and characterized in the scope of this thesis are based on the InGaAs/InAlAs material system. Figure 3.2 shows a schematic [QCD](#) design for a peak detection wavelength of 6  $\mu\text{m}$ . The optical transition takes place in well A. The impinging photons of matching wavelength are absorbed and electrons are elevated from the lower level (level 1) to the excited level

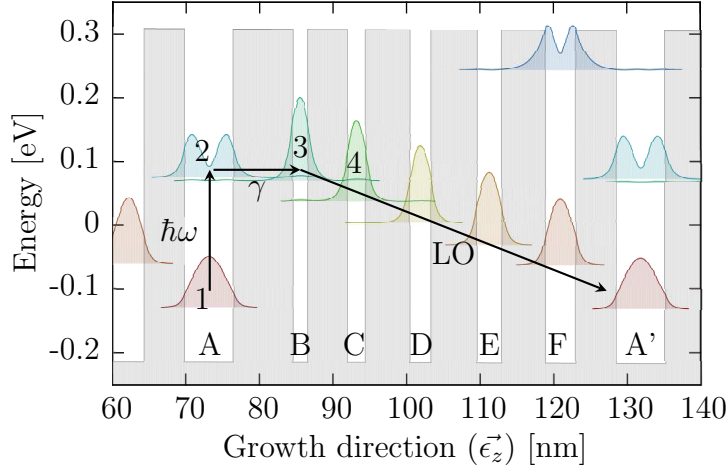


**Figure 3.2:** A standard QCD design with resonant tunneling extraction. The active well A with the optical transition  $\hbar\omega$  corresponding to  $\lambda = 6\ \mu\text{m}$  between level 1 and 2. The excited electrons are extracted by resonant tunneling from QW A to B via transition  $\gamma$  to level 3. The extracted carriers scatter down the extractor levels by LO-phonon scattering (arrow LO). After the LO-phonon extraction the electrons are scattered to the ground level of the active well of the next period (A').

(level 2) in QW A. The transition energy between the two levels corresponds to

$$E_{\text{Opt}} = \hbar\omega = \frac{hc}{\lambda} \quad (3.11)$$

with the reduced Planck constant  $\hbar$ , the light angular frequency  $\omega$  or alternatively the Planck constant  $h$ , the speed of light  $c$  and the light wavelength  $\lambda$ . According to that the transition energy is  $\approx 204\ \text{meV}$ .

From the excited level 2 in QW A, the electrons are extracted to QW B by resonant tunneling to level 3. From there, the photo excited electrons are scattered, dominantly by longitudinal optical (LO) phonons, from B to C and D and so on. Finally they reach the ground level (lower level) of the active well of the next period A'. There, the carriers can be excited again by photon absorption and the described process repeats. The states B-F which form the extractor LO-phonon ladder of the period are spaced by the LO-phonon energy  $E_{\text{LO}}$ . Hence, the level in QW B is  $E_{\text{LO}}$  higher than the level in C. The active well of the period (A/A') is Si doped to provide sufficient carriers to excite under illumination. The extractor stages which transport the excited carriers to the next period lead to a net current transport in the heterostructure. Due to this built in field, carrier transport is possible without external bias. The active zone (AZ) consists of  $N_{\text{Per}}$  periods sandwiched between highly doped contact layers with GeAuNiAu ohmic contacts on both sides. The contacts inject and extract electrons which results in the external measured photocurrent.

The design shown in figure 3.2 is a vertical transition resonant tunneling extraction design with a single extractor level in QW B and LO-phonon transitions from B down to A'. The doping is placed in the active wells (A, A'). The design is with all levels aligned for 300 K operation temperature.

### 3.2.1 Responsivity

Quantum cascade detectors have in comparison to photoconductive QWIPs a lower responsivity. Nevertheless, QCDs offer the advantage of detection in a wide power range of the incident radiation without saturation effects. The responsivity for a QCD based on its design parameters can be expressed as

$$R_P = \frac{\lambda q}{hc} \eta_{\text{abs}} g_p \quad (3.12)$$

with the speed of light  $c$ , the absorption efficiency  $\eta_{\text{abs}}$  and the photodetector gain  $g_p$  according to equation (3.6). At a fixed design wavelength for responsivity optimization the absorption efficiency  $\eta_{\text{abs}}$ , the extraction efficiency  $p_e$  and the number of periods  $N_{\text{Per}}$  in the AZ can be adjusted.

To increase the responsivity for a given wavelength, the absorption efficiency  $\eta_{\text{abs}}$  can be altered by the coupling scheme and the cavity design. The doping concentration is an extra parameter which impacts the absorption efficiency. Alternatively the number of periods  $N_{\text{Per}}$  can be decreased or the extraction efficiency  $p_e$  increased by reducing the barrier thickness between well A and B (figure 3.2). The impact of these modifications onto the detectivity are described in section 3.2.8.

### 3.2.2 Extraction efficiency

The extraction efficiency  $p_e$  and the device resistance are the two major optimization parameters for high performance detectors. The extraction efficiency is the probability for an electron excited by photon absorption to be extracted to the LO-phonon ladder and be scattered down to the lower level of the next period (level 1 in A'). This probability at the first glance is most significant at the first extractor QW (B). It expresses the ratio between the number of photo excited electrons extracted by resonant tunneling to the number of excited photo electrons which scatter back to the ground level of the active zone (A) before they are extracted through path  $\gamma$  (figure 3.2). A naive approximation of the extraction efficiency can be made assuming the resonant tunneling extraction to be fast in comparison to the scattering

rates

$$p_e = \frac{\tau_{2,1}^{-1}}{\tau_{2,1}^{-1} + \tau_{3,4}^{-1}} \quad (3.13)$$

with the  $\tau_{2,1}$  the lifetime of transitions from level 2 to 1 and  $\tau_{3,4}$  for the transition from level 3 in well B to level 4 in well C (figure 3.2). This approximation is very inaccurate for elevated temperatures due to thermal induced backscattering of electrons e.g. from level 4 to level 3 which clearly impacts  $\tau_{3,4}$ . The Vienna Schrödinger Poisson (VSP) simulator model calculates the extraction efficiencies based on a ratio of carriers (electrons) reaching the next period and carriers being scattered back to the ground level of the optical transition. A period with its previous and following period is considered, hence a three period model.

For resonant tunneling extraction the barrier thickness and the level alignment is essential. A thin barrier between QW A and B leads to a high tunneling rate and extraction efficiency but a low device resistance.

### 3.2.3 Absorption efficiency

The light coupling geometry has major impact on the absorption efficiency  $\eta_{\text{abs}}$ . For standard characterizations to compare different device designs a  $45^\circ$  polished facet mesa geometry is used. Mesa type ISB devices are sensitive to TM polarized light only. Coupling geometries such as two dimensional diffraction gratings, which couple unpolarized light can exceed the absorption efficiency of mesa devices significantly. Light coupling for different designs is covered in chapter 4. Absorption efficiency can be limited by a low carrier concentration in QW A (figure 3.2) even if a sufficient doping concentration was applied. This effect can be attributed to thermal excitation of carriers to the previous periods extractor levels, called thermal backfilling.

**Thermal backfilling** For device designs with equally spaced LO-phonon steps down to the next active well with equally  $\approx 34$  meV spacing, the responsivity drops for elevated temperatures. The carriers in the ground level of the active well get excited to the last ladder level of the previous period. Hence the carrier concentration spreads between the active well ground level and the last extractor state of the previous level. This reduces the available carriers for optical excitation and reduces the absorption. As a result the responsivity drops.

This effect can be reduced by designing the last step between these levels to have a larger energy separation i.e.  $\Delta E > 34$  meV. This reduces the thermal excitation of carriers to the previous period and prevents a performance drop due to a reduced

carrier concentration in the active wells.

### 3.2.4 Noise

The noise characteristics of QCDs are responsible for their superior performance at elevated temperature and room temperature. Detection at 300 K is enabled by the built in field extraction of the photo excited carriers. In contrast to photoconductive QWIPs, QCDs exhibit nearly no dark current  $I_d$ . For read out and amplification this is an advantage since read out circuits are not saturated by dark current at elevated temperatures. Due to that, QCDs are considered as a promising detector type for focal plane array (FPA) integration.

**Dark current noise** is shot noise, hence Poisson distributed and according to Liu et al. [129] the mean square dark current noise can be expressed as

$$i_{\text{dark}}^2 = 4qg_n I_d \Delta f \quad (3.14)$$

with the dark current  $I_d$ , the measurement bandwidth  $\Delta f$  and the photodetector noise gain  $g_n = g_p$  for a conventional detector. To keep the dark current noise as low as possible under biased conditions a high device resistance is desired.

Due to the photovoltaic operation of QCDs above  $T_{\text{BLIP}}$ , Johnson-Nyquist noise is considered to be the main noise contribution. Dark current does not limit the performance of QCDs, if operated unbiased.

**Johnson Nyquist noise** contribution for unbiased operated QCDs is the limiting noise source above  $T_{\text{BLIP}}$ . The root mean square Johnson-Nyquist noise current is

$$i_{\text{J,n}} = \sqrt{\frac{4k_B T \Delta f}{R}} \quad (3.15)$$

with the Boltzmann constant  $k_B$ , the temperature  $T$ , the measurement bandwidth  $\Delta f$  and the resistance  $R$  [130].

**Background noise** Below  $T_{\text{BLIP}}$  the background radiation is the dominating noise source. For cooled detector array operation, the background radiation has to be limited. Commonly a cold shield is used which leaves only the field of view (FOV) open towards the imaged scene. Background noise is photon noise caused by carrier excitation due to the impinging background radiation emissivity. With the excited

carriers generating the noise photocurrent  $I_{\text{Ph},n}$  the photon noise mean square current can be expressed as

$$i_{\text{Ph},n}^2 = qg_n I_{\text{Ph},n} \Delta f \quad (3.16)$$

similar to equation (3.14). Besides that amplifier noise and other system noise sources have to be considered for optimization of an imaging device.

### 3.2.5 Resistance

Due to the dominance of Johnson-Nyquist noise the differential resistance  $R_0$  of a QCD directly impacts the specific detectivity  $D^*$  and all connected SNR based figures of merit. The device resistance is related to the barrier thicknesses and the coupling of the levels within a period and between the neighboring periods of the AZ. A. Delga showed a QCD resistance model [131] which is followed in the simulations. All ISB transitions are accounted to retrieve a equivalent resistance circuit of the AZ. This includes thereby all intentional transitions and also the possible parasitic transitions in a period and between the periods (inter-period transitions) [47, 132].

The main task for resistance optimization is to eliminate or minimize parasitic transitions within a period and between neighboring periods in the AZ design. A useful method to identify current paths in the heterostructure is to calculate or fit the activation energy  $E_A$  to the resistance plot over the temperature. Alternatively the resistance area product over the temperature is used. Transitions matching the activation energy dominate the resistance characteristics. Hence, a activation energy significantly lower than the optical transition energy is a hint for a parasitic transition.

### 3.2.6 Non radiative scattering mechanisms

Scattering leads to transitions between subbands or within a subband. They are referred to as intersubband (ISB) and intrasubband scattering processes respectively. These scattering mechanisms can be grouped to elastic processes such as ionized impurity, surface roughness scattering and non elastic processes such as phonon scattering. Intersubband transitions are dominated by non-radiative scattering transitions. Phonon, ionized impurity, interface roughness and electron-electron scattering are the major processes to be observed in ISB devices.

Scattering can be described again by Fermi's golden rule with an general interaction Hamiltonian describing the specific scattering process for intersubband



scattering

$$P_{i,f}^{inter} = \frac{1}{\tau_{i,f}} = \frac{2\pi}{\hbar} \sum \left\langle \left| \chi_{i,\vec{k}} \right| H_{\text{scatt}} \left| \chi_{f,\vec{k}'} \right|^2 \right\rangle \delta \left( E(i, \vec{k}) - E(f, \vec{k}') - \Delta E \right) \quad (3.17)$$

and intrasubband scattering

$$P_{i,f}^{intra} = \frac{1}{\tau_{i,f}} = \frac{2\pi}{\hbar} \sum \left\langle \left| \left( \chi_{i,\vec{k}} \left| H_{\text{scatt}} \right| \chi_{i,\vec{k}'} \right) - \left( \chi_{f,\vec{k}} \left| H_{\text{scatt}} \right| \chi_{f,\vec{k}'} \right) \right|^2 \right\rangle \delta \left( E(i, \vec{k}) - E(f, \vec{k}') \right) \quad (3.18)$$

with the scattering Hamiltonian  $H_{\text{scatt}}$  and the energies of the process which are conserved. For elastic scattering processes the energy  $\Delta E = 0$  and for inelastic scattering  $\Delta E \neq 0$ . The linewidth broadening introduced by the scattering mechanism can be described by

$$\Gamma_{i,f} = \frac{\hbar}{\tau_{i,f}} \quad (3.19)$$

The resulting linewidth, dependent on the **ISB** and intrasubband contribution is according to T. Ando [133] defined by  $\Gamma(E)_{\text{Op}} = 1/2(\Gamma(E)_{\text{intra}} + \Gamma(E)_{\text{inter}})$ , where the **FWHM** is given by  $2\Gamma_{\text{Op}}$ . The broadening introduced by the electron mobility  $\mu$  referred to as transport energy broadening

$$\Gamma_{\text{Tr}} = \frac{2\hbar}{\tau_{\text{Tr}}} = \frac{2\hbar q}{m^* \mu} \quad (3.20)$$

with the effective mass  $m^*$  is reported to be low in comparison to  $\Gamma_{\text{Op}}$  for GaAs wells at low temperature. For increasing temperatures towards room temperature the contribution of the mobility increases [133, 134].

**Phonon scattering** Phonons are lattice vibrations with the lattice atoms oscillating in longitudinal or transverse direction with respect to the phonon propagation direction. Depending on the displacement of the lattice atoms they are referred to as optical phonons or acoustic phonons. For the first neighboring atoms move in the opposite direction (in opposite phase) whereas for the second neighboring atoms are displaced in the same direction (in phase). Due to the lattice vibration the crystal potential is perturbed. The deformation of the lattice changes the potential which gives rise to a deformation potential. This perturbation can be described by the Fröhlich interaction.

**Longitudinal optical phonon scattering** or short LO-phonon scattering is the dominating process for polar III-V semiconductor compounds for levels spaced  $E >$

$E_{\text{LO}}$ . Two levels spaced in approximately  $E_{\text{LO}} = \hbar\omega_{\text{LO}}$  have a strongly reduced upper level lifetime. The oscillation of the polar lattice leads to a electric field which can be expressed as a potential which interacts with the electrons. This interaction is referred to as Fröhlich interaction. The scattering Hamiltonian  $H_{\text{scatt}}$  is described by

$$H_{\text{Fr}} = (-e)\phi_{\text{LO}} = (ieF/q)u_{\text{LO}} \quad (3.21)$$

For InGaAs and GaAs a LO-phonon energy of  $E_{\text{LO}} = 34\text{meV}$  and  $E_{\text{LO}} = 35\text{meV}$  respectively, can be assumed [17].

**Impurity scattering** Doping of the active well introduces ionized impurities at the doping position. The process of elastic scattering of charge carriers (electrons) on the Coulomb potential of these local charged impurities is called ionized impurity scattering [135]. The scattering rate is dependent on the doping concentration [136].

As the active well of the QCD is doped to provide sufficient carriers for photo excitation their influence to the upper state lifetime has to be considered. The doping position therefore has direct impact on the non radiative scattering time back to the ground level of the active well.

### 3.2.7 Doping concentration

The doping concentration has direct impact to the device resistance. High doping concentrations allow for higher absorption coefficients  $\alpha_{\text{isb}}$  and therefore an increased absorption efficiency which leads to a higher responsivity. The increased responsivity has clearly to be payed by a lower resistance which decreases the specific detectivity  $D^*$ . In standard QCD designs in contrast to bi-functional materials the active well is doped. Consequently, the design is more robust against over- or under-doping and the level alignments most importantly the extractor level alignment is maintained. The disadvantage of this method is the increased impurity scattering in the active well reducing the upper state lifetime and thereby the extraction efficiency.

### 3.2.8 Design trade-off

Based on the effects and parameters discussed in the previous section several trade-offs have to be made to optimize a detector design.

**Number of periods** The number of periods directly influences the responsivity if the absorption efficiency is kept constant. This can be seen from equations (3.6) and (3.12). Lets consider a design with a low number of periods e.g. between 1 and

10 periods, with additionally a reduced barrier thickness between the active well and the first extractor well to increase the extraction efficiency  $p_e$ . The result would be if all levels are aligned properly, a high extraction efficiency over  $\approx 50\%$  and a responsivity of several tens of mA/W for a modified state of the art III-V design. At the same time, due to the low number of periods the AZ would have about a third of the thickness of a design with 30 periods. Consequently, a very low resistance of the device is obtained. Additionally, the resistance decreases by the thinner barrier between the active well and the extractor stages. Recalling equation (3.7) the low resistance results in a low specific detectivity  $D^*$ . Moreover, the assumption of constant absorption efficiency is bad for mesa devices, since a lower number of periods reduces the already short absorption length which corresponds to the AZ thickness. This then leads to a lower absorption efficiency.

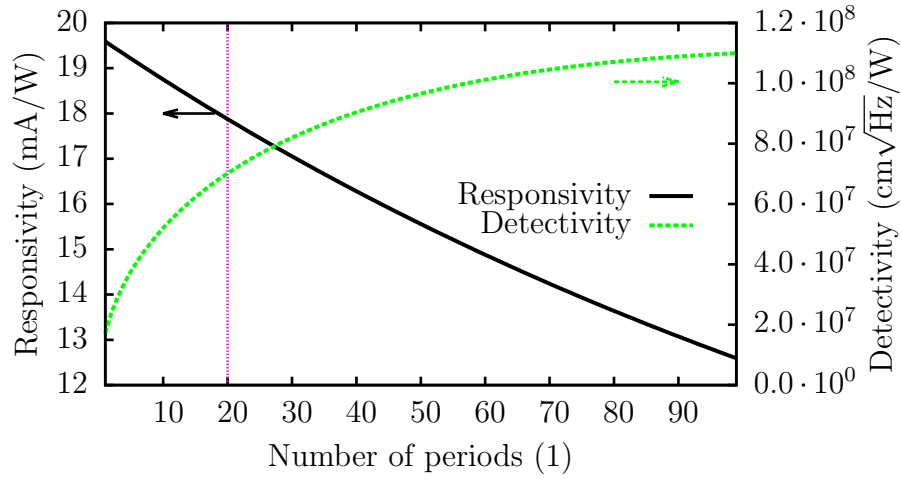


**Figure 3.3:** The impact of different numbers of AZ periods  $N_{\text{per}}$  on the Johnson noise limited specific detectivity  $D_j^*$  and the responsivity  $R_P$  for QCD design C0342, simulated in  $45^\circ$   $100\mu\text{m} \times 100\mu\text{m}$  mesa configuration. A good trade-off is at 20 up to 40 periods for mesa devices.

The same case can be observed for a pure detectivity improvement. If the number of periods is increased i.e.  $50 > N_{\text{per}}$  and all barriers are designed to be thick with low coupling between the QWs, the resistance  $R$  increases if we neglect parasitic transitions at this point. At the other hand the extraction efficiency  $p_e$  would be reduced. According to equation (3.6) the now high number of periods and the low extraction efficiency leads to a very low  $g_p$  in equation (3.12), hence a low responsivity.

This trade off is the classic QCD design challenge. F. Giorgetta has shown this first [128]. A simulation for the responsivity and detectivity for QCD design C0342 in mesa configuration and different numbers of periods  $N_{\text{per}}$  is depicted in figure

3.3. For this design, which is intended for grating coupling 20 periods were chosen. For grating coupling the absorption efficiency  $\eta_{\text{abs}}$  is higher in comparison to mesa devices. As a result the lower number of periods promotes the responsivity more efficiently.

A very similar observation can be made for the doping concentration. A high doped active well leads to an increased absorption coefficient  $\alpha_{\text{isb}}$  which increases the absorption efficiency  $\eta_{\text{abs}}$ . At the same time the device resistance is decreased, which again results in a lowered detectivity. In general 20 up to 30 periods is a good compromise.

**Active well design** The optical transition in the active well can be designed to be a vertical transitions between two bound levels 1 and 2 as depicted in figure 3.2. This design scheme is the standard resonant tunneling extraction method. Another option is a diagonal transition design demonstrated by Reininger et al. [137]. For diagonal optical transition QCDs the transition takes place between the ground level of the active well and the neighboring well. Thereby, the transition is directly to the first (highest energy) level of the extraction cascade and the design does not use resonant tunneling extraction.

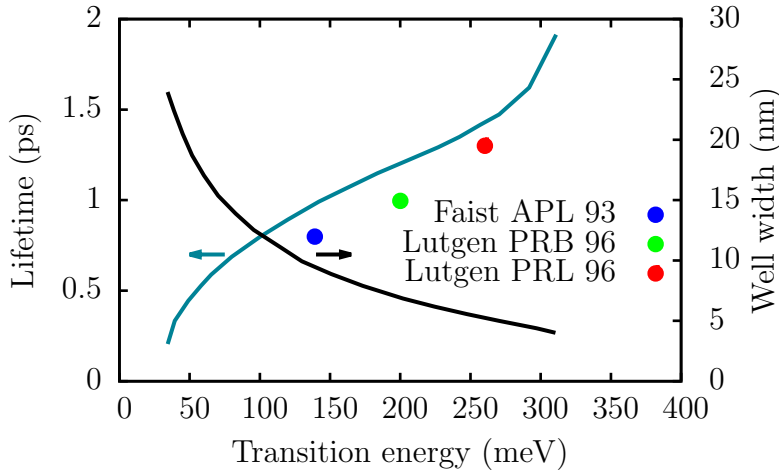


**Figure 3.4:** Lifetimes for non-radiative transitions in a quantum well for different transition energies and well widths. The solid lines are calculations and the dots literature data. Data from [100].

The diagonal transition scheme is more favorable for longer MIR wavelength QCD designs, since the non-radiative carrier lifetime of the vertical transition in the active well becomes shorter for low transition energies (figure 3.4). This means, that  $\tau_{2,1}$  becomes shorter and therefore the extraction efficiency  $p_e$  becomes lower. To investigate the performance difference between a vertical and a diagonal transition QCD for the  $4\mu\text{m} - 5\mu\text{m}$  wavelengths region, two designs [48] were compared. Sample C0115 is a vertical transition detector with the optical transition between levels 1 and 2 and the resonant tunneling extraction between levels 2 and 3 (figure 3.5 a).

Sample C0119 is a diagonal transition design with the optical transition between QWs A and B, hence between level 1 and 3 in figure 3.5 b. The carriers are then extracted from 3 directly towards QW A'. Due to the possible optical transition from the ground level 1 to level 2 in QW A (figure 3.5 b) diagonal transition designs show a secondary photocurrent peak at a shorter wavelength than the diagonal transition energy.

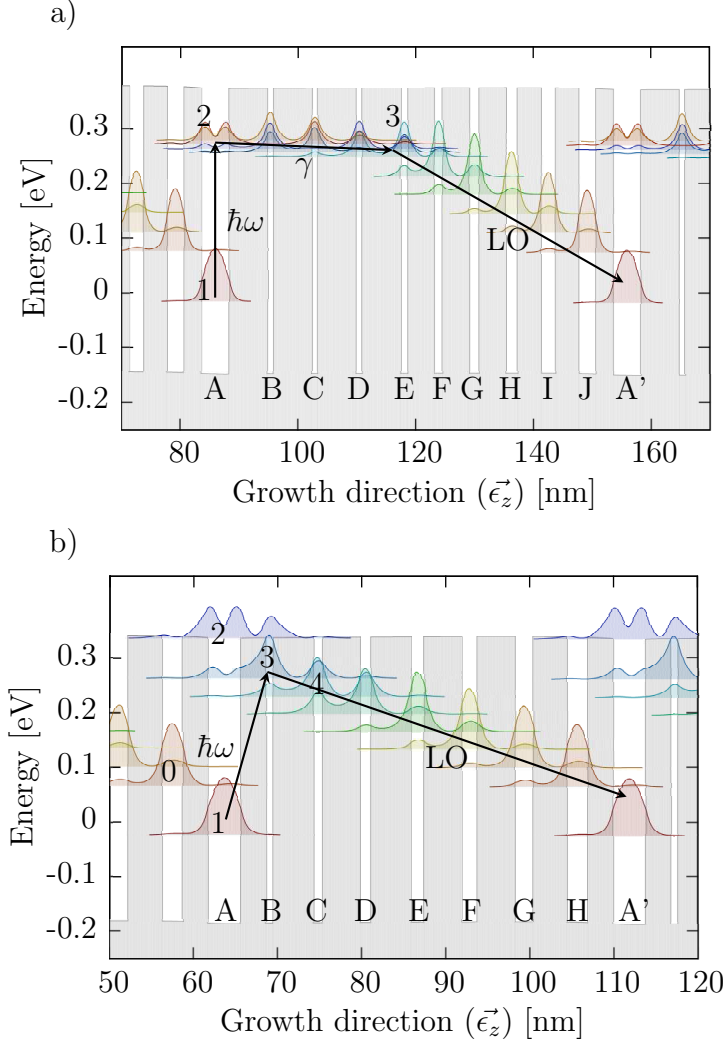


**Figure 3.5:** Comparison designs for short wavelengths QCDs around  $4.5\mu\text{m}$  wavelength. Vertical transition design C0115 a) with resonant tunneling extraction. Diagonal transition design C0119 similar to Reininger et al. [137] with the optical transition between well A and B. Due to the transition from 1 to 2 diagonal transition designs have a secondary photocurrent peak.

To compare the performances the room temperature photocurrent response for the diagonal and the vertical transition design was compared. The diagonal transition design shows a broader spectral response from  $3.5\mu\text{m}$  to  $5.5\mu\text{m}$ . The growth thickness variations of the narrow well B which defines the upper level (3), have more impact on the transition energy. The peak responsivity is approximately 25% lower than for the vertical transition design. Nevertheless, the total photocurrent response is higher due to the broadband character of the material. The second peak for C0119 at  $2700\text{ cm}^{-1}$  is due to the transition from 1 to 2 (figure 3.5 b). Carrier

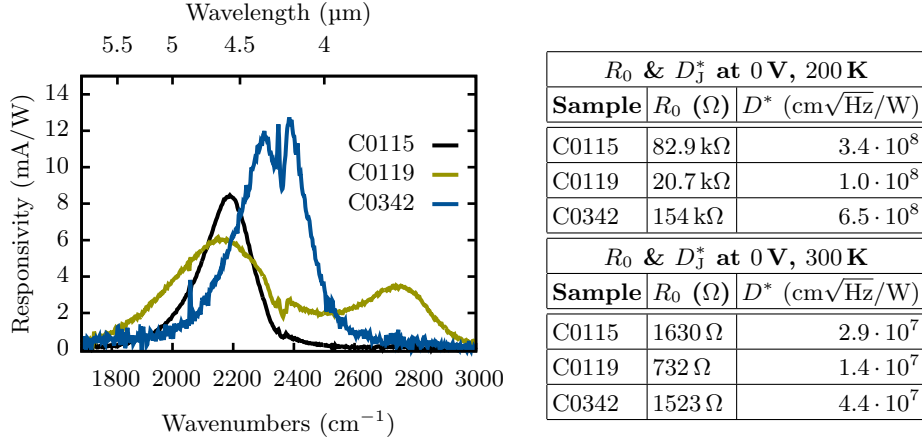


**Figure 3.6:** Comparison of the samples with vertical transition design C0115 and diagonal transition design C0119 at room temperature.

extraction from 2 is then also over 3 and the LO-phonon ladder. In addition to the higher peak responsivity the vertical transition design exhibits a higher differential resistance at room temperature (figure 3.6). This can also be seen from the lower activation energy of 202 meV of sample C0119 in comparison to 246 meV for sample C0115. The 202 meV correspond to the transition from level 1 to level 4 in figure 3.5 b if due to the higher active well doping a slightly higher Fermi level is considered. The longer upper state lifetime for narrow QWs (figure 3.4) in combination with the higher dipole matrix element of the vertical transition can compensate for the lower extraction efficiency in comparison to the diagonal design.

Sample C0119 includes superlattice (SL) contacts between the highly doped bottom and top contact layer. The SL promotes carrier injection to the ground level of the first active well of the AZ. The second SL ensures carrier extraction from the last period to the contact layer. In comparison measurements with a sample without SL contacts a very low improvement of the photocurrent response was observed.

Depending on the operation temperature and wavelength either a vertical or diagonal transition scheme may be favorable. The diagonal transition design gives the best performance at the long wavelength side of the MIR spectral region, whereas the horizontal design is efficient at short MIR wavelengths (figure 3.6). Performance optimization of the material in combination with the cavity characteristics is a promising option. Optimization for critical coupling in high Q cavities based on the diagonal transition design is covered in [138, 139].

### 3.3 Design and optimization

The first sample designed for the 4.5  $\mu\text{m}$  region and optimized for performance was C0115. Due to the in comparison to longer wavelength QCDs higher optical transition energy in the active well a vertical transition scheme was chosen. This ensures a comparable or better performance in comparison to the diagonal transition design in terms of peak responsivity  $R_P$  and resistance  $R_0$ . The design then had to be wavelength matched to the target wavelength of 4.3  $\mu\text{m}$  at 240 K operation temperature. The following section describes the wavelength matching and then discusses the final design as an example for the design considerations presented in this chapter.

#### 3.3.1 Wavelength matching

To precisely tune the QCD materials peak response several samples have been grown and characterized. Sample C0115 is one of the first material designs processed and characterized around 4.5  $\mu\text{m}$  wavelength which exhibits reasonable room temperature performance. Starting from this sample, a series of devices was designed (B. Schwarz), grown and characterized for wavelength matching to the strong  $\text{CO}_2$  absorption region (figure 3.8) around 4.3  $\mu\text{m}$  wavelength.

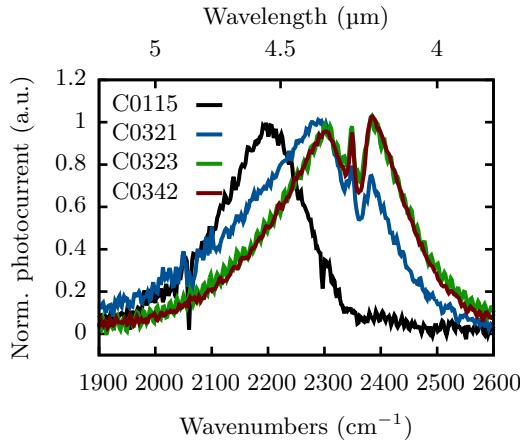


**Figure 3.7:** Series of samples grown for wavelength matching. Starting with sample C0115 in consecutive numbering. Sample C0323 would already hit the target wavelength as seen by the strong  $\text{CO}_2$  absorption valley. Sample C0342 is the final sample and an exact regrowth of C0232 since contact layer doping was unintentionally low in sample C0323.

The samples show in consecutive numbering a shift towards the target wavelength region (figure 3.7). The sample series has an active well thickness order of 4.7 nm, 4.45 nm and 4.3 nm for samples C0115, C0321 and C0323/C0342 respectively, which shows the steps for wavelength calibration of the growths.

#### 3.3.2 Example design for $\text{CO}_2$ sensing and array integration

The following design gives an example for the design considerations discussed in this chapter. The heterostructure design is by B. Schwarz and is published in Harrer et al.

[144]. This design is the final layer structure after wavelength matching as described before. It is used for array integration as discussed in chapter 5 and exhibits a peak detection wavelength of  $4.3\text{ }\mu\text{m}$ . Around this wavelength strong MIR absorption of  $\text{CO}_2$  can be observed. In the atmosphere the major part of the two stable  $\text{CO}_2$  isotopes is  $^{12}\text{CO}_2$  and the vast minority is  $^{13}\text{CO}_2$  with only a fraction of about 1.11% [145]. Therefore, only  $^{12}\text{CO}_2$  was taken into account. The characteristic absorption spectrum is shown in figure 3.8 with its two peaks.

The QCD design was conducted using the Vienna Schrödinger Poisson framework (VSP) [146] extended by a QCD simulation toolkit. A standard vertical transition design was chosen with resonant tunneling extraction. The simulation and design is based on a three period model, where a period and its two neighboring periods model all possible transitions. Hence transitions within a period and to the next and the previous period. The design exhibits three de-localized states forming the upper level in the active well A (figure 3.9 a). The extraction efficiencies shown were computed for all levels of the design. This enables to find regions with low electron transport efficiency in the resonant tunneling extractor as well as in the LO-Phonon ladder. In addition, parasitic scattering paths based on unwanted transitions in the design can be identified easily. The active zone, optimized for grating coupling, consists of 20 periods sandwiched between two highly conducting contact layers. For the detailed layer structure consult appendix A for sample number C342. The total AZ thickness is  $1.364\text{ }\mu\text{m}$ .

The extraction efficiency from the active well A to the first extractor state B is determined by a weighted average of the three de-localized state extraction efficiencies. The energy levels in the following wells are designed to be spaced by the LO-phonon energy ( $\approx 34\text{ meV}$ ) to efficiently scatter the excited carriers to the next active well

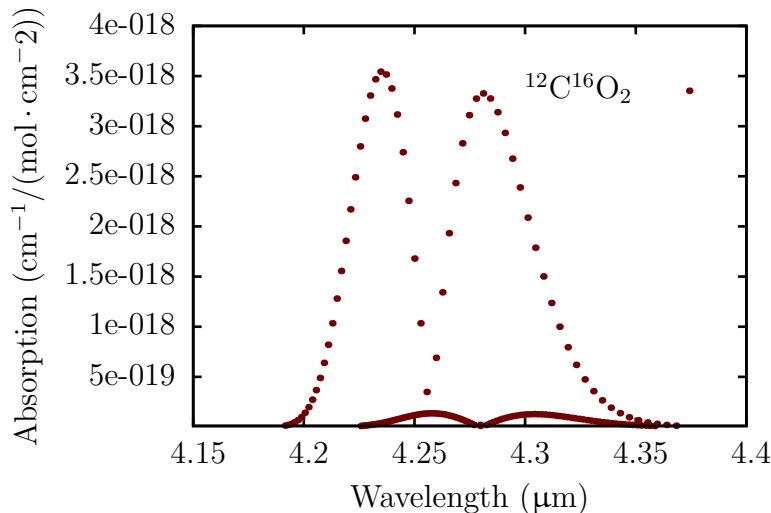


**Figure 3.8:** Absorption spectrum of  $^{12}\text{C}^{16}\text{O}_2$  around  $4.3\text{ }\mu\text{m}$  wavelength at  $T = 296\text{ K}$  [140, 141, 142, 143] for comparison purposes with the photocurrent spectra of the measured detector device.



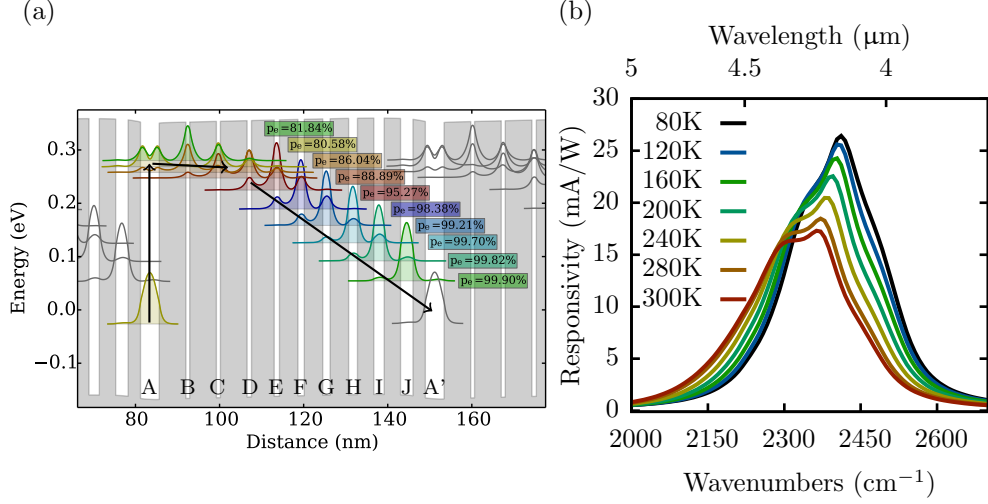


**Figure 3.9:** Simulated band structure of the QCD device C0342 a) with the extraction efficiencies plotted in the colored boxes for the corresponding levels. The simulated responsivity b) is slightly higher than in the measurements due to neglected AZ to contact layer resistances. As published in [144].

A'. The last step from well J to the active well of the next period A' is chosen exhibit a larger energy difference. This prevents thermal back filling (thermal excitation) of electrons from the ground level of A' to J at elevated temperatures.

The simulated responsivity spectrum (figure 3.9 b) shows the characteristic red shift with increasing temperatures. The simulated responsivity does not account for contact resistances at the contact layer to Au interface. Further, the resistance of the contact layers to the first respectively last period of the AZ is not included. This may cause the slightly lower measured responsivity in comparison to the simulations (figure 3.10 a). The two valleys in the responsivity spectrum are due to the strong CO<sub>2</sub> absorption. These two absorption features align well with the responsivity peak for temperatures between 240 K and room temperature. The presented design minimizes parasitic transitions which results in an increased device resistance in comparison to previous samples (figure 3.10 b).

The wavelength matching process showed in practice that even if the peak response wavelength of QCDs can be designed in a stable well known material system such as InGaAs/InAlAs, precise wavelength control depends on the knowledge of exact material parameters, a solid simulation environment and stable growth conditions and layer thicknesses. The design reaches at room temperature about 14 mA/W responsivity and  $4.6 \cdot 10^7 \text{ cm}\sqrt{\text{Hz}}/\text{W}$  Johnson noise limited detectivity in mesa configuration.

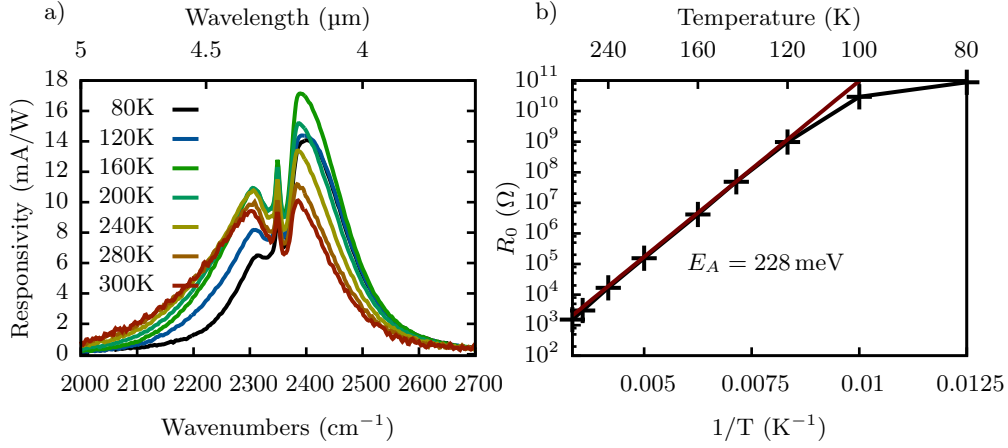


**Figure 3.10:** 45° mesa device results with the strong CO<sub>2</sub> absorption visible by the two valleys in the photocurrent response. As published in [144].

## 3.4 Characterization

Device characterization involves the crystal growth characterization by X-ray diffraction, the electrical voltage-current characteristics and the spectral characterization including the determination of figures of merit such as responsivity and detectivity including their temperature dependency.

### 3.4.1 Fourier transform infrared spectroscopy

Photocurrent spectra were measured with a Fourier transformation infrared spectrometer (FTIR). In the field of infrared spectroscopy it is common to measure the wavelength of MIR light in wavenumbers  $\text{cm}^{-1}$  or  $1/\text{cm}$ . Wavenumbers are related to wavelength  $\lambda$  given in meter by

$$\nu = \frac{1}{\lambda} \quad (3.22)$$

A FTIR consists of a Michelson interferometer, a globar source and one or more internal detectors. Additional ports allow the use of external detectors and sources in various wavelength ranges. Dependent on the optic components such as the windows, beam splitter and detector it can be operated in a wide wavelength range.

Figure 3.11 shows a schematic FTIR with the Michelson interferometer including the beam splitter and the fixed and the moving mirror. The device is equipped with windows for MIR and far-infrared measurements and different beamsplitters for MIR and LWIR radiation. An internal or external light source is passed through the Michelson interferometer and the interfering beam path from the fixed and moving mirror is recorded with a detector. The resulting interferogram is a plot

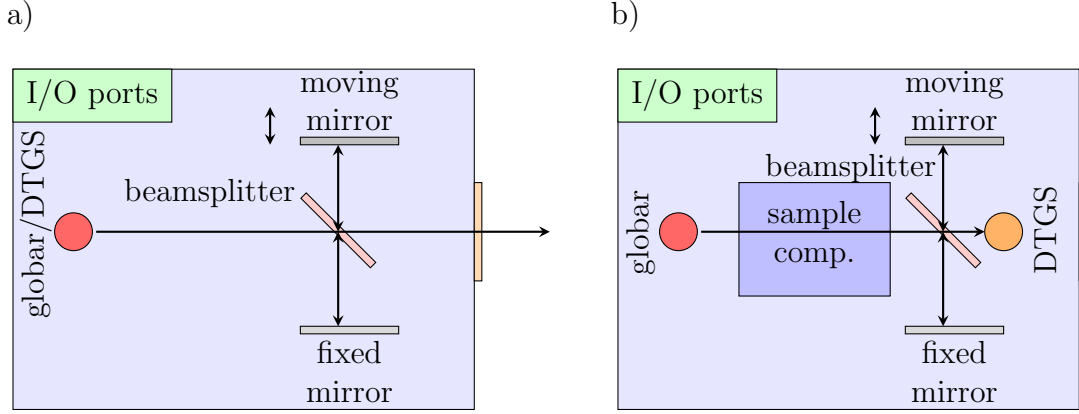


**Figure 3.11:** Fourier transformation infrared spectrometer (FTIR) with the beamsplitter, the MIR globar source, a fixed mirror and a moving mirror. The configuration for detector/laser characterization a) uses the internal DTGS detector of the spectrometer for laser characterization and the internal globar MIR source for detector (QCD) characterization. Sample transmission measurements are commonly done in configuration b) with the internal source and detector.

of the detector signal over the path difference. Dependent on the measurement needs and the noise level several scans can be averaged to increase the SNR. This relationship can be expressed as

$$\text{SNR} \propto \sqrt{N} \quad (3.23)$$

where  $N$  is the number of scans [147]. The spectrum is obtained by Fourier transformation of the interferogram. The resolution of the spectrum, hence the ability to distinguish between two different spectral features near to each other is proportional to the maximum mirror displacement of the moving mirror  $\Delta$  measured in cm.

$$\text{Res} \propto \frac{1}{\Delta} \quad (3.24)$$

State of the art FTIRs allow for measurements in continuous scan mode, where the moving mirror advances continuously. The major advantage of this method is the relatively low measurement time which allows for averaging several scans but no time resolved spectral characterizations. The step scan mode of a FTIR records the detector signal for a defined time with the moving mirror in different static positions. This method results in a longer measurement time up to several hours depending on the averaging time per mirror position, but provides time resolved spectra.

As seen in figure 3.1, the choice of the appropriate detector for the FTIR measurement task is important, since their spectral characteristics may differ strongly. This applies also to the choice of the source and beamsplitter. Due to that, the

absolute signals of QCDs and QCLs operating at different wavelengths can not be directly compared.

For detector photocurrent characterization the QCD is used as external detector of the spectrometer. The QCD signal is amplified with a battery powered transimpedance amplifier (TIA) and fed back into the spectrometer, where the signal is recorded and results in the interferogram. For standard detector characterizations between 50 and 100 scans were made with a resolution of  $4\text{ cm}^{-1}$  in continuous scan mode. The SR570 TIA was set to  $1\text{ }\mu\text{A/V}$  amplification in low noise mode with a 6 dB bandpass filter from 3 Hz to 30 kHz, without bias voltage and without offset current. The bandpass filter cut-off frequencies have to be set according to the FTIR scan speed and the chopper frequency. Both have to be within the pass frequency window.

QCL characterization utilizes the internal DTGS detector of the spectrometer, where the QCL acts as the external light source. For beam alignment the DTGS signal is passed to a lock-in amplifier from the FTIR I/O ports. The lock-in reference is provided by the QCL pulser trigger signal.

### 3.4.2 Current voltage characterization

The current voltage characterization provides the differential resistance needed for detectivity calculations. Besides that, the activation energy based on the differential resistance over temperature can be extracted. The current voltage characteristics (IV) was measured from a device temperature of 80 K up to 300 K in 20 K or 40 K steps. From each IV measurement the differential resistance

$$R_0 = \frac{\partial U}{\partial I} \quad (3.25)$$

at  $U = 0\text{ V}$  was extracted. The measurements were conducted in dark conditions and at the same temperatures under illuminated condition. Obviously the dark condition IV characteristics are used for the extraction of the differential resistance and the illuminated measurements can be used for photocurrent extraction for different bias points. Figure 3.12 shows a typical IV characterization for a QCD for different temperatures in dark conditions. The cryostat window is covered on all sides to shield the device from impinging radiation. The differential resistance over the device temperature (Figure 3.12 b) exhibits a decay of the device resistance for elevated temperatures. The Arrhenius graph of the resistance over  $1/T$  and its activation energy is fitted and compared to the optical transition energy of the detector.

All IV measurements were done using a Keithley 2636A source meter unit

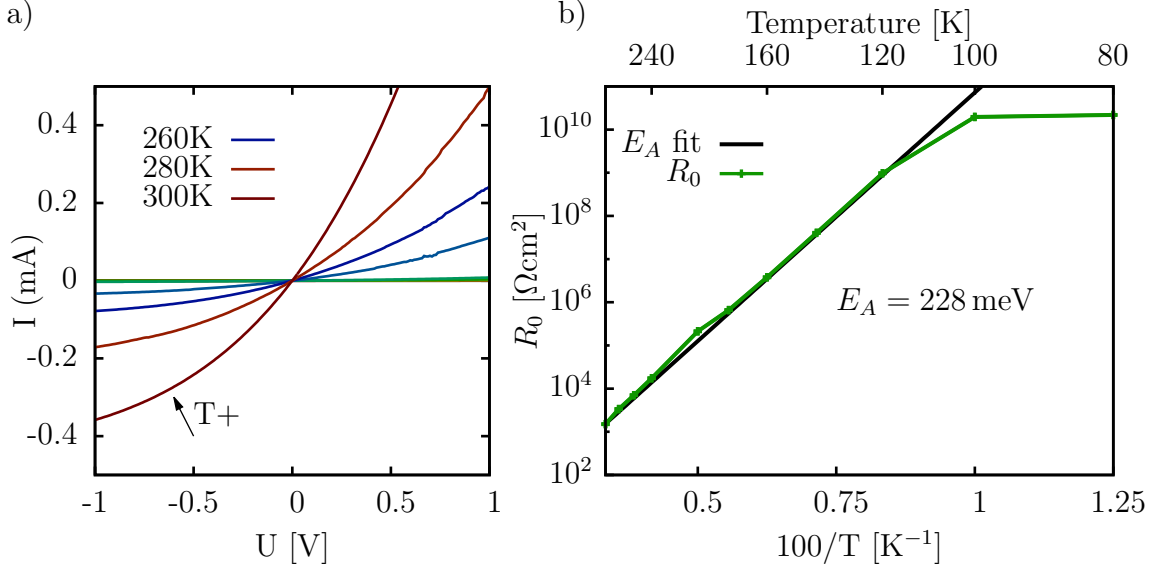


**Figure 3.12:** Typical IV characteristics of a  $100 \mu\text{m} \times 100 \mu\text{m}$  mesa QCD with the current voltage characterization a) in dark condition with non Ohmic behavior. The extracted differential b) resistance  $R_0$  around  $U = 0\text{V}$  for temperatures from 80 K up to room temperature. The fitted line is the activation energy retrieved from the differential resistance. Data from sample C0116A.

(SMU). The measurement voltage was set in 200 steps between  $-1 \text{ V} \cdots 1 \text{ V}$  with a settling time of 20 ms. For comparison purposes alternatively to figure 3.12 b) the resistance area product  $R_0 A$  can be plotted over  $1/T$ .

### 3.4.3 Resistance limitations

Due to their in comparison to photoconductive QWIPs low detector resistance special attention to the resistance limitations of the measurement equipment is necessary when characterizing QCDs. The SR570 TIA features an input resistance of  $100 \Omega$  with 20 kHz bandwidth, when set to  $1 \mu\text{A/V}$  amplification. This is very close to the device resistance of typical QCD designs which have commonly  $500 \Omega$  up to  $1.5 \text{ k}\Omega$  at room temperature. Especially at temperatures above 200 K towards room temperature the detector resistance may approach resistances comparable to the TIA input resistance. This leads to significant measurement errors, which have to be avoided by the choice of a proper amplification range (resistance) or corrected by the calculation of the current ratio through the detector and the amplifier input.

Due to this possible error source it is a good practice for temperature performance characterizations to record the spectra, the IV and the lock-in voltage at every temperature step included in the characterization. Subsequently, the lock-in signal, and the integral over the photocurrent spectrum is plotted over the temperature (figure

3.13). The ratio between the **FTIR** measured integrated photocurrent response and the lock-in signal should not change significantly. The lock-in measurement uses an optical chopper operated at frequencies well below 1 kHz. In contrast to that the **FTIR** mirrors move at speeds corresponding to a frequency of 1.6 kHz up to 20 kHz signals, depending on the **FTIR** settings (commonly 5 kHz was used). Due to the frequency dependence of the amplifier at higher frequency (**FTIR** measurement) the amplification is lower. An increasing lock-in voltage to **FTIR** measured integrated photocurrent response ratio towards room temperature is a hint for increasing measurement errors due to a too low device resistance (too high amplifier input resistance) for the used amplifier settings.

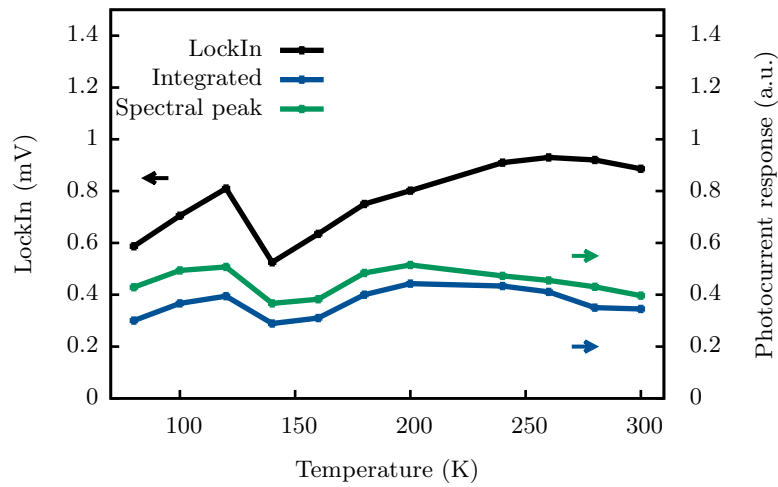


**Figure 3.13:** Comparison of the lock-in signal, the peak photocurrent response and the integrated photocurrent response at different temperatures to check for measurement errors caused by a too low input resistance of the transimpedance amplifier (TIA). For elevated temperatures the ratio between the lock-in signal and the integrated photocurrent response changes which is a hint for a too high input resistance (amplification).

### 3.4.4 Responsivity

For device characterizations the **QCD** is illuminated by a calibrated global source. Global calibration has to be checked prior the characterization using a power meter. The typical radiation power of the **FTIR** global source (figure 3.1) is in the range of 1.7 mW up to 3.3 mW depending on the beamsplitter and optics used. The global source emission spectrum is then characterized using the power meter unit as an external detector for the **FTIR**. Subsequently, the obtained spectrum is integrated over the wavelength  $\lambda$  and normalized by the total power measured before to get the power density spectrum of the source. The reference measurements are done at

80 K device temperature in a cryostat. First the photocurrent spectrum is recorded with the global beam focused onto the QCD by a  $f = 50,8$  mm lens. The thereby obtained spectrum is scaled in arbitrary units. In a second measurement step the detector current is measured using a Keithley power meter unit. The photocurrent spectrum is then integrated over  $\lambda$  and normalized with the measured current  $I_{\text{ph}}$ . The responsivity can then be calculated as

$$R(\lambda) = \frac{I_{\text{S}}(\lambda)}{P_{\text{i}}(\lambda)M} \quad (3.26)$$

with the normalized photocurrent spectrum  $I_{\text{S}}(\lambda)$  and the incident radiation power density spectrum  $P_{\text{i}}(\lambda)$  from the calibration measurement with the power meter. The factor  $M$  accounts for the fraction of global radiation impinging on the device and corrections due to the optical setup. Since the incident total radiation power is measured outside of the cryostat with the  $f = 50.8$  mm lens but the detector characterization is done with the device in the cryostat, the transmission of the cryostat window has to be corrected. The window transmission was determined to be  $\approx 70\%$ . Additionally the shadowing of the cryostat window in the focus cone of the lens is accounted. The intensity distribution of the focused global beam is measured with a x-y motorized stage. The fraction of incident power on the QCD is then determined and included in  $M$ . Based on this procedure, the peak responsivity  $R_{\text{P}}$  is the responsivity at the peak of the responsivity spectrum obtained from equation (3.26).

### 3.4.5 Absolute photocurrent

To determine the responsivity  $R(\lambda)$  and  $R_{\text{P}}$  of a detector as described in section 3.4.4, the absolute photocurrent spectrum has to be obtained. FTIR measurements provide the spectral photocurrent response of the detector without calibration. An absolute photocurrent reference is needed to normalize the photocurrent spectrum. QCDs provide the highest photocurrents at low temperatures. It is favorable to conduct the absolute current measurements at 77 K or 80 K, where the Johnson noise contribution is low and the photocurrent high in comparison to room temperature. Nevertheless, absolute currents in the range of several nA have to be measured. For this purpose a Keithley 2636A source meter unit (SMU) was used directly connected to the cryostat output. First the cryostat windows were covered and the background current was measured. Then the absolute current was measured in illuminated aligned conditions. The difference of the two measurements was used as absolute photocurrent for responsivity calculations.

### 3.4.6 Sample preparation

The characterization of detector designs has been conducted on  $100\text{ }\mu\text{m} \times 100\text{ }\mu\text{m}$  mesa devices with a  $45^\circ$  polished facet for light coupling.

**Wire bonding** is used to connect the detector mesa top contact and the bottom contact layer to a printed circuit board (PCB). From the PCB wire connections can be made to the measurement devices used. Bond wire lengths were below 15 mm.

**Facet polishing** Facet polishing was done by manual polishing with a  $45^\circ$  angle chock. The sample is fixed onto the chock upside down with acetone-soluble wax. Polishing was done in water with diamond polishing disks from  $9\text{ }\mu\text{m}$  followed by  $3\text{ }\mu\text{m}$  and  $1\text{ }\mu\text{m}$  roughness.



## ENHANCED LIGHT COUPLING

The light detection efficiency strongly depends on the radiation coupling to the detector element. Hence the incident radiation on the detection device needs to be coupled to the active element which then converts the radiation power to an externally measurable quantity. The efficiency of this process is described by the so called quantum efficiency  $\eta$  used in two different forms.

First, the internal quantum efficiency  $\eta_{\text{in}}$  gives the ratio of the number of photo-generated electrons contributing to the detector signal to the number of absorbed photons. In other words, it denotes the probability that an absorbed photon generates an electron which is extracted to the measurement circuit.

Second, the external quantum efficiency  $\eta_{\text{ex}}$  is defined, which includes in addition the absorption efficiency  $\eta_{\text{abs}}$ . The absorption efficiency is the ratio of the number of photons impinging the outer device border to the number of photons being absorbed by the active optical transition in the active well of the **QCD**. This means, for  $\eta_{\text{ex}}$  the photons impinging the outer border of the device are taken into account for the probability of an photo-generated electron to be extracted. Losses by absorption in non radiation converting parts of the device, such as the contact layers or parasitic transitions are included in the absorption efficiency.

Consequently the introduced efficiencies are connected by

$$\eta_{\text{ex}} = \eta_{\text{abs}}\eta_{\text{in}} \quad (4.1)$$

For a given detector material, i.e. an active element, an increase of the external quantum efficiency  $\eta_{\text{ex}}$  results in an improved detector performance. This can either be done by the enhancement of the internal quantum efficiency or the enhancement of the absorption efficiency. Besides a sufficient absorption efficiency

other requirements such as coupling from a defined spatial direction, illumination angle, wavelength  $\lambda$ , or a specific geometry of the device have to be considered. For intersubband (ISB) devices in particular the intersubband selection rules have to be met which is a constraint for the electric field polarization.

The most basic coupling can be considered as an active zone (AZ) material, directly sensitive to unpolarized surface normal incident light. These materials do not need an additional light coupling structure. Examples for such a coupling scheme are micro-bolometer and interband photodiode type detectors. However, in this configuration scattered light from other mesa or pixel edges and the surrounding housing has to be taken into account.

## 4.1 Mesa devices

For intersubband detectors which are subjected to the intersubband (ISB) selection rules [148] a coupling scheme based on a polished facet is commonly used for performance evaluation and comparison purposes. Liu et al. evaluated the accuracy of the selection rules for mesa devices to comply with theoretical investigations in 1988 [115]. A 45° facet is ground onto the sample edge and polished. The facet is illuminated as illustrated in figure 4.1 and couples the electric field component polarized in growth direction to the AZ. As depicted, this method is only sensitive to transverse-magnetic (TM) polarized light which exhibits an electric field component in growth direction ( $\vec{e}_z$ ). For spectral characterizations a thermal global source is focused on the facet of the sample with a spot size of  $\approx 3$  mm in diameter, depending on the used equipment.

This geometry can be fabricated relatively fast and offers comparability between different material based detector samples. Nevertheless, it is not suitable for commercial detector products. Single mesa devices or a small numbers of mesa devices should not be cleaved or isolated to separate detector packages. In this case the majority of the detector material per wafer area would not be used.

The absorption efficiency  $\eta_{\text{abs}}$  of a 45° facet mesa device is given by

$$\eta_{\text{abs}} = T_{\text{facet}} \left( 1 - e^{-\sqrt{2}\alpha_{\text{isb}}L_{\text{Act}}} \right) \quad (4.2)$$

where  $T_{\text{facet}}$  is the facet transmittance,  $\alpha_{\text{isb}}$  the absorption coefficient and  $L_{\text{Act}}$  the thickness of the AZ. Due to the limited number of periods, the thickness of the AZ is low which leads to a  $\eta_{\text{abs}}$  in the range of up to 30% only. To compensate for the short absorption length for mesa devices  $\alpha_{\text{isb}}$  can be increased by a high doping concentration, with all trade-off consequences. Optionally, the facet transmittance

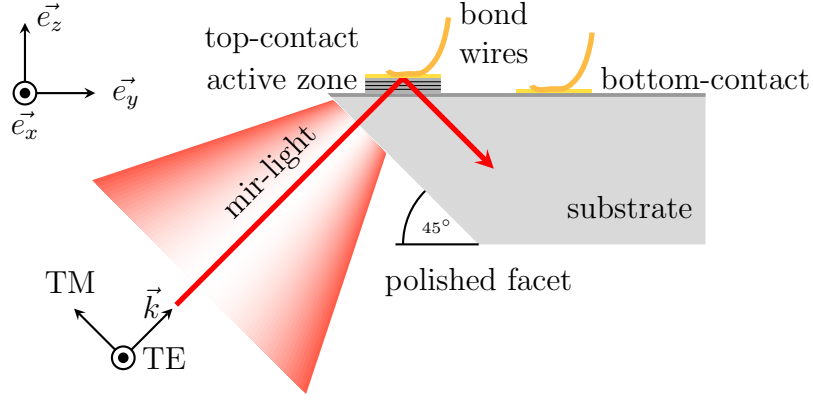


**Figure 4.1:** The  $45^\circ$  polished facet light coupling configuration for mesa devices is a standard method for detector material characterization. The electric field component is illustrated for transverse-magnetic (TM) and transverse-electric (TE) polarized light. TM polarized light exhibits an electric field component in growth direction in contrast to TE polarized light which can not be directly coupled to optical intersubband transitions.

can be improved by an anti-reflection coating (ARC).

For responsivity considerations as discussed in chapter 3 the total incident power  $P$  on the mesa device has to be considered. The mesa area which collects incident radiation is due to the  $45^\circ$  facet given by

$$A_{\text{Mesa,eff}} = A_{\text{Mesa}} \cos(\pi/4) = \frac{A_{\text{Mesa}}}{\sqrt{2}} \quad (4.3)$$

with the area  $A_{\text{Mesa}}$  defined by the mesa dimensions. The mesa dimensions for samples presented in this work are  $A_{\text{Mesa}} = 100 \mu\text{m} \times 100 \mu\text{m}$ .

Further improvements of the absorption efficiency  $\eta_{\text{abs}}$  can be made with geometry modifications such as a longer absorption length or light collection and focusing as discussed in the following sections.

## 4.2 Facet based absorption geometries

Besides the  $45^\circ$  facet mesa devices several similar geometries can be used. Multi-pass geometries with two parallel  $45^\circ$  facets and multi-pass geometries with two perpendicular facets are common for absorption measurements where radiation is passed through the sample and collected at a detector. Multiple passes through the AZ can be promoted by refractive index contrast or Au surfaces on top of the contact layer. These geometries with large mesa sizes or even complete heterostructure covered samples with a top Au reflection layer are suitable for Fourier transforma-

tion infrared spectrometer (FTIR) measurements in the sample compartment. The radiation passes the AZ multiple times depending on the sample length. Further, Brewster angle coupling to polished facets is used to minimize reflections.

**Ridge detectors** In plane light coupling to a ridge geometry detector is a simple way to reach high absorption efficiencies due to the long absorption length available. QCD designs with a very low number of periods (below 10 down to 1) can be operated very efficiently in this configuration. For these devices with a low number of periods the absorption length in mesa configuration is very short due to the thin AZ which results in a low absorption efficiency and overall reduced performance. Ridge detection by coupling to the ridge facet requires waveguide layers as for QCL structures. Furthermore, for performance evaluation, one has to ensure that only light entering through the ridge facet is coupled to the AZ. For that purpose either a highly doped substrate can be used or a double metal structure processed to block light entering from the substrate side. Light coupling from the top surface of the ridge is blocked by the Au top contact surface. For ridge type absorption geometries the absorption efficiency can be defined in the form

$$\eta_{\text{abs}} = \gamma_c \left(1 - e^{-(\alpha_w + \Gamma\alpha_{\text{isb}})L_r}\right) \frac{\alpha_{\text{isb}}}{\alpha_{\text{isb}} + \alpha_w} \quad (4.4)$$

where  $\gamma_c$  is the coupling efficiency,  $\Gamma$  is the mode confinement factor of the coupled mode in the ridge geometry and  $L_r$  the absorption length i.e. the ridge length and  $\alpha_w$  the wave guide losses. For e.g. a facet illuminated ridge  $\gamma_c$  would equal the facet transmission  $T_{\text{facet}}$ . In more complex coupling geometries as discussed later  $\gamma_c$  denotes the over all coupling efficiency. Recently a QCD was reported in ridge coupled configuration. The results for the ridge geometry responsivity presented clearly show that the concept is promising [149].

### 4.3 Grating coupling

A well established method for light coupling is grating coupling. The grating structure allows to couple light from surface normal radiation to intersubband devices which are subjected to the ISB selection rules. Grating coupling is also utilized for e.g. surface emitting QCLs. Being a standard method for pixel arrays and focal plane arrays (FPAs) it has shown its effectiveness, commercial readiness and performance in combination with QWIP cameras [150, 151] and single mode DFB QCLs [69, 82].

Different variations are possible including etched gratings, structured to an additional semiconductor layer or directly into the top contact layer of a structure. Another option is a pure metal hole grating design without etching the semiconductor material as presented in section 6.4.

**Pixel detectors** Integrated grating coupled pixel detectors are substrate bottom side illuminated inducing additional requirements on the design. Figure 4.2 illustrates such a full metal covered diffraction grating. In this configuration, radiation can be coupled to the active zone. The grating is defined by the involved materials and a set of grating parameters which include the grating period  $p$  the grating depth  $d$  and the width  $w$ . The period and the width define the grating duty cycle  $D = w/p$ . Diffraction gratings can be described by the grating equation

$$p \sin(\Theta_m) = m\lambda \quad (4.5)$$

with the grating period  $p$ , the angle of incidence  $\Theta_m$ , the grating order  $m$  and the wavelength  $\lambda$ . For FPAs the assumption  $\Theta_m \approx 0$  is valid which corresponds to normal incident radiation. A good starting point for simulations and optimization of the parameters is for the grating period  $p$  in the range of the radiation wavelength inside of the detector material and a duty cycle of  $\approx 50\%$ .

Pixel detectors can be designed for line gratings and two dimensional gratings which couple linearly polarized or unpolarized light respectively. It is obvious that a pixel sensitive to unpolarized light is favorable for imaging applications and detection of thermal sources in general. Nevertheless, polarization selectivity is advantageous in other applications such as detection of linearly polarized laser radiation.

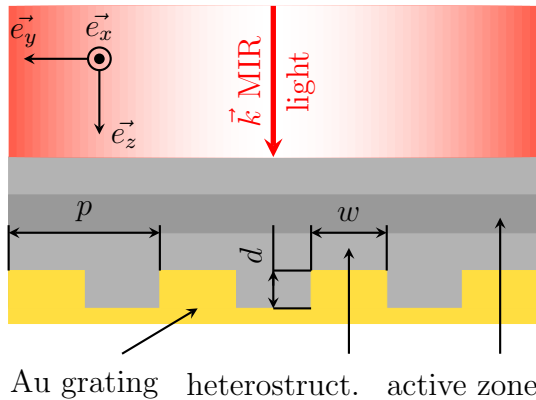


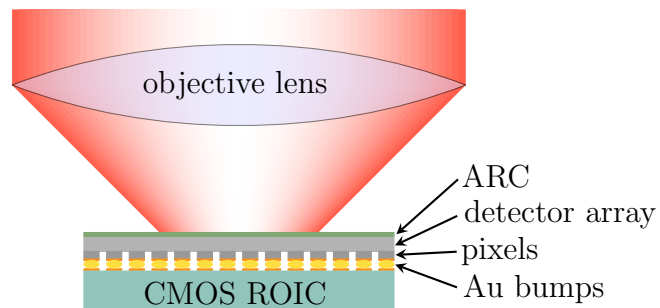
**Figure 4.2:** Grating parameters for a full metal grating in the commonly used bottom side illumination configuration. The coordinate system indicates the directions in comparison to figure 4.1 (mesa configuration).

Large pixel count FPAs require besides sensor dimensions of several millimeters a small pixel pitch. The ratio of grating covered pixel surface to edge surface changes depending on the absolute pixel area. Edge effects and the grating filling factor

have to be taken into account. Grating coupling efficiency has been investigated by Lundqvist et al. [150] for different mesa sizes with and without waveguiding. An up to two times higher integrated quantum efficiency is reported for 45  $\mu\text{m}$  pixel size and a two dimensional grating in comparison to 45° mesa devices. Andersson et al. reported on 92% quantum efficiency of a waveguide two dimensional grating detector [152].

Contact lines and pixel access is a major design challenge for pixel arrays. Pixel counts which are sufficient to resemble an image of a scene can not be directly contacted by wire bonding. In contrast to linear arrays which scan a scene line by line substrate side illuminated grating coupling allows to contact all pixels separately which is a requirement to retrieve a true two dimensional image, as required for 2<sup>nd</sup> and 3<sup>rd</sup> generation thermal imagers. With the grating fabricated on the top side of the pixel in combination with bottom side illumination as illustrated in figure 4.3, very short connections between the pixel contact pads and the amplification circuit are feasible. This is essential to keep the parasitic capacitance and inductance low as well as the total contact resistance. The short contact lines also increase the robustness against surrounding electromagnetic radiation noise. The full metal 2<sup>nd</sup> order grating surface acts as the top contact of the corresponding pixel. The ISB detector pixel array is then bonded to a read out integrated circuit (ROIC) with the substrate side of the array facing towards the scene. The ROIC is mostly a complementary metal oxide semiconductor (CMOS) circuit which consists of a read out circuit, a sample and hold part, amplifier and a output and control logic with an I/O interface. On the polished substrate surface of the pixel array a ARC coating can be applied.

**Figure 4.3:** Flip-chip bonded configuration of a FPA detector with its ROIC. The pixel top contacts are connected to their corresponding contact pads on the CMOS circuit.



## 4.4 Plasmonic lens quantum cascade detectors

This section discusses the publication *Plasmonic lens enhanced mid-infrared quantum cascade detector* published in Applied Physics Letters [153].

The field of plasmonics - which in combination with photonics lead to a manifold of novel device principles - describes collective charge oscillations in different materials, device structures and particles. Plasmons allow guiding, coupling and focusing light down to a sub-wavelength level [154, 155]. Plasmonics have been applied to two dimensional systems such as graphene [156] and heterostructures in the form of ISB plasmons [157, 158]. Surface plasmon polaritons (SPPs) are local charge oscillations in highly conducting layers, most prominently in metal layers coupled to photons. Alternatively sufficient highly doped semiconductor layers which exhibit metal like behavior, support surface plasmon propagation [159]. The collective charge oscillations interact with light waves propagating along a metal - dielectric interface. Often this interface is the metal - air or metal - vacuum interface of metal structures on a carrier substrate.

Surface waves are known for more than 50 years [160], but only recently the ability to fabricate nm scale metal structures and nanoparticle synthesis enabled the investigation of sub wavelength photonics. A good review on SPP photonics is the book by Brongersma and Kik [161] and the review by W. L. Barnes et al. [162] while the book by S. A. Maier [163] gives a good introduction to the fundamentals of the topic. The book by S. Enoch is a more detailed resource on plasmonic grating theory and covers SPP wave theory in chapter 4 in [164].

#### 4.4.1 Fundamentals

This section presents an introduction to the basics of surface plasmon polaritons (SPPs) starting with Maxwell's equations and material properties to show the characteristic SPP dispersion in comparison to the free space light dispersion. The main sources used for the fundamentals are the books by S. A. Maier [163], G. Reider [165] and J. D. Jackson [166].

**Maxwell's equations** The macroscopic Maxwell equations express the link between the electric field  $\vec{E}$ , the magnetic field  $\vec{H}$  to their sources, which are the electric charge- and current density. In their basic form, they do not include any material

properties

$$\begin{aligned}
 \vec{\nabla} \times \vec{E} &= -\frac{\partial \vec{B}}{\partial t} \\
 \vec{\nabla} \cdot \vec{B} &= 0 \\
 \vec{\nabla} \cdot \vec{D} &= \rho \\
 \vec{\nabla} \times \vec{H} &= \vec{J} + \frac{\partial \vec{D}}{\partial t}
 \end{aligned} \tag{4.6}$$

where  $\rho$  is the charge density,  $\vec{J}$  the current density,  $\vec{B}$  the magnetic flux density and  $\vec{D}$  the electric displacement field. For electromagnetic fields in vacuum these equations can be written as

$$\begin{aligned}
 \vec{\nabla} \times \vec{E} &= -\frac{\partial \vec{B}}{\partial t} \\
 \vec{\nabla} \cdot \vec{B} &= 0 \\
 \epsilon_0 \vec{\nabla} \cdot \vec{E} &= \rho \\
 \frac{1}{\mu_0} \vec{\nabla} \times \vec{B} &= \vec{J} + \frac{\epsilon_0 \partial \vec{E}}{\partial t}
 \end{aligned} \tag{4.7}$$

using the constants  $\epsilon_0$  and  $\mu_0$ , denoting the vacuum permittivity and vacuum permeability respectively. These constants provide the connections between the electric displacement and the electric field and similarly for the magnetic quantities

$$\begin{aligned}
 \vec{D} &= \epsilon_0 \vec{E} \\
 \vec{B} &= \mu_0 \vec{H}
 \end{aligned} \tag{4.8}$$

in vacuum. With equation (4.7) the fields can be calculated for configurations where all sources, hence  $\rho$  and  $\vec{J}$  are known [166]. In bulk materials this would involve the exact knowledge of all atomic charges and their positions at any time. This is due to their number and exact determination impossible to compute and even not needed in most cases. Rather average macroscopic fields are computed using material equations, which describe the effect due to the material structure on fields in large distances. This approach gives accurate results for distances large in comparison to the atomic distances [165].

For non vacuum field configurations the connections of equation (4.8) can not be used. For a general material they can be expressed as

$$\vec{D} = \epsilon_0 \vec{E} + \vec{P} = \epsilon_0 (1 + \tilde{\chi}) \vec{E} \tag{4.9}$$



$$\vec{B} = \mu_0(\vec{H} + \vec{M}) \quad (4.10)$$

where  $\tilde{\chi}$  is the electric susceptibility tensor, and  $\vec{M}$  the magnetization. The electric susceptibility  $\tilde{\chi}$  describes the macroscopic average of the electric moment density of the material. It is in general dependent on the electric field intensity, hence is nonlinear

$$\tilde{\chi}(\vec{E}) = \chi^{(1)} + \chi^{(2)}\vec{E} + \chi^{(3)}\vec{E}\vec{E} + \dots \quad (4.11)$$

with the linear part  $\chi^{(1)}$  and the higher order parts  $\chi^{(n)}$  [165].

**Material properties** Since metals such as gold and silver are common metal layers structured for SPP coupling, guidance and focusing, a model is required, which provides the material properties in the form of (4.9) and (4.10) valid for the frequency range to be investigated. For non magnetic materials and most materials in the optic frequency spectrum the magnetization  $\vec{M}$  can be omitted [163, 165].

The motion of charge carriers in an external electric field can be expressed as

$$m_e\ddot{x} + b\dot{x} + ax = -q\vec{E}(t) \quad (4.12)$$

with the electron mass  $m_e$ , the displacement  $x$ , the elementary charge  $q$  and the external electric field  $\vec{E}$ . The part  $-q\vec{E}(t)$  is the Coulomb force. For periodic excitations  $\vec{E} = E_0 e^{-j\omega t}$ , the solution is given by

$$\vec{x}(\omega) = \frac{-q/m_e}{((a/m_e)^2 - \omega^2) + j\omega(b/m_e)} \vec{E}(\omega). \quad (4.13)$$

Introducing the charge carrier density  $n_e$ , the electric dipole moment  $\vec{p} = -q\vec{x}$ , the frequency  $\omega_0 = a/m_e$  and  $\Gamma = b/m_e$  the polarization is given by

$$\vec{P}(\omega) = n_e \frac{q^2/m_e}{(\omega_0^2 - \omega^2) + j\omega\Gamma} \vec{E}(\omega). \quad (4.14)$$

With equation (4.9) the permittivity  $\epsilon$  can be expressed by the oscillator model

$$\begin{aligned} \tilde{\epsilon}(\omega) &= \left( 1 + \frac{q^2 n_e}{m_e \epsilon_0} \frac{1}{(\omega_0^2 - \omega^2) + j\omega\Gamma} \right) \\ &= \left( 1 + \frac{\omega_p^2}{(\omega_0^2 - \omega^2) + j\omega\Gamma} \right) \end{aligned} \quad (4.15)$$

with the plasma frequency  $\omega_p = \sqrt{\frac{q^2 n_e}{m_e \epsilon_0}}$ . Further, the real and imaginary part of the

permittivity can be obtained by splitting equation (4.15) to the following expressions

$$\begin{aligned}\epsilon' &= 1 + \omega_p^2 \frac{(\omega_0^2 - \omega^2)}{(\omega_0^2 - \omega^2)^2 + \omega^2 \Gamma^2} \\ \epsilon'' &= -\omega_p^2 \frac{\omega \Gamma}{(\omega_0^2 - \omega^2)^2 + \omega^2 \Gamma^2}\end{aligned}\tag{4.16}$$

In the infrared region a simplification can be made if the bound electrons with their resonance frequency  $\omega_0$  are neglected  $\omega_0 = 0$ . This means for highly conducting metals modeled by a free electron gas that the force on the deflected charge carrier expressed by  $ax$  in equation (4.12) can be omitted. For  $\omega_0 = 0$ , equations (4.16) can be rewritten to

$$\begin{aligned}\epsilon' &= 1 - \frac{\omega_p^2}{\omega^2 + \Gamma^2} \\ \epsilon'' &= -\frac{\omega_p^2 \Gamma}{\omega^3 + \omega \Gamma^2}\end{aligned}\tag{4.17}$$

For example Au which was used as metal layer for SPPs in the scope of this thesis, the parameters for equation (4.17) are  $\omega_p = 7,25 \cdot 10^4 \text{ cm}^{-1}$  and  $\Gamma = 2,16 \cdot 10^2 \text{ cm}^{-1}$  [167]. The real and imaginary part of the permittivity and the refractive index for these parameters are shown in figure 4.4 for the MIR wavelength region. The plot is based on equations (4.17) for the permittivity and equations (4.19) for the refractive index. Figure 4.4 also shows clearly the large deviations in literature reported optical constants for Au. R. L. Olmon et al. [168], presents a extensive comparison of literature data on Au of the past decades and concludes that systematic measurement errors led to the diverging data reported previously. Additionally in the paper data for evaporated, single crystal and templates stripped Au is presented including fit parameters.

The real part  $\text{Re}[\tilde{\epsilon}] = \epsilon'$  and imaginary part  $\text{Im}[\tilde{\epsilon}] = \epsilon''$  of the complex permittivity  $\tilde{\epsilon}$  is linked to the complex refractive index by

$$\tilde{n} = n + i\kappa\tag{4.18}$$

by the expressions

$$\begin{aligned}n &= \sqrt{\frac{1}{2} \left[ \sqrt{\epsilon'^2 + \epsilon''^2} + \epsilon' \right]} \\ \kappa &= \sqrt{\frac{1}{2} \left[ \sqrt{\epsilon'^2 + \epsilon''^2} - \epsilon' \right]}\end{aligned}\tag{4.19}$$

The other way round the real and imaginary part of the refractive index is linked

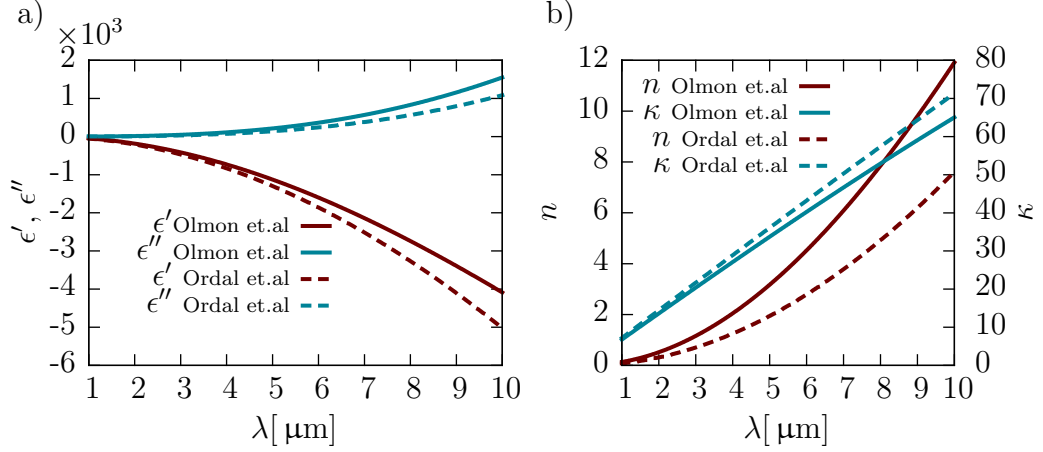


**Figure 4.4:** Drude model for Au with the a) real part  $\epsilon'$  and imaginary part  $\epsilon''$  of the complex permittivity and b) the real part  $n$  and imaginary part  $\kappa$  of the complex refractive index for mid-infrared (MIR) wavelengths. The fit parameters are taken from [167] and [168] and illustrate the large deviations between the literature reported dielectric function over frequency.

to equation (4.17) by

$$\begin{aligned}\epsilon' &= n^2 - \kappa^2 \\ \epsilon'' &= -2n\kappa\end{aligned}\tag{4.20}$$

with the extinction coefficient  $\kappa$  which describes the dampening of the wave propagating in the material. Note that the sign of  $\kappa$  for dampening is defined in different ways depending on the literature and simulation model. COMSOL Multiphysics, which was utilized for the optic simulations in this thesis defines the imaginary part  $\epsilon''$  and the extinction coefficient  $\kappa$  of absorbing materials as negative ( $\kappa < 0$  or equivalent  $\epsilon'' < 0$ ).

**Surface wave propagation** Surface plasmon polaritons propagating at the interface of a dielectric and a metal are longitudinal surface waves. For non magnetizable materials without external current densities  $\vec{J} = 0$ , equations (4.6) can be written as

$$\begin{aligned}\vec{\nabla} \times \vec{E} &= -\mu_0 \frac{\partial \vec{H}}{\partial t} \\ \vec{\nabla} \times \vec{H} &= \frac{\partial \vec{D}}{\partial t}\end{aligned}\tag{4.21}$$

With the curl operator applied to the left and right side of the first expression and using the second expression this leads to

$$\vec{\nabla} \times \vec{\nabla} \times \vec{E} = -\mu_0 \frac{\partial^2 \vec{D}}{\partial t^2}. \quad (4.22)$$

This expression can be rearranged using the identity  $\vec{\nabla} \times (\vec{\nabla} \times \vec{f}) = \vec{\nabla}(\vec{\nabla} \cdot \vec{f}) - \nabla^2 \vec{f}$  to

$$-\nabla^2 \vec{E} = -\mu_0 \frac{\partial^2 \vec{D}}{\partial t^2}. \quad (4.23)$$

Since there is no charge accumulation, hence  $\vec{\nabla} \cdot \vec{D} = 0$  or equivalently using  $c_0 = \frac{1}{\sqrt{\epsilon_0 \mu_0}}$ , this results in

$$\nabla^2 \vec{E} - \frac{\epsilon}{c_0^2} \frac{\partial^2 \vec{E}}{\partial t^2} = 0. \quad (4.24)$$

Equation (4.24) is the wave equation for the electric field in linear isotropic media. In complex notation with  $\partial/\partial t = j\omega$  and  $\vec{E} = E_0(z)e^{-j\omega t}$  it reads

$$\nabla^2 \vec{E} + \epsilon k_0^2 \vec{E} = 0 \quad (4.25)$$

A similar equation as (4.24) can be formulated for  $\vec{H}$ . Equations of this type are referred to as Helmholtz equations. A surface wave propagating in  $\vec{e}_y$  direction as depicted in figure 4.5 with the electric field  $\vec{E} = E_0(z)e^{-jk_y y}$  is described by

$$\frac{\partial^2 \vec{E}(z)}{\partial z^2} + (k_0^2 \epsilon - \beta^2) \vec{E} = 0 \quad (4.26)$$

where  $\beta$  is the propagation constant. Equation (4.26) is the wave equation for the electric field of the wave propagating on the metal - air interface (figure 4.5). For the magnetic part a similar equation can be obtained. Since SPPs are TM polarized waves they have only the non-zero field components  $\vec{H}_x$ ,  $\vec{E}_y$  and  $\vec{E}_z$  when propagating in  $\vec{e}_y$  direction. The equation for TM wave propagation in  $\vec{e}_y$  direction is

$$\frac{\partial^2 \vec{H}_x}{\partial z^2} + (k_0^2 \epsilon - \beta^2) \vec{H}_x = 0. \quad (4.27)$$

For the electric field components of the wave

$$\begin{aligned} \vec{E}_y &= -j \frac{1}{\omega \tilde{\epsilon}} \frac{\partial \vec{H}_x}{\partial z} \\ \vec{E}_z &= -\frac{\beta}{\omega \tilde{\epsilon}} \vec{H}_x \end{aligned} \quad (4.28)$$

can be derived. According to Maier [163] for the metal the following ansatz can be used

$$\begin{aligned}\vec{H}_x &= A_1 e^{j\beta y} e^{k_m z} \\ \vec{E}_y &= -iA_1 \frac{1}{\omega \tilde{\epsilon}_m} k_m e^{j\beta y} e^{k_m z} \\ \vec{E}_z &= -A_1 \frac{\beta}{\omega \tilde{\epsilon}_m} e^{j\beta y} e^{k_m z}\end{aligned}\tag{4.29}$$

Similarly this ansatz for the dielectric part of the interface is

$$\begin{aligned}\vec{H}_x &= A_2 e^{j\beta y} e^{-k_d z} \\ \vec{E}_y &= iA_2 \frac{1}{\omega \tilde{\epsilon}_d} k_d e^{j\beta y} e^{-k_d z} \\ \vec{E}_z &= -A_1 \frac{\beta}{\omega \tilde{\epsilon}_d} e^{j\beta y} e^{-k_d z}\end{aligned}\tag{4.30}$$

Additionally at the interface the following boundary conditions have to be satisfied

$$\begin{aligned}\|\vec{E}\| \times \vec{n} &= \|\vec{E}_\parallel\| = 0 \\ \|\vec{D}\| \cdot \vec{n} &= \|\vec{D}_z\| = (\tilde{\epsilon}_d \vec{E}_z - \tilde{\epsilon}_m \vec{E}_z) \cdot \vec{n} = \sigma = 0 \\ \|\vec{H}\| \times \vec{n} &= \|\vec{H}_\parallel\| = \vec{K} = 0\end{aligned}\tag{4.31}$$

where  $\vec{n}$  is the surface normal vector of the interface. Since we do not allow surface charge accumulation,  $\sigma = 0$  and no surface currents, hence  $\vec{K} = \vec{J}/l = 0$ . With equations (4.30) and (4.29) and these boundary conditions the following expressions hold

$$\begin{aligned}A_1 &= A_2 \\ \frac{k_d}{k_m} &= -\frac{\tilde{\epsilon}_d}{\tilde{\epsilon}_m} \\ k_d^2 &= \beta^2 - k_0^2 \tilde{\epsilon}_d \\ k_m^2 &= \beta^2 - k_0^2 \tilde{\epsilon}_m\end{aligned}\tag{4.32}$$

**Dispersion** The SPP dispersion relation can be obtained from equations (4.32) which reads

$$k_{\text{Spp}} = k_0 \sqrt{\frac{\tilde{\epsilon}_d \tilde{\epsilon}_m}{\tilde{\epsilon}_d + \tilde{\epsilon}_m}}\tag{4.33}$$

where  $\tilde{\epsilon}_d$  is the complex permittivity of the dielectric,  $\tilde{\epsilon}_m$  the complex permittivity of the metal and  $\vec{k}_0$  the free space propagation wave vector. A fundamental requirement

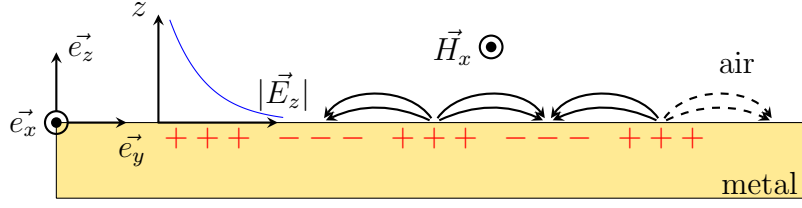


**Figure 4.5:** Schematic drawing of a surface plasmon polariton (SPP) wave propagating in  $\vec{e}_y$  direction on the metal - air interface. The electric field  $|\vec{E}(z)|$  decays exponentially with increasing normal distance from the interface. The field is illustrated for the allowed **TM** waves. The arrows show the electric field dependent on the charge oscillation in the metal layer depicted by the + and - symbols.

for **SPP** to be bound to the metal - dielectric surface is that the real parts of the permittivities  $\text{Re}[\tilde{\epsilon}_d]$  and  $\text{Re}[\tilde{\epsilon}_m]$  need to have opposite signs. For common metals used in plasmonics such as Au and Ag which have  $\text{Re}[\tilde{\epsilon}_m] < 0$ , this is satisfied. In addition to [163] explanations for **SPP** propagation on different surfaces including the metal-dielectric interface can be found in [169].

**Coupling** to surface plasmon polaritons (**SPPs**) can be achieved in several ways. Wave excitation can be done by coupling of light to **SPPs** or by excitation by electron beams. For light coupling the essential task is to ensure wave vector matching between the light and the **SPP** wave. Hence, the wave vector mismatch between the impinging light and the **SPP** wave according to equation (4.33) has to be overcome. One of the standard methods is the Otto and Kretschmann configuration [170] utilizing a prism. A metal film is deposited onto the prism and **TM** polarized light is then coupled into a high refractive index prism to overcome the momentum mismatch (figure 4.6 b). The Otto configuration is very similar but has an air gap between the prism and the metal surface (figure 4.6 c).

An effect reported in the more recent past is the extraordinary optical transmission (**EOT**) effect. Two forms of the effect were reported, where the light transmission through a sub-wavelength hole in a metal film and a hole array is analyzed respectively. A total transmission normalized to the area larger than unity can be observed, first reported in 1998 by Ebbesen et al. [171] for hole arrays. The spectral transmission peak was reported at wavelengths corresponding to approximately 10 times the hole diameter with an area normalized transmission of over 2. The extraordinary optical transmission phenomenon is based on **SPP** excitation, when the photon wave vector and the grating vector match the plasmon wave vector. The grating vector is defined by the period of the hole array. A theoretic model of the effect is presented in [172]. Hence the **EOT** effect is another method for **SPP**

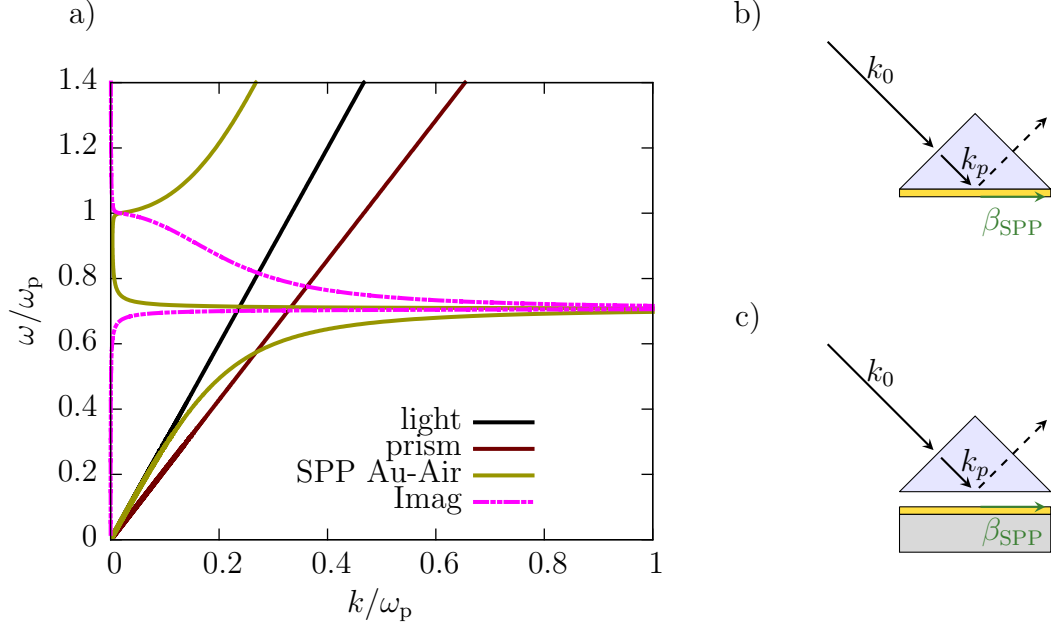


**Figure 4.6:** The surface plasmon polariton (SPP) a) dispersion relation based on equation (4.33) for an Au-Air interface. The SPP dispersion does not cross the light line, hence there is no direct coupling between free space propagating MIR radiation and SPPs. The second linear dispersion is for a prism with a refractive index of  $n = 1.4$  which has an intersection with the SPP wave vector. Therefore, the light coupling utilizing a prism b) in the Kretschmann configuration is possible. The Otto configuration c) uses a prism as well but couples through the evanescent part of the light.

excitation by light.

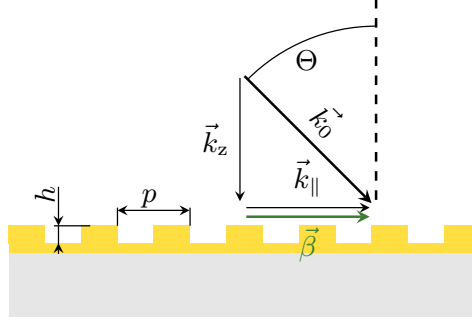
Grating coupling is a straight forward method to couple incident light to SPP waves. Different grating types can be applied such as sinusoidal grating shapes [173] or rectangular grating structures. The grating enables for wave vector matching between the SPP wave and the incident light beam with the wave vector  $\vec{k}_0$ . The incident light wave vector can be split to  $k_{x,y} = k_0 \sin(\Theta)$  and  $k_z = k_0 \cos(\Theta)$ . The coupling condition is fulfilled, if the in plane wave vector  $k_{\parallel}$  matches the SPP wave vector  $\beta$

$$\beta = k_0 \sin(\Theta) \pm n\vec{k}_g \quad (4.34)$$

with the angle of incidence  $\Theta$ , the grating wave vector  $\vec{k}_g = 2\pi/p$  and  $n = 1, 2, 3 \dots$  being integers to form the grating wave vector multiples  $n\vec{k}_g$ . This basic coupling condition according to [163] is illustrated in figure 4.7. An indication for SPP coupling can be seen in the back reflected spectra, where dips can be observed in the spectrum, if the grating is illuminated with a broadband source. These spectral dips are a consequence of the generated SPP waves.

More elaborate models for grating coupling are based on the highly cited paper by

**Figure 4.7:** Grating coupling of SPPs requires the in plane wave vector  $\vec{k}_{\parallel}$  of the impinging light to match the SPP wave vector  $\beta$ . This requirement is expressed by equation (4.34).



A. Hessel and A. Oliner in 1965 [174], presenting a theory for the Woods anomalies [175], observed in the reflectance spectrum of optic diffraction gratings. Two types of resonances are described which are Rayleigh type diffraction and surface waves on the grating. The surface waves on the grating are SPPs which re-irradiate. MIR plasmon grating coupling and re-irradiation on silver films has been shown by J.W. Cleary et al. [176], investigating a simplified model based on Hessel and Oliner [174]. Measurements are presented which indicate good but not exact match with the reported model. The influence of the grating shape is investigated with its influence on the higher harmonic SPP excitations. The model describes the grating as a modulated surface impedance based on a modulation index as a function of the grating permittivity, depth and light wavelength.

In general numeric simulations can give a good feeling for grating coupling of SPP waves if a few key aspects are taken into account. Material parameters have to be chosen suitable to the wavelength range, a sufficiently fine mesh has to be used for the model to converge and simplifications to two dimensional models should be made. A major drawback is the computational effort and time needed for full three dimensional finite element simulations. Fine meshing is needed due to the material properties of the metal layers to provide converging stable results.

Grating coupling has been utilized for a manifold of device designs including nano focusing [177] and light coupling to a NIR detector [178, 179]. Plasmon grating coupling can be also applied for light emission, hence coupling radiation from SPP waves to free propagating light. This has been applied e.g. for emission beam shaping of a quantum cascade laser (QCL) [86, 180].

**Propagation length** The surface plasmon polariton (SPP) propagation length imposes a major restriction to device design. It defines the device dimensions such as interconnect and interaction lengths. The decay of the SPP roots in re-irradiation of the wave and losses in the material. Hence due to the material properties and scattering rates they are material dependent. Based on the propagation constant  $\beta$



the propagation length is defined as

$$L_{\text{Spp}} = \frac{1}{2\text{Im}[\beta]} \quad (4.35)$$

based on the imaginary part of the **SPP** wave vector  $\beta$ . More intuitively it can be described by the distance from the launch position  $x = 0$  in which the **SPP** decays to  $\frac{1}{e}$ . The propagation length  $L_{\text{Spp}}$  depends on the confinement of the wave to the metal-dielectric interface and the related re-irradiation and on the losses in the metal layer.

As mentioned already in section 4.4.1 the plasma frequency is defined as

$$\omega_p = \sqrt{\frac{q^2 n_e}{m_e^* \epsilon_0}} \quad (4.36)$$

with the elementary charge  $q$ , the carrier (electron) concentration  $n_e$  the electron effective mass  $m_e$  and the vacuum permittivity  $\epsilon_0$ . Gold and silver have plasma frequencies in the visible spectral range. Therefore, in the **MIR** range the frequencies are well below  $\omega_p$  and the ohmic losses relatively low and the **SPP** weakly bound to the surface.

The scattering processes in a thin metal film are dependent on the material structure. Hiramatsu et al. report on the influence of the Au thin film grain size on the **SPP** propagation length and the enhancement possible by annealing the thermal evaporated Au layer [181]. Propagation lengths from 9 mm for a non annealed sample up to 14.7 mm for a twice annealed sample are reported at a wavelength of 10.6  $\mu\text{m}$ . A device structure with two diffraction gratings for in- and outcoupling was used. The authors attribute the increase of propagation length to the larger grain size of the annealed Au, which was verified by atomic force microscopy (**AFM**) measurements of the surface structure. The authors compare their measurements to calculations based on Au material parameters presented in [182] and get good agreement. Since precise material parameters are vital for propagation length calculations significant deviations may be faced for different reported material constants. According to Hiramatsu et al. [181]  $L_{\text{Spp}}$  for the metal-dielectric interface can be approximated as

$$L_{\text{Spp}} \approx \frac{c}{\omega} \left( \frac{\epsilon' + 1}{\epsilon'} \right)^{3/2} \frac{\epsilon'^2}{\epsilon''} \approx \frac{c}{\omega} \frac{\epsilon'^2}{\epsilon''} \quad (4.37)$$

provided that  $\epsilon'' < |\epsilon'|$  and  $|\epsilon'| \gg 1$ , with the speed of light  $c$  and the angular frequency  $\omega$ . A comparison of propagation lengths calculated from Drude fits as depicted in figure 4.4 and equation (4.35) is shown in figure 4.8. For different material

parameters again deviating results can be observed (figure 4.8 b) as mentioned in [168] and the previous section. In this graph re-irradiation losses are neglected and a rough approximation of the propagation length is given for the MIR wavelength range.

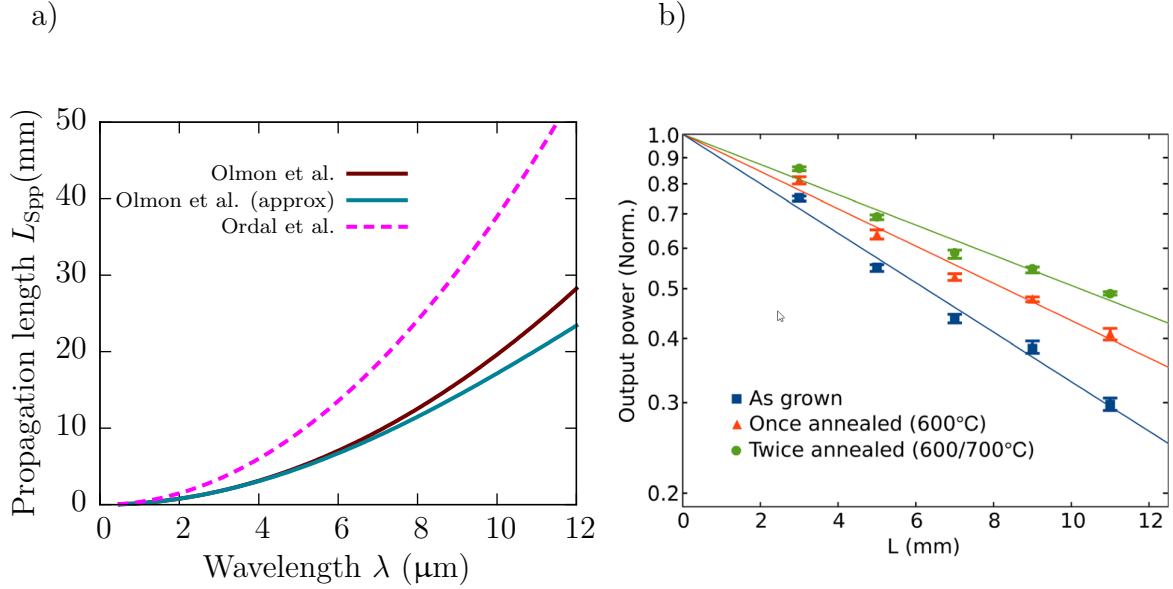
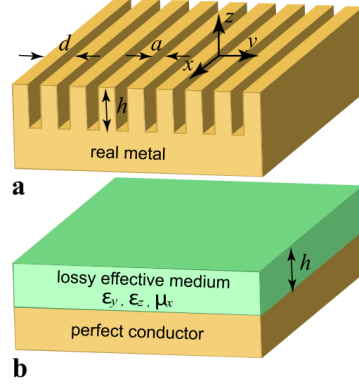


**Figure 4.8:** Approximation a) of the propagation length neglecting re-irradiation losses based on different material parameters reported in the literature. Olmon et al. provided the most recent data in 2012. The calculations are based on Drude model fits reported in the corresponding resource [168]. The measured output power over the propagation distance b) for differently processed Au-air interfaces as reported by Hiramatsu et al. [181] with propagation length of 9 mm for the a untreated Au sample, 12 mm one time annealed and 14.7 mm for a two time annealed sample. Subfigure b) taken from [181].

**Spoof plasmon guiding** Sub-wavelength surface structures designed to effectively guide surface plasmon polariton (SPP) waves are also known as spoof plasmon structures [183] which offer an attractive alternative to thin metal layers for SPP guiding. The SPP guiding structure is designed to exhibit a by design determined effective dielectric constant  $\epsilon_{eff}$ . In general the periodic structures defining these effective material properties are deeply sub-wavelength in size and period (figure 4.9 a). Periodic sub-wavelength grooves are structured into the metal layer with a period  $d$ , depth  $h$  and a groove width  $a$ . The metal forming this structure has the permittivity  $\epsilon_m$  which is surrounded by the permittivity of the dielectric  $\epsilon_d$ , which in most cases is air. Such a system can be described as a three layer stack of materials (figure 4.9 b) as reported by A. Rusina et al. in [184]. The sub-wavelength structure is modeled as an effective medium on top of the metal layer with air, or a dielectric on

top as depicted in figure 4.9. This structures geometry is very similar to a standard grating but not to be confused with the grating coupler to excite SPPs from incident radiation.

**Figure 4.9:** Periodic sub-wavelength groove structure a) for spoofing SPPs on a structured metal-dielectric interface. The sub-wavelength structure can be approximated b) by a three layer structure and an effective dielectric constant. Image taken from [184].



#### 4.4.2 Plasmonic lens detector design

The specific detectivity  $D^*$  of a detector represents the signal to noise ratio (SNR) normalized by the detector area and the measurement bandwidth as described in detail in section 3.1.1. A method to increase both the detectivity  $D$  (not normalized by the area) and the absolute detector signal is to enhance the light collection, hence the amount of radiation which couples to the device and at the same time keep the noise level constant. Essentially this means to increase the optical active area. With equation (3.7) and the resistance  $R_0$  for a square QCD mesa one can write

$$D_J^* = R_P \sqrt{\frac{AR_0}{4k_B T}} = R_P \sqrt{\frac{A \frac{\rho_0 h}{A}}{4k_B T}} \quad (4.38)$$

with the specific differential resistance  $\rho_0$  and the mesa height  $h$  roughly approximating the mesa resistance. It is obvious that by a simple scaling of the detector,  $D^*$  can not be increased.

A possible solution is to decouple the differential device resistance  $R_0$  responsible for the Johnson-Nyquist noise term

$$\text{NSD} = \frac{4k_B T}{R_0} \quad (4.39)$$

from the area which couples to the impinging radiation. Equation (4.39) expresses the noise spectral density (NSD), with the Boltzmann constant  $k_B$  and the temperature  $T$ . With the resistance decoupled from the total detector area, the optical

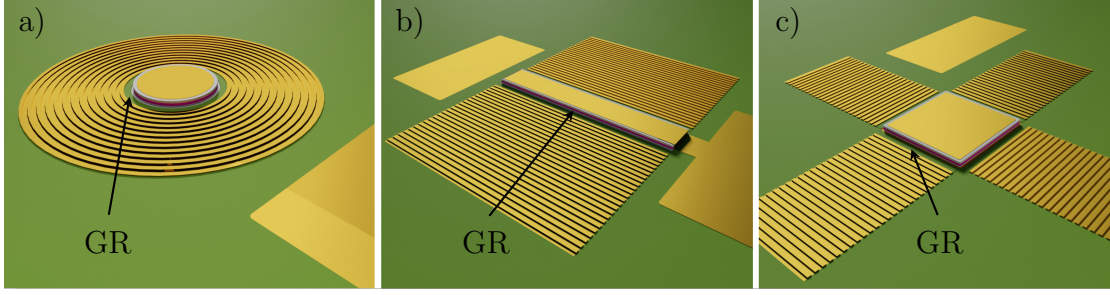


**Figure 4.10:** Plasmonic lens device structures a) with a circular plasmonic lens surrounding the round QCD active mesa in the center. Line shape plasmonic structure b) with plasmonic structures left and right to the detector mesa. Star shaped design c) with a  $100\text{ }\mu\text{m} \times 100\text{ }\mu\text{m}$  QCD mesa in the center. The magenta colored section on the mesa facets indicates the position of the active zone (AZ) sandwiched between the contact layers. The guiding region (GR) is between the grating lens and the detector element's facet. The Au surfaces nearby the plasmonic structures are the bottom contacts of the detector. The top contacts are located on top of the QCD elements in the center.

active area can be increased, while the heterostructure area is kept small, which results in a high detector element resistance.

Plasmonic structures offer the possibility to couple light on a comparable large surface and focus it to a small detector element. Moreover, the device can be designed to couple surface normal incident radiation. The device structures depicted in figure 4.10 consist of the electrical active QCD element in the center of a plasmonic lens structure. Three different but similar designs were conceived which differ by the shape of the plasmonic structure and the QCD detector elements shape. For all the structures the coupling principle is the same. Normal incident MIR radiation impinges the corrugated surfaces, couples to surface plasmon polaritons (SPPs) which propagate on the plasmonic structure. The part of the SPP waves propagating towards the mesa are guided in a dielectric loaded guiding region to the QCD elements facet. These dielectric loaded guiding regions are illustrated as the green stripe surrounding the QCD element in circular shape (figure 4.10 a) and in line shape (figure 4.10 b and c).

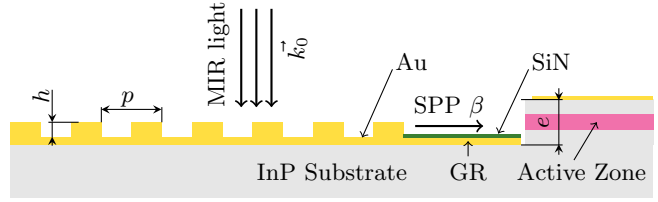
#### 4.4.3 Coupling and propagation

The plasmonic lens structure surrounding the QCD element has two purposes. First it couples and collects light from a - in comparison to the QCD element - large surface. Hence it increases the amount of light collected by the detector. Second it focuses and guides the coupled radiation in form of SPP waves to the active zone of

the detector element. Both tasks have been analyzed in this thesis utilizing numeric simulations with COMSOL Multiphysics.

Grating coupling has been investigated for different combinations of grating parameters. The light coupling and SPP propagation configuration is depicted in figure 4.11 introducing the geometry parameters. These are, the total etch depth  $e$  which strongly influences the end-fire coupling efficiency, the grating depth  $h$  and the grating period  $p$  influencing the coupling efficiency to the SPP waves excited on the lens surface. The guiding region dimensions and the thickness of the SiN dielectric layer are additional parameters to optimize the total coupling efficiency.

**Figure 4.11:** Cross section to illustrate the radiation coupling using a plasmonic lens with a grating surface. The design parameters are the grating height  $h$ , period  $p$ , duty cycle and SiN layer thickness. End fire coupling to the active zone is adjusted with the total etch depth  $e$ .



The magenta colored area indicates the active zone (AZ) of the detector element in the center. The MIR light impinges the lens surface with the wave vector  $k_0$  and is coupled to the grating, focused to the guiding region as SPP wave with the propagation constant  $\beta$  and coupled to the wave guide embedded AZ by end-fire coupling. Note that the schematic drawing is not to scale.

#### 4.4.4 Simulations

The simulations have been conducted with a cross section model of the device structure to reduce the computational effort required. Consequently, the circular shaped devices (figure 4.10 a) and the linear type devices (figure 4.10 b,c) could be represented by their cross section rotation and translation symmetry respectively. The cross section consists of the substrate layer at the bottom followed by the layer structure as grown by MBE. Hence the bottom cladding layer, the AZ and the top cladding finished by the highly doped top contact layer. The cladding layers provide the waveguide properties for the AZ. The top contact is modeled as a Au surface. The outer side, hence the opposite side of the detector element was terminated with a perfectly matched layer (PML) which lets radiation pass through the simulation domain border without reflections. A PML is a boundary condition used for wave equation based models to limit the simulation domain with ideally no simulation

artifacts. The wave excitation was incorporated at the top of the air region of the model using a scattering boundary condition. The polarization of the impinging radiation was chosen to be perpendicular to the grating grooves  $\vec{e}_z$ . Therefore, the scattering boundary condition was defined to emit a wave in  $-\vec{e}_y$  direction with the electric field vector in  $-\vec{e}_x$  direction (figure 4.12 a). The electric field amplitude for the simulations was determined by

$$|\vec{E}_x| = \sqrt{\frac{2Z_0 I}{n}} \quad (4.40)$$

with the free space wave impedance  $Z_0 = \sqrt{\frac{\epsilon_0}{\mu_0}} \approx 377 \Omega$ , the refractive index of the material  $n$  and the power density  $I$  in  $\text{W}/\text{cm}^2$ . The power density was fixed with  $1 \text{ W}/\text{cm}^2$  with  $n = 1$  to account for the excitation in air. By the choice of the propagation direction in  $-\vec{e}_y$  direction, normal incidence of the impinging light is ensured. The centered detector element was modeled according to the layer structure of material H853. The detailed layer structure is given in the appendix section A. Figure 4.12 b shows a typical electric field configuration for the electric field component  $\vec{E}_y$  for grating coupling, SPP propagation on the grating, SPP propagation in the dielectric loaded guiding region, end-fire coupling to the AZ and wave guiding in the AZ.

The optimization was started with simulations covering the grating coupling and propagation of the excited SPP. Simulations for different structures have been conducted in which all SPP excitation is achieved by grating coupling. For three different configurations the electric field characteristics were simulated and compared. The first structure consists of the grating coupler and a metal-air interface for SPP guiding. This configuration represents the situation discussed in section 4.4.1. Due to the low confinement of SPPs to the metal-dielectric interface in the MIR wavelength region the propagation has comparable high losses and low propagation lengths. The electric field simulations reflect this low confinement as depicted in figure 4.13 a.

Two alternative approaches were investigated by numeric simulations which provide higher mode confinement. Mode confinement has major impact onto the end-fire coupling efficiency to the active zone and the re-irradiation losses which lower the propagation length. The first approach is based on sub-wavelength patterned grooves in the metal layer to spoof SPPs (4.13 b). By patterning the metal at the metal-dielectric interface the effective permittivity of the metal layer can be adjusted and thereby the dispersion of the SPP [183]. For the spoof SPP guide a period  $d = 1.5 \mu\text{m}$ , a groove width  $a = 0.45 \mu\text{m}$  and a groove depth of  $h = 0.8 \mu\text{m}$

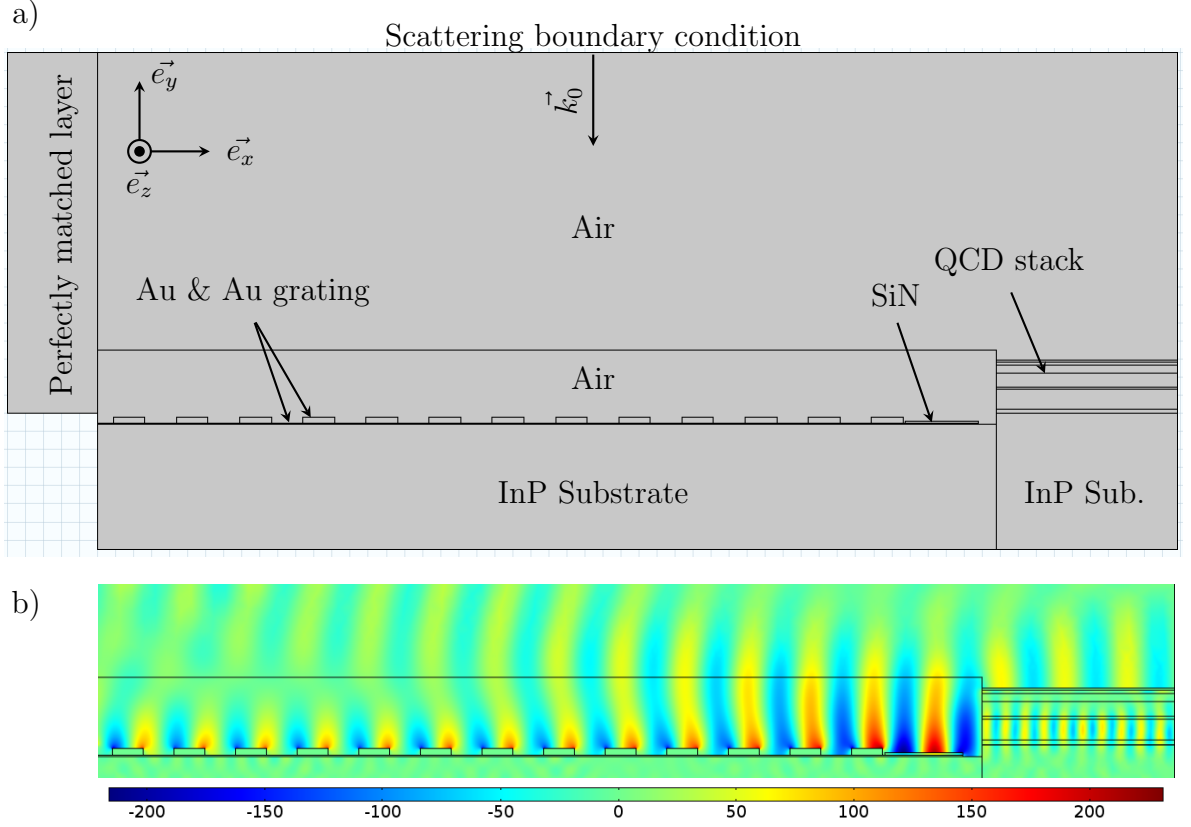


**Figure 4.12:** The simulation domain a) is bound by the scattering boundary condition at the top, which excites the input electromagnetic wave (MIR light). To the left the domain is bound by a PML to prevent perturbing simulation artifacts such as reflections on the left. The QCD stack from top to bottom consists of the Au metal top contact, the top contact layer, the top cladding layer, the AZ and the bottom cladding. A typical electric field distribution in  $\vec{e}_y$  ( $E_y$ ) direction on the grating lens and the coupling area is shown in subfigure b.

was used according to figure 4.9.

The second approach is based on a thin dielectric layer on top of the metal-air interface. Dielectric loading with SiN layers provides strongly enhanced mode confinement (4.13 c) and propagation length with minimal fabrication effort in comparison to sub-wavelength patterned structures. The SiN layer thickness for the simulation shown is 250 nm. A detailed investigation of the properties of SiN loaded Au SPP waveguides can be found in [48].

To investigate on the differences between these three methods to implement the guiding region, the electric field distribution in growth direction  $\vec{E}_y(y)$  was simulated (figure 4.14). A cut line positioned approximately in the distance of the detector elements facet from the grating lens structure was chosen. This distance corresponds approximately to the length of the guiding region. According to the electric field distribution on this cut line, in the height over the guide where the center of the



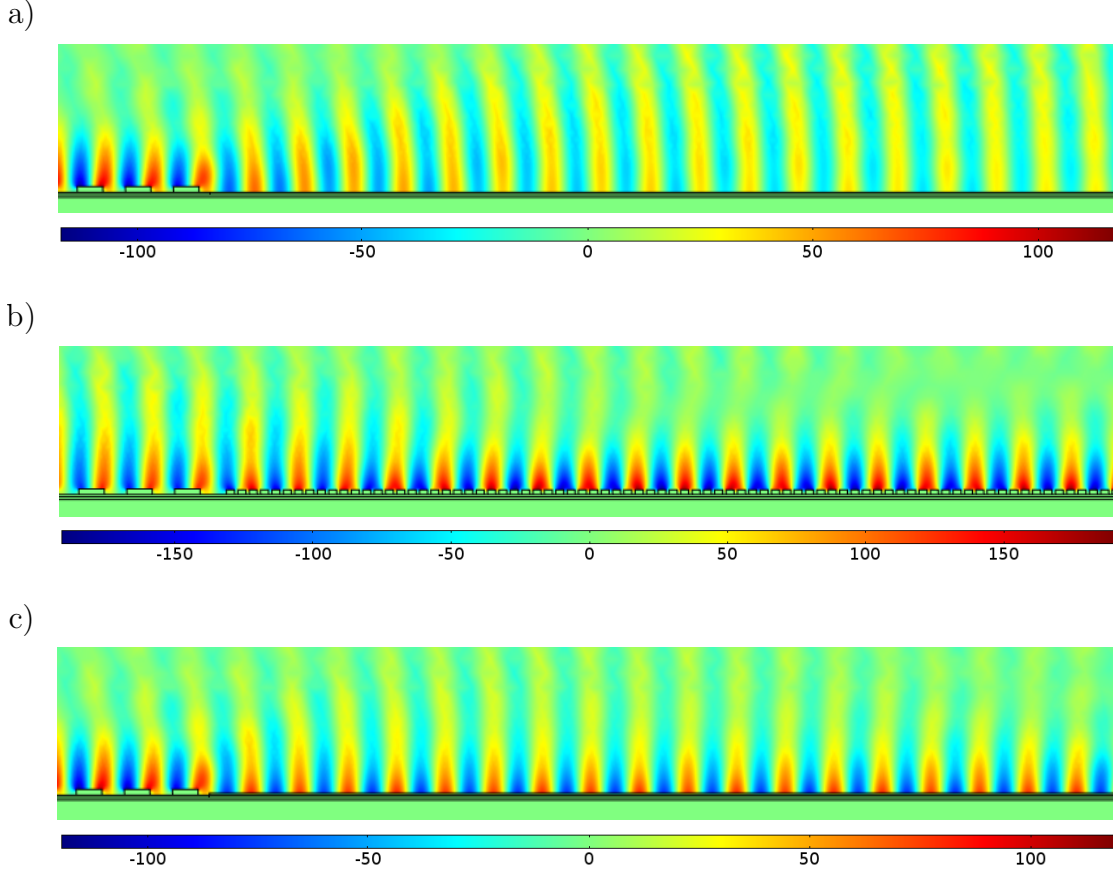


**Figure 4.13:** Three different SPP propagation structures with their electric field distribution. The pure metal-air interface a) with an Au layer shows a very low confined mode with high re-irradiation losses. The spoof plasmon structure b) provides a higher mode confinement to the interface by the sub-wavelength structured Au grooves which leads to lower re-irradiation losses and higher propagation length. The dielectric loaded guiding region c) shows comparable mode confinement without the need of sub-wavelength patterning the surface.

AZ is located, the SiN loaded guide is favorable. Since the dielectric loaded guiding region provided sufficient coupling efficiency the spoof plasmon structure solution was not implemented. A major drawback of a spoof SPP guiding region is the need of electron-beam lithography to ensure the required sub-wavelength structure size patterning in the MIR wavelength range.

The influence of the grating period, depth, grating period number and the SiN layer thickness onto the coupling efficiency has been investigated by simulation for the ideal total etch depth.

The peak absorption of the used QCD material is around  $1580\text{ cm}^{-1}$  at room temperature, which is slightly shifted to the short wavelength side in comparison to the  $1540\text{ cm}^{-1}$  ( $6.5\text{ }\mu\text{m}$ ) design wavelength of the material. The ideal grating period for an excitation at the design wavelength was determined to be  $p = 6.4\text{ }\mu\text{m}$



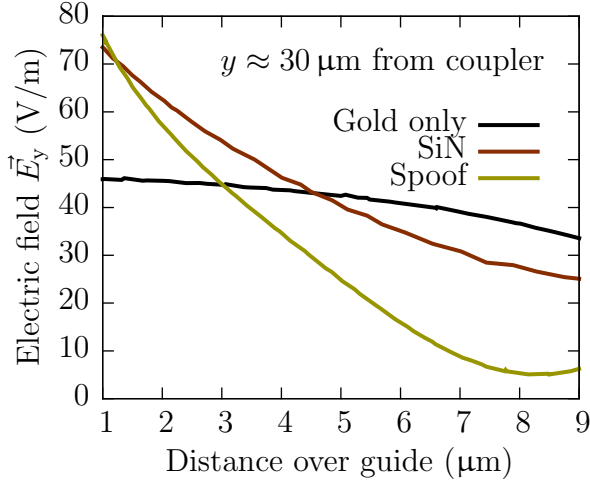


**Figure 4.14:** Simulated intensity of the electric field in  $\vec{e}_y$  direction ( $\vec{E}_y$ ) over the SPP guide for the different guide types. The position is in  $\approx 30 \mu\text{m}$  distance from the grating coupler, which is in the range of the distance to the detector element facet.

at a grating depth of  $h = 700 - 750 \text{ nm}$ . The simulated absorption efficiency over different wavelengths normal incident excitation is shown in figure 4.15 using the simulation configuration shown in figure 4.12 a. The highest coupling efficiency in simulations was observed for a dielectric loaded guiding region with a SiN thickness of  $200 - 250 \text{ nm}$ .

The grating parameters were chosen to minimize back reflection from the grating lens surface, hence maximize the coupling to SPPs propagating on the grating surface and the guiding region. In the simulations a total etch depth of  $e \approx 6.7 \mu\text{m}$  depending on the exact material structure and a SiN thickness of  $200 \text{ nm}$  show maximum mode overlap for end-fire coupling to the AZ. The total absorption saturates at a certain number of grating periods. Hence, the lens size effectively contributing to the radiation coupled to the active zone is limited. Above 15 periods saturation effects are observed in the simulations (figure 4.15 a). This corresponds to  $96 \mu\text{m}$  length for the grating period of  $6.4 \mu\text{m}$ .

#### 4.4.5 Fabrication

All plasmonic lens devices were fabricated from a bi-functional QCLD material H853 but operated in QCD mode, hence unbiased exclusively (figure 4.16). This material was chosen due to the cladding layers which provide the waveguide properties for the AZ. Fabrication tests have been done with material H861. The growth sheets for both materials are documented in appendix A. The bottom and top cladding layer provide a waveguide for the active zone (AZ). Since no deep sub-wavelength structures were fabricated for the device detecting at  $\lambda = 6.5 \mu\text{m}$  all processing steps are compatible to standard technology without the need of e-beam lithography.

In the first processing step the detector elements SiN etch hardmask is deposited by plasma enhanced vapor deposition (PECVD). Subsequently, the detector element

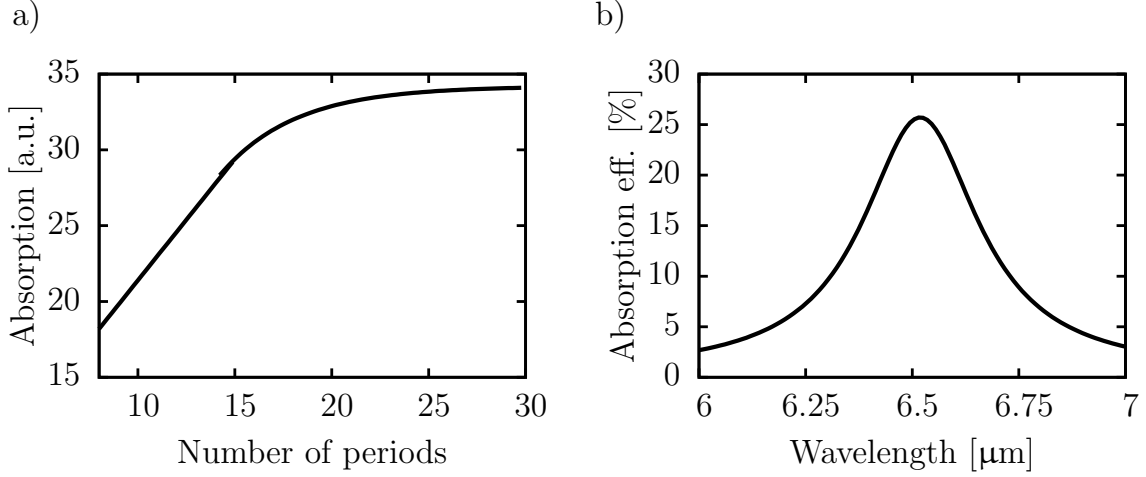


**Figure 4.15:** Simulated total absorption (fit) a) over the total number of grating periods determining the plasmonic lens size. Simulated absorption efficiency for normal incident excitation with a maximum b) at 6.5 μm wavelength normal incident excitation.

in the center is structured by reactive ion etching (RIE). After hardmask removal the total etch depth  $e$  is measured with a Dektak profilometer.

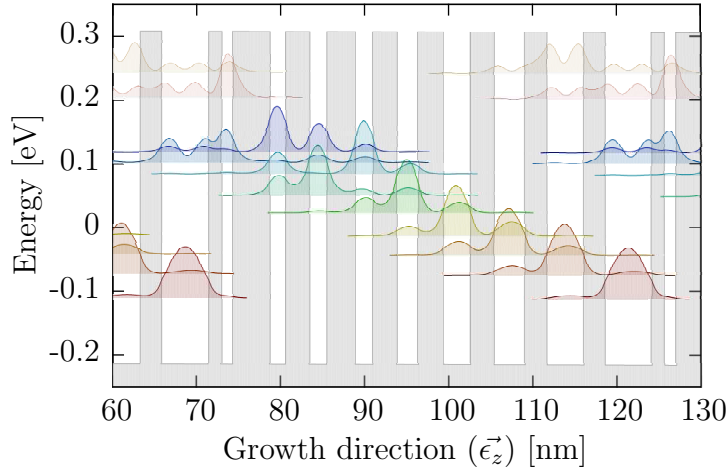


**Figure 4.16:** Band structure of the bi-functional material H853 in unbiased condition, hence in detector operation. The states which are not relevant for detector operation are plotted semi transparent. The bi-functional material was chosen due to the cladding layers which provide efficient waveguiding.

The grating lens fabrication starts with the deposition of SiN with a thickness corresponding to the desired grating depth. Then the grating structure is transferred by photolithography using a mask aligner. This is the key lithography process for this type of device. Two requirements have to be met by this lithography step. First, the lens has to be exactly around the detector element. Second, the lithography resolution/quality directly influences the grating geometry such as duty cycle, period

and edge quality. Best results could be obtained with 1:1 diluted AZ5214 resist in hard contact exposure mode. Since the total etch depth  $e$  as depicted in figure 4.11 is relatively high, the detector element mesa is several micrometers higher than the lens plane. Hence, the lithography mask is in contact with the detector elements top contact layer. As a result this limits the minimal distance between the lithography plane (in etch depth  $e$ ) and the mask. The hard contact mode minimizes this distance and thereby the lithography errors by diffraction. The SiN layer is then structured by RIE optimized for vertical edges. The lens Ti/Au metalization is sputter deposited onto the structured SiN bars/rings by a lift-off process. The last step is the contact metalization by sputter deposition. The alloy Ti/Au/Ni/Au forms ohmic contacts with the highly doped contact layer. The contacts are optionally annealed for 120 s at 360°C.

The finished devices are glued onto a Cu carrier with a small printed circuit board (PCB) for electrical contacts. The Ti/Au/Ni/Au contacts on the detector device are manually wire-bonded to the PCB contact areas. The top contacts were directly wire bonded from the top contact on the detector element to the PCB and the bottom contacts from the bottom contact areas nearby the plasmonic lenses to the PCB. Scanning electron microscope (SEM) images of the three device designs are shown in figure 4.17. A typical lithography error as observed several times due to a too large distance between the mask and the SiN layer for lens structuring is shown in figure 4.17 b.

#### 4.4.6 Results

All three different device designs were designed to exhibit a large number of periods for the plasmonic lens. This decision should prevent the signal to be limited by the amount of MIR radiation which can be collected. Comparison measurements to the plasmonic lens devices were done using 45° mesa devices with a mesa size of  $100\text{ }\mu\text{m} \times 100\text{ }\mu\text{m}$ .

The three plasmonic lens device types have a detector element size of  $100\text{ }\mu\text{m} \times 100\text{ }\mu\text{m}$  for the star shape device,  $70\text{ }\mu\text{m}$  diameter for the circular shape device and  $250\text{ }\mu\text{m} \times 40\text{ }\mu\text{m}$  for the linear grating device. That implies the circular lens device having a 2.6 times smaller electric active area than the mesa device. The star shape device and the linear grating device have the same electric active detector element size (area  $A$ ) as the reference 45° mesa detector.

Characterization was done as described in section 3.4 with the devices mounted in a cryostat illuminated by the global source of the FTIR spectrometer. First a pure photocurrent characterization was done comparing the absolute photocurrent

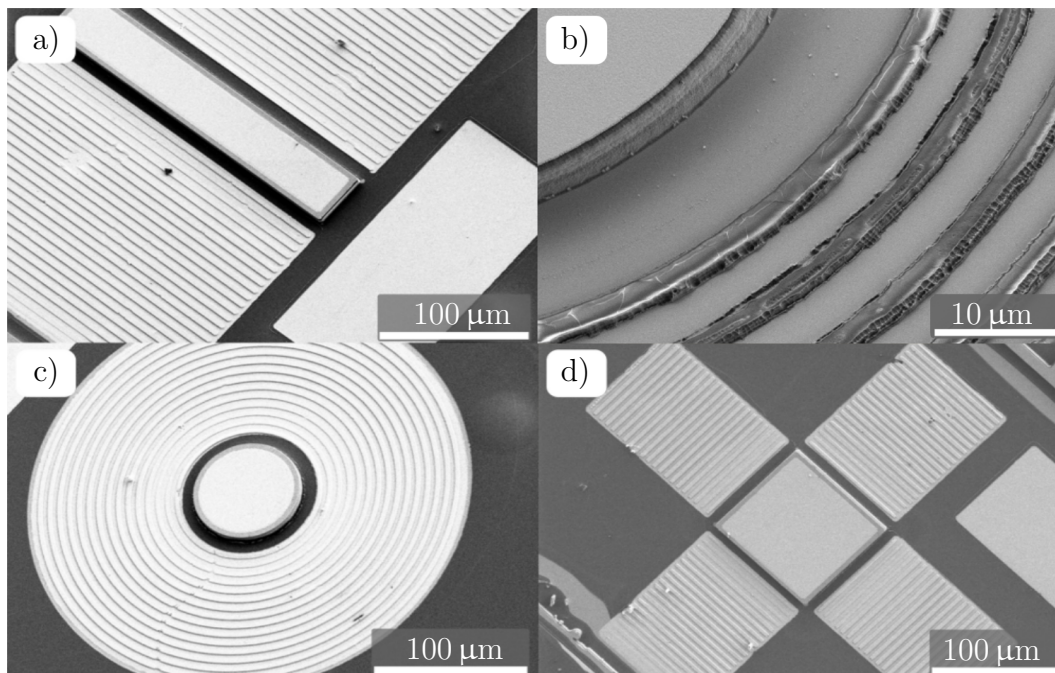


**Figure 4.17:** Scanning electron microscope images of finished plasmonic lens QCD devices with a) line grating shape, c) circular shape and d) star shaped lens. The most challenging processing step is the lens lithography which may result in lithography errors as seen in b), if the mask to SiN or resist distance is too high. Therefore, hard contact mode exposure was used to achieve the best results.

spectrum of all device types with the mesa device as shown in figure 4.18.

The temperature dependent photocurrent characteristics show a different behavior than mesa devices. Besides the enhanced photocurrent in general a lower photocurrent drop for increasing temperatures is observed in comparison to the mesa type (reference) detectors. The highest temperature dependency of the photocurrent response is observed for the mesa device which shows a drop by  $\approx 75\%$  (figure 4.18 a and b). In comparison the line shape device shows a photocurrent drop around 45% and the star shape device around 30%.

The plasmonic lens devices exhibit up to a factor 2.5 higher photocurrent at 80 K (line and star shape) and up to 5 and 6 times higher photocurrent than the mesa device at room temperature for the line shape and the star shape device respectively. Hence all plasmonic lens devices show a lower drop of the photocurrent response.

For the circular shape device the situation is similar if the reduced QCD element size is taken into account. As mentioned, the electric active element size for the circular shaped device is by a factor 2.6 smaller than the mesa reference device. Even with this reduced size the photocurrent response at 80 K is slightly higher than for the mesa device. At room temperature the enhancement is even more pronounced, where the photocurrent response is a factor of 3 higher than for the reference device

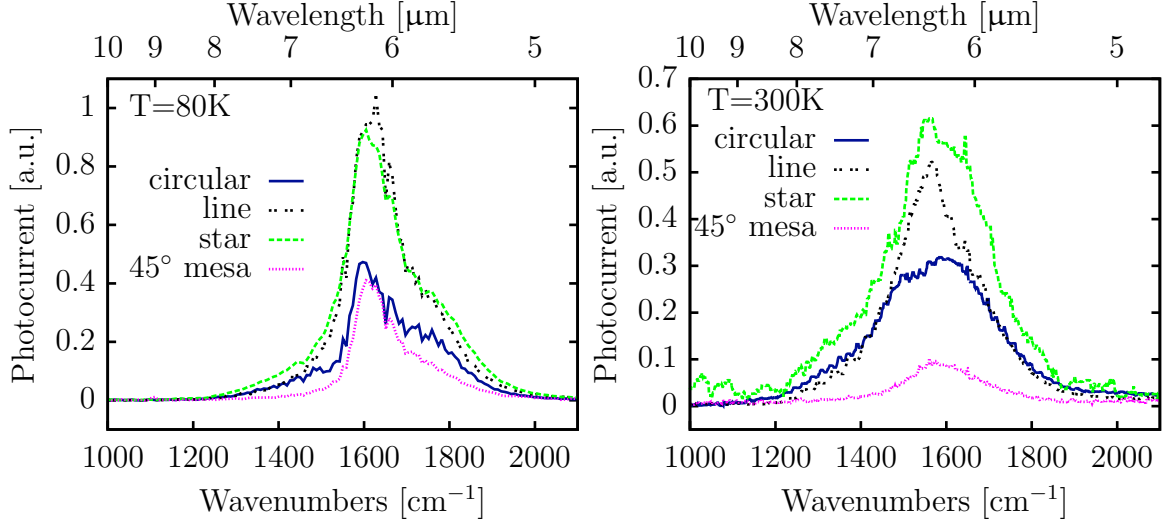


**Figure 4.18:** Photocurrent comparison of the three different plasmonic lens device types at 80 K and at room temperature. The reference device is the 45° mesa device. As published in [153].

(figure 4.18 b). Due to the illumination of the device with a  $f = 50.8$  mm lens the angle of incidence is distributed around normal incidence. As a result light coupling in the entire spectral sensitivity range of the QCD material can be assumed.

A direct comparison of the temperature dependent normalized photocurrent spectrum for a plasmonic lens device in comparison to the mesa device is shown in figure 4.19 a and b. The mesa device is processed and measured in the same processing batch with other SPP lens devices. A clear improvement in temperature stability and performance is observed for the plasmonic lens devices.

The relative photocurrent enhancement is in general higher for elevated temperatures. The observed enhancement can be attributed to the different geometry of the mesa device and the SPP lens detectors. The mesa device suffers from a decreasing absorption coefficient  $\alpha_{\text{isb}}$  at elevated temperatures combined with a short absorption length. Recalling equation (4.2)

$$\eta_{\text{abs}} = T_{\text{facet}} \left( 1 - e^{-\sqrt{2}\alpha_{\text{isb}}L_{\text{Act}}} \right) \quad (4.41)$$

we can compare the absorption lengths of the different coupling configurations. The absorption length for mesa devices is

$$L_{\text{abs}} = \sqrt{2}L_{\text{Act}} \quad (4.42)$$

with the thickness of the AZ given by  $L_{\text{Act}}$ . Since  $L_{\text{Act}}$  is in the range of  $\approx 1.85$   $\mu\text{m}$ , the absorption length  $L_{\text{abs}}$  is short. At elevated temperatures due to the lowered

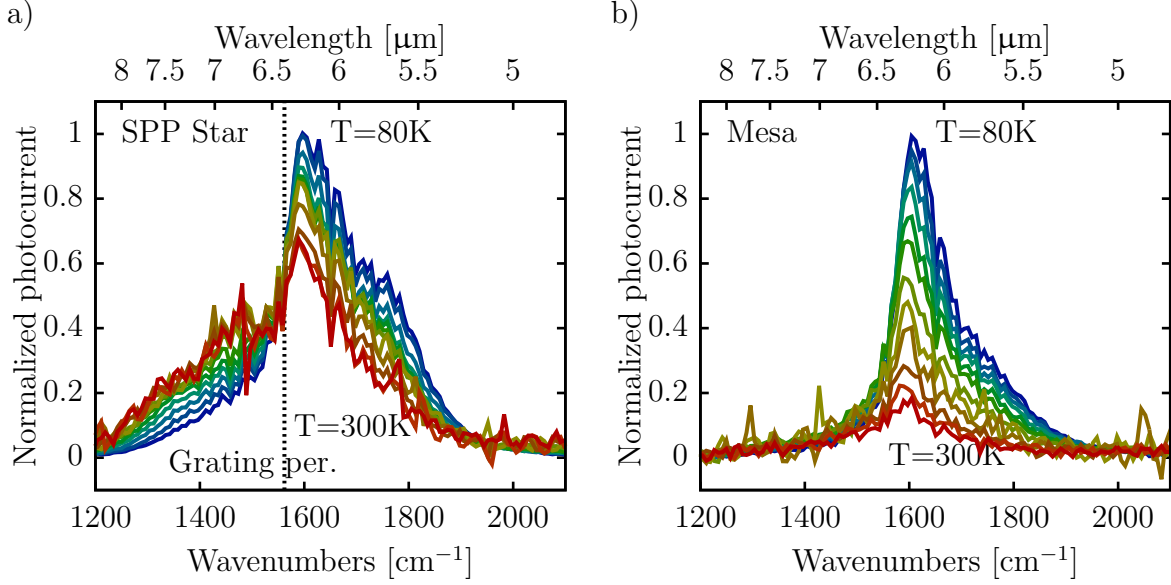


**Figure 4.19:** Comparison of the temperature dependent photocurrent response of a SPP lens detector device a) with a star shape lens and a mesa device b) in 45° facet illuminated configuration. The plasmonic lens device is illuminated by surface normal incident radiation from a global source. Subfigure a) modified from [153].

absorption coefficient  $\alpha_{\text{isb}}$  and the short absorption length the absorption efficiency  $\eta_{\text{abs}}$  is low and the mesa device exhibits a very low photocurrent response.

In contrast, the plasmonic lens devices offer a relatively long wave guide embedded AZ which results in roughly an order of magnitude longer absorption length

$$L_{\text{abs}} = \Gamma L_{\text{Mesa}} \quad (4.43)$$

with the mode confinement factor  $\Gamma$  and the detector elements width (diameter)  $L_{\text{Mesa}}$ . In this case due to the SPP waves coupled by end-fire coupling the maximum absorption length is related to the width (diameter) of the detector element. Consequently, for SPP lens devices the absorption efficiency similar to equation (4.4), neglecting wave guide losses can be written as

$$\eta_{\text{abs}} = \gamma_c (1 - e^{-\Gamma \alpha_{\text{isb}} L_{\text{Mesa}}}) \quad (4.44)$$

where  $\gamma_c$  is over all coupling efficiency. Again in comparison to the mesa device the difference in absorption length can be expressed as

$$\Gamma L_{\text{Mesa}} \gg \sqrt{2} L_{\text{Act}} \quad (4.45)$$

with the variables as described for equation (4.41) and (4.44). The lower perfor-



Sample	T	type	$I_{\text{Ph}}$ increase
H853L3	80 K	mesa	1
H853L1	80 K	line	2.5
H853L2	80 K	star	2.25
H853L1	80 K	circular	1.2 ( $\approx 3.12$ )
H853L3	300 K	mesa	1
H853L1	300 K	line	5
H853L2	300 K	star	6
H853L1	300 K	circular	3 ( $\approx 7.8$ )

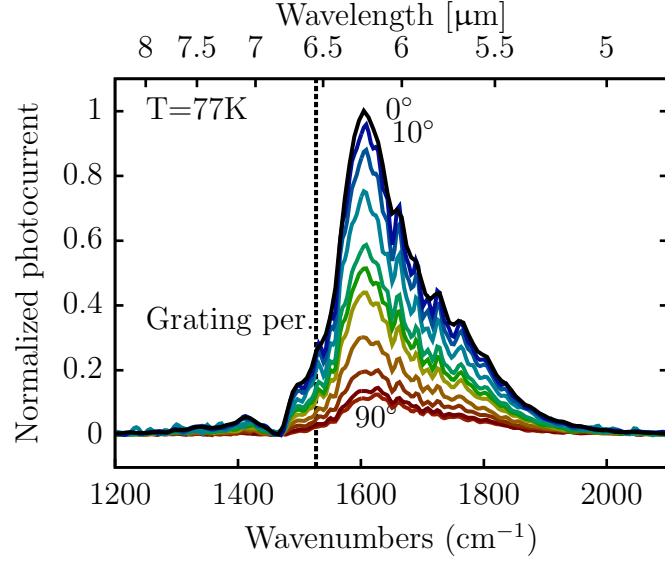
**Table 4.1:** Comparison of the photocurrent increase  $I_{\text{Ph}}$  of the plasmonic lens quantum cascade detector (QCD) device types with respect to the  $45^\circ$  mesa device at 80 K and 300 K. The photocurrent increase in brackets is normalized to the same electric active area as the reference device.

mance decrease with temperature is due to the higher absorption efficiency which gains impact towards room temperature. Hence the lower  $\alpha_{\text{isb}}$  at high temperatures is compensated by a longer absorption length available. A comparison for the photocurrent enhancement for the different device types is presented in table 4.1.

**Polarization selectivity** Due to the linear grating of the line grating lens devices such as depicted in figure 4.17 a, a polarization sensitivity is observed. The polarization selectivity was investigated for different angles of linearly polarized light impinging in surface normal direction. Grating coupling is most efficient for light linearly polarized with the electric field component perpendicular to the grating slits. A polarizer was used in the beam path and the photocurrent spectrum recorded for different polarizer angles as depicted in figure 4.20. For increasing angles the photocurrent response drops, due to a lower fraction of the impinging light being coupled to the grating lens. Hence with increasing angles the fraction of the electric field component perpendicular to the grating slits drops. This polarization selectivity can be useful for spectroscopy applications, where two different linear polarized light sources could be used and separately detected. This polarization selective surface normal incident detection of orthogonal linear polarized sources can minimize crosstalk between two detector devices.

**Propagation length** The surface plasmon polariton (SPP) propagation length was determined by a spatial resolved photocurrent measurement. A line grating plasmonic lens device was mounted on a two axis linear motorized stage. The plasmonic lens was then moved in the focus spot of a  $f = 50.8$  mm lens while the photocurrent was recorded (figure 4.21 a). The spatial resolution of the measurement was  $2 \mu\text{m}$

**Figure 4.20:** Polarization selectivity of a line grating device. The detector is illuminated by normal incident linearly polarized light from a global using a polarizer. For increasing polarization angles, a lower fraction of the light is polarized with the electric field vector perpendicular to the grating slits. The remaining signal for  $90^\circ$  is due to the polarizer efficiency. As published in [153].



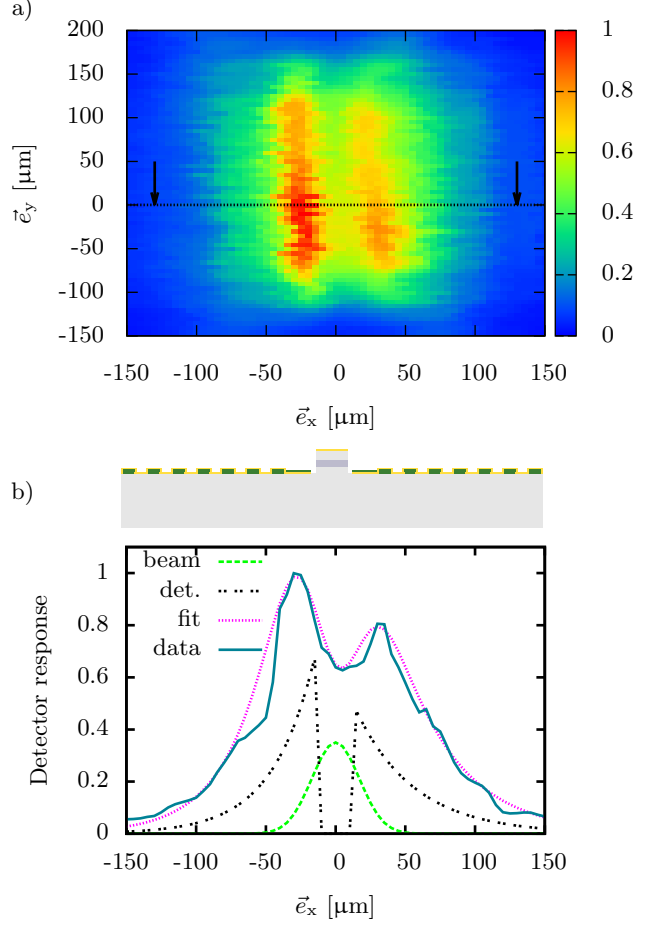
in  $\vec{e}_x$  and  $\vec{e}_y$  direction. This corresponds to the plane perpendicular to the surface normal illumination axis. The intensity stays relatively constant for lines parallel to the grating slits, or equally for constant distances to the detector element facet. The variations visible can be attributed to processing imperfections. Since the coupling efficiency is dependent on the distance between the end of the guiding region and the facet, slightly misaligned structures lead to signal variations. The difference in signal intensity between the left and right side plasmonic lens has its origin also in slight misalignments, mostly when the left grating lens and guiding region has a smaller distance to the facet than the right or vice versa.

Prominently visible is a strong drop of the photoresponse in a stripe between the two elongated maxima. This is due to the QCD element with no light coupling structure on top. The top surface of the detector element is covered with Au to provide a top contact for the structure. Hence the top of the QCD element is strongly reflecting with no light coupling to the AZ. The remaining signal is due to the size of the focus spot and the resulting scattering on the first grating periods of the lens towards the facet.

A cross section of the detector signal perpendicular to the grating slits (in  $\vec{e}_x$  direction) as shown in figure 4.21 b can be fitted by a Gauß function as a model for the impinging beam and a detector function which describes the intensity of the propagating SPP wave on the lens. From this detector function the SPP propagation length can be estimated. Based on the  $1/e$  decay distance definition of the propagation length, a fit to the detector response (data) in 4.21 b gives a propagation length of  $L_{\text{SPP}} = 49 \mu\text{m}$ . By the spatial measurement and the fitted propagation length (figure 4.21 b) a detector signal from pure edge scattering to the mesa facet could be precluded.



**Figure 4.21:** Spatial distribution of the detector signal for a line grating device with the minimum at the position corresponding to the detector element in the center. Since light coupling is not possible directly to the Au top contact covered QCD element, a minimum is observed at this position. The distribution in a cut plane parallel to  $\vec{e}_x$  can be fitted as a convolution of a device function with a Gauß beam. From this fit a SPP propagation length of  $L_{\text{Spp}} = 49 \mu\text{m}$  can be extracted. As published in [153].



**Reduced lens dimensions** With the propagation length  $L_{\text{Spp}}$  determined by the spatial resolved measurement the ideal detector dimensions can be determined in a straight forward way. Intuitively a larger lens would lead to more light being collected and therefore to a higher photocurrent response. Since the propagation length  $L_{\text{Spp}}$  on the grating lens is limited an arbitrary large lens would not collect more light. Once the distance from the detector element to the outer edge of the lens or similarly, the lens radius  $r_{\text{Lens}}$  to the lens middle is several times larger than the propagation length ( $L_{\text{Spp}} \ll r_{\text{Lens}}$ ) the SPP wave does not reach the AZ of the QCD element anymore. Considering the propagation length this means an exponential decay of the photocurrent contribution with increasing distance from the facet.

In terms of the device responsivity an oversized lens size ( $L_{\text{Spp}} \ll r_{\text{Lens}}$ ) leads to more impinging radiation power to be considered in the responsivity calculation. Hence the power to be considered scales directly with the device area but the photocurrent contribution is subjected to the exponential decay. This is equivalent to a decrease of the responsivity  $R_{P,\text{Spp}}$  in equation (3.1) for oversize lenses.

Consequently, a maximum lens size can be found. If a maximum lens size is considered in such a way that the longest distance for a SPP wave to travel on the

80K		
Parameter	Star shape SPP QCD	Mesa
meas. $D^*$ (cm $\sqrt{\text{Hz}}/\text{W}$ )	$3.2 \cdot 10^9$	$\approx 2.6 \cdot 10^9$
meas. $R_P$ (mA/W)	2.5	$\approx 7$
meas. $R_0$ ( $\Omega$ )	$1.13e7$	$6.04e6$
approx. $2L_{\text{Spp}}$ $D^*$ (cm $\sqrt{\text{Hz}}/\text{W}$ )	$3.9 \cdot 10^9$	-
approx. $2L_{\text{Spp}}$ $R_P$ (mA/W)	3.5	-
300K		
Parameter	Star shape SPP QCD	Mesa
meas. $D^*$ (cm $\sqrt{\text{Hz}}/\text{W}$ )	$7.1 \cdot 10^6$	$\approx 2.7 \cdot 10^6$
meas. $R_P$ (mA/W)	1.6	$\approx 1.6$
meas. $R_0$ ( $\Omega$ )	492.5	474
approx. $2L_{\text{Spp}}$ $D^*$ (cm $\sqrt{\text{Hz}}/\text{W}$ )	$8.4 \cdot 10^6$	-
approx. $2L_{\text{Spp}}$ $R_P$ (mA/W)	2.2	-

**Table 4.2:** Comparison of the responsivity and detectivity for the star shape device with large lens dimensions (meas.) and limited lens and detector size (approx.). The limited lens size values are calculated with a cut off of the coupled radiation at a distance from the detector element facet of two times the SPP propagation length  $L_{\text{Spp}}$ , as measured. The difference in device resistance at 80 K is not due to geometry, but can be attributed to bad performing bottom contacts.

lens is approximately  $L_{\text{Spp}}$  up to  $2L_{\text{Spp}}$ , no unused excess lens/detector area reduces the responsivity  $R_{P,\text{Spp}}$  and specific detectivity  $D_{J,\text{Spp}}^*$ .

### Possible detectivity enhancement

The mesa device detectivity for  $45^\circ$  facet illumination can be directly calculated from equation (3.7).

$$D_{J,\text{Mesa}}^* = R_{P,\text{Mesa}} \sqrt{\frac{A_{\text{Mesa}} R_{0,\text{Mesa}}}{4k_{\text{B}} T}} \quad (4.46)$$

with  $A_{\text{Mesa}} = (100 \times 100) \mu\text{m}^2$ . The differential resistance around zero bias voltage  $R_{0,\text{Mesa}}$  can be directly extracted from IV measurements as described in section 3.4.2. The peak responsivity  $R_{P,\text{Mesa}}$  has to be determined by the methods described in section 3.4.4 based on equation (3.26). The incident power is calculated from the spatial power distribution and the effective device area (equation (4.3)).

The SPP lens devices have an optical active area defined by the total area occupied by the detector device. Even if the area of the detector element in the center could be omitted - it is optically not directly coupling to surface normal radiation - according to the definition of the responsivity, it has to be included. A key feature of the plasmonic device design is that the device resistance is not increased due to lens size. Extending the lens area and thereby the total area  $A$  does not decrease the

device type	electric active $A_{\text{De}} (\mu\text{m}^2)$	total area $A (\mu\text{m}^2)$	reduced area $A, 2L_{\text{Spp}} (\mu\text{m}^2)$
mesa	10000	10000	-
SPP line	10000	91000	59000
SPP star	10000	66000	49200
SPP circular	3850	66960	66960

**Table 4.3:** Detector element sizes for the different device designs. The total device area is as fabricated and the reduced  $2L_{\text{Spp}}$  is if all lens regions with a distance more than  $2L_{\text{Spp}}$  away from the detector element facet are omitted. The area which contributes to the resistance of the device, hence the Johnson noise is  $A_{\text{De}}$ .

device differential resistance  $R_0$ , as it would be the case for a mesa device. For size considerations, the differential resistance of the detector element  $R_{0,\text{De}}$  in the center of the plasmonic lens devices, can be approximated by

$$R_{0,\text{De}} = \frac{\rho_{0,\text{De}} h}{A_{\text{De}}} \quad (4.47)$$

with the detector element height  $h$ , the detector element area (electrical active)  $A_{\text{De}}$  and the specific differential resistance around 0 V denoted by  $\rho_{0,\text{De}}$ . For detectivity considerations again the total detector area  $A$  has to be taken into account. With the detectivity from equation (3.7), equation (4.47) and the area definitions, the detectivity of the SPP lens detectors can be expressed easily

$$D_{\text{J,Spp}}^* = R_{P,\text{Spp}} \sqrt{\frac{A R_{0,\text{De}}}{4k_B T}} = R_{P,\text{Spp}} \sqrt{\frac{A \rho_{0,\text{De}} h}{4k_B T A_{\text{De}}}} \quad (4.48)$$

where  $R_{P,\text{Spp}}$  is the responsivity of the plasmonic lens detector. A summary of the total detector area  $A$  and the electrical active detector element size  $A_{\text{De}}$  is given in table 4.3.

From equation (4.48) it is obvious that the detectivity enhancement by extending the optically active area is only possible if the plasmonic lens devices have the same or a better responsivity than the mesa device. Table 4.2 gives an example for the star shape device type figures of merit at 80 K and at room temperature. At 80 K the responsivity of the mesa device is higher than for the SPP star shape device. This is besides the higher  $\alpha_{\text{isb}}$  at low temperatures, due to the lens size exceeding the propagation length limitation.

At room temperature a detectivity enhancement is possible, since the responsivity of the reference mesa device is similar to the SPP star shape detectors responsivity even if the plasmonic lens is too large. This is due to the absorption efficiency compensating the lower absorption coefficient as discussed before. The table gives

also an calculated approximation, if only a reduced lens size of e.g.  $2L_{\text{Spp}}$  maximum distance from the facet to the lens edge is considered. In this comparison for responsivity calculation, the same polarization factor for both devices is used. An approximation of the mesa detectivity results in comparison to the star shape plasmonic lens device in factor 2.6 enhancement of the specific detectivity at room temperature.

**Short conclusion** It can be concluded that for the presented coupling scheme the on-lens propagation length is the key parameter. A limiting factor is the excitation of SPP waves both, towards the detector element and away from the detector element which leads to losses. In addition, due to the re-radiation of SPPs on the grating lens, the propagation length is lower than for pure metal-dielectric loaded plasmon waveguides. The performance increase towards elevated temperatures can be attributed to the absorption efficiency of the coupling scheme. The plasmonic lens coupling scheme is therefore also well suited for detector designs with a low number of periods since the absorption length is not decreased due to the lower number of periods, as it would be the case for  $45^\circ$  mesa devices. Therefore a higher responsivity increase can be assumed.

## 4.5 Alternative coupling methods

The following alternative light coupling schemes have not been investigated in the scope of this thesis but are mentioned for the sake of completeness.

### 4.5.1 Meta material coupling

Meta materials are micro- and nanostructures which resemble an artificial material with unique material properties such as close to perfect absorption or reflectance. Meta materials consist of symmetric spatial repetitions of identical building blocks referred to as meta-atoms. These meta-atoms, by design tailor the electromagnetic properties of the meta material. This is possible to such an extent, that material properties such as a negative refractive index can be achieved [185]. Recently double metal meta material structures were demonstrated which exhibit nearly unity absorbance in the MIR region [186, 187, 188]. Meta material surfaces offer the advantage of array integration and strong electric field enhancement. Meta material based detection of THz radiation had been demonstrated using a THz QCL material combined with a meta material surface [189].

### 4.5.2 Surface normal coupling

In the field of grating based coupling random corrugations [190] and random grating [191] based coupling has been shown for QWIP detectors.

Meander and spiral like structures with a wet etch fabricated sidewall modification for QCDs were demonstrated lately [192]. The side walls of the detector elements were fabricated to be shaped close to an elliptic surface to couple the light to the active zone of the neighboring element. The method is reported to work independent of the detection wavelength. The design extends in addition the optical active surface for light coupling which enhances the detectivity up to a factor of two in a similar way as reported for the plasmonic lens QCDs.

### Photonic crystal detectors

An attractive method to design detectors is to process their material as a photonic crystal. The photonic crystal couples to surface normal incident light and acts as a cavity for resonant absorption. Various photonic crystal detectors have been shown processed from QWIPs [34] and QCDs [193]. The photonic crystal cavity offers an additional set of parameters which allow for optimization of the cavity - detector material compound [40]. Simulations for critical coupling to photonic crystal detectors have been shown by P. Reininger et al. [138, 139]



## QUANTUM CASCADE DETECTOR ARRAYS

Single detector elements such as presented in chapter 4 are the starting point for array considerations. Besides single detector performance, for detector arrays several additional challenges have to be faced. These include pixel and electric contact geometry, light coupling, forward looking optics design, cooling equipment if needed, system noise limitation, production costs, reliability and quality.

Intersubband (ISB) detector arrays have proven their excellent low temperature performance realized as QWIP cameras which offer mega-pixel dual color resolution and high speed detection due to the low scattering times of ISB transitions. Besides the classic figures of merit for detectors such as the responsivity  $R_p$  and detectivity  $D^*$  the operation temperature  $T$  at which the desired performance is ensured is a key aspect for array devices. Moreover, the signal to noise ratio (SNR), often expressed as the noise equivalent temperature difference (NETD), pixel to pixel signal fluctuations, the number of pixels of an array, the system size, weight and power consumption define the overall performance.

Array type detectors demand for low noise and low power amplification which lead to the application of read out integrated circuits (ROICs) being an essential building block of an imaging system. Read out integrated circuits are commonly used for detector arrays to establish an electric connection to the pixel, sample the detector signal, amplify the sampled pixel signal and provide an organized way of access to the pixel signals/data to an external system. Two design approaches are established, where either rows and columns of pixels are grouped or every pixel is supplied with an own single amplifier unit.

This chapter starts with basic considerations needed for the development of imaging devices. Then the development of a low pixel count quantum cascade detector (QCD) pixel array for integration in a sensing system is presented. The applica-

tion for this array is remote detection of human victims in the scope of search and rescue operations. The basics of infrared detection and imaging are well described in [127] which is the major source for the theory part of the chapter.

## 5.1 Basic considerations

A detection system oriented towards a scene to be imaged or sensed in a remote detection setup has to direct radiation onto the pixel array. These pixel arrays are commonly referred to as focal plane arrays (FPAs). An objective is used to project the scene within the field of view onto the FPA. Fundamental considerations for the optics have to include the FPA dimensions, the pixel density and from that the resulting total number of pixels. Further the wavelength range is essential for the choice of the lens material and optional lens anti-reflection coating (ARC).

The next step is to determine the radiation power which impinges on a single pixel of the FPA when the system is oriented towards the scene. Different per pixel power  $P_{i,\text{Pix}}$  levels have to be assumed for different scene conditions. The power level gives a first estimation of the required peak responsivity  $R_P$  and the necessary amplification for further signal processing. At this point two different setups are possible.

**Passive imaging devices** First a completely passive imaging device, where the radiation power on the pixel of a FPA originates from the scene and its objects exclusively without any other sources. This choice requires a sufficient performing detector device in terms of the detectivity  $D^*/\text{NETD}$  and responsivity  $R_P$  and sufficient background radiation in the wavelength range of interest. This method offers two advantages which can be essential depending on the application. The device does not need to provide power for an additional scene illumination and nearly unnoticeable observations are possible. The drawback of passive illumination is that specific scene conditions may lead to low contrast and/ or no visible image. This may be the case if the background radiation available approaches levels with pixel power differences below the NEP.

**Active imaging devices** The second option is a combination of an imaging device based on e.g. a FPA imager and an active illumination source. This approach can be attractive in conditions, where the scene offers not enough background radiation power at the operation wavelength of the imager. A general drawback of active scene illumination is that the illumination source can be detected by others if the observed



beings have sensitive eyes or equipment at the illumination wavelength. Already in the 1940s active night vision devices were used for military applications. They had one of their first sad appearing as the Zielgerät 1229 in World War II. An active light bulb illumination with a infrared-pass filter was used for scene illumination [194]. In modern systems active illumination with single mode laser sources can be used for remote detection of substances, which are mostly gases. This system can also be extended to multi-wavelength illumination to identify different gaseous substances.

### 5.1.1 Radiation power

Considering Planck's radiation law for the emissivity of a blackbody the radiation power emitted by a surface can be estimated from

$$L(\lambda, T) = \frac{2\pi hc^2}{\lambda^5} \frac{1}{e^{\frac{hc}{\lambda k_B T}} - 1}, \quad (5.1)$$

with Planck's constant  $h$ , the speed of light  $c$ , the wavelength  $\lambda$  and the Boltzmann constant  $k_B$ . Figure 5.1 shows the blackbody emission over the wavelength for different temperatures. Note the difference to the global (Figure 3.1) which has a higher temperature than the average scene with  $\approx 300$  K background and the peak shift to lower wavelength for higher temperatures. According to figure 5.1 the available power per pixel is dependent on the operation wavelength of the device. For detection around  $4.3 \mu\text{m}$  wavelength lower background radiation power is available than for detection at e.g.  $9.5 \mu\text{m}$ .

Besides the spectral radiation power the field of view of the imaging device limits the amount of collected radiation. The focal length and the aperture size of the objective used to project the scene onto the pixel array determines the f-number

$$f_{\#} = \frac{f}{D}, \quad (5.2)$$

with the focal length  $f$  and the effective aperture diameter  $D$ .

Based on the spectral power (emissivity)  $L(\lambda, T)$  in figure 5.1 calculated from equation (5.1) the power per pixel can be derived. To get the total radiation power, the emissivity is integrated over the wavelength range, the detector pixels are sensitive to within the field of view. The solid angle  $\theta$  defines the field of view which in combination with the integrated emissivity in the range  $\lambda_1 \cdots \lambda_2$  gives the radiation power density  $\tilde{P}$

$$\tilde{P} = \int_{\lambda_1}^{\lambda_2} L(\lambda) d\lambda. \quad (5.3)$$

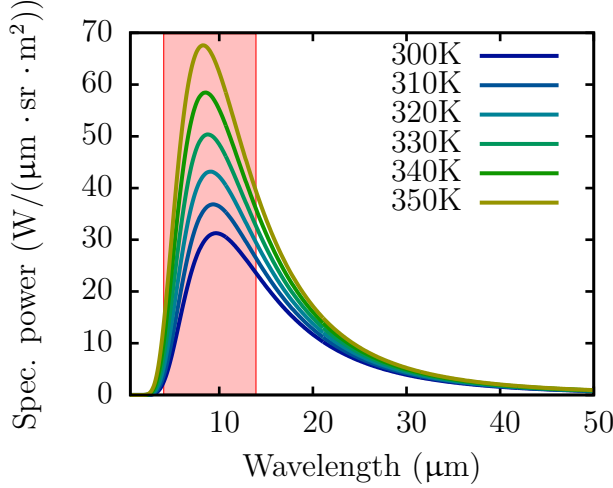


**Figure 5.1:** Spectral radiation power according to Planck's radiation law and an ideal blackbody for temperatures starting at room temperature and above. The red shaded area marks the range from 4 μm up to 14 μm commonly used for MIR imaging devices.

As described before  $\tilde{P}$  strongly depends on the operation wavelength of the device. With the f-number  $f_{\#}$ , the pixel area  $A$  and the power density  $\tilde{P}$ , the power per pixel  $P_{i,\text{Pix}}$  can be expressed as

$$P_{i,\text{Pix}} = \frac{A}{4f_{\#}^2 + 1} \tilde{P}. \quad (5.4)$$

Typical per pixel power levels are depending on the wavelength in the low nW range. For a frequency based derivation consult [128] and for comparison data for QWIP FPAs [127]. Based on the estimated  $P_{i,\text{Pix}}$  the required responsivity for a sufficient photocurrent signal can be estimated according to

$$I_{\text{Ph}} \approx R_P P_{i,\text{Pix}}. \quad (5.5)$$

### 5.1.2 Focal plane arrays

A variety of different FPA technologies have been realized so far. High resolution QWIP imagers, room temperature mobile low pixel count micro-bolometer cameras, type II superlattice detectors and mercury cadmium telluride (MCT) systems grown on Si substrates, to name a few. All of these technologies exhibit advantages for specific applications, when compromises can be made such as low resolution, low wavelength selectivity or high energy consumption.

**Requirements** Commercially produced FPAs need numerous requirements to be met to be economically efficient. First substrates for their growth need to be available in sufficient number at moderate prices. For many years MCT detector arrays could only be grown onto very expensive diamond substrates until Si substrate based growth was realized [14]. The number of pixels is an essential figure of merit for

the identification capabilities of scene objects and individuals at great distance from the imaging device [195]. Mobile, handheld or head mounted systems are restricted in packaging volume, weight and most important in energy consumption. This directly explains the need for uncooled respectively room temperature operable passive imaging devices. At the moment compromises are necessary in terms of costs or performance. As an example currently commercially available micro-bolometers are restricted in response time but offer cost effective room temperature thermal imaging systems with relatively low pixel counts.

**Third generation** imaging devices are currently investigated by the community. They are e.g. sensitive in two separate wavelength regions which enables for absolute temperature determination. They are required to have high pixel counts, in cooled or uncooled applications. A third generation FPA is combined with a ROIC providing on chip signal processing and supports high frame rates, detectivity or thermal resolution in comparison to second generation devices [196]. Type II superlattice detectors [26] are a promising platform for high speed thermal imaging devices in the long-wave infrared (LWIR) [27, 197] up to megapixel sized FPAs [32].

QWIP cameras show high detectivity and pixel counts and can be integrated as dual color imagers at relatively high costs per device. Their major drawback is the required low operation temperature, which is not accessible by thermoelectric cooler (TEC) systems. An analysis of the major competitors of third generation imagers can be found in [196]. A summary of 2<sup>nd</sup> and earlier generations of imaging devices can be found in [53].

**Geometry** Standard MIR devices have a pixel pitch between 10  $\mu\text{m}$  and 40  $\mu\text{m}$  [127]. A high filling factor is desired. A basic geometric requirement is a ROIC which matches the pixel pitch of the FPA. The FPA thermal expansion has to be taken into account. For cooled device types the compound of the FPA and the ROIC has to sustain many thermal cycles between room temperature and the operation temperature of the detector. For arrays based on heterostructures grown onto a semiconductor substrate after flip-chip bonding, the substrate side can be thinned to minimize substrate absorption and mechanical in plane stress induced by thermal expansion. For silicon based ROICs a thermal expansion coefficient of  $2.6 \times 10^{-6} \text{ K}^{-1}$  can be assumed, whereas in the case of an ISB detector grown on InP a thermal expansion coefficient of  $4.8 \times 10^{-6} \text{ K}^{-1}$  has to be accounted [198, 17], both at room temperature.

## 5.2 Quantum cascade detector array integration

This part describes the design, fabrication and results of a low pixel count quantum cascade detector prototype pixel array. The design decisions are described first including the geometric and electric considerations, then the results are presented. The array is based on the integration scheme briefly introduced in section 4.3.

The following part is based on the publication *4.3  $\mu\text{m}$  quantum cascade detector in pixel configuration*, published in Optics Express 2016 [144]. The chapter closes with a short description of the integrated device developed together with our collaborators based on the presented QCD array.

### 5.2.1 Motivation

Quantum cascade detectors offer a variety of advantageous properties over existing imaging detectors which make it worth to investigate towards QCD based FPAs. QCDs are capable of multi-wavelength or broadband detection [122] depending on their design. Multi-spectral detection can be currently achieved by two different methods. First, two different types of cascade periods can be stacked which are sensitive to different wavelength regions. Second, a diagonal transition design can be employed which is sensitive to two different wavelengths. A diagonal transition design sensitive to 8  $\mu\text{m}$  and 4.5  $\mu\text{m}$  with 30 identical periods as depicted in figure 5.2 has been shown in our group [137].

As mentioned in chapter 3 the operation wavelength of the device can be designed precisely by adjusting the layer thicknesses of the active zone (AZ) independent from the material composition as it is the case for bandgap detectors. They exhibit a photo response with a spectral width, typically in the range of  $200\text{ cm}^{-1}$  up to  $500\text{ cm}^{-1}$  depending on the design. Therefore, QCDs are perfectly suited to detect in a well defined narrow bandwidth which is beneficial for remote sensing applications.

QCDs can be operated at room temperature while they have many advantages in common with QWIPs, such as the availability of mature material systems such as InGaAs/InAlAs and fast response times. The mature MBE and MOCVD growth technology combined with the good substrate availability is another key advantage of the technology. These properties are a promising base for novel sensing arrays and imaging devices.

### 5.2.2 Detector design

The sample used for integration was C0342 presented in section 3.3.2 which is the final sample of a series of wavelength matching growths to precisely hit the target

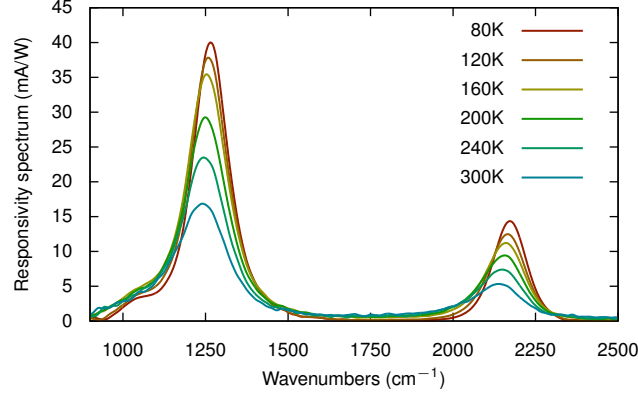


**Figure 5.2:** Responsivity spectrum for a diagonal transition QCD sensitive to two different wavelengths with 30 identical periods. Image taken from [137].

wavelength of  $4.3\ \mu\text{m}$  at 240 K device temperature and above. Thereby the peak responsivity  $R_P$  matches with the strong  $\text{CO}_2$  absorption lines. Previous samples have already confirmed the validity of the design decisions by similar detector performance but have their peak responsivity at wavelengths around  $4.5\ \mu\text{m}$ .

### 5.2.3 Single pixel test structures

The design of the detector array is the succeeding step after the detector design, growth, processing and characterization of a single element. The array is designed to be illuminated from the substrate side and couple the incident light with a two dimensional diffraction grating to the active zone of the QCD. In array structures which are capable to be extended to high pixel counts a contact scheme has to be found, which allows all pixels to be contacted without obstructing the beam path. This also means that the electric characteristics such as contact resistance and capacitance for all pixels should be as equal as possible. A common way to realize such pixel array contacts is to reserve one side of the array for electric connections and amplifier structures and the other side for optic coupling. For noise performance it is favorable to keep the distance between the detector element, hence the pixel and the amplifier as short as possible. This prevents line capacitances and inductances from introducing noise, signal distortions and lowered rise times.

Prior to the array design, test structures were made to characterize detectors in pixel configuration in the laboratory environment. Single pixel structures with  $50\ \mu\text{m} \times 50\ \mu\text{m}$  and  $67\ \mu\text{m} \times 67\ \mu\text{m}$  have been processed. These test structures were designed with extended top contacts for manual wire bonding (figure 5.3 a and b). Illumination of the test structures is through the substrate side as for the final array.

The two dimensional diffraction grating on top of the pixels was fabricated by laser

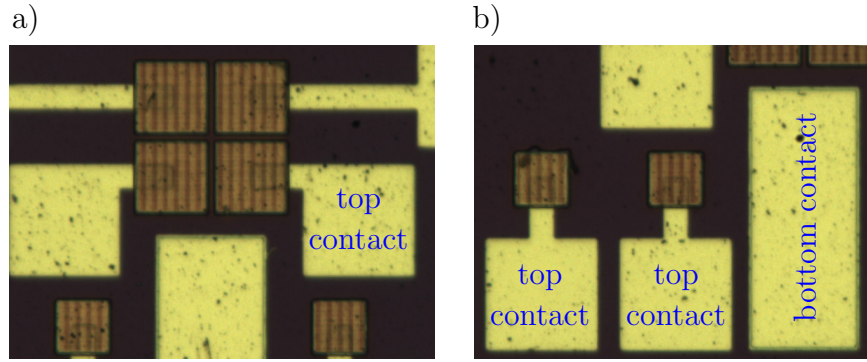


**Figure 5.3:** Microscope images of single pixel test structures for grating fabrication and light coupling tests. Both have a common bottom contact for 4 large and 4 small pixels. The large test pixels are a)  $67\ \mu\text{m} \times 67\ \mu\text{m}$  and the small pixels b) are  $50\ \mu\text{m} \times 50\ \mu\text{m}$ . The extended contact surfaces for manual wire bonding are on top of a SiN insulation layer. The two dimensional diffraction grating is a full metal Au grating which also serves as the pixel top contact. The structure depicted is substrate illuminated and processed from sample K086C.

lithography with a Heidelberg DWL 66fs laser lithography system. The grating is full Au covered and acts as top contact for the electric pixel connections. The test structures are isolated by a SiN layer. The extended contact surfaces of the test structures are  $100\ \mu\text{m}$  in square.

**Grating lithography** The diffraction grating lithography has major influence to the light coupling efficiency. For the wavelength range around  $4.3\ \mu\text{m}$  grating periods around  $1.4\ \mu\text{m}$  are needed, considering the refractive index of the pixel structure. To test different grating periods direct lithography without a mask is favorable. The necessary feature size is within the specifications of the Heidelberg DWL 66fs. Therefore, the test structures were exposed with the 2 mm write head, which gives the best resolution but also a short depth of field of about  $1\ \mu\text{m}$ . As an etch mask SiN was used which resulted in sufficient resolution (figure 5.4 a).

Nevertheless, the test structures revealed a lack of reproducibility of the lithography results. A major concern is the uniformity of the grating duty cycle, which could not be ensured in the long run. Typically strong duty cycle variations and lithography resolution variations were observed for grating structures with hole dimensions below  $1\ \mu\text{m}$  in diameter. As a consequence the decision had been made to switch to electron beam lithography (figure 5.4 b) which gives reliable high resolution but results in a longer processing time. This could be confirmed with photocurrent measurements on the test pixel structure in comparison to  $45^\circ$  mesa detectors from the same material. The grating lithography resolutions have large impact onto the light coupling efficiency according to the area normalized photocurrent measurements of



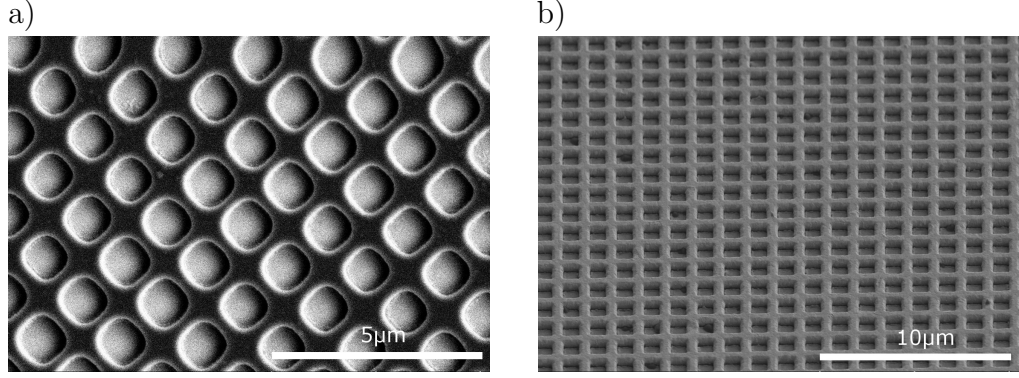


**Figure 5.4:** Two dimensional grating lithography for  $4.3\ \mu\text{m}$  operation wavelength with a grating period around  $1.4\ \mu\text{m}$  exposed a) by a DWL 66fs laser exposure and b) electron beam lithography.

the small ( $50\ \mu\text{m} \times 50\ \mu\text{m}$ ) and large ( $67\ \mu\text{m} \times 67\ \mu\text{m}$ ) area test pixels with the mesa device (figure 5.5 b). The difference between the small and the large pixels can be attributed to an increasing fraction of the optical area being occupied by the mesa edges which are not grating covered and processing imperfections.

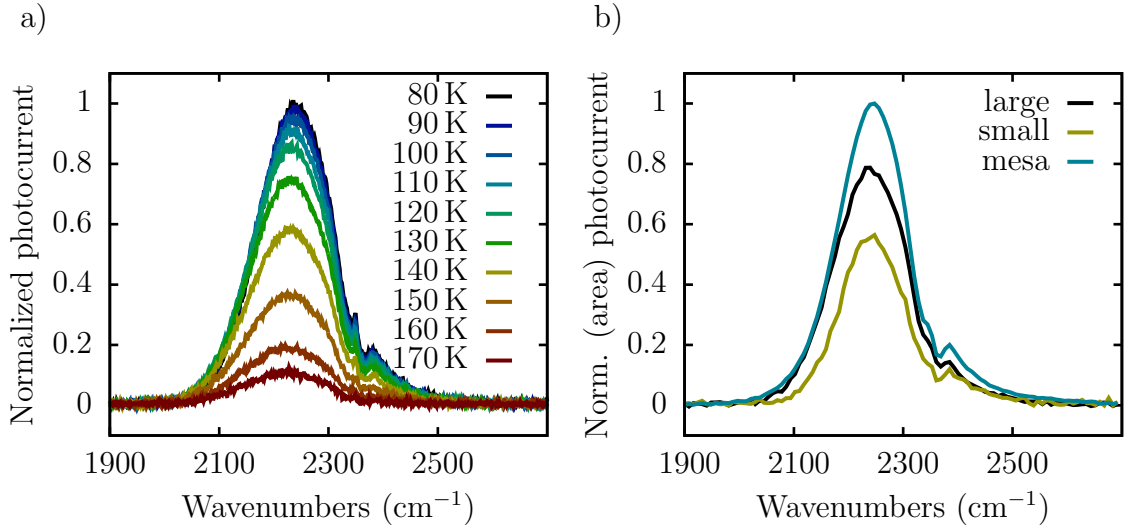


**Figure 5.5:** Photocurrent measurements a) for early design  $67\ \mu\text{m} \times 67\ \mu\text{m}$  test pixels from material K086. Detector area normalized photocurrent measurements b) of the test pixel structure show a relatively low light coupling performance of the laser lithography processed diffraction gratings. Large test pixels are  $67\ \mu\text{m} \times 67\ \mu\text{m}$ , small test pixels  $50\ \mu\text{m} \times 50\ \mu\text{m}$  and mesas  $100\ \mu\text{m} \times 100\ \mu\text{m}$ .

It has to be noted, that the feature sizes in general do not require electron beam lithography in industrial batch processing. With constant grating periods which do not have to be adjusted for a prototype devices of different materials optical mask lithography can be used.

**Anti reflection coating** On the polished InP substrate bottom side an SiN anti-reflection coating (ARC) is used. For 4.3  $\mu\text{m}$  wavelength a layer thickness of 580 nm SiN was deposited via PECVD. According to photocurrent measurements with and without the coating 20% up to 30% photocurrent increase could be realized with the ARC.

### 5.2.4 Light coupling simulations

Due to the ROIC design which requires bottom contacts for each pixel a bottom contact layer had to be introduced. This is in contrast to QWIP cameras, which use a common bottom contact or substrate contact as bottom contact. To verify the light coupling and optimize the grating parameters for the pixels using the final QCD design a simulation model was implemented. The parameters to be optimized are according to section 4.3 and figure 4.2.

The optical simulations were conducted using COMSOL Multiphysics. A two dimensional model with the layer structure of the material according to the growth sheets was used. The semiconductor heterostructure was modeled with all complex refractive indices for each layer of the structure including the substrate and the contact layers. The AZ was modeled as a material with an anisotropic permittivity to account for the ISB selection rule. This method allows also directly to account only for the absorption parts, which contribute to the photocurrent in the real geometry. The absorption of the AZ in growth direction was provided by a fit to the simulated absorption  $\alpha_{\text{isb}}$  obtained from the VSP framework [146] heterostructure simulations. The refractive index of the AZ was averaged according to the InGaAs/InAlAs ratio of the period stack in the same manner as for the simulations of the SPP QCDs. The complex permittivity tensor for the AZ obtained has the form

$$\tilde{\epsilon}_{\text{AZ}} = \begin{pmatrix} \epsilon_{xx} & \epsilon_{xy} & \epsilon_{xz} \\ \epsilon_{yx} & \epsilon_{yy} & \epsilon_{yz} \\ \epsilon_{zx} & \epsilon_{zy} & \epsilon_{zz} \end{pmatrix} = \begin{pmatrix} \epsilon_{xx} & 0 & 0 \\ 0 & \epsilon_{yy} & 0 \\ 0 & 0 & \epsilon_{zz} \end{pmatrix} \quad (5.6)$$

where  $\epsilon_{yy} = \epsilon'_{yy} + i\epsilon''_{yy}$  is the complex permittivity in growth direction. The wavelength dependent absorption  $\alpha_{\text{isb}}(\lambda)$  (figure 5.6 a) obtained from the VSP simulations is connected to  $\epsilon_{yy}$  by

$$\epsilon_{yy} = (\sqrt{\epsilon} + i\kappa_{\text{isb}})^2 \quad (5.7)$$

with  $\epsilon = \epsilon_{xx} = \epsilon_{zz}$  according to the InGaAs/InAlAs ratio. The imaginary part of



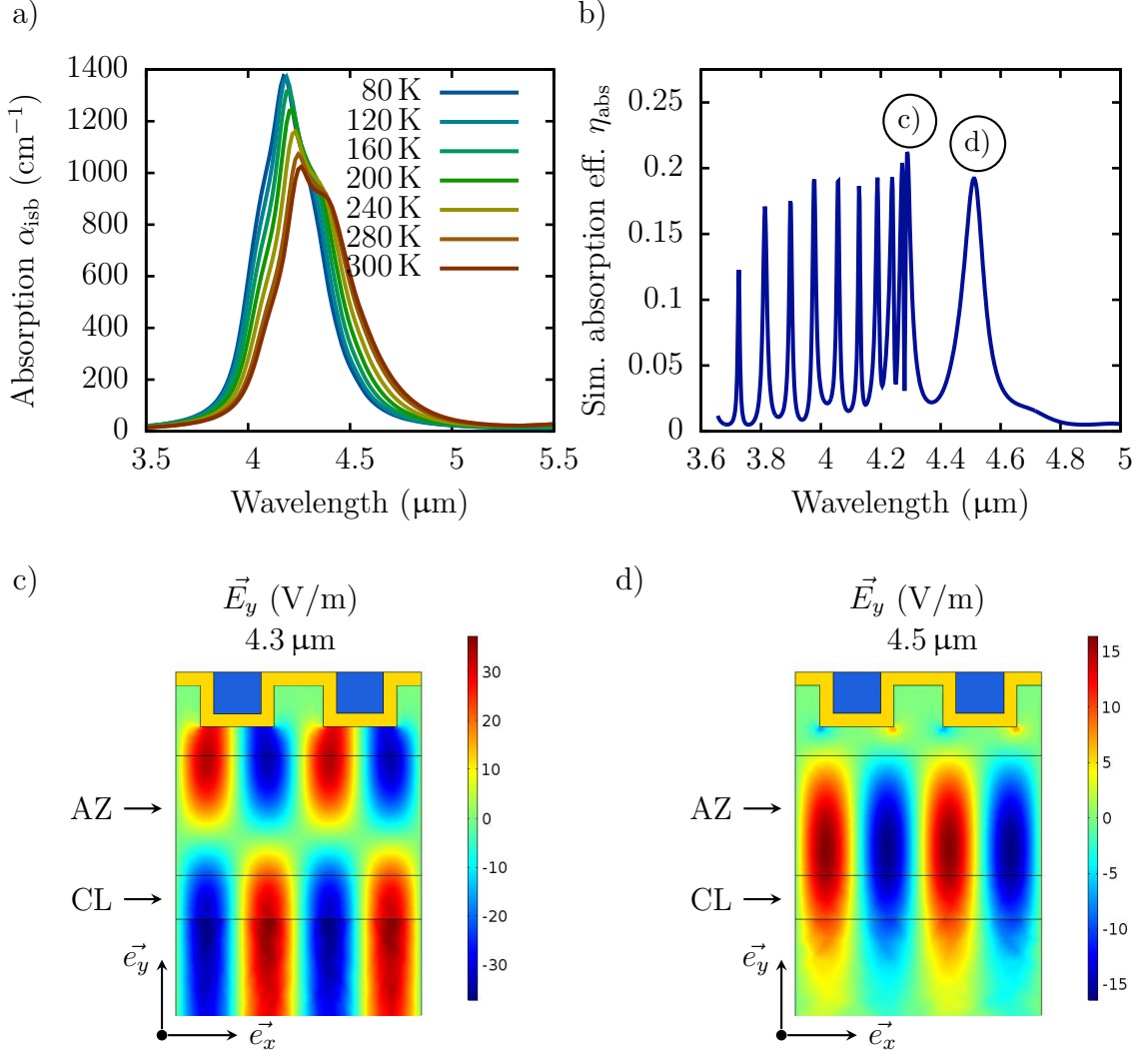


**Figure 5.6:** Simulated absorption coefficient  $\alpha_{\text{isb}}$  a) obtained from VSP simulations and used as input parameter for the light coupling simulations (300 K) for the b) absorption efficiency. Subfigure c) shows the electric field distribution in growth direction  $\vec{E}_y$  for the  $\lambda = 4.3 \mu\text{m}$  peak and the main peak d) to the longer wavelength side.

the complex refractive index  $\underline{n} = n - i\kappa$  is given by

$$\kappa_{\text{isb}} = \frac{\alpha_{\text{isb}} c}{4\pi f} = \frac{\alpha_{\text{isb}} \lambda}{4\pi} \quad (5.8)$$

where  $c$  is the speed of light,  $f$  the frequency and  $\lambda$  the wavelength. Refractive index and absorption data for Au was used as reported in the paper of Ordal et al. [167] compiling data from e.g. Bennet et al. [199].

The simulated absorption efficiency for the final array design shows several peaks near to the main peak around 4.5  $\mu\text{m}$  wavelength with an absorption efficiency slightly above 20% (figure 5.6 b). Initially the pixel design should be compati-

ble to laser lithography processing of the two dimensional grating structure. The laser exposure device (Heidelberg Instruments DWL 66fs) is limited in resolution at about  $0.8 - 1 \mu\text{m}$  feature size considering the processed test pixel structures. To maintain compatibility to laser exposure even if the final devices were processed using electron beam lithography a grating period of  $1.4 \mu\text{m}$  was used. By this decision the electric field distribution in the active zone according to figure 5.6 c was obtained in the wavelength region of the photocurrent peak. Thereby the design can be easily extended to a larger area and larger pixel counts, which require layer exposure or optical mask lithography.

### 5.2.5 Pixel array

The array prototype is subjected to geometric constraints given by the ROIC. The prototype ROIC requires a pixel pitch of  $225 \mu\text{m}$  in  $x$  and  $y$  direction and supports  $8 \times 8$  pixels. Clearly, this is a lower pixel count than state of the art devices with a larger pixel pitch but sufficient for a proof of concept prototype. All dimensions including the ROIC can be reduced to smaller pixel pitch and pixel size, hence high pixel counts. The nominal grating dimensions used are a period  $p$  of  $1.4 \mu\text{m}$  a duty cycle of 0.4 and a grating depth  $d$  of  $450 \text{ nm}$ . The grating structure is covered with a  $600 \text{ nm} - 700 \text{ nm}$  thick Au film. The thickness is needed for the flip-chip bonding steps to ensure sufficient layer stability and adhesion for the Gold-Stud-Bumping step.

The ROIC designed by P.Kejik at École polytechnique fédérale de Lausanne (EPFL) is optimized for amplification of sources with low output resistance. This is required since QCDs typically show relatively low resistance area products at elevated temperatures. The per pixel amplification circuits need separate bottom and top contacts for each pixel with all pixels being operated electrically isolated from each other. This poses some design restrictions on the QCD array.

Since the ROIC requires a relatively large pixel pitch two array configurations are possible. First a sparse pixel with a pixel which covers only a fraction of the available  $225 \mu\text{m} \times 225 \mu\text{m}$  cell (figure 5.7 a). Second a full pixel design covering the entire available area, hence everything except the contact surfaces needed for the bottom contact (figure 5.7 b).

If we recall the definition of the detectivity  $D^*$  from equation (3.7)

$$D_J^* = R_P \sqrt{\frac{AR_0}{4k_B T}} \quad (5.9)$$

and use the approximation of a constant peak responsivity  $R_P$  and a constant specific

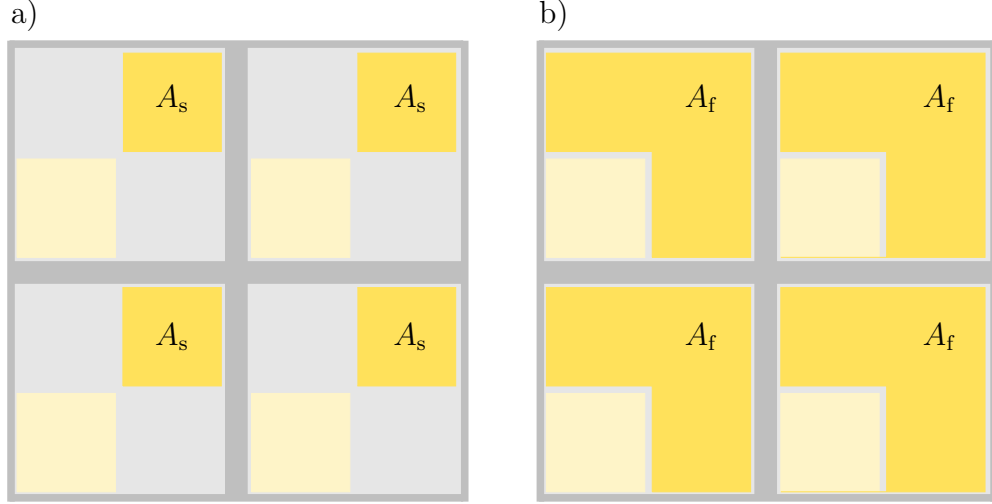


**Figure 5.7:** Possible pixel configurations due to the relatively large pixel pitch of  $225\text{ }\mu\text{m}$  of the prototype ROIC. Sparse pixel design a) with a small fraction of the available size covered by the pixel. Full pixel design b) with the maximum area possible covered with active material. The gray bars mark the insulation trenches that are etched through the highly doped contact layer. The bright squares are the bottom contacts and the darker filled areas the pixels shapes.

differential device resistance  $\rho_0$  for both. Then, the sparse pixels detectivity  $D_s^*$  and the full pixel detectivity  $D_f^*$  (figure 5.7 b) can be estimated directly. To simplify the situation and omit the dimensions of the insulation trenches we can make the assumption

$$A_f = 3A_s \quad (5.10)$$

with  $A_f$  the full pixel area and  $A_s$  the sparse pixel area. With the device resistance

$$R_0 = \frac{\rho h}{A}, \quad (5.11)$$

where  $h$  is the pixel height,  $A$  the pixel area and  $\rho_0$  the specific differential resistance, we can express the detectivities and see directly that they are the same as expected.

$$\begin{aligned} D_s^* &= R_P \sqrt{\frac{A_s R_{0,s}}{4k_B T}} = R_P \sqrt{\frac{A_s \rho_0 h}{4k_B T A_s}} \\ D_f^* &= R_P \sqrt{\frac{A_f R_{0,f}}{4k_B T}} = R_P \sqrt{\frac{3A_s \rho_0 h}{4k_B T 3A_s}} \end{aligned} \quad (5.12)$$

Therefore, the specific detectivity  $D_j^*$  for both design options is the same. At the other hand if we make a step back from the detectivity  $D^*$  to the signal to noise ratio (SNR). Hence, without normalizing to the detector area  $A$ , with Johnson-Nyquist noise contribution only using equation (3.15) the signal to noise ratios can

be expressed as

$$\begin{aligned} \text{SNR}_s &= \frac{I_{\text{Ph},s}}{i_{n,s}} \approx \frac{R_p P_{i,s}}{\sqrt{\frac{4k_B T \Delta f}{R_{0,s}}}} \\ \text{SNR}_f &= \frac{I_{\text{Ph},f}}{i_{n,f}} \approx \frac{R_p P_{i,f}}{\sqrt{\frac{4k_B T \Delta f}{R_{0,f}}}} = \frac{R_p 3P_{i,s}}{\sqrt{\frac{4k_B T \Delta f}{R_{0,s/3}}}} \end{aligned} \quad (5.13)$$

with the photo currents  $I_{\text{Ph},f} = 3I_{\text{Ph},s}$  and the pixel resistances  $R_{0,f} = R_{0,s}/3$ . This leads then to

$$\text{SNR}_f = \sqrt{3} \text{SNR}_s \quad (5.14)$$

This means that with larger pixel sizes clearly no detectivity but to some extent a better SNR can be gained. Additionally the ratio between the active grating area and unused edge regions of the mesa surface may improve dependent on the pixel shape. A high filling factor as provided by the full pixel design is also favorable due to the better material usage and pixel density, once the pixel count is increased.

Nevertheless, the absolute pixel resistance is a boundary condition in the array design which has to be met. The full pixel design has a too low pixel resistance to be compatible with the custom made ROIC. The design resistance required in normal operation conditions is  $10^5 \Omega$ , which is satisfied for the sparse pixel design at temperatures below  $T \approx 220 \text{ K}$ . In future designs the pixel size could be slightly reduced to better match the resistance design point of the ROIC.

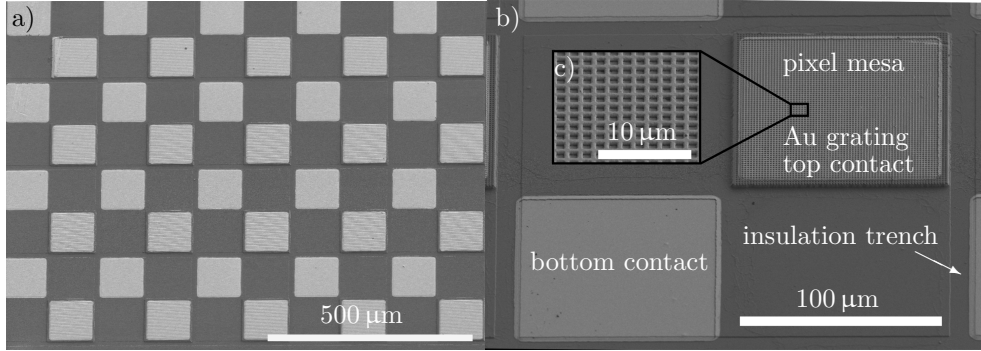


**Figure 5.8:** Section of the QCD pixel array a) with 64 pixels separately contacted and isolated by an insulation trench. The sparse pixel size is  $109 \mu\text{m}$  in square. Each pixel surrounded by the insulation trench b) comprises a bottom and a top contact. The two dimensional diffraction grating serves also as the top contact. Figure as published in [144].

The sparse pixel design with 64 pixels is processed from material C0342 with all pixels isolated from each other (figure 5.8 a). The insulation trenches are etched through the bottom contact layer (figure 5.8 b). The bottom contact is sputter

deposited directly on the highly doped bottom contact layer. The sparse pixel dimensions are  $109\text{ }\mu\text{m} \times 109\text{ }\mu\text{m}$  in size.

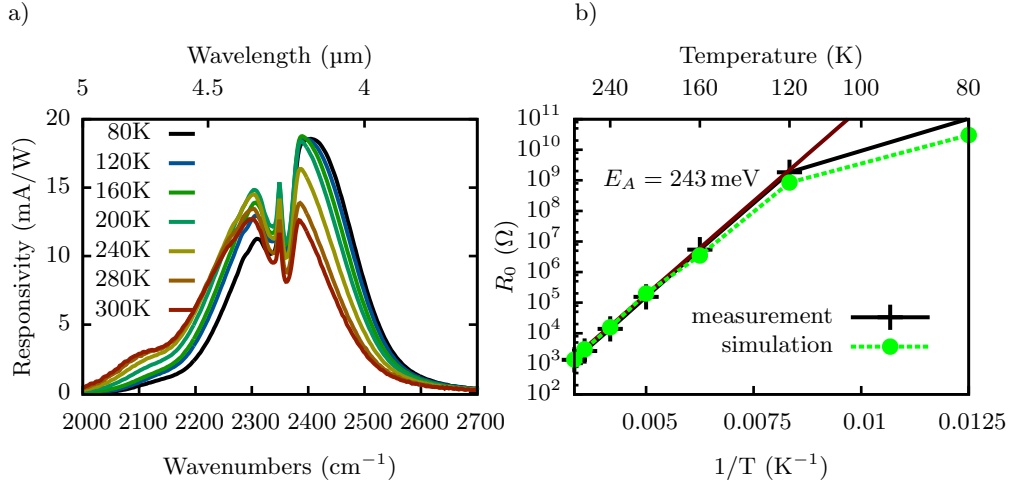


**Figure 5.9:** Responsivity a) of a typical single pixel of the  $8 \times 8$  QCD array. The pronounced valleys are due to the strong  $\text{CO}_2$  absorption around  $4.3\text{ }\mu\text{m}$  wavelength, as shown in figure 3.8. The low performance drop at increasing temperatures can be accounted to the high coupling efficiency of the grating coupling scheme. The measured resistance b) of the pixel matches well to the simulations. As published in [144].

Single pixels of the array were characterized by FTIR measurements and IV characterizations. The photocurrent response shows two pronounced valleys due to the  $\text{CO}_2$  absorption (figure 5.9 a). At room temperature a responsivity of  $16\text{ mA/W}$  could be achieved. The performance drops with increasing operation temperature is lower than for the same material in  $45^\circ$  polished facet configuration (figure 3.10 a). This can be accounted to the higher coupling efficiency of the grating coupling configuration. It had been observed, that a high coupling efficiency reduces the performance drop compensating the lower absorption  $\alpha$  at elevated temperatures. The temperature dependence of the responsivity and detectivity is shown in figure 5.10 a which shows only a minimal responsivity drop from 80 K up to the intended operation temperature of 240 K where a responsivity of  $18\text{ mA/W}$  and a detectivity of  $2 \cdot 10^8\text{ cm}\sqrt{\text{Hz}}/\text{W}$  is obtained.

The influence of the geometry onto the performance drop has also been observed comparing the  $45^\circ$  mesa devices to the plasmonic lens QCDs in chapter 4.4.6. Remarkable responsivity values have also been reported for QCDs in ridge configuration, hence with long absorption length and therefore high coupling efficiency also for decreasing  $\alpha$  at room temperature [99, 149].

It has to be noted that the polarization selectivity is accounted in equation (3.26) in the factor  $M$ . The two dimensional diffraction grating in pixel configuration

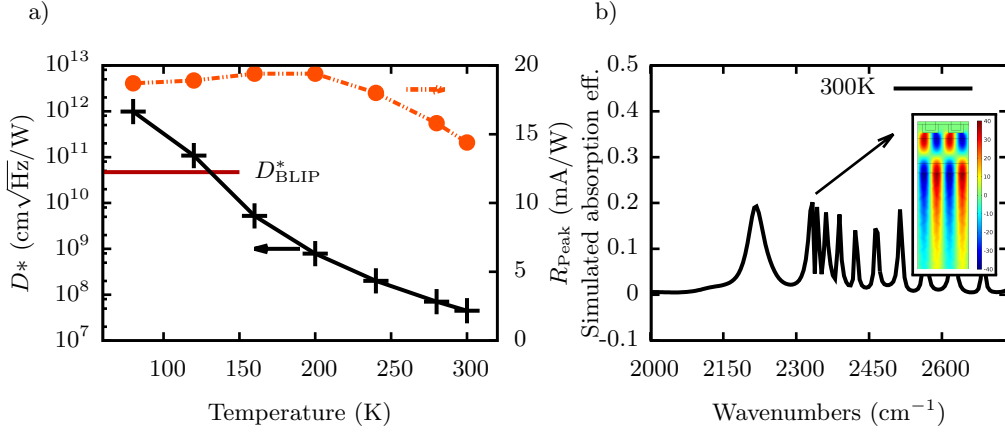


**Figure 5.10:** Responsivity and specific detectivity over the operation temperature of an array pixel. The background limited detectivity  $D_{BLIP}^*$  is for a FOV of  $\pi$ . The numerical simulated absorption efficiency of a pixel with the electric field intensity for the operation wavelength in the inset. As published in [144].

is sensitive to both polarization directions (x-direction and y-direction), hence the polarization factor is 1. In 45° mesa configuration, due to the polarization selection rules the device is sensitive to TM-polarized light only. This results in a polarization factor of 0.5 accounted in  $M$ . This means that for the same illumination conditions in pixel configuration twice the power is accounted to be incident on the detector for responsivity calculations.

The mentioned low responsivity drop for elevated temperatures has also a positive impact on the detectivity. The optimization for a high resistance while maintaining a high responsivity leads to a pixel resistance of  $\approx 1.3\text{ k}\Omega$  at room temperature. The resistance model described in 3.2.5 fits very well to the measurement data extracted from IV measurements (figure 5.9 b). This is an essential requirement to identify parasitic current paths and to accurately simulate the QCD detectivity  $D^*$  by numeric heterostructure simulations.

The simulated absorption efficiency for normal incident MIR light for various wavelengths was obtained by the simulation methods described in section 5.2.4 (figure 5.10 b).

In conclusion, the responsivity and detectivity results in pixel array configuration show that array integration is possible for QCD devices while the responsivity and detectivity performance is maintained or enhanced due to the light coupling scheme which also results in a low performance drop for elevated, TEC reachable operation temperatures or room temperature. The grating optimization allowed lead to pixel performance slightly above mesa values which is a significant improvement in comparison to the first pixel test structures. The custom ROIC is designed for input



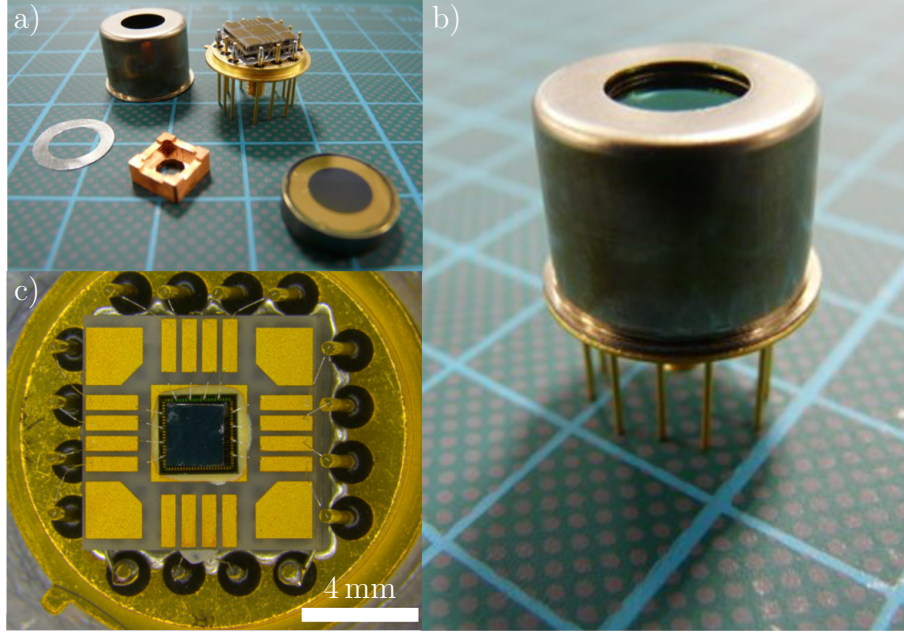


**Figure 5.11:** Components a) of the TO-8 package, with a copper cold shield and two stage TEC for the QCD array. The polished substrate side of the array c) faces in forward direction towards the ARC coated germanium window. The ROIC is connected to the adapter PCB by wire-bonding. The finished and packaged device b) after nitrogen purging and sealing. Image courtesy IZM Fraunhofer Berlin as published in [144].

currents from the detector of 5 pA up to 50 pA without saturation effects. Considering the spectral width of the detector in pixel configuration a response from  $\lambda_1 = 3.9 \mu\text{m}$  to  $\lambda_1 = 4.7 \mu\text{m}$  can be expected at a maximum. According to equations (5.3) and (5.4) an absolute maximum photocurrent of  $I = 45 \text{ pA}$  can be estimated for a  $f_{\#} = 1.8$  lens. Therefore, the final array is well in the specifications for the integrated system.

Further integration would result in higher pixel numbers and smaller pixel sizes. From a technological point of view this can be done without major challenges to be faced, as long as the pixel size is large in comparison to the detection wavelength. With lower pixel sizes the absolute pixel resistance could be further increased which offers more design freedom for the ROIC and the amplification scheme.

### 5.2.6 Integration and packaging

The majority of integration steps were conducted by collaborators. This section gives a brief overview of the considerations made.

The finished array is flip-chip bonded to the ROIC by Au stud-bumping. A light coupling scheme as discussed in section 4.3 was followed. Array packaging and flip-

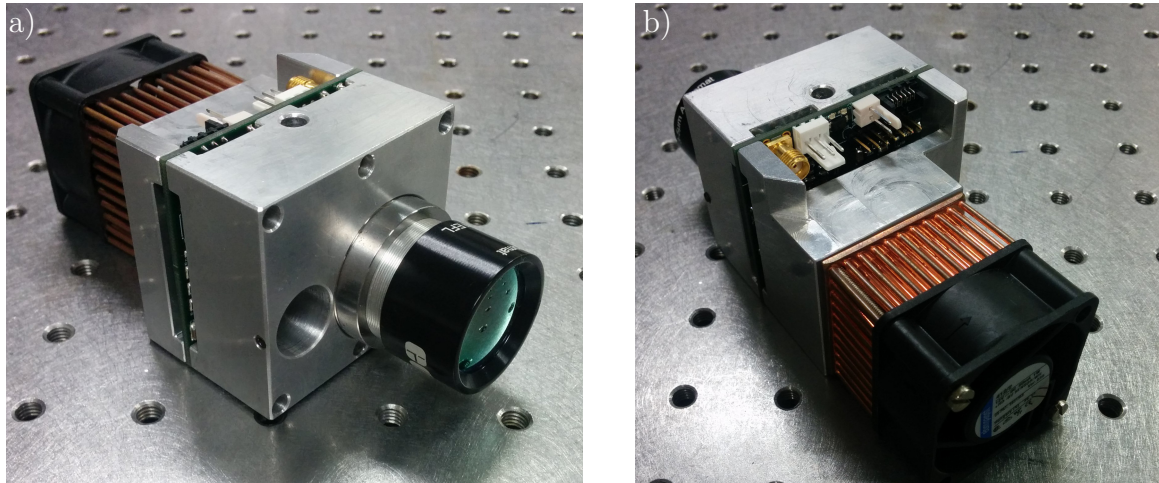


**Figure 5.12:** Integrated QCD array with mechanical support milled from aluminum with the mounted objective lens. The copper cooling block is connected to the TO-8 housing via a heat conducting copper rod. The system design was done at Université de Neuchâtel.

chip bonding was conducted by IZM Fraunhofer in Berlin. This process requires a relatively high Au layer thickness on the bottom and top contact pads of the pixels. Due to this requirement the full metal grating top contacts and the separate bottom contacts for all pixels were processed with a minimum layer thickness of 500 nm. In addition to the metal layer thickness precise cleaving of the arrays is necessary for further wire bonding to the adapter PCB and the TO-8 housing. Since the substrate side faces towards the scene, the array is on top of the ROIC when mounted. If the array edges are too broad (i.e. over 250  $\mu\text{m}$ ), the QCD array covers the bonding pads of the ROIC in a way that wire bonding to the PCB is not possible anymore. A picture of the wire bonds for a precisely cleaved array is shown in figure 5.11 c.

The packaging of the array consists of a two stage thermoelectric cooler (TEC) stack with an adapter PCB on top. The polished substrate side of the array faces in forward looking direction towards the ARC coated germanium window of the package (figure 5.11 b). The ROIC is contacted by wire bonding to the adapter PCB which then connects to the TO-8 package. A copper cold shield is mounted and thermally connected to the TEC cooling stack to shield for background radiation which is outside of the field of view (FOV) (figure 5.11 a). The germanium windows were glued to the gold cap of the package for testing purposes. The final version of the package has windows with Ti/Au sputter deposited solder surfaces for soldering the windows to the gold cap. The TO-8 package is purged with nitrogen prior to sealing. The TO-8 package is then soldered to a connector board to be mounted to the QCD module of the integrated system (figure 5.12).



The integrated system consists of a cooling system with an electric cooling fan, a copper heat sink connected to a copper heat conducting finger. The heat conducting finger is connected to the TO-8 housing of the array. A controller board controls the cooling system with the external fan and the two stage **TEC** in the TO-8 housing. It further interfaces to the serial peripheral interface (**SPI**) interface of the **ROIC** to read out pixel data and set the control parameters for the read out process. These are i.g. the working clock of the **ROIC** the read out mode, the target array temperature and the number of samples per pixel to average. The mechanical support structure for the array is fabricated from bulk aluminum. It connects all moving parts of the **QCD** system and provides an adjustable objective mount for the  $f = 40\text{ mm}$ ,  $f_{\#} = 1.8$  achromatic **ARC** coated lens. Optionally an alignment laser can be mounted next to the objective lens to provide a red dot alignment reference for other optical imaging systems. Mechanical and optic beam engineering was done at Université de Neuchâtel.



## BI-FUNCTIONAL QUANTUM CASCADE SENSING

Optic systems used for spectroscopy applications or communication systems require a light source and a detector. Such an optic system for light emission and detection can either use discrete components being packaged separately and then combined to a device or an integrated approach with most components combined on a single chip can be pursued. Fully integrated systems with light source, interaction region, analyte handling and light detection on a single chip are often referred to as lab-on-a-chip. This chapter discusses two prototype integrated bi-functional gas sensors featuring external interaction regions. A first proof of concept device is introduced and characterized including gas measurements. Based on these results a revised design is demonstrated.

### 6.1 Direct absorption gas sensing

Direct absorption spectroscopy of gases requires a sufficiently long interaction region to measure signal changes due to the small light absorption in the gas. With short interaction regions the light attenuation at the measurement wavelength is too low to accurately measure a signal difference. Compared with liquid sensing, gaseous analytes exhibit rather low absorption which requires long interaction lengths typically in the order of meters up to tens or hundreds of meters. One option is to use multipass gas-cells to extend the interaction length [200, 201]. Two approaches are possible to enhance the limit of detection. The concentration of the absorbing analyte can be increased or the interaction length can be extended.

**Robustness** is a key aspect in terms of the applicability of a sensor. The utilization of pulsed operated DFB single mode QCLs for light emission is a robust choice. The

thermal load is relatively low in comparison to *CW* operation and thereby, low energy consuming *TEC* stabilization in compact housings is feasible. The *DFB* grating defines the emission wavelength in a small temperature tunable range. Consequently, temperature stabilization is essential for precise wavelength stability. An advantage of these sources over external cavity *QCLs* is their stability against mechanical vibrations. To give an example, for mobile external cavity laser based sensor systems a significant part of the engineering work has to be devoted to vibration damping. Furthermore, the *DFB* grating prevents mode hopping which eliminates this possible noise source [202]. Sensing systems which require multiple emission wavelengths can be assembled from arrays of *DFB QCLs*. The signal processing effort for direct absorption spectroscopy is low, compared with other techniques like dual comb spectroscopy [97]. For industry applications fast maintainable and replaceable plug and play devices are demanded. Direct absorption spectroscopy with temperature stabilized *DFB QCLs* offers a promising starting point to face this challenge.

Bi-functional sensing has been shown for liquids with a fully integrated on chip sensor [99]. There the interaction region is defined by a dielectric loaded surface plasmon polariton (*SPP*) waveguide between a *QCL* light source and a detector element fabricated from the same material (figure 6.1 a). The length of the interaction region is in the range of 50  $\mu\text{m}$  up to 200  $\mu\text{m}$ . With advanced waveguide designs and optimized dielectric loading propagation lengths up to the mm range seem to be possible. Nevertheless, this is too short for most gaseous analytes.

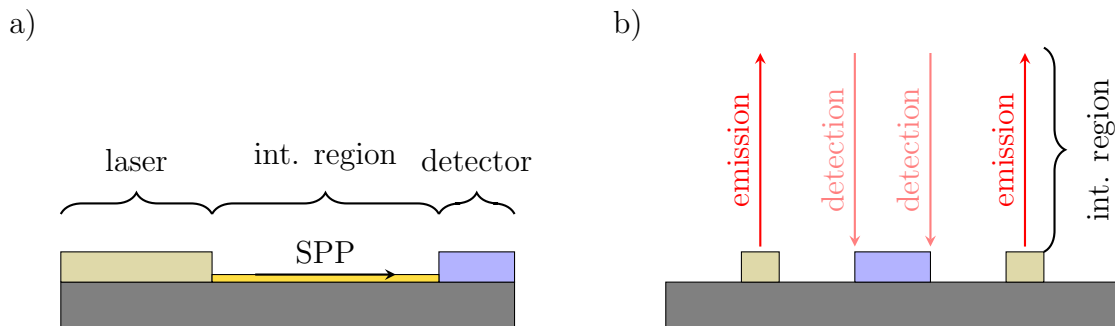


**Figure 6.1:** Light coupling and interaction region configurations for a) lab-on-a-chip devices with source, detector, waveguide and interaction region on the integrated device [48] with interaction region lengths up to the mm range and b) surface operation devices as presented in this chapter. Surface operation mode devices for low absorption analytes have an interaction region external to the chip to allow for interaction lengths in the range of several cm up to meters.

A possible solution is to decouple the interaction region from the sensor surface but keep the source and the detector monolithically integrated. Light emission and detection is integrated onto the sensor including all coupling geometries. Light is

emitted from the sensor, passes an external interaction region and is then coupled back to the sensor (figure 6.1 b). Surface normal operation offers additionally a direct way of multi-wavelength integration in form of an array which consists of similar devices operating at different wavelengths within the usable gain spectrum of a bi-functional material.

## 6.2 Quantum cascade laser basics

A major challenge for MIR sensing has been and still is the availability of stable laser sources. The possibility to design the emission wavelength of a QCL device purely by the layer thicknesses of a heterostructure provides the flexibility needed for molecular fingerprinting and sensor devices.

A typical QCL design consists of the active periods which form the AZ, a waveguide design and a resonator. The most common material system for QCLs is InGaAs/InAlAs which form the wells and the barriers respectively. The emission wavelength and the carrier transport is determined by the design of the heterostructure layers. Electrons are injected to an upper laser level by an injector region designed as a superlattice. The injector has to efficiently provide charge carriers (electrons) and prevent leakage currents either to the continuum or parasitic paths. In order to efficiently supply the charge carriers, the injector is usually n-doped and acts as an electron reservoir. The optical transition takes place between the upper laser level 3 and the lower laser level 2 (figure 6.2). The energy levels 2 and 1 exhibit an energy spacing which strongly favors LO-phonon scattering to efficiently depopulate the lower laser level. From level 1 the electrons enter the injector of the subsequent period of the AZ. This means that an electron passing the AZ generates multiple photons depending on the number of periods and unwanted but possible leakage paths. To ensure population inversion, the lifetime of the optical transition  $\tau_{3,2}$  has to be longer than the lifetime  $\tau_{2,1}$ . After exceeding the mirror and waveguide losses net gain is provided.

For an increasing number of periods  $N_{\text{Per}}$  the AZ gets thicker, which increases the optical confinement factor  $\Gamma$ . The threshold current is reduced and the total laser voltage to maintain the electric field is increased.

A common fundamental description of this three level system is based on rate equations. The lifetime requirement for population inversion is

$$\tau_{3,2} > \tau_{2,1}. \quad (6.1)$$

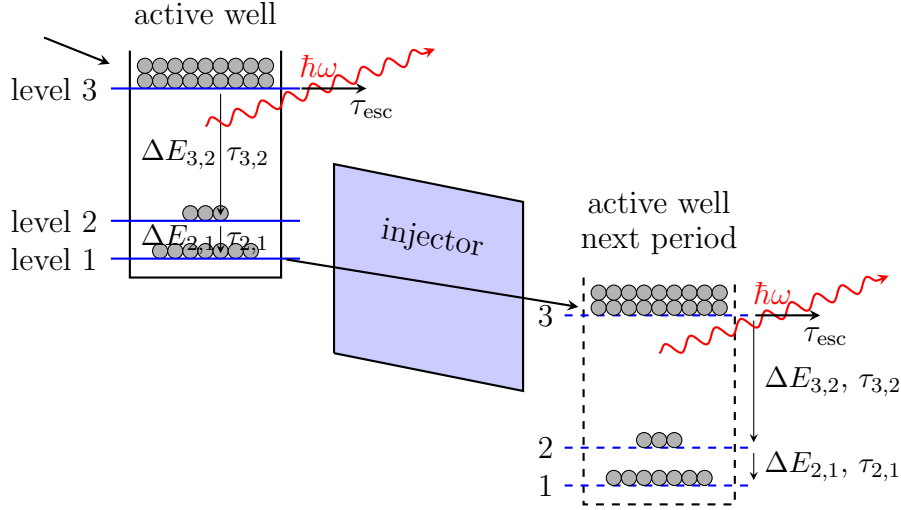


**Figure 6.2:** Operating principle of a QCL with one schematic period of the AZ. Electrons are injected to the upper laser level by the injector region. The optical transition takes place between level 3 and level 2 with an emission wavelength corresponding to the energy  $\Delta E_{3,2}$ . The extractor ensures a fast depopulation of the lower laser level by LO-phonon scattering from level 2 to level 1. The extracted electrons enter the injector of the next period.

For the upper laser level the lifetime can be expressed as

$$\tau_3^{-1} = \tau_{3,2}^{-1} + \tau_{2,1}^{-1} + \tau_{\text{esc}}^{-1}, \quad (6.2)$$

where  $\tau_{\text{esc}}$  attributes the carrier loss to the continuum (figure 6.2). The slope efficiency, which is a figure of merit for QCLs is then defined as

$$\frac{dP}{dI} = \frac{h\nu}{q} \frac{\tau_{\text{eff}}}{\tau_{\text{eff}} + \tau_2} \frac{\alpha_m}{\alpha_{\text{tot}}}, \quad (6.3)$$

where  $P$  is the output power,  $I$  the injected current,  $h$  Planck's constant,  $q$  the elementary charge,  $\alpha_m$  the mirror losses,  $\alpha_{\text{tot}} = \alpha_m + \alpha_w$  the total losses consisting of the mirror and waveguide losses and  $\tau_{\text{eff}}$  is defined by

$$\tau_{\text{eff}} = \tau_3 \frac{1 - \tau_2}{\tau_{3,2}}. \quad (6.4)$$

In most designs  $\tau_2$  is determined by the LO-phonon scattering time.

The threshold current density of a device is reached, when the total losses  $\alpha_{\text{tot}}$  equal the gain. Hence

$$J_{\text{th}} = \frac{\alpha_w + \alpha_m}{g\Gamma} \quad (6.5)$$

with the confinement factor  $\Gamma$  and the gain  $g$ .

A variety of AZ designs have been shown, including vertical transitions [66] and diagonal optical transition, three well active region, two phonon resonance and bound to continuum design. Good sources for AZ designs, basic equations and descriptions are the review by C. Gmachl [203] and the book by J. Faist [100]. For modeling the paper by C. Jirauschek [204] is an excellent source.

## 6.3 Bi-functional quantum cascade material

In 2002, D. Hofstetter reported on the photocurrent response of QCL structures [43]. In combination with the photovoltaic QWIPs [116], this established the field of quantum cascade detectors (QCDs) with operating temperatures up to room temperature as discussed in chapter 3. Nevertheless, a wavelength mismatch between the lasing wavelength and the photocurrent response peak in QCL structures inhibited the detection and emission of light with the same material. One of the main tasks for a bi-functional design is to compensate for the wavelength mismatch to get approximately the same optical transition energy in biased and unbiased operation mode (figure 6.3). Depending on the bias conditions, a bi-functional material operates as a QCD or as a QCL and detects and emits light, given a laser cavity is provided.

Wavelength matching in high performance (2<sup>nd</sup> generation) QCLD materials is achieved by a two stage extractor design. The extractor of the lower laser level in biased operation consists of two parts. The horizontal extractor exhibits thick barriers for wavelength matching and the vertical extractor part offers fast LO-phonon depopulation to the next periods injector.

In unbiased operation the levels which act as injector to the upper laser level have to align in a way that an efficient extractor for QCD operation is formed. Hence the photo excited carriers have a high extraction efficiency (figure 6.3 lower part).

Besides the heterostructure design the QCLD material requires a waveguide design such as for pure QCL materials to provide the required mode confinement in the cavity. QCLD materials allow, as QCDs, detection in a wide power range without saturation effects. All gas sensing devices presented are based on high performance (the 2<sup>nd</sup> generation) bi-functional QCLD materials.

## 6.4 Bi-functional gas-sensing device

This part of the chapter is based on the paper *Mid-infrared surface transmitting and detecting quantum cascade device for gas-sensing* published in Scientific Reports in

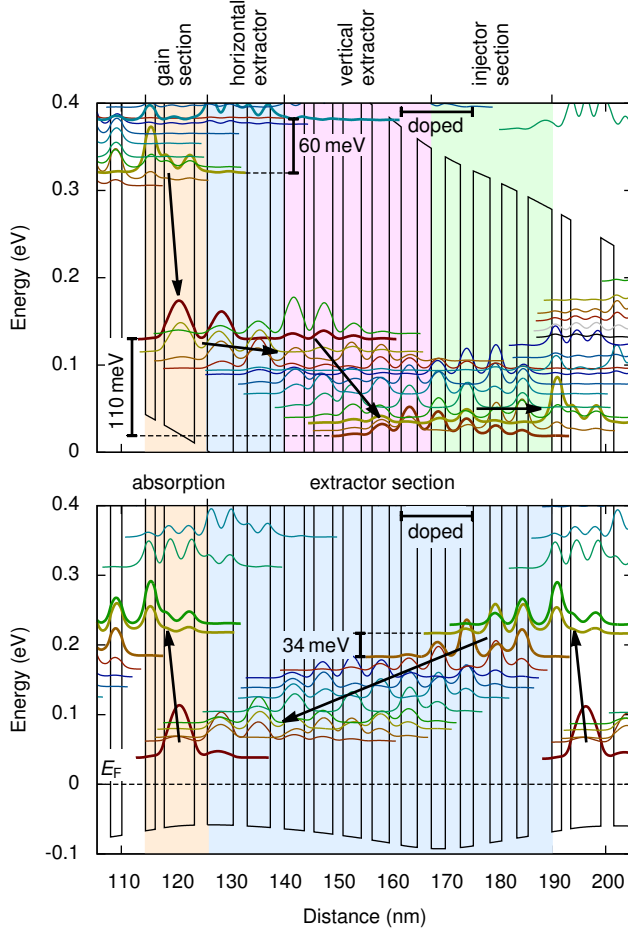


**Figure 6.3:** Band structure of a second generation bi-functional material in biased condition (upper) for regions of the material in laser operation. For wavelength matching a two stage horizontal and vertical extraction scheme is implemented to achieve wavelength matching. In unbiased condition (lower) the material is in photovoltaic detection mode. The detector operation principle is similar to QCD materials. The doped region corresponds to the LO-phonon staircase in the detector mode. Image from [205]

2016 [206].

Based on the considerations for the required interaction region length for gases, a surface operation mode bi-functional prototype sensor was designed. The light emission and light detection is perpendicular to the chip surface, hence surface normal light coupling for emission and detection is implemented.

The device is processed from one material growth into emitting and detecting structures with separate electric contacts. Thereby, both source and detector are integrated on a single chip. The emitting cavity is operated as pulsed QCL and the detector structure as unbiased photovoltaic mode detector. The bi-functional gas sensing devices are processed from material C0120 which is a high performance bi-functional QCLD material for same frequency lasing and detection around  $\lambda = 6.5\mu\text{m}$  based on the InGaAs/InAlAs material system [205].

**Source** The surface emitting QCL structure is a ring-QCL with a 2<sup>nd</sup> order distributed feedback grating optimized for surface emission [207]. A ring-QCL exhibits a narrow emission angle in comparison to Fabry-Pérot (FP) laser ridges. Therefore, beam collimation is possible with lower NA lenses than for ridge devices. Due to the



mode selection by the DFB grating the ring-QCL emits single mode MIR light. The exact wavelength can be defined by the DFB grating period within the gain spectrum of the QCLD material. The surface operation mode allows in future designs, for two dimensional integration of multiple devices as an array to cover multiple emission wavelengths similar to figure 1.4 b. The ring cavity has an outer diameter of 400  $\mu\text{m}$  with a width of 11  $\mu\text{m}$  (figure 6.5 a). The grating period of the DFB grating is 2.1  $\mu\text{m}$  with a duty cycle of 0.5 etched into the top cladding layer. The laser threshold is at 3 kA/cm<sup>2</sup> which is a typical value for a bi-functional ring-QCL with this geometry. However, lower values have been reported for QCL only materials [208, 209]. The laser is operated with 100 ns pulse duration and a repetition rate of 5 kHz up to 20 kHz depending on the desired optical emission power. Laser emission is at 1514 cm<sup>-1</sup>.

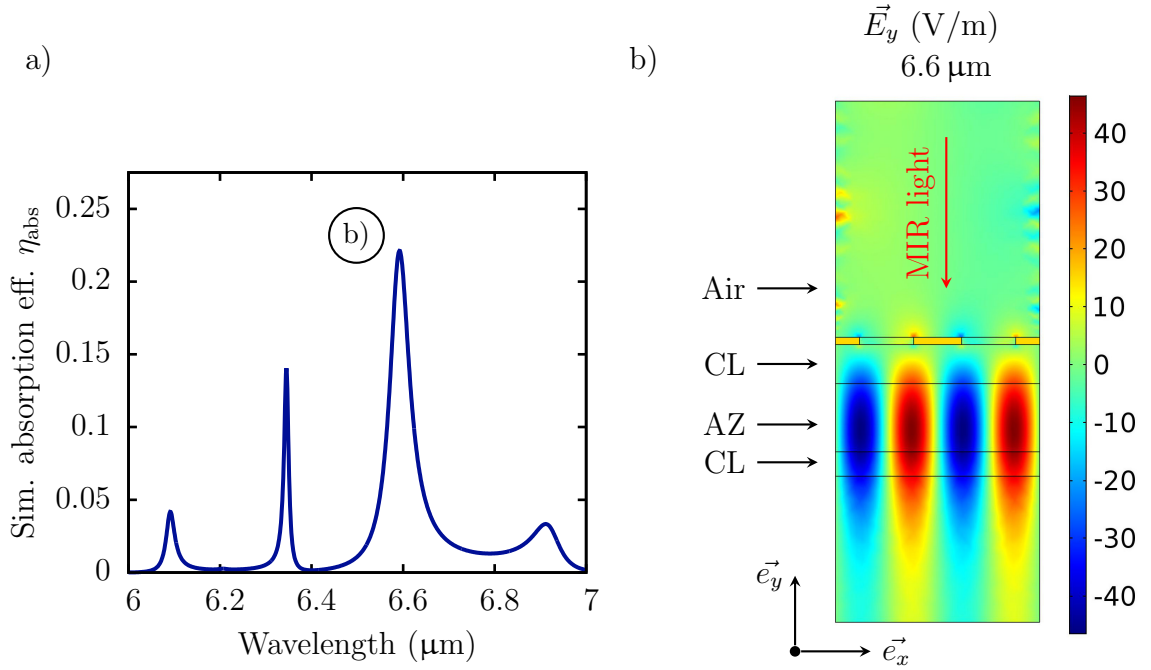


**Figure 6.4:** Metal hole grating detector element simulations for the bi-functional gas-sensing device. Absorption efficiency a) for the layer structure of sample C0120. The radiation impinges surface normal from the air side and couples b) to the active zone below the metal hole layer by the electric field  $\vec{E}_y$ . The electric field distribution  $\vec{E}_y$  in b) corresponds to the marked peak in a).

Pulsed operation mode offers sufficient output power for most absorption spectroscopy applications. Moreover, wavelength tuning can be used to shift the DFB single mode wavelength for several wavenumbers [81] which provides a way of fine adjustment to absorption lines of interest.

The laser top contact is extended to the outer side of the ring cavity in a quadratic shape as depicted in figure 6.5 a. The extended contact pad is insulated by an SiN

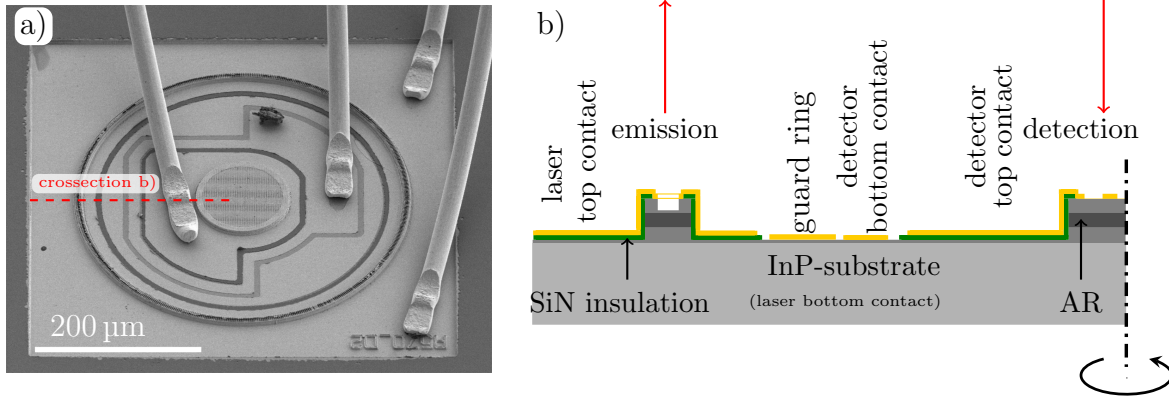


**Figure 6.5:** Scanning electron microscope image a) of the bi-functional surface emitting and detecting device with direct bond wires. The detector element is in the center of the ring-QCL with a metal hole grating to couple the normal incident MIR light. The cross section b) marked in the SEM image depicts the emitting and detecting parts of the design. The contact surfaces for the detector are centered inside the ring cavity with a bottom contact and the extended top contact. As published in [206].

electric insulation layer. The substrate is used as laser bottom contact.

**Detector** The detector element is centered inside the ring cavity of the QCL. The detector element has an outer diameter of 113 μm and couples the light utilizing a two dimensional metal hole grating on top of the (top) contact layer. The grating parameters were determined by numerical simulations similar to the simulations presented in section 5.2.4. The light coupling was optimized for surface normal incident radiation from the air side (figure 6.4). A grating period of  $p = 2 \mu\text{m}$  and a duty cycle of 0.48 was used. This hole grating also acts as the top contact of the detector with an extended contact pad. The detector element has a separate bottom contact which contacts the highly doped bottom contact layer. With these two separate contacts the detector element can be operated in unbiased photovoltaic mode simultaneously with the ring-QCL in pulsed mode.

### 6.4.1 Characterization

Both emission and detection were first characterized in separate steps. The ring-QCL was investigated by a standard light current voltage (LIV) characterization utilizing a FTIR spectrometer and the internal DTGS detector. The detector characterization was done utilizing the global source of the FTIR similar to the detector characterizations presented in section 3.4.4. First a basic bi-functional characterization was conducted without a gas cell using a flat mirror to verify the detection

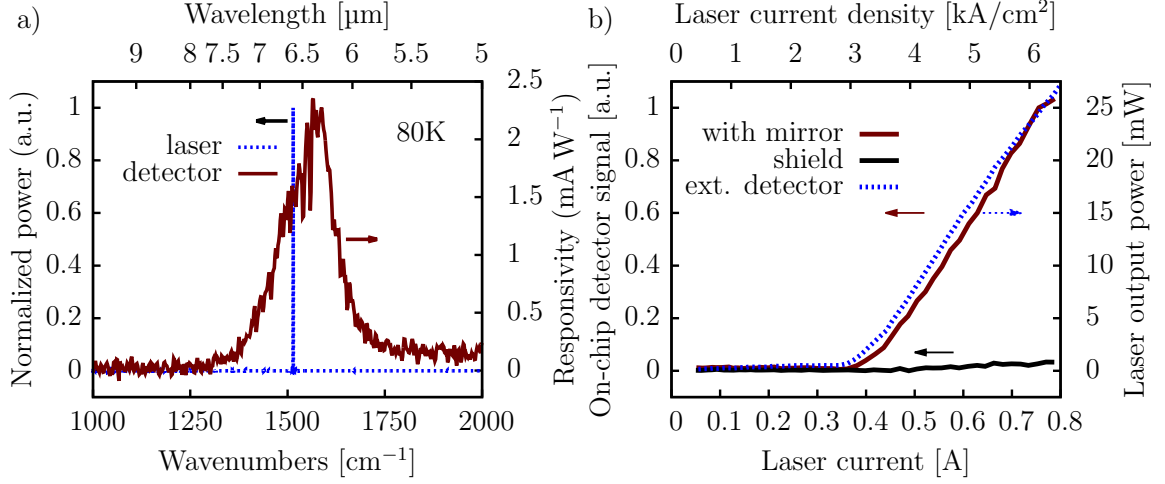


**Figure 6.6:** Wavelength overlap a) of the single mode emission from the ring-QCL and the detector elements photocurrent spectrum. The on chip detector elements response in comparison to an external DTGS detector of the FTIR over the laser current. As published in [206].

of back reflected on-chip emitted light. A chopper in the beam path has to be operated at a different frequency than the laser repetition frequency (5 kHz, 10 kHz, 20 kHz) to provide the needed selectivity for lock-in amplification of the detector signal and to eliminate electrical cross talk. Light detection of the reflected light could be achieved with distances between sensor and mirror of up to a meter. Larger distances were not tested. Nevertheless, lower distances in the range of 400 mm - 500 mm showed more efficient coupling.

Subsequently a gas cell was added into the beam path. In this setup the ring-QCL was operated in pulsed operation mode inside a cryostat at 77 K. The emitted light was collimated by an  $f = 50.8$  mm lens, passed through the chopper, the gas-cell and was reflected on the flat Au mirror (figure 6.7). To verify correct light coupling between the emitted beam and the reflected light, the detector signal was measured with the on chip detector in two different configurations. First, the signal was recorded over the laser current for the beam path with the N<sub>2</sub> flooded gas-cell. Second, the measurement was repeated with a blocked beam path. The beam was blocked by covering the flat mirror with a black low reflective shield. The remaining detector signal for the blocked path (figure 6.6 b) is due to the reflections on the gas-cell and cryostat windows. The comparison between these two configurations shows clearly that the on-chip detector signal originates from the mirror reflected, on-chip emitted light. In addition to that, the comparison of the laser characterization, obtained with the external DTGS detector of the FTIR and the on-chip detector signal match considering a coupling efficiency induced scaling factor.

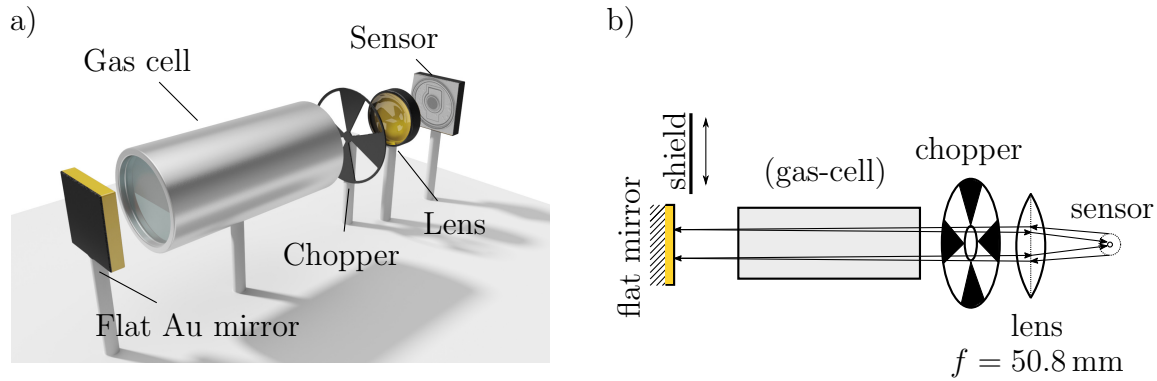


**Figure 6.7:** Measurement setup a) for bi-functional operation of the sensor. The emitted light is collimated by the lens passed through the optical chopper and reflected by the flat Au mirror. Depending on the measurement the setup was used without the gas-cell for basic characterization of the device and with the gas-cell for sensing experiments. Best optical alignment b) is achieved with the lens slightly out of focus. Subfigure a) modified from [210] and b) as published in [206].

For all configurations the same threshold current of the ring-QCL was observed.

The highest coupling efficiency between the emitted and back reflected light is achieved with the lens slightly out of focus (figure 6.7 b). To verify the intensity distribution on the on-chip detector element as a result of the reflected beam, far field measurements were conducted. The far field of the ring-QCL emission was recorded by an x-y motorized stage with the device cooled in the cryostat as for the bi-functional experiments. Longer distances between the sensor and the mirror are possible, hence longer gas-cells can be used if the analyte absorption requires longer interaction regions.

### 6.4.2 Gas sensing

For all gas sensing experiments a 100 mm long gas-cell with a diameter of 49 mm was used. The distance between the sensor and the flat Au mirror was 440 mm. This setup as depicted in figure 6.7 b results in a total interaction length of 200 mm due to the beam passing the cell twice.

For proof of concept measurements at the detection wavelength of  $1514 \text{ cm}^{-1}$ , isobutane and propane were chosen. These gases can be handled safely in the lab environment and are easily available. The analyte was prepared as a mixture of isobutane or propane with nitrogen by mass flow controllers and pumped through the gas cell with a rate of 3 L/min. The gas mixture was kept at a pressure of 1060 hPa and a temperature of 300 K. Prior the measurements the gas-cell was flooded with pure nitrogen and the beam path was aligned to the maximum of the

on chip detector signal. For different concentrations of isobutane in nitrogen and propane in nitrogen the detector signal was recorded over the increasing laser current in pulsed operation mode with 100 ns pulse duration and 20 kHz repetition rate. All data points were recorded with 1 s integration time.

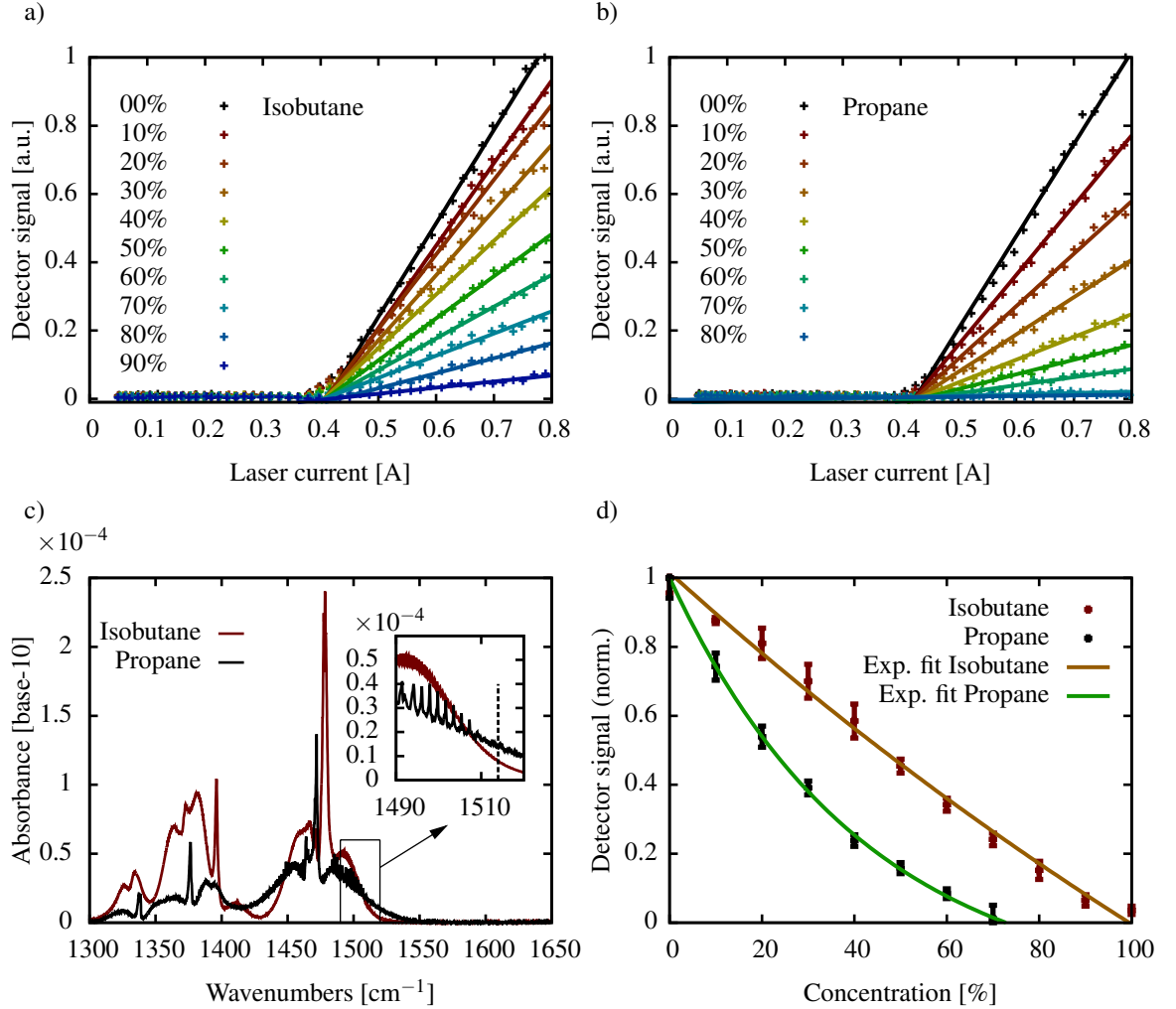


**Figure 6.8:** Proof of concept gas-sensing measurements with the 1<sup>st</sup> generation bi-functional gas sensor. The on chip detector signal over the laser current varies according to the gas concentration in the gas-cell. Isobutane a) shows a lower absorption than propane b) at the test wavelength of  $1514\text{ cm}^{-1}$ . Due to the higher absorption of propane the measurable gas concentration range is limited. The measurement wavelength is located at the short wavelength end of the c) absorption spectrum of the test gases. Subfigure d) shows an exponential fit of the normalized detector signal over the gas concentration. As published in [206].

Depending on the absorption of the analyte and the concentration of the test gas in nitrogen the on chip detector signal changes. The mixture of isobutane and nitrogen could be measured in a wide concentration range between 0% isobutane and 90% isobutane in nitrogen (figure 6.8 a). With increasing isobutane concentration

the detector signal drops until the on chip signal is at the noise level. Propane exhibits a higher absorption at the operation wavelength of the device (figure 6.8 c) and therefore a lower measurable concentration range of up to 70% for the same interaction length (figure 6.8 b). The measurement points are marked by the crosses, whereas the lines are linear fits between 0.44 A and 0.8 A for the given concentration.

The detector signals for different concentrations of the gas mixture were extracted at 0.8 A laser current from the linear fit functions and plotted over the concentration of the corresponding test gas in nitrogen (figure 6.8 d). Both test gases mixed with nitrogen show according to Beer-Lambert's law the expected exponential behavior. The higher absorbing propane results in a steeper exponential decay for increasing propane concentration in nitrogen.

### 6.4.3 Light coupling

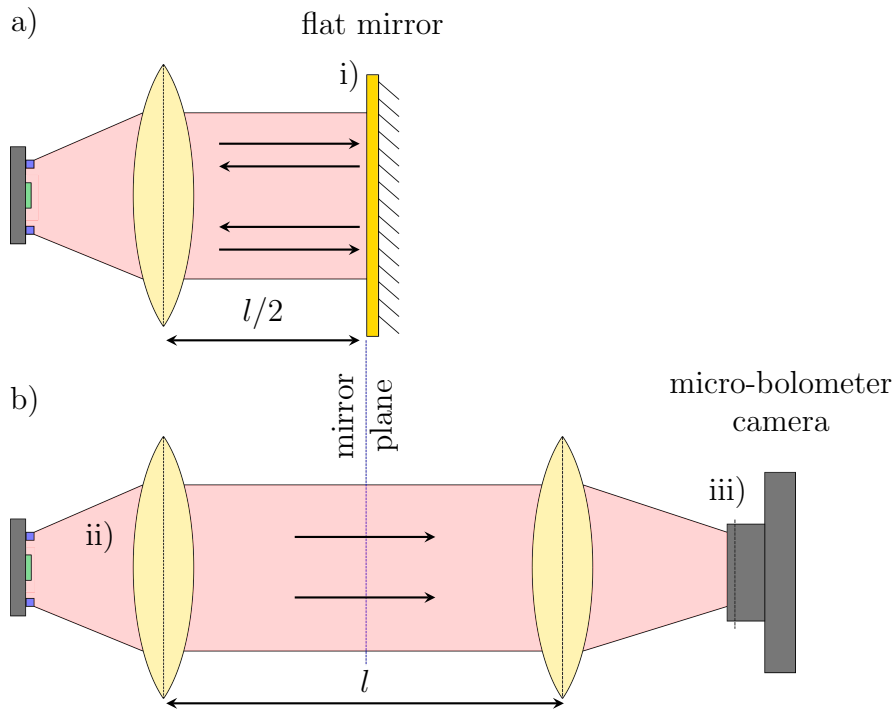


**Figure 6.9:** Setup for micro-bolometer camera measurements of the intensity distribution. The sensing configuration a) is extended by a second lens b) to re-focus the beam onto the camera similar to the situation in the sensing configuration. The magnified image of the emitting ring was recorded in position i, the far field in position ii (not to scale) and the re-focused intensity distribution in position iii.

Due to the geometry of the ring-QCL and its far field, light coupling to the detector element from the back reflected beam is inefficient. To investigate on the spatial intensity distribution micro-bolometer camera images and a far field mapping were

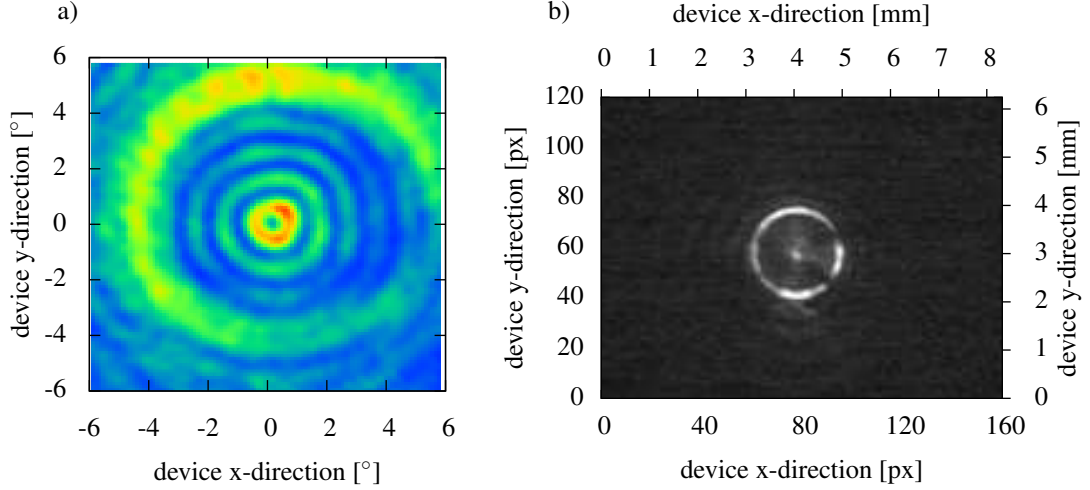


**Figure 6.10:** Farfield a) of the ring-QCL emission from the sensor mounted in the cryostat without further focusing by a lens. The concentric intensity distribution with the central minimum is typical for ring-QCLs without far field modifications. Magnified image of the emitting ring-QCL after the lens with the dark spots originating from the detector element's bond wires crossing the cavity. Both measurements were recorded in 300 mm distance from the sensor.

recorded. The far field measurement shows strong reflections on the cryostat windows and the typical intensity distribution of a standard ring-QCL without grating based far field modifications. The concentric intensity fringes and the intensity minimum in the far field center (figure 6.10) lead to an intensity distribution where just a fraction of the light can be coupled back to the detector element centered in the ring-QCL. The broad intensity ring at  $\pm 4^\circ$  of the far field is due to reflections on the cryostat window. The measurement position (not to scale) for this far field is according to position (ii) in figure 6.9 b).

In a next step a magnified image of the emitting ring-QCL was recorded with a micro-bolometer camera with  $160 \times 120$  pixels and  $52 \mu\text{m}$  pixel pitch. The image was taken after light collimation by the lens in 300 mm distance from the sensor corresponding to position (i) in figure 6.9 a). Besides the ring shaped emitting surface two dark spots are visible on the ring which are due to the bond wires of the detector element crossing the ring cavity (figure 6.10 b). As mentioned before, best coupling efficiency was achieved with the lens slightly out of focus. This means that the beam is not perfectly collimated in the path between the lens and the mirror (figure 6.7 b). This could also be verified by bolometer camera images at different distances from the lens similar to position i in figure 6.9 a). For that purpose the lens was positioned for best coupling efficiency (highest detector signal), hence in sensing configuration. The image of the ring cavity changes slightly in size depending on the distance from the lens, which confirms the non perfectly collimated beam shape.



To investigate on the intensity distribution which can be expected on the sensor due to the reflected light, the micro-bolometer camera was placed after a second lens, also with  $f = 50.8$  mm focal length corresponding to position (iii) in figure 6.9 b. The distance between the two lenses was chosen to be two times the distance between the lens and the mirror in the sensing configuration. The camera plane was positioned with respect to the second lens in the same distance as the sensor from the first lens. With this setup an image of the re-focused beam was recorded to resemble the intensity distribution expected from the beam reflected on the flat mirror. The micro-bolometer camera image taken in this configuration shows that only a low fraction of the reflected light is coupled back onto the detector element (figure 6.11). The central spot, mostly caused by stray light is the major contribution to the on-chip detector signal. This causes a relatively low coupling efficiency and detector signal.

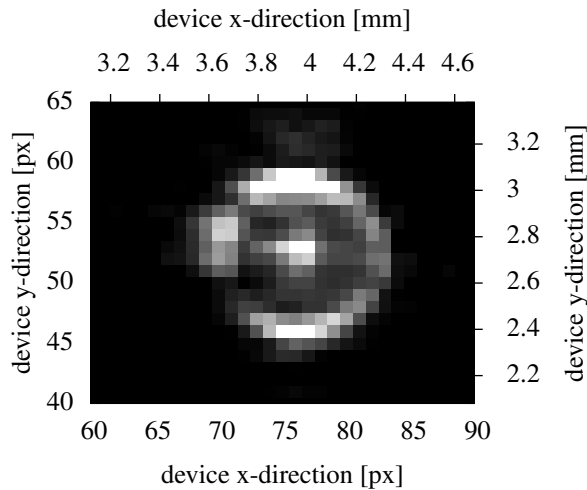


**Figure 6.11:** Image of the refocused beam after a second lens to check for the intensity distribution similar as from the beam reflected on the flat mirror. Most of the reflected light intensity is not coupled back to the detector element which leads to a relatively low coupling efficiency.

## 6.5 Revised bi-functional gas sensing device

The 1<sup>st</sup> generation gas sensing device presented in section 6.4 is strongly limited by the optical coupling efficiency seen from the micro-bolometer camera images. Moreover the electrical crosstalk limits the operation temperature and the limit of detection. An additional minor drawback of the 1<sup>st</sup> generation device is that integration of multiple wavelengths leads to different optical paths for every emitting ring-QCL.



### 6.5.1 Device design

To overcome these performance limiting issues a 2<sup>nd</sup> generation revised device was conceived, which includes an improved contact design, multi-wavelength operation and an enhanced geometry for higher light coupling efficiency. The revised sensor is based on two concentric bi-functional distributed feedback (DFB) ring-QCLDs with separate contacts. The device is as before processed from a high performance bi-functional material C0280 which is a regrowth of material C0120. The concentric ring cavities are designed for two slightly different DFB grating periods to exhibit two different single mode emission wavelengths separated by several wavenumbers. As the first device, the enhanced design is processed monolithically from one material. The following section is based on the publication *Remote Sensing with Commutable Monolithic Laser and Detector* published in ACS photonics in 2016 [210].

The device (figure 6.12) allows both ring structures to be commutable operated in biased pulsed laser operation and in unbiased detector operation. Both, the emitting and the detecting surfaces are ring shaped and exhibit similar diameters. The ring surfaces, when operated as detector, have a larger diameter than the detector element of the 1<sup>st</sup> generation design. Consequently, a higher coupling efficiency between the emitted and the reflected and re-focused beam is expected based on the observations presented before. The outer ring diameter is similar to the 1<sup>st</sup> generation 400  $\mu\text{m}$ , whereas the inner ring diameter is 330  $\mu\text{m}$ . Due to the concentric ring design both emission beams are located on the same optical axis in surface normal direction. This allows for sensing with both wavelengths without additional external optical elements and without an additional optical path being introduced.

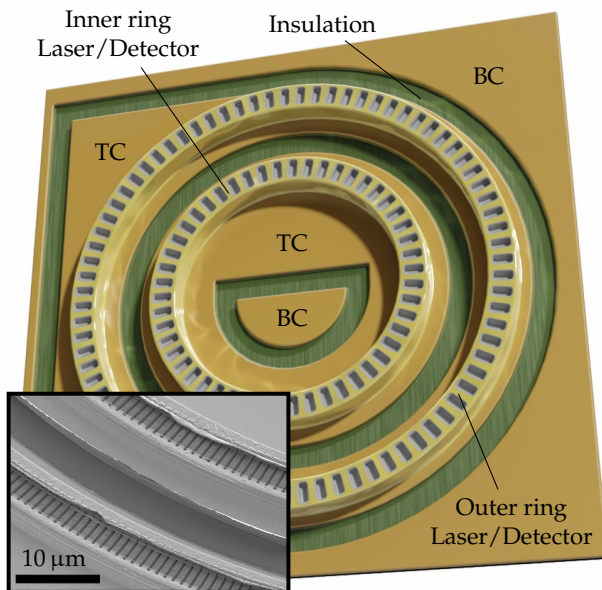


**Figure 6.12:** Revised sensor design with two concentric separately contacted bi-functional DFB ring-QCLs. The two ring cavities have a diameter of 400  $\mu\text{m}$  and 330  $\mu\text{m}$  respectively and have two slightly different single mode emission wavelengths. Both rings can be operated as laser and as detector. The inset shows a scanning electron microscopy image of the two rings with the DFB grating on top. As published in [210]

The device operates around  $1500\text{ cm}^{-1}$  which is in the  $6.7\text{ }\mu\text{m}$  wavelength range. The slightly different wavelength in comparison to the first proof of concept design is due to the higher operation temperature at room temperature and different DFB grating periods. The design features separate top and bottom contacts for both ring cavities. The substrate contact is not used as bottom contact in laser operation in order to reduce the electrical crosstalk. The basic device characterization was done very similar as described for the 1<sup>st</sup> generation device with a separate laser and detector characterization and then the subsequent bi-functional characterization for both cavities.

Figure 6.13 in the upper part illustrates the spectral overlap of the outer ring operated in laser mode showing single mode emission and in unbiased detector operation. The lower part shows similarly the results for the inner ring. In comparison to the emission wavelength separation, the photocurrent spectral response of the two rings in detector operation is relatively broad. Therefore, each of the two rings can detect the light emitted by the corresponding other ring. This means that the inner ring can detect light emitted from the outer ring and vice versa.

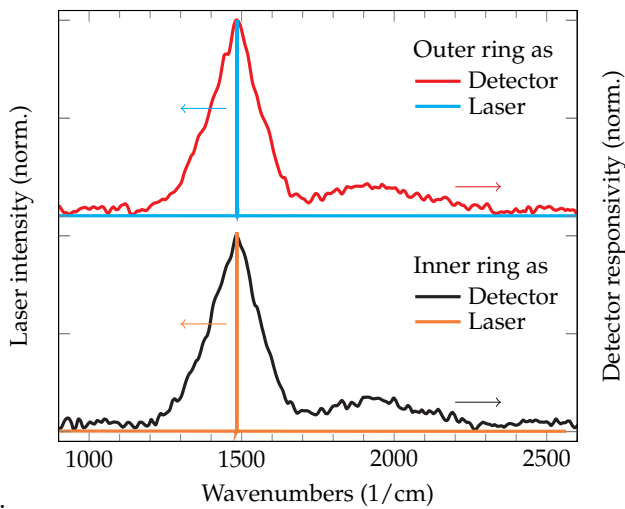


**Figure 6.13:** Spectral FTIR characterization of the rings operated as laser and as detector for the outer ring (top) and the inner ring (bottom). Both rings show single mode emission in laser operation. As published in [210]

**Detector operation** In contrast to the proof of concept device light coupling in detector operation is achieved via the same 2<sup>nd</sup> order DFB grating as used for laser operation. This is essential to allow for commutable operation as emitter and detector of the ring cavities. For both rings operating in detector mode a responsivity of  $1.2\text{ mA/W}$  was measured at a wavelength of  $1481\text{ cm}^{-1}$ . Numerical simulations were conducted to investigate on the light coupling to the DFB gratings [210]. The detector performance is lower in comparison to a ridge configuration or in general facet coupled geometries due to the cladding layers which are necessary for laser

waveguiding which introduce an additional distance between the grating and the active zone.

The detector signal was recorded with a SR570 pre-amplifier set to 200 nA/V, low noise mode with a 6 dB bandpass filter and a lock-in amplifier with the lock-in voltage as the detector signal used for the sensing experiments. The chopper frequency for the lock-in amplifier was set to 300 Hz which is, as described for the 1<sup>st</sup> generation device, at a different frequency than the laser repetition rate.

**Laser operation** Depending on the choice of the emission wavelength the inner or the outer ring-QCL can be operated to emit light. For gas-sensing experiments the lasers were operated in pulsed mode with up to 40 kHz repetition rate with 100 ns pulse duration. The outer and inner ring provide 79 mW at 1484.3 cm<sup>-1</sup> and 100 mW at 1483.3 cm<sup>-1</sup> output power respectively. These results were obtained in a light current voltage LIV characterization utilizing the calibrated DTGS detector of the FTIR.

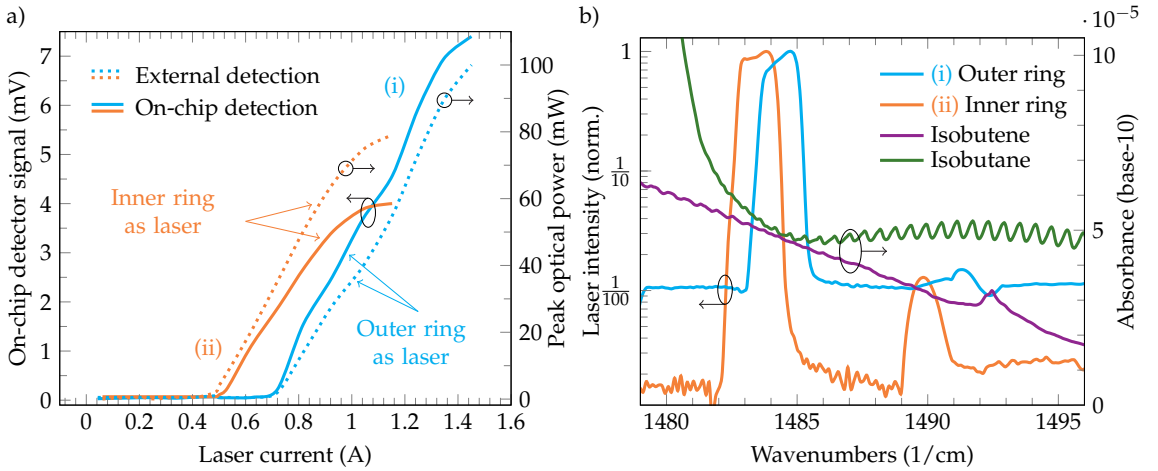


**Figure 6.14:** Comparison of the two operation modes a) for external DTGS detection and on-chip detection with the ring cavities. The outer ring as laser (i) and the inner ring as detector and the inner ring as laser (ii) and the outer ring as detector over the laser current. The dashed lines show the detector signal for external detection and the solid lines the on-chip detector signal lock-in voltage. The single mode emission wavelengths b) of the two concentric ring-QCL devices in comparison to the absorption spectrum of the two test gases. The outer ring wavelength is located in a region with the two gases having nearly the same absorption whereas the inner ring emits at a slightly longer wavelength where isobutane exhibits slightly stronger absorption. Modified from [210].

### 6.5.2 Gas sensing

For the gas-sensing experiments the same setup as for the proof of concept devices was used which again results in a total interaction length of 200 mm. As discussed before, first the bi-functional operation was verified and compared to the external detector signals obtained from the DTGS detector. Both operation modes were characterized. In the first mode (i) the outer ring is operated in laser mode and the inner ring in detector mode and similarly in mode (ii) the inner ring operated in laser mode and the outer ring in detector mode. Considering a coupling efficiency based scaling factor, both operation modes show a good agreement of the on-chip detector signal with the external DTGS measured detector signal. The difference of the (absolute) threshold currents for the inner ring and the outer ring is due to their different size (figure 6.14 a).

For gas sensing experiments isobutene  $C_4H_8$  and isobutane  $C_4H_{10}$  concentrations in nitrogen were measured. The test gas mixture was prepared as for the measurements discussed previously. The two emission wavelengths of the device are located at two different positions of the absorption spectrum of these gases. The emission of the outer ring is located at a position of the absorbance spectrum where both gases exhibit nearly the same absorption whereas the inner ring emits at a slightly longer wavelength where isobutane exhibits stronger absorption than isobutene (figure 6.14 b). The spectral width is due to their temperature induced shift over the laser pulse which is  $1.4\text{ cm}^{-1}$  for a pulse duration of 100 ns. The spectra were recorded for laser currents of 1.45 A and 1.15 A for the outer and the inner ring respectively.

For the gas measurements of the revised design the detector signal was averaged over 120 data points with a lock-in time constant of 0.5 s, hence the number of measurements was increased at half the integration time in comparison to the measurements presented in figure 6.8 a & b. The gases under test were mixed with nitrogen and pumped into the gas-cell.

The shape of the absorption spectrum of isobutene is linearly changing in the range and the near surrounding of the two emission wavelengths of the sensor whereas the absorption of isobutane has a more quadratic characteristic around the operation wavelengths of the sensor (figure 6.14 b). The emission wavelength of the inner ring (mode ii) is expected to face stronger attenuation for isobutane than the emission wavelength of the outer ring (mode i).

The results for isobutene show a very similar detector signal for both operation modes (figure 6.15 a). As a result, the absorbances of isobutene ( $A_{C_4H_8}$ ) extracted from the isobutene measurement for both operation modes are close to each other. For the outer ring operated as laser,  $A_{C_4H_8(i)} = 4.75 \times 10^{-5}$  was extracted and for

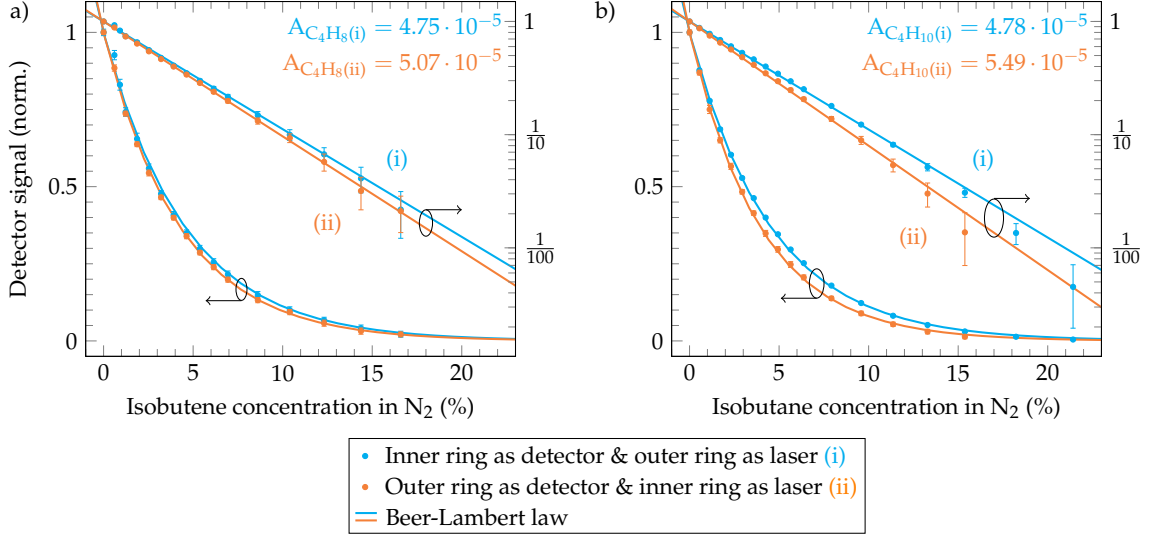


**Figure 6.15:** On chip detector signal over various gas concentrations for a) isobutene and b) isobutane for both sensor operation modes, hence two slightly different operation wavelengths. The measurement samples (dots) are well aligned on the exponential fits (solid lines) according to the Beer-Lambert law. Both y-axes show the detector signal in different scales. Modified from [210].

the inner ring operated as laser  $A_{C_4H_8(ii)} = 5.07 \times 10^{-5}$ . This is expected since the absorption of isobutene is stronger at the emission wavelength of the inner ring (i).

For the isobutane measurements a similar behavior with a larger difference in the extracted absorbances was observed (figure 6.15 b). Due to the quadratic like dependence of the absorbance in the operation wavelength range, for the inner ring a significantly stronger absorption  $A_{C_4H_{10}(ii)} = 5.49 \times 10^{-5}$  was extracted. In comparison, for operation mode (i) with the outer ring emitting  $A_{C_4H_{10}(i)} = 4.78 \times 10^{-5}$  was extracted. These results confirm the characteristics of the absorption spectrum with respect to the measurement wavelengths as illustrated in figure 6.14 b.

Due to the ring shape of the emitting and detecting surfaces of the sensor the light coupling efficiency could be improved. In combination with the revised contact design the electrical crosstalk was reduced. This enables for a  $3\sigma$  limit of detection of 397 ppm with the sensor operated at room temperature.

### 6.5.3 Light coupling

In contrast to the 1<sup>st</sup> generation device the coupling efficiency could be increased by the ring shape and size of the sensor region operated in detector mode. Nevertheless the alignment needs to be very precise to re-focus the light from the mirror reflection onto the ring cavity (figure 6.16 a). For misaligned beam paths the detector signal does not vanish, but a low detector signal is observed. In this case the reflected

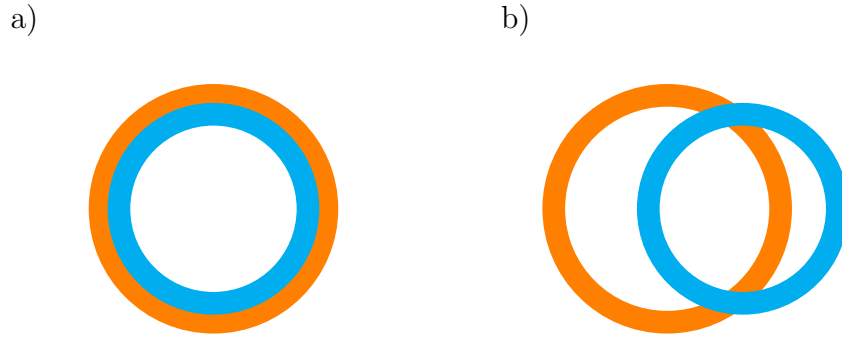


**Figure 6.16:** Ideal light coupling mode a) for the two ring shape bi-functional laser/detector cavities. The ring shaped intensity distribution (orange) reflected from the mirror impinges the second ring operated as detector (blue) in a concentric way. In a misaligned setup b) the intensity pattern (orange) crosses the detector operated ring only.

intensity distribution crosses the ring shaped detector at two points (figure 6.16 b).

## SUMMARY AND OUTLOOK

### 7.1 Summary

Within the scope of this thesis three topics have been investigated: first, light coupling to quantum cascade detectors (QCDs) by plasmonic lenses, second, the integration of QCDs to pixel array devices and third, the development of a novel surface emitting and detecting bi-functional gas sensor for external interaction regions.

An alternative light coupling method for quantum cascade detectors (QCDs) with the capability to enhance the room temperature detectivity  $D_j^*$  was shown. This was achieved by increasing the optical active area of the device by a plasmonic lens. The electrical active detector element was kept small to limit the resistance and noise. Various **plasmonic lens QCD** designs were shown which are sensitive to unpolarized surface normal incident radiation or polarization sensitive to linearly polarized light. For plasmonic lens coupling the surface plasmon polariton propagation length was identified to be the significant parameter for the detector performance. Plasmonic lenses with a diameter up to two times this characteristic length were determined to contribute to the detector signal. For the shown  $6.5\text{ }\mu\text{m}$  wavelength devices this corresponds to a lens radius of up to  $\approx 98\text{ }\mu\text{m}$ . Due to the plasmonic lens structures a photocurrent increase by up to a factor of 6 and a specific detectivity increase up to a factor 2.6 at room temperature could be realized in comparison to the  $45^\circ$  mesa reference device.

Quantum cascade detector performance strongly depends on the light coupling and absorption geometry. Absorption geometries with long absorption lengths offer high absorption efficiency also at low doping concentrations and thereby increased resistance and detectivity. Coupling geometries such as end fire coupling to the facet of a wave guide embedded detector active zone are a promising way for per-



formance improvement. On-chip light focusing as shown with the plasmonic lens devices utilizes this coupling scheme. As a result strongly improved temperature performance, i.e. a lower performance drop for elevated temperatures was observed. The longer absorption length available compensates for the decreasing absorption coefficient when the operation temperature approaches room temperature.

In this work, various QCD designs have been processed and characterized to optimize for a short wavelength mid-infrared detector design at  $\lambda = 4.3\text{ }\mu\text{m}$  wavelength. An optimized vertical transition design was determined to exhibit the best performance over a diagonal transition design in this wavelength range. Wavelength matching by multiple sample growths and characterizations was conducted to precisely hit the strong  $\text{CO}_2$  absorption at operation temperatures of 240 K up to room temperature. Based on test pixel structures and numerical simulations light coupling by a two dimensional diffraction grating was optimized. The detector was further integrated to a  $8 \times 8$  **prototype pixel array** compatible to a custom read out integrated circuit for thermo-compression flip-chip bonding. The characterized single pixels from the array show an improved performance over the mesa configuration devices. In conclusion it could be shown that QCDs can be integrated to pixel arrays with similar or better responsivity and detectivity than  $45^\circ$  facet mesa devices (figure 7.1). Additionally, the grating coupling scheme offers improved temperature performance in comparison to the  $45^\circ$  facet illumination configuration.

Finally two novel integrated **gas sensor** concepts were demonstrated based on a high performance bi-functional quantum cascade heterostructure [205]. These two surface emitting and detecting monolithic integrated gas sensing devices for external interaction regions are operating in the  $6.5\text{ }\mu\text{m}$  wavelength region. Both designs are suitable for multi-wavelengths array integration. The revised sensor design offers multi-wavelengths operation along the same optical axis. Additionally, the operation temperature could be increased from 80 K to room temperature by a revised electrical contact design and improved coupling efficiency. The surface operation mode enables for interaction regions external to the integrated device and therefore for long interaction region measurements as needed by low absorption analytes. For both devices as a part of this thesis proof of concept gas measurements were conducted in a wide concentration range reaching a limit of detection of 397 ppm for the revised design. The integration of the QCL emitter and detector on a single gas sensing chip is a step further towards compact integrated sensing solutions. In principle the required laser pulsing and detector measurement electronics can be engineered to relatively compact sizes which enables these devices to be applied in mobile applications.



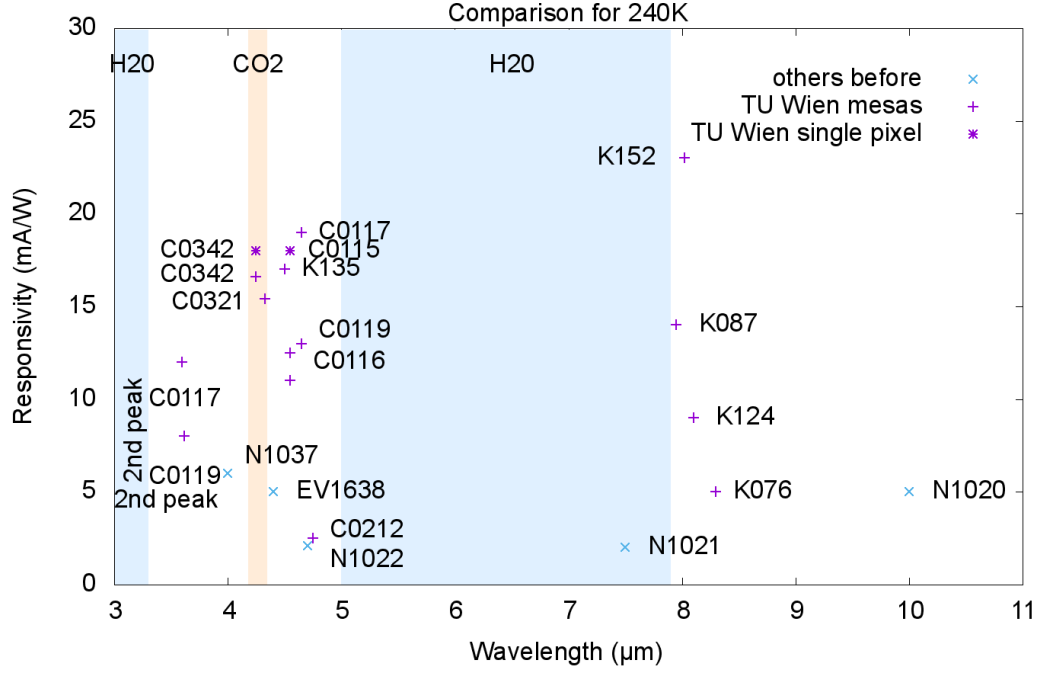


**Figure 7.1:** Progress of QCD development by our research group during detector development for array integration in comparison to several literature reported samples before the thesis, all at 240 K operation temperature. Sample C0342 is the final design used for array integration. Other samples are different vertical transition and diagonal transition designs. The 2<sup>nd</sup> peak is the shorter wavelength photocurrent peak for diagonal transition designs (see figure 5.2). Sample C0321 is a non wavelength matched version of the final design (C0342).

## 7.2 Outlook

Based on the results presented in this work, possible future investigations are suggested in the following to further advance towards increased performance detection and sensing devices.

**Plasmonic lens quantum cascade detectors** For future designs a QCD material specifically designed for plasmonic lens coupling would lead, in addition to the photocurrent enhancement, to competitive results for the absolute figures of merit. A wave guide embedded QCD only design with a low number of periods, combined with a lens diameter of approximately one up to two times the propagation length on the lens should be considered. Further optimization could then be done to reduce the QCD detector element size to a minimum, which still offers sufficient absorption length and compensate for the reduced absorption coefficient at elevated temperatures. This increases the absolute resistance and leaves more device area for the plasmonic structures. Moreover, blazed gratings also known as echelette gratings

and their applicability to plasmonic lens QCDs could be investigated to enhance the focusing towards the detector element. This could include blazed grating designs similar as shown by B. Bai et al. [211].

**Quantum cascade detector arrays** In future designs the pixel size should be reduced to achieve a higher pixel density. Thereby the absolute pixel resistance increases and offers more flexibility for the amplifier design in terms of input resistance.

**Bi-functional gas sensing device** For bi-functional sensing with long interaction regions which are separate from the chip, electrical crosstalk and the coupling efficiency of the back reflected light are limiting factors. Even if the electrical crosstalk could be reduced by a contact design with different bottom and top contacts for the laser and the detector, there is still the need for an optical chopper. An easy way to potentially lower the electrical crosstalk is to better insulate the emitting and detecting parts of the sensor from each other. Future designs need to integrate the sensor without an optical chopper. This can be done by a design with a continuous wave laser source to reduce the crosstalk to a constant offset. Thereby, the signal to noise ratio can be improved, even if pulsed operation is favorable due to the lower thermal load and power consumption. For all laser operation modes pulsed, continuous wave or heterodyne schemes temperature stabilization with a thermoelectric element should be applied.

The intensity distribution of the reflected light re-focused onto the sensor's detector element has high impact on the device performance. According to the intensity maps shown, a combined design of a ring-QCL with a plasmonic lens detector element can be considered. Light coupling by the plasmonic structure is possible on a large surface inside of the ring which then focuses onto a small unbiased region in the center. The plasmonic lens coupling and focusing properties are promising for this purpose. Since the center where the detector element is placed, has no intensity in the standard ring-QCL far field, the intensity loss would be low.

**Meta material absorber quantum cascade detector** Meta materials enable for exciting novel absorber schemes. They offer the possibility to collect light from extended surface areas with the meta atoms designed for the operation wavelength of the device. Recently meta material absorbers in the THz [212] and mid-infrared spectral region were shown by simulation [213] and measurement [187, 214]. High resolution lithography enables to fabricate meta material structures in the infrared spectral region. The combination of a room temperature high resistance QCD design could be integrated replacing the dielectric layer of a meta material absorber for a

future design. Challenges to be faced are a sufficient high active zone (AZ) resistance and thin contact layers to maximize the interaction volume of the AZ and the absorber. The high resistance design is required to allow for a sufficient thin AZ necessary for the absorbers double metal geometry. A low doping concentration in combination with a low number of periods  $N_{\text{Per}} < 10$  may meet this requirement. The low number of periods would promote the responsivity. In combination with a high resistance AZ and the high absorption efficiency by the meta material absorber overall device performance could be improved.

The main processing challenge for such a design is the double metal structure and the lithography for the meta surface on top of the top contact layer. Double metal cavity processing is well known form THz QCL designs [76].

A drawback of the concept is the area utilization of the detector. All areas not contributing to light coupling, hence with no mode overlap according to the intersub-band selection rule lower the device resistance and thereby the detectivity without contributing to the photoresponse.



## GROWTH SHEETS

This section documents the molecular beam epitaxy (MBE) growth sheets for the materials used in the scope of this thesis. The tables are split in assembly like overviews and detailed tables which contain the information of the gradings and the active zone. The growth sheets start with the top contact layer towards the substrate at the bottom line of the tables.

## A.1 H853

Material H853 is a 1<sup>st</sup> generation bi-functional QCLD material which was used in pure detector operation for the plasmonic lens enhanced photodetectors reported in chapter 4.4.2. The bi-functional material offers waveguiding as needed for QCL operation which is essential for end-fire coupling to the detector element.

H853 Overview				
Material	Thickness (nm)	x(%)	Doping (cm <sup>-3</sup> )	Description
In <sub>x</sub> Ga <sub>1-x</sub> As	10	53	Si: $1 \times 10^{20}$	Top contact layer
In <sub>x</sub> Ga <sub>1-x</sub> As	350	53	Si: $8 \times 10^{18}$	
Grading 4	25	-		See additional table
In <sub>x</sub> Al <sub>1-x</sub> As	800	52	Si: $2 \times 10^{17}$	
In <sub>x</sub> Al <sub>1-x</sub> As	1800	52	Si: $1 \times 10^{17}$	
Grading 3	25	-		See additional table
In <sub>x</sub> Ga <sub>1-x</sub> As	300	53	Si: $5 \times 10^{16}$	
Grading 2	13.5	-		See additional table
AZ	35 x 52.8	active region + injector		See additional table
In <sub>x</sub> Ga <sub>1-x</sub> As	500	53	Si: $5 \times 10^{16}$	
Grading 1	25	-		See additional table
InP	lattice matched		$2 - 4 \times 10^{17}$	Substrate

**Table A.1:** Growth sheet overview for H853 QCLD samples. AZ thickness 1848 nm, thickness to AZ start 3023.5 nm, minimum etch depth through AZ 4871.5 nm

H853 Grading 4				
Material	Thickness (nm)	x(%)	Doping (cm <sup>-3</sup> )	Description
In <sub>x</sub> Al <sub>1-x</sub> As	0.8	52	Si: $2 \times 10^{17}$	
In <sub>x</sub> Ga <sub>1-x</sub> As	4.2	53	Si: $2 \times 10^{17}$	
In <sub>x</sub> Al <sub>1-x</sub> As	1.6	52	Si: $2 \times 10^{17}$	
In <sub>x</sub> Ga <sub>1-x</sub> As	3.4	53	Si: $2 \times 10^{17}$	
In <sub>x</sub> Al <sub>1-x</sub> As	2.5	52	Si: $2 \times 10^{17}$	
In <sub>x</sub> Ga <sub>1-x</sub> As	2.5	53	Si: $2 \times 10^{17}$	
In <sub>x</sub> Al <sub>1-x</sub> As	3.4	52	Si: $2 \times 10^{17}$	
In <sub>x</sub> Ga <sub>1-x</sub> As	1.6	53	Si: $2 \times 10^{17}$	
In <sub>x</sub> Al <sub>1-x</sub> As	4.2	52	Si: $2 \times 10^{17}$	
In <sub>x</sub> Ga <sub>1-x</sub> As	0.8	53	Si: $2 \times 10^{17}$	

H853 Grading 3				
Material	Thickness (nm)	x(%)	Doping (cm <sup>-3</sup> )	Description
In <sub>x</sub> Ga <sub>1-x</sub> As	0.8	53	Si: $1 \times 10^{17}$	
In <sub>x</sub> Al <sub>1-x</sub> As	4.2	52	Si: $1 \times 10^{17}$	
In <sub>x</sub> Ga <sub>1-x</sub> As	1.6	53	Si: $1 \times 10^{17}$	
In <sub>x</sub> Al <sub>1-x</sub> As	3.4	52	Si: $1 \times 10^{17}$	
In <sub>x</sub> Ga <sub>1-x</sub> As	2.5	53	Si: $1 \times 10^{17}$	
In <sub>x</sub> Al <sub>1-x</sub> As	2.5	52	Si: $1 \times 10^{17}$	
In <sub>x</sub> Ga <sub>1-x</sub> As	3.4	53	Si: $1 \times 10^{17}$	
In <sub>x</sub> Al <sub>1-x</sub> As	1.6	52	Si: $1 \times 10^{17}$	
In <sub>x</sub> Ga <sub>1-x</sub> As	4.2	53	Si: $1 \times 10^{17}$	
In <sub>x</sub> Al <sub>1-x</sub> As	0.8	52	Si: $1 \times 10^{17}$	

H853 Grading 2				
Material	Thickness (nm)	x(%)	Doping (cm <sup>-3</sup> )	Description
In <sub>x</sub> Al <sub>1-x</sub> As	2.8	52		
In <sub>x</sub> Ga <sub>1-x</sub> As	3.7	53		
In <sub>x</sub> Al <sub>1-x</sub> As	2.6	52		
In <sub>x</sub> Ga <sub>1-x</sub> As	4.4	53		

H853 Grading 1				
Material	Thickness (nm)	x(%)	Doping (cm <sup>-3</sup> )	Description
In <sub>x</sub> Al <sub>1-x</sub> As	0.5	52		
In <sub>x</sub> Ga <sub>1-x</sub> As	4.5	53		
In <sub>x</sub> Al <sub>1-x</sub> As	1.0	52		
In <sub>x</sub> Ga <sub>1-x</sub> As	4.0	53		
In <sub>x</sub> Al <sub>1-x</sub> As	1.5	52		
In <sub>x</sub> Ga <sub>1-x</sub> As	3.5	53		
In <sub>x</sub> Al <sub>1-x</sub> As	2.0	52		
In <sub>x</sub> Ga <sub>1-x</sub> As	3.0	53	$1 \times 10^{17}$	
In <sub>x</sub> Al <sub>1-x</sub> As	2.5	52	$1 \times 10^{17}$	
In <sub>x</sub> Ga <sub>1-x</sub> As	2.5	53	$1 \times 10^{17}$	

H853 Active Zone				
Material	Thickness (nm)	x(%)	Doping (cm <sup>-3</sup> )	Description
In <sub>x</sub> Al <sub>1-x</sub> As	2.5	52		
In <sub>x</sub> Ga <sub>1-x</sub> As	5.6	53		
In <sub>x</sub> Al <sub>1-x</sub> As	1.5	52		
In <sub>x</sub> Ga <sub>1-x</sub> As	1.4	53		
In <sub>x</sub> Al <sub>1-x</sub> As	4.4	52		
In <sub>x</sub> Ga <sub>1-x</sub> As	1.9	53		
In <sub>x</sub> Al <sub>1-x</sub> As	2.8	52		
In <sub>x</sub> Ga <sub>1-x</sub> As	2.1	53		
In <sub>x</sub> Al <sub>1-x</sub> As	3.4	52		
In <sub>x</sub> Ga <sub>1-x</sub> As	2.1	53	$2 \times 10^{17}$	
In <sub>x</sub> Ga <sub>1-x</sub> As	2.8	52	$2 \times 10^{17}$	
In <sub>x</sub> Al <sub>1-x</sub> As	2.6	53	$2 \times 10^{17}$	
In <sub>x</sub> Ga <sub>1-x</sub> As	3.0	52	$2 \times 10^{17}$	
In <sub>x</sub> Al <sub>1-x</sub> As	3.2	53		
In <sub>x</sub> Al <sub>1-x</sub> As	2.8	52		
In <sub>x</sub> Ga <sub>1-x</sub> As	3.7	53		
In <sub>x</sub> Al <sub>1-x</sub> As	2.6	52		
In <sub>x</sub> Ga <sub>1-x</sub> As	4.4	53		



## A.2 C0120/C0280

Material C0120 is a 2<sup>nd</sup> generation high performance bi-functional QCLD material which was used for the proof of concept gas sensing devices. The revised version of the gas sensing devices was processed from material C0280 which is a regrowth of C0120 presented here.

C0120 Overview				
Material	Thickness (nm)	x(%)	Doping (cm <sup>-3</sup> )	Description
In <sub>x</sub> Ga <sub>1-x</sub> As	10	53	Si: $1 \times 10^{20}$	Top contact layer 1
In <sub>x</sub> Ga <sub>1-x</sub> As	350	53	Si: $8 \times 10^{18}$	Top contact layer 2
Grading 4	25	-		See additional table
In <sub>x</sub> Al <sub>1-x</sub> As	800	52	Si: $2 \times 10^{17}$	
In <sub>x</sub> Al <sub>1-x</sub> As	1200	52	Si: $1 \times 10^{17}$	
Grading 3	25	-		See additional table
In <sub>x</sub> Ga <sub>1-x</sub> As	400	53	Si: $5 \times 10^{16}$	
In <sub>x</sub> Al <sub>1-x</sub> As	2	52	Si: $1 \times 10^{17}$	
In <sub>x</sub> Ga <sub>1-x</sub> As	7	53	Si: $1 \times 10^{17}$	
In <sub>x</sub> Al <sub>1-x</sub> As	2	52	Si: $1 \times 10^{17}$	
In <sub>x</sub> Ga <sub>1-x</sub> As	6	53	Si: $1 \times 10^{17}$	
In <sub>x</sub> Al <sub>1-x</sub> As	2	52	Si: $1 \times 10^{17}$	
In <sub>x</sub> Ga <sub>1-x</sub> As	5	53	Si: $1 \times 10^{17}$	
In <sub>x</sub> Al <sub>1-x</sub> As	2	52	Si: $1 \times 10^{17}$	
AZ	35 x 75.5	active region + injector		See additional table
Grading 2	49.8	-		See additional table
In <sub>x</sub> Ga <sub>1-x</sub> As	550	53	Si: $5 \times 10^{16}$	
Grading 1	25	-		See additional table
InP	latticematched		$1 \times 10^{17}$	Substrate

**Table A.2:** Overview for C0120 QCLD samples. Slab thickness 6103.3 nm, thickness to AZ start 2834 nm, minimum etch depth through AZ 5478.5 nm

C0120 Grading 4				
Material	Thickness (nm)	x(%)	Doping (cm <sup>-3</sup> )	Description
In <sub>x</sub> Al <sub>1-x</sub> As	0.8	52	Si: $2 \times 10^{17}$	
In <sub>x</sub> Ga <sub>1-x</sub> As	4.2	53	Si: $2 \times 10^{17}$	
In <sub>x</sub> Al <sub>1-x</sub> As	1.6	52	Si: $2 \times 10^{17}$	
In <sub>x</sub> Ga <sub>1-x</sub> As	3.4	53	Si: $2 \times 10^{17}$	
In <sub>x</sub> Al <sub>1-x</sub> As	2.5	52	Si: $2 \times 10^{17}$	
In <sub>x</sub> Ga <sub>1-x</sub> As	2.5	53	Si: $2 \times 10^{17}$	
In <sub>x</sub> Al <sub>1-x</sub> As	3.4	52	Si: $2 \times 10^{17}$	
In <sub>x</sub> Ga <sub>1-x</sub> As	1.6	53	Si: $2 \times 10^{17}$	
In <sub>x</sub> Al <sub>1-x</sub> As	4.2	52	Si: $2 \times 10^{17}$	
In <sub>x</sub> Ga <sub>1-x</sub> As	0.8	53	Si: $2 \times 10^{17}$	

C0120 Grading 3				
Material	Thickness (nm)	x(%)	Doping (cm <sup>-3</sup> )	Description
In <sub>x</sub> Al <sub>1-x</sub> As	0.8	52	Si: $1 \times 10^{17}$	
In <sub>x</sub> Ga <sub>1-x</sub> As	4.2	53	Si: $1 \times 10^{17}$	
In <sub>x</sub> Al <sub>1-x</sub> As	1.6	52	Si: $1 \times 10^{17}$	
In <sub>x</sub> Ga <sub>1-x</sub> As	3.4	53	Si: $1 \times 10^{17}$	
In <sub>x</sub> Al <sub>1-x</sub> As	2.5	52	Si: $1 \times 10^{17}$	
In <sub>x</sub> Ga <sub>1-x</sub> As	2.5	53	Si: $1 \times 10^{17}$	
In <sub>x</sub> Al <sub>1-x</sub> As	3.4	52	Si: $1 \times 10^{17}$	
In <sub>x</sub> Ga <sub>1-x</sub> As	1.6	53	Si: $1 \times 10^{17}$	
In <sub>x</sub> Al <sub>1-x</sub> As	4.2	52	Si: $1 \times 10^{17}$	
In <sub>x</sub> Ga <sub>1-x</sub> As	0.8	53	Si: $1 \times 10^{17}$	

C0120 Grading 2				
Material	Thickness (nm)	x(%)	Doping (cm <sup>-3</sup> )	Description
In <sub>x</sub> Ga <sub>1-x</sub> As	4.8	53		
In <sub>x</sub> Al <sub>1-x</sub> As	2.6	52		
In <sub>x</sub> Ga <sub>1-x</sub> As	4.3	53		
In <sub>x</sub> Al <sub>1-x</sub> As	2.6	52		
In <sub>x</sub> Ga <sub>1-x</sub> As	3.7	53		
In <sub>x</sub> Al <sub>1-x</sub> As	1.8	52		
In <sub>x</sub> Ga <sub>1-x</sub> As	3.5	53		
In <sub>x</sub> Al <sub>1-x</sub> As	1.9	52		
In <sub>x</sub> Ga <sub>1-x</sub> As	3.4	53		
In <sub>x</sub> Al <sub>1-x</sub> As	2	52		
In <sub>x</sub> Ga <sub>1-x</sub> As	3.2	53		
In <sub>x</sub> Al <sub>1-x</sub> As	2.2	52		
In <sub>x</sub> Ga <sub>1-x</sub> As	4.3	53	Si: $5 \times 10^{17}$	
In <sub>x</sub> Al <sub>1-x</sub> As	2.6	52	Si: $5 \times 10^{17}$	
In <sub>x</sub> Ga <sub>1-x</sub> As	4.3	53	Si: $5 \times 10^{17}$	
In <sub>x</sub> Al <sub>1-x</sub> As	2.6	52	Si: $5 \times 10^{17}$	

C0120 Grading 1				
Material	Thickness (nm)	x(%)	Doping (cm <sup>-3</sup> )	Description
In <sub>x</sub> Al <sub>1-x</sub> As	0.5	52		
In <sub>x</sub> Ga <sub>1-x</sub> As	4.5	53		
In <sub>x</sub> Al <sub>1-x</sub> As	1.0	52		
In <sub>x</sub> Ga <sub>1-x</sub> As	4.0	53		
In <sub>x</sub> Al <sub>1-x</sub> As	1.5	52		
In <sub>x</sub> Ga <sub>1-x</sub> As	3.5	53		
In <sub>x</sub> Al <sub>1-x</sub> As	2.0	52		
In <sub>x</sub> Ga <sub>1-x</sub> As	3.0	53	Si: $1 \times 10^{17}$	
In <sub>x</sub> Al <sub>1-x</sub> As	2.5	52	Si: $1 \times 10^{17}$	
In <sub>x</sub> Ga <sub>1-x</sub> As	2.5	53	Si: $1 \times 10^{17}$	

C0120 Active Zone				
Material	Thickness (nm)	x(%)	Doping (cm <sup>-3</sup> )	Description
In <sub>x</sub> Ga <sub>1-x</sub> As	4.8	53		
In <sub>x</sub> Al <sub>1-x</sub> As	2.6	52		
In <sub>x</sub> Ga <sub>1-x</sub> As	4.3	53		
In <sub>x</sub> Al <sub>1-x</sub> As	2.6	52		
In <sub>x</sub> Ga <sub>1-x</sub> As	3.7	53		
In <sub>x</sub> Al <sub>1-x</sub> As	1.8	52		
In <sub>x</sub> Ga <sub>1-x</sub> As	3.5	53		
In <sub>x</sub> Al <sub>1-x</sub> As	1.9	52		
In <sub>x</sub> Ga <sub>1-x</sub> As	3.4	53		
In <sub>x</sub> Al <sub>1-x</sub> As	2.0	52		
In <sub>x</sub> Ga <sub>1-x</sub> As	3.2	53		
In <sub>x</sub> Al <sub>1-x</sub> As	2.2	52		
In <sub>x</sub> Ga <sub>1-x</sub> As	3.0	53	Si: $1.5 \times 10^{17}$	
In <sub>x</sub> Al <sub>1-x</sub> As	2.6	52	Si: $1.5 \times 10^{17}$	
In <sub>x</sub> Ga <sub>1-x</sub> As	2.6	53	Si: $1.5 \times 10^{17}$	
In <sub>x</sub> Al <sub>1-x</sub> As	2.8	52	Si: $1.5 \times 10^{17}$	
In <sub>x</sub> Ga <sub>1-x</sub> As	2.4	53	Si: $1.5 \times 10^{17}$	
In <sub>x</sub> Al <sub>1-x</sub> As	3.1	52		
In <sub>x</sub> Ga <sub>1-x</sub> As	2.2	53		
In <sub>x</sub> Al <sub>1-x</sub> As	2.8	52		
In <sub>x</sub> Ga <sub>1-x</sub> As	2.1	53		
In <sub>x</sub> Al <sub>1-x</sub> As	4.4	52		
In <sub>x</sub> Ga <sub>1-x</sub> As	1.8	53		
In <sub>x</sub> Al <sub>1-x</sub> As	1.7	52		
In <sub>x</sub> Ga <sub>1-x</sub> As	4.6	53		
In <sub>x</sub> Al <sub>1-x</sub> As	2.4	52		

## A.3 K086

Material K086 is the regrowth of K084 which is a  $4.3\mu\text{m}$  design wavelength QCD which is a development design for FPA detectors used for single pixel light coupling tests described in section 5.2.3.

K086 Overview				
Material	Thickness (nm)	x(%)	Doping ( $\text{cm}^{-3}$ )	Description
$\text{In}_x\text{Ga}_{1-x}\text{As}$	50	53	Si: $5 \times 10^{18}$	Top contact layer 2
$\text{In}_x\text{Ga}_{1-x}\text{As}$	600	53	Si: $1 \times 10^{17}$	Top contact layer 1
$\text{In}_x\text{Ga}_{1-x}\text{As}$	4.5	53		Extra barrier
AZ	10 x 105.15	active region		See additional table
InP	latticematched		$1 - 2 \times 10^{17}$	Substrate

**Table A.3:** Growsheet for K086 QCD test samples. Slab thickness: 1706 nm, thickness to AZ 654.5 nm, minimum etch depth 1706 nm

K086 Active Zone				
Material	Thickness (nm)	x(%)	Doping (cm <sup>-3</sup> )	Description
In <sub>x</sub> Ga <sub>1-x</sub> As	4.9	53	Si: 1 × 10 <sup>18</sup>	active well
In <sub>x</sub> Al <sub>1-x</sub> As	7.0	52		
In <sub>x</sub> Ga <sub>1-x</sub> As	1.1	53		
In <sub>x</sub> Al <sub>1-x</sub> As	6.5	52		
In <sub>x</sub> Ga <sub>1-x</sub> As	1.15	53		
In <sub>x</sub> Al <sub>1-x</sub> As	6.5	52		
In <sub>x</sub> Ga <sub>1-x</sub> As	1.2	53		
In <sub>x</sub> Al <sub>1-x</sub> As	6.5	52		
In <sub>x</sub> Ga <sub>1-x</sub> As	1.25	53		
In <sub>x</sub> Al <sub>1-x</sub> As	6.5	52		
In <sub>x</sub> Ga <sub>1-x</sub> As	1.3	53		
In <sub>x</sub> Al <sub>1-x</sub> As	6.5	52		
In <sub>x</sub> Ga <sub>1-x</sub> As	1.35	53		
In <sub>x</sub> Al <sub>1-x</sub> As	6.5	52		
In <sub>x</sub> Ga <sub>1-x</sub> As	1.4	53		
In <sub>x</sub> Al <sub>1-x</sub> As	4.5	52		
In <sub>x</sub> Ga <sub>1-x</sub> As	1.5	53		
In <sub>x</sub> Al <sub>1-x</sub> As	6.5	52		
In <sub>x</sub> Ga <sub>1-x</sub> As	1.6	53		
In <sub>x</sub> Al <sub>1-x</sub> As	6.5	52		
In <sub>x</sub> Ga <sub>1-x</sub> As	1.7	53		
In <sub>x</sub> Al <sub>1-x</sub> As	6.5	52		
In <sub>x</sub> Ga <sub>1-x</sub> As	1.8	53		
In <sub>x</sub> Al <sub>1-x</sub> As	6.5	52		
In <sub>x</sub> Ga <sub>1-x</sub> As	1.9	53		
In <sub>x</sub> Al <sub>1-x</sub> As	4.5	52		

## A.4 C0115

Material C0115 is the first design for QCD performance optimization around 4.3  $\mu\text{m}$  and base sample for wavelength matching for the succeeding samples C0321 to C0342.

C0115 Overview				
Material	Thickness (nm)	x(%)	Doping ( $\text{cm}^{-3}$ )	Description
$\text{In}_x\text{Ga}_{1-x}\text{As}$	800	53	Si: $1.5 \times 10^{18}$	Top contact layer
$\text{In}_x\text{Al}_{1-x}\text{As}$	5	52		Extra barrier
AZ	20 x 70.05	active region		See additional table
$\text{In}_x\text{Ga}_{1-x}\text{As}$	500	53	Si: $1.5 \times 10^{18}$	Bottom contact layer
InP	lattice matched		semi insulating	Substrate

**Table A.4:** Growsheet for C0115 QCD samples. Slab thickness: 2706 nm, thickness to AZ 805 nm, minimum etch depth 2206 nm

C0115 Active Zone				
Material	Thickness (nm)	x(%)	Doping ( $\text{cm}^{-3}$ )	Description
$\text{In}_x\text{Ga}_{1-x}\text{As}$	4.7	53	Si: $8 \times 10^{17}$	active well
$\text{In}_x\text{Al}_{1-x}\text{As}$	6.5	52		
$\text{In}_x\text{Ga}_{1-x}\text{As}$	1.05	53		
$\text{In}_x\text{Al}_{1-x}\text{As}$	6.5	52		
$\text{In}_x\text{Ga}_{1-x}\text{As}$	1.05	53		
$\text{In}_x\text{Al}_{1-x}\text{As}$	6.5	52		
$\text{In}_x\text{Ga}_{1-x}\text{As}$	1.1	53		
$\text{In}_x\text{Al}_{1-x}\text{As}$	6.5	52		
$\text{In}_x\text{Ga}_{1-x}\text{As}$	1.2	53		
$\text{In}_x\text{Al}_{1-x}\text{As}$	4.5	52		
$\text{In}_x\text{Ga}_{1-x}\text{As}$	1.45	53		
$\text{In}_x\text{Al}_{1-x}\text{As}$	4.5	52		
$\text{In}_x\text{Ga}_{1-x}\text{As}$	1.7	53		
$\text{In}_x\text{Al}_{1-x}\text{As}$	4.5	52		
$\text{In}_x\text{Ga}_{1-x}\text{As}$	2.05	53		
$\text{In}_x\text{Al}_{1-x}\text{As}$	4.0	52		
$\text{In}_x\text{Ga}_{1-x}\text{As}$	2.4	53		
$\text{In}_x\text{Al}_{1-x}\text{As}$	4.0	52		
$\text{In}_x\text{Ga}_{1-x}\text{As}$	2.85	53		
$\text{In}_x\text{Al}_{1-x}\text{As}$	3.0	52		

## **A.5 C0119**

Material C0119 (a regrowth of C0117) is a 4.5  $\mu\text{m}$  QCD diagonal transition design for comparison to vertical transition short MIR wavelengths QCDs. Additionally the design has superlattice contacts to test for enhanced carrier injection and extraction from and to the contacts.



C0119 Overview				
Material	Thickness (nm)	x(%)	Doping (cm <sup>-3</sup> )	Description
In <sub>x</sub> Ga <sub>1-x</sub> As	50	53	Si: $5 \times 10^{18}$	Top contact layer
In <sub>x</sub> Ga <sub>1-x</sub> As	750	53	Si: $1 \times 10^{17}$	Top contact layer
In <sub>x</sub> Al <sub>1-x</sub> As	3	52	Si: $5 \times 10^{17}$	Contact SL start
In <sub>x</sub> Ga <sub>1-x</sub> As	8	53	Si: $5 \times 10^{17}$	
In <sub>x</sub> Al <sub>1-x</sub> As	3	52	Si: $5 \times 10^{17}$	
In <sub>x</sub> Ga <sub>1-x</sub> As	7.5	53	Si: $5 \times 10^{17}$	
In <sub>x</sub> Al <sub>1-x</sub> As	3	52	Si: $5 \times 10^{17}$	
In <sub>x</sub> Ga <sub>1-x</sub> As	7	53	Si: $5 \times 10^{17}$	
In <sub>x</sub> Al <sub>1-x</sub> As	3	52	Si: $5 \times 10^{17}$	
In <sub>x</sub> Ga <sub>1-x</sub> As	6.5	53	Si: $5 \times 10^{17}$	
In <sub>x</sub> Al <sub>1-x</sub> As	3	52	Si: $5 \times 10^{17}$	
In <sub>x</sub> Ga <sub>1-x</sub> As	6	53	Si: $5 \times 10^{17}$	
In <sub>x</sub> Al <sub>1-x</sub> As	4.5	52	Si: $5 \times 10^{17}$	
AZ	20 x 70.05	active region		See additional table
In <sub>x</sub> Ga <sub>1-x</sub> As	3	53	Si: $1 \times 10^{17}$	Contact SL start
In <sub>x</sub> Al <sub>1-x</sub> As	2	52	Si: $1 \times 10^{17}$	
In <sub>x</sub> Ga <sub>1-x</sub> As	3	53	Si: $1 \times 10^{17}$	
In <sub>x</sub> Al <sub>1-x</sub> As	2	52	Si: $1 \times 10^{17}$	
In <sub>x</sub> Ga <sub>1-x</sub> As	3.5	53	Si: $1 \times 10^{17}$	
In <sub>x</sub> Al <sub>1-x</sub> As	2	52	Si: $1 \times 10^{17}$	
In <sub>x</sub> Ga <sub>1-x</sub> As	4.0	53	Si: $1 \times 10^{17}$	
In <sub>x</sub> Al <sub>1-x</sub> As	2	52	Si: $1 \times 10^{17}$	
In <sub>x</sub> Ga <sub>1-x</sub> As	4.5	53	Si: $1 \times 10^{17}$	
In <sub>x</sub> Al <sub>1-x</sub> As	2	52	Si: $1 \times 10^{17}$	
In <sub>x</sub> Ga <sub>1-x</sub> As	5	53	Si: $1 \times 10^{17}$	
In <sub>x</sub> Al <sub>1-x</sub> As	2	52	Si: $1 \times 10^{17}$	
In <sub>x</sub> Ga <sub>1-x</sub> As	5.5	53	Si: $1 \times 10^{17}$	
In <sub>x</sub> Al <sub>1-x</sub> As	2	52	Si: $1 \times 10^{17}$	
In <sub>x</sub> Ga <sub>1-x</sub> As	6	53	Si: $1 \times 10^{17}$	
In <sub>x</sub> Al <sub>1-x</sub> As	2	52	Si: $1 \times 10^{17}$	
In <sub>x</sub> Ga <sub>1-x</sub> As	6.5	53	Si: $1 \times 10^{17}$	
In <sub>x</sub> Al <sub>1-x</sub> As	2	52	Si: $1 \times 10^{17}$	
In <sub>x</sub> Ga <sub>1-x</sub> As	7	53	Si: $1 \times 10^{17}$	
In <sub>x</sub> Al <sub>1-x</sub> As	2	52	Si: $1 \times 10^{17}$	
In <sub>x</sub> Ga <sub>1-x</sub> As	7.5	53	Si: $1 \times 10^{17}$	
In <sub>x</sub> Al <sub>1-x</sub> As	2	52	Si: $1 \times 10^{17}$	
In <sub>x</sub> Ga <sub>1-x</sub> As	500	53	Si: $1.5 \times 10^{18}$	Bottom contact layer
InP	lattice matched		semi insulating	Substrate

**Table A.5:** Growsheet for C0119 QCD samples. Slab thickness: 2706 nm, thickness to AZ 805 nm, minimum etch depth 2206 nm

C0119 diagonal transition Active Zone				
Material	Thickness (nm)	x(%)	Doping (cm <sup>-3</sup> )	Description
In <sub>x</sub> Ga <sub>1-x</sub> As	3.9	53	Si: 1.5 × 10 <sup>18</sup>	active well
In <sub>x</sub> Al <sub>1-x</sub> As	3.0	52		
In <sub>x</sub> Ga <sub>1-x</sub> As	0.85	53		
In <sub>x</sub> Al <sub>1-x</sub> As	4.8	52		
In <sub>x</sub> Ga <sub>1-x</sub> As	1.1	53		
In <sub>x</sub> Al <sub>1-x</sub> As	4.5	52		
In <sub>x</sub> Ga <sub>1-x</sub> As	1.25	53		
In <sub>x</sub> Al <sub>1-x</sub> As	4.8	52		
In <sub>x</sub> Ga <sub>1-x</sub> As	1.55	53		
In <sub>x</sub> Al <sub>1-x</sub> As	4.5	52		
In <sub>x</sub> Ga <sub>1-x</sub> As	1.8	53		
In <sub>x</sub> Al <sub>1-x</sub> As	4.5	52		
In <sub>x</sub> Ga <sub>1-x</sub> As	2.15	53		
In <sub>x</sub> Al <sub>1-x</sub> As	4.0	52		
In <sub>x</sub> Ga <sub>1-x</sub> As	2.5	53		
In <sub>x</sub> Al <sub>1-x</sub> As	3.0	52		

## A.6 C0321

Material C0321 is the second design for QCD wavelength matching to the CO<sub>2</sub> absorption around 4.3  $\mu\text{m}$ .

C0321 Overview				
Material	Thickness (nm)	x(%)	Doping (cm <sup>-3</sup> )	Description
In <sub>x</sub> Ga <sub>1-x</sub> As	800	53	Si: $1.5 \times 10^{18}$	Top contact layer
In <sub>x</sub> Al <sub>1-x</sub> As	5	52		Extra barrier
AZ	20 x 65.7	active region		See additional table
In <sub>x</sub> Ga <sub>1-x</sub> As	500	53	Si: $1.5 \times 10^{18}$	Bottom contact layer
InP	lattice matched		semi insulating	Substrate

**Table A.6:** Growsheet for C0321 QCD samples. Slab thickness: 2619 nm, thickness to AZ 805 nm, minimum etch depth 2119 nm

C0321 Active Zone				
Material	Thickness (nm)	x(%)	Doping (cm <sup>-3</sup> )	Description
In <sub>x</sub> Ga <sub>1-x</sub> As	4.45	53	Si: $8 \times 10^{17}$	active well
In <sub>x</sub> Al <sub>1-x</sub> As	5.5	52		
In <sub>x</sub> Ga <sub>1-x</sub> As	1.0	53		
In <sub>x</sub> Al <sub>1-x</sub> As	5.5	52		
In <sub>x</sub> Ga <sub>1-x</sub> As	1.0	53		
In <sub>x</sub> Al <sub>1-x</sub> As	5.5	52		
In <sub>x</sub> Ga <sub>1-x</sub> As	1.1	53		
In <sub>x</sub> Al <sub>1-x</sub> As	5.5	52		
In <sub>x</sub> Ga <sub>1-x</sub> As	1.2	53		
In <sub>x</sub> Al <sub>1-x</sub> As	4.5	52		
In <sub>x</sub> Ga <sub>1-x</sub> As	1.45	53		
In <sub>x</sub> Al <sub>1-x</sub> As	4.5	52		
In <sub>x</sub> Ga <sub>1-x</sub> As	1.7	53		
In <sub>x</sub> Al <sub>1-x</sub> As	4.5	52		
In <sub>x</sub> Ga <sub>1-x</sub> As	2.05	53		
In <sub>x</sub> Al <sub>1-x</sub> As	4.0	52		
In <sub>x</sub> Ga <sub>1-x</sub> As	2.4	53		
In <sub>x</sub> Al <sub>1-x</sub> As	4.0	52		
In <sub>x</sub> Ga <sub>1-x</sub> As	2.85	53		
In <sub>x</sub> Al <sub>1-x</sub> As	3.0	52		

## A.7 C0323/C0342

Material C0342 (a regrowth of C0323) is the final design with bottom and top contact layer used for the [QCD FPA](#) demonstrator for CO<sub>2</sub> absorption sensing and imaging described in section 5.2.5.

C0342 Overview				
Material	Thickness (nm)	x(%)	Doping (cm <sup>-3</sup> )	Description
In <sub>x</sub> Ga <sub>1-x</sub> As	800	53	Si: $1.5 \times 10^{18}$	Top contact layer
In <sub>x</sub> Al <sub>1-x</sub> As	5	52		Extra barrier
<a href="#">AZ</a>	20 x 68.2	active region		See additional table
In <sub>x</sub> Ga <sub>1-x</sub> As	500	53	Si: $1.5 \times 10^{18}$	Bottom contact layer
InP	lattice matched		semi insulating	Substrate

**Table A.7:** Growsheet for C0323/C0342 [QCD](#) samples. Slab thickness: 2669 nm, thickness to [AZ](#) 805 nm, minimum etch depth 2168 nm

C0342 Active Zone				
Material	Thickness (nm)	x(%)	Doping (cm <sup>-3</sup> )	Description
In <sub>x</sub> Ga <sub>1-x</sub> As	4.3	53	Si: $8 \times 10^{17}$	active well
In <sub>x</sub> Al <sub>1-x</sub> As	6.5	52		
In <sub>x</sub> Ga <sub>1-x</sub> As	0.85	53		
In <sub>x</sub> Al <sub>1-x</sub> As	6.5	52		
In <sub>x</sub> Ga <sub>1-x</sub> As	0.9	53		
In <sub>x</sub> Al <sub>1-x</sub> As	6.5	52		
In <sub>x</sub> Ga <sub>1-x</sub> As	1.0	53		
In <sub>x</sub> Al <sub>1-x</sub> As	5.5	52		
In <sub>x</sub> Ga <sub>1-x</sub> As	1.2	53		
In <sub>x</sub> Al <sub>1-x</sub> As	4.5	52		
In <sub>x</sub> Ga <sub>1-x</sub> As	1.45	53		
In <sub>x</sub> Al <sub>1-x</sub> As	4.5	52		
In <sub>x</sub> Ga <sub>1-x</sub> As	1.7	53		
In <sub>x</sub> Al <sub>1-x</sub> As	4.5	52		
In <sub>x</sub> Ga <sub>1-x</sub> As	2.05	53		
In <sub>x</sub> Al <sub>1-x</sub> As	4.0	52		
In <sub>x</sub> Ga <sub>1-x</sub> As	2.4	53		
In <sub>x</sub> Al <sub>1-x</sub> As	4.0	52		
In <sub>x</sub> Ga <sub>1-x</sub> As	2.85	53		
In <sub>x</sub> Al <sub>1-x</sub> As	3.0	52		

## DEVICES

This part of the Appendix lists the used devices for cleanroom processing of the samples and the devices used for measurements.

### **B.1 Cleanroom devices**

- Oxford Instruments PECVD
- Oxford Instruments ICP RIE
- Dektak profilometer
- Süss Microtec MJB4 mask aligner
- Heidelberg Instruments DWL66fs
- Reith e-line
- Von Ardenne Sputter

### **B.2 Measurement devices**

- Stanford Research Preamplifier SR570 [TIA](#)
- Bruker Equinox 55 [FTIR](#)
- Bruker Vertex70v FTIR [FTIR](#)
- Keithley 2636A Sourcemeter

- EG&G Princeton Applied Research Lock-in Amplifier 5210
- EG&G Instruments DSP Lock-in Amplifier 7265
- Ophir power meter
- HMS Light Beam Chopper 220
- HP8114A Pulse generator
- Cryo Con 23B temperature controller

## BIBLIOGRAPHY

- [1] H. G. J. Kayser. *Handbuch der Spectroscopie*. Leipzig, S. Hirzel (1901) – cited on page 1.
- [2] E. S. Barr. *Historical survey of the early development of the infrared spectral region*. American Journal of Physics 28 (1): 42–54 (1960). doi: [10.1119/1.1934975](https://doi.org/10.1119/1.1934975) – cited on page 1.
- [3] W. Herschel. *Experiments on the refrangibility of the invisible rays of the sun*. Philosophical Transactions of the Royal Society of London 90: 284–292 (1800) – cited on page 1.
- [4] S. P. Langley. *The bolometer*. American Metrological Society 22 (1881) – cited on page 3.
- [5] K. W. Busch and M. A. Busch. *Multielement Detection Systems for Spectrochemical Analysis (Chemical Analysis: A Series of Monographs on Analytical Chemistry and Its Applications)*. Wiley-Interscience (1990) – cited on page 3.
- [6] M. J. E. Golay. *Theoretical consideration in heat and infrared detection, with particular reference to the pneumatic detector*. Review of Scientific Instruments 18 (5): 347–356 (1947). doi: [10.1063/1.1740948](https://doi.org/10.1063/1.1740948) – cited on page 3.
- [7] A. Rogalski, P. Martyniuk and M. Kopytko. *Challenges of small-pixel infrared detectors: a review*. Reports on Progress in Physics 79 (4): 046501 (2016). doi: [10.1088/0034-4885/79/4/046501](https://doi.org/10.1088/0034-4885/79/4/046501) – cited on page 3.
- [8] K. J. Tielrooij, L. Piatkowski, M. Massicotte, A. Woessner, Q. Ma, Y. Lee, K. S. Myhro, C. N. Lau, P. Jarillo-Herrero, N. F. van Hulst and F. H. L. Koppens. *Generation of photovoltage in graphene on a femtosecond timescale through efficient carrier heating*. Nature Nanotechnology 10 (5): 437–443 (2015). doi: [10.1038/nnano.2015.54](https://doi.org/10.1038/nnano.2015.54) – cited on page 4.
- [9] S. Cherednichenko, P. Khosropanah, E. Kollberg, M. Kroug and H. Merkel. *Terahertz superconducting hot-electron bolometer mixers*. Physica C: Su-

- perconductivity 372376, Part 1: 407 – 415 (2002). doi: [10.1016/S0921-4534\(02\)00711-6](https://doi.org/10.1016/S0921-4534(02)00711-6) – cited on page 4.
- [10] W. Smith. *Effect of light on selenium during the passage of an electric current*. Nature 7: 303–303 (1873) – cited on page 4.
- [11] A. Rogalski. *Infrared Detectors*. CRC Press (2011) – cited on page 4.
- [12] T. W. Case. *Notes on the change of resistance of certain substances in light*. Physical Review 9: 305–310 (1917). doi: [10.1103/PhysRev.9.305](https://doi.org/10.1103/PhysRev.9.305) – cited on page 4.
- [13] J. Caniou. *Passive Infrared Detection: Theory and Applications*. Springer (2010) – cited on page 4.
- [14] J. B. Varesi, R. E. Bornfreund, A. C. Childs, W. A. Radford, K. D. Maranowski, J. M. Peterson, S. M. Johnson, L. M. Giegerich, T. J. Lyon and J. E. Jensen. *Fabrication of high-performance large-format MWIR focal plane arrays from MBE-grown HgCdTe on 4" silicon substrates*. Journal of Electronic Materials 30 (6): 566–573 (2001). doi: [10.1007/BF02665836](https://doi.org/10.1007/BF02665836) – cited on pages 4 and 98.
- [15] M. F. Vilela, K. R. Olsson, E. M. Norton, J. M. Peterson, K. Rybnicek, D. R. Rhiger, C. W. Fulk, J. W. Bangs, D. D. Lofgreen and S. M. Johnson. *High-performance M/LWIR dual-band HgCdTe/Si focal-plane arrays*. Journal of Electronic Materials 42 (11): 3231–3238 (2013). doi: [10.1007/s11664-013-2798-2](https://doi.org/10.1007/s11664-013-2798-2) – cited on page 4.
- [16] S. Adachi. *Indium Antimonide (InSb)*, 268–278. Springer US, Boston, MA (1999). doi: [10.1007/978-1-4615-5247-5\\_27](https://doi.org/10.1007/978-1-4615-5247-5_27) – cited on page 4.
- [17] M. Levinshtein, S. Rumyantsev and M. Shur, editors. *Handbook Series on Semiconductor Parameters - Volume 1: Si, Ge, C (Diamond), GaAs, GaP, GaSb, InAs, InP, InSb*. World Scientific Publishing Company (1996) – cited on pages 4, 19, 42, and 99.
- [18] E. Michel, J. Xu, J. D. Kim, I. Ferguson and M. Razeghi. *InSb infrared photodetectors on si substrates grown by molecular beam epitaxy*. IEEE Photonics Technology Letters 8 (5): 673–675 (1996). doi: [10.1109/68.491591](https://doi.org/10.1109/68.491591) – cited on page 4.



- 
- [19] L. Shkedy, T. Markovitz, Z. Calahorra, I. Hirsh and I. Shtrichman. *Megapixel digital InSb detector for midwave infrared imaging*. Optical Engineering 50 (6): 061008–061008–8 (2011). doi: [10.1117/1.3572163](https://doi.org/10.1117/1.3572163) – cited on page 4.
- [20] T. P. Pearsall and R. W. Hopson. *Growth and characterization of lattice-matched epitaxial films of  $Ga_xIn_{1-x}As/InP$  by liquid-phase epitaxy*. Journal of Electronic Materials 7 (1): 133–146 (1978). doi: [10.1007/BF02656025](https://doi.org/10.1007/BF02656025) – cited on page 5.
- [21] R. Tsu and L. Esaki. *Tunneling in a finite superlattice*. Applied Physics Letters 22 (11): 562–564 (1973). doi: [10.1063/1.1654509](https://doi.org/10.1063/1.1654509) – cited on page 5.
- [22] R. F. Kazarinov and R. A. Suris. *Possibility of the amplification of electromagnetic waves in a semiconductor with a superlattice*. Fiz Tech Poluprovodn 5 (4): 707 (1971) – cited on page 5.
- [23] L. L. Chang, L. Esaki, W. E. Howard and R. Ludeke. *The growth of a GaAs-GaAlAs superlattice*. Journal of Vacuum Science & Technology 10 (1): 11–16 (1973). doi: [10.1116/1.1317919](https://doi.org/10.1116/1.1317919) – cited on page 5.
- [24] L. L. Chang, L. Esaki and R. Tsu. *Resonant tunneling in semiconductor double barriers*. Applied Physics Letters 24 (12): 593–595 (1974). doi: [10.1063/1.1655067](https://doi.org/10.1063/1.1655067) – cited on page 5.
- [25] J. J. Coleman. *Metal-metal chemical vapor deposition for optoelectronic devices*. Proceedings of the IEEE 85 (11) (1997) – cited on page 5.
- [26] D. L. Smith and C. Mailhot. *Proposal for strained type II superlattice infrared detectors*. Journal of Applied Physics 62 (6): 2545–2548 (1987). doi: [10.1063/1.339468](https://doi.org/10.1063/1.339468) – cited on pages 5 and 99.
- [27] C. Mailhot and D. L. Smith. *Long wavelength infrared detectors based on strained  $InAsGa_{1-x}In_xSb$  type II superlattices*. Journal of Vacuum Science & Technology A 7 (2): 445–449 (1989). doi: [10.1116/1.576201](https://doi.org/10.1116/1.576201) – cited on pages 5 and 99.
- [28] Y. Wei, A. Gin, M. Razeghi and T. J. Brown. *Type II InAs/GaSb superlattice photovoltaic detectors with cutoff wavelength approaching  $32\ \mu m$* . Applied Physics Letters 81 (19): 3675–3677 (2002). doi: [10.1063/1.1520699](https://doi.org/10.1063/1.1520699) – cited on page 5.

- [29] S. Maimon and G. W. Wicks. *nBn detector, an infrared detector with reduced dark current and higher operating temperature*. Applied Physics Letters 89 (15): 151109 (2006). doi: [10.1063/1.2360235](https://doi.org/10.1063/1.2360235) – cited on page 5.
- [30] C. Canedy, E. Aifer, J. Warner, I. Vurgaftman, E. Jackson, J. Tischler, S. Powell, K. Olver, J. Meyer and W. Tennant. *Controlling dark current in type II superlattice photodiodes*. Infrared Physics & Technology 52 (6): 326 – 334 (2009). doi: [10.1016/j.infrared.2009.09.004](https://doi.org/10.1016/j.infrared.2009.09.004). Proceedings of the International Conference on Quantum Structure Infrared Photodetectors (QSIP) 2009 – cited on page 5.
- [31] S. A. Pour, E. K. Huang, G. Chen, A. Haddadi, B.-M. Nguyen and M. Razeghi. *High operating temperature midwave infrared photodiodes and focal plane arrays based on type II InAs/GaSb superlattices*. Applied Physics Letters 98 (14): 143501 (2011). doi: [10.1063/1.3573867](https://doi.org/10.1063/1.3573867) – cited on page 5.
- [32] P. Manurkar, S. Ramezani-Darvish, B. M. Nguyen, M. Razeghi and J. Hubbs. *High performance long wavelength infrared mega-pixel focal plane array based on type II superlattices*. Applied Physics Letters 97 (19): 193505 (2010). doi: [10.1063/1.3514244](https://doi.org/10.1063/1.3514244) – cited on pages 5 and 99.
- [33] B. F. Levine, K. K. Choi, C. G. Bethea, J. Walker and R. J. Malik. *New 10  $\mu$ m infrared detector using intersubband absorption in resonant tunneling GaAlAs superlattices*. Applied Physics Letters 50 (16): 1092–1094 (1987). doi: [10.1063/1.97928](https://doi.org/10.1063/1.97928) – cited on page 5.
- [34] S. Kalchmair. *Photonic Crystal Intersubband Photodetectors*. Ph.D. thesis, TU Wien (2012) – cited on pages 6 and 93.
- [35] S. Kalchmair. *Detectivity enhancement in quantum well infrared photodetectors utilizing a photonic crystal slab resonator*. Optics Express 20, No. 5: 5623 (2012). doi: [10.1364/OE.20.005622](https://doi.org/10.1364/OE.20.005622) – cited on page 6.
- [36] S. Schartner, S. Kalchmair, A. M. Andrews, P. Klang, W. Schrenk and G. Strasser. *Post-fabrication fine-tuning of photonic crystal quantum well infrared photodetectors*. Applied Physics Letters 94 (23): 231117 (2009). doi: [10.1063/1.3152769](https://doi.org/10.1063/1.3152769) – cited on page 6.
- [37] R. Gansch. *Tuning of Resonances in Photonic Crystal Slabs*. Master’s thesis, TU Wien (2010) – cited on page 6.

- 
- [38] A. Harrer. *Resonance Tuning of Photonic Crystal Intersubband Detectors*. Master's thesis, TU Wien (2013) – cited on page 6.
- [39] R. Gansch, S. Kalchmair, H. Detz, A. M. Andrews, P. Klang, W. Schrenk and G. Strasser. *Higher order modes in photonic crystal slabs*. Optics Express 19 (17): 15990–15995 (2011). doi: [10.1364/OE.19.015990](https://doi.org/10.1364/OE.19.015990) – cited on page 6.
- [40] R. Gansch. *Photonic crystals as resonant cavities for photodetectors*. Ph.D. thesis, TU Wien (2014) – cited on pages 6 and 93.
- [41] P. Rauter, G. Mussler, D. Grtzmacher and T. Fromherz. *Tensile strained SiGe quantum well infrared photodetectors based on a light-hole ground state*. Applied Physics Letters 98 (21): 211106 (2011). doi: [10.1063/1.3593134](https://doi.org/10.1063/1.3593134) – cited on page 6.
- [42] H. Schneider, P. Koidl, F. Fuchs, B. Dischler, K. Schwarz and J. D. Ralston. *Photovoltaic intersubband detectors for 3-5  $\mu\text{m}$  using GaAlAs quantum wells sandwiched between AlAs tunnel barriers*. Semiconductor Science and Technology 6 Nr. 12C (1991). doi: [10.1088/0268-1242/6/12C/024](https://doi.org/10.1088/0268-1242/6/12C/024) – cited on pages 6 and 31.
- [43] D. Hofstetter, M. Beck and J. Faist. *Quantum-cascade-laser structures as photodetectors*. Applied Physics Letters 81 (15): 2683–2685 (2002). doi: [10.1063/1.1512954](https://doi.org/10.1063/1.1512954) – cited on pages 6, 31, and 119.
- [44] M. Graf. *Design and characterization of far- and mid-infrared quantum cascade detectors*. Ph.D. thesis, Université de Neuchâtel (2006) – cited on page 6.
- [45] F. Giorgetta. *Design, fabrication, and testing of intersubband infrared photodetectors operating at wavelengths between 2  $\mu\text{m}$  and 17  $\mu\text{m}$* . Ph.D. thesis, Université de Neuchâtel (2007) – cited on page 6.
- [46] A. Delga. *Du phénomène quantique au dispositif macroscopique, transport électronique dans les détecteurs inter-sousbandes*. Ph.D. thesis, Université Paris Diderot (2012) – cited on page 6.
- [47] L. Gendron, M. Carras, A. Huynh, V. Ortiz, C. Koeniguer and V. Berger. *Quantum cascade photodetector*. Applied Physics Letters 85 (14): 2824–2826 (2004). doi: [10.1063/1.1781731](https://doi.org/10.1063/1.1781731) – cited on pages 6 and 40.
- [48] B. Schwarz. *Monolithic integration of mid-infrared photonics*. Ph.D. thesis, TU Wien (2015) – cited on pages 6, 44, 79, and 116.

- [49] S. Gunapala, S. Bandara, J. K. Liu, J. Mumolo, D. Ting, C. J. Hill, J. Nguyen, B. Simolon, J. Woolaway, S. Wang, W. Li, P. LeVan and M. Tidrow. *Demonstration of megapixel dual-band QWIP focal plane array*. IEEE Journal of Quantum Electronics 46 (2): 285–293 (2010). doi: [10.1109/JQE.2009.2024550](https://doi.org/10.1109/JQE.2009.2024550) – cited on page 6.
- [50] K. W. Berryman, S. A. Lyon and M. Segev. *Mid-infrared photoconductivity in inas quantum dots*. Applied Physics Letters 70 (14): 1861–1863 (1997). doi: [10.1063/1.118714](https://doi.org/10.1063/1.118714) – cited on page 6.
- [51] S. D. Gunapala, S. V. Bandara, C. J. Hill, D. Z. Ting, J. K. Liu, S. B. Rafol, E. R. Blazejewski, J. M. Mumolo, S. A. Keo, S. Krishna, Y. C. Chang and C. A. Shott. *640 x 512 pixels long-wavelength infrared (LWIR) quantum-dot infrared photodetector (QDIP) imaging focal plane array*. IEEE Journal of Quantum Electronics 43 (3): 230–237 (2007). doi: [10.1109/JQE.2006.889645](https://doi.org/10.1109/JQE.2006.889645) – cited on page 6.
- [52] A. V. Barve and S. Krishna. *Photovoltaic quantum dot quantum cascade infrared photodetector*. Applied Physics Letters 100 (2): 021105 (2012). doi: [10.1063/1.3675905](https://doi.org/10.1063/1.3675905) – cited on page 7.
- [53] A. Rogalski. *History of infrared detectors*. Opto-Electronics Review 20 (3): 279–308 (2012). doi: [10.2478/s11772-012-0037-7](https://doi.org/10.2478/s11772-012-0037-7) – cited on pages 7 and 99.
- [54] R. Braunstein. *Radiative transitions in semiconductors*. Physical Review 99 (6): 1892–1893 (1955). doi: [10.1103/physrev.99.1892](https://doi.org/10.1103/physrev.99.1892) – cited on page 7.
- [55] R. S. Eng, J. F. Butler and K. J. Linden. *Tunable diode laser spectroscopy: An invited review*. Optical Engineering 19 (6): 196945–196945– (1980). doi: [10.1117/12.7972642](https://doi.org/10.1117/12.7972642) – cited on page 7.
- [56] M. Gehrtz, A. T. Young, H. S. Johnston and W. Lenth. *High-frequency-modulation spectroscopy with a lead-salt diode laser*. Optics Letters 11 (3): 132–134 (1986). doi: [10.1364/OL.11.000132](https://doi.org/10.1364/OL.11.000132) – cited on page 7.
- [57] M. Grabherr, M. Miller, R. Jager, R. Michalzik, U. Martin, H. J. Unold and K. J. Ebeling. *High-power vcsels: single devices and densely packed 2-d-arrays*. IEEE Journal of Selected Topics in Quantum Electronics 5 (3): 495–502 (1999). doi: [10.1109/2944.788411](https://doi.org/10.1109/2944.788411) – cited on page 7.

- 
- [58] D. Sanchez, L. Cerutti and E. Tournié. *Single-mode monolithic GaSb vertical-cavity surface-emitting laser*. Optics Express 20 (14): 15540–15546 (2012). doi: [10.1364/OE.20.015540](https://doi.org/10.1364/OE.20.015540) – cited on page 7.
- [59] C. H. Lin, R. Q. Yang, D. Zhang, S. J. Murry, S. S. Pei, A. A. Allerman and S. R. Kurtz. *Type II interband quantum cascade laser at 3.8  $\mu\text{m}$* . Electronics Letters 33 (7): 598–599 (1997). doi: [10.1049/el:19970421](https://doi.org/10.1049/el:19970421) – cited on page 7.
- [60] R. Q. Yang, J. L. Bradshaw, J. D. Bruno, J. T. Pham and D. E. Wortman. *Mid-infrared type II interband cascade lasers*. IEEE Journal of Quantum Electronics 38 (6): 559–568 (2002). doi: [10.1109/JQE.2002.1005406](https://doi.org/10.1109/JQE.2002.1005406) – cited on page 8.
- [61] W. W. Bewley, C. L. Canedy, C. Kim, M. Kim, C. D. Merritt, J. Abell, I. Vurgaftman and J. R. Meyer. *Continuous-wave interband cascade lasers operating above room temperature at  $\lambda = 4.7 - 5.6 \mu\text{m}$* . Optics Express 20 (3): 3235–3240 (2012). doi: [10.1364/OE.20.003235](https://doi.org/10.1364/OE.20.003235) – cited on page 8.
- [62] C. Borgentun, C. Frez, R. M. Briggs, M. Fradet and S. Forouhar. *Single-mode high-power interband cascade lasers for mid-infrared absorption spectroscopy*. Optics Express 23 (3): 2446–2450 (2015). doi: [10.1364/OE.23.002446](https://doi.org/10.1364/OE.23.002446) – cited on page 8.
- [63] M. von Edlinger, R. Weih, J. Scheuermann, L. Nähle, M. Fischer, J. Koeth, M. Kamp and S. Höfling. *Monolithic single mode interband cascade lasers with wide wavelength tunability*. Applied Physics Letters 109 (20): 201109 (2016). doi: [10.1063/1.4968535](https://doi.org/10.1063/1.4968535) – cited on page 8.
- [64] I. Vurgaftman, R. Weih, M. Kamp, J. R. Meyer, C. L. Canedy, C. S. Kim, M. Kim, W. W. Bewley, C. D. Merritt, J. Abell and S. Höfling. *Interband cascade lasers*. Journal of Physics D: Applied Physics 48 (12): 123001 (2015). doi: [10.1088/0022-3727/48/12/123001](https://doi.org/10.1088/0022-3727/48/12/123001) – cited on page 8.
- [65] J. Faist, F. Capasso, D. L. Sivco, C. Sirtori, A. L. Hutchinson and A. Y. Cho. *Quantum Cascade Laser*. Science 264 (5158): 553–556 (1994). doi: [10.1126/science.264.5158.553](https://doi.org/10.1126/science.264.5158.553) – cited on page 8.
- [66] J. Faist, F. Capasso, C. Sirtori, D. L. Sivco, A. L. Hutchinson and A. Y. Cho. *Continuous wave operation of a vertical transition quantum cascade laser above  $T = 80 \text{ K}$* . Applied Physics Letters 67 (21): 3057–3059 (1995). doi: [10.1063/1.114863](https://doi.org/10.1063/1.114863) – cited on pages 8 and 119.

- [67] J. Faist, F. Capasso, C. Sirtori, D. L. Sivco, J. N. Baillargeon, A. L. Hutchinson, S. N. G. Chu and A. Y. Cho. *High power mid-infrared ( $\lambda \approx 5\mu\text{m}$ ) quantum cascade lasers operating above room temperature*. Applied Physics Letters 68 (26): 3680–3682 (1996). doi: [10.1063/1.115741](https://doi.org/10.1063/1.115741) – cited on page 8.
- [68] M. Beck, D. Hofstetter, T. Aellen, J. Faist, U. Oesterle, M. Illegems, E. Gini and H. Melchior. *Continuous wave operation of a mid-infrared semiconductor laser at room temperature*. Science 295 (5553): 301–305 (2002). doi: [10.1126/science.1066408](https://doi.org/10.1126/science.1066408) – cited on page 8.
- [69] J. Faist, C. Gmachl, F. Capasso, C. Sirtori, D. L. Sivco, J. N. Baillargeon and A. Y. Cho. *Distributed feedback quantum cascade lasers*. Applied Physics Letters 70 (20): 2670–2672 (1997). doi: [10.1063/1.119208](https://doi.org/10.1063/1.119208) – cited on pages 8 and 60.
- [70] E. Mujagić, C. Schwarzer, Y. Yao, J. Chen, C. Gmachl and G. Strasser. *Two-dimensional broadband distributed-feedback quantum cascade laser arrays*. Applied Physics Letters 98 (14): 141101 (2011). doi: [10.1063/1.3574555](https://doi.org/10.1063/1.3574555) – cited on pages 8 and 9.
- [71] Y. Bai, N. Bandyopadhyay, S. Tsao, S. Slivken and M. Razeghi. *Room temperature quantum cascade lasers with 27 % wall plug efficiency*. Applied Physics Letters 98 (18): 181102 (2011). doi: [10.1063/1.3586773](https://doi.org/10.1063/1.3586773) – cited on page 8.
- [72] M. Troccoli, L. Diehl, D. P. Bour, S. W. Corzine, N. Yu, C. Y. Wang, M. A. Belkin, G. Hofler, R. Lewicki, G. Wysocki, F. K. Tittel and F. Capasso. *High-performance quantum cascade lasers grown by metal-organic vapor phase epitaxy and their applications to trace gas sensing*. Journal of Lightwave Technology 26 (21): 3534–3555 (2008). doi: [10.1109/JLT.2008.925056](https://doi.org/10.1109/JLT.2008.925056) – cited on page 8.
- [73] A. Hugi, G. V. ans S. Blaser, H. Liu and J. Faist. *Mid-infrared frequency comb based on a quantum cascade laser*. Nature 492: 229–233 (2012). doi: [10.1038/nature11620](https://doi.org/10.1038/nature11620) – cited on pages 8 and 11.
- [74] J. Devenson, D. Barate, O. Cathabard, R. Teissier and A. N. Baranov. *Very short wavelength ( $\lambda = 3.1 - 3.3\mu\text{m}$ ) quantum cascade lasers*. Applied Physics Letters 89 (19): 191115 (2006). doi: [10.1063/1.2387473](https://doi.org/10.1063/1.2387473) – cited on page 8.
- [75] R. Köhler, A. Tredicucci, F. Beltram, H. E. Beere, E. H. Linfield, A. G. Davies, D. A. Ritchie, R. C. Iotti and F. Rossi. *Terahertz*



- semiconductor-heterostructure laser*. Nature 417 (6885): 156–159 (2002). doi: [10.1038/417156a](https://doi.org/10.1038/417156a) – cited on page 8.
- [76] M. Brandstetter, C. Deutsch, M. Krall, H. Detz, D. C. MacFarland, T. Zederbauer, A. M. Andrews, W. Schrenk, G. Strasser and K. Unterrainer. *High power terahertz quantum cascade lasers with symmetric wafer bonded active regions*. Applied Physics Letters 103 (17): 171113 (2013). doi: [10.1063/1.4826943](https://doi.org/10.1063/1.4826943) – cited on pages 9 and 139.
- [77] C. Gmachl, D. L. Sivco, R. Colombelli, F. Capasso and A. Y. Cho. *Ultra-broadband semiconductor laser*. Nature 415 (6874): 883–887 (2002). doi: [10.1038/415883a](https://doi.org/10.1038/415883a) – cited on page 9.
- [78] Y. Yao, W. O. Charles, T. Tsai, J. Chen, G. Wysocki and C. F. Gmachl. *Broadband quantum cascade laser gain medium based on a continuum-to-bound active region design*. Applied Physics Letters 96 (21): 211106 (2010). doi: [10.1063/1.3431577](https://doi.org/10.1063/1.3431577) – cited on page 9.
- [79] A. Hugi, R. Terazzi, Y. Bonetti, A. Wittmann, M. Fischer, M. Beck, J. Faist and E. Gini. *External cavity quantum cascade laser tunable from 7.6 to 11.4 $\mu$ m*. Applied Physics Letters 95 (6): 061103 (2009). doi: [10.1063/1.3193539](https://doi.org/10.1063/1.3193539) – cited on page 9.
- [80] A. Hugi, R. Maulini and J. Faist. *External cavity quantum cascade laser*. Semiconductor Science and Technology 25 (8): 083001 (2010). doi: [10.1088/0268-1242/25/8/083001](https://doi.org/10.1088/0268-1242/25/8/083001) – cited on page 9.
- [81] M. Brandstetter, A. Genner, C. Schwarzer, E. Mujagić, G. Strasser and B. Lendl. *Time-resolved spectral characterization of ring cavity surface emitting and ridge-type distributed feedback quantum cascade lasers by step-scan ft-ir spectroscopy*. Optics Express 22 (3): 2656–2664 (2014). doi: [10.1364/OE.22.002656](https://doi.org/10.1364/OE.22.002656) – cited on pages 9 and 121.
- [82] W. Schrenk, N. Finger, S. Gianordoli, L. Hvozdar, G. Strasser and E. Gornik. *Surface-emitting distributed feedback quantum-cascade lasers*. Applied Physics Letters 77 (14): 2086–2088 (2000). doi: [10.1063/1.1313807](https://doi.org/10.1063/1.1313807) – cited on pages 9 and 60.
- [83] E. Mujagić, S. Scharfner, L. K. Hoffmann, W. Schrenk, M. P. Semtsiv, M. Wienold, W. T. Masselink and G. Strasser. *Grating-coupled surface emitting quantum cascade ring lasers*. Applied Physics Letters 93 (1): 011108 (2008). doi: [10.1063/1.2958910](https://doi.org/10.1063/1.2958910) – cited on page 9.

- [84] R. Paiella, F. Capasso, C. Gmachl, H. Y. Hwang, D. L. Sivco, A. L. Hutchinson, A. Y. Cho and H. C. Liu. *Monolithic active mode locking of quantum cascade lasers*. Applied Physics Letters 77 (2): 169–171 (2000). doi: [10.1063/1.126913](https://doi.org/10.1063/1.126913) – cited on page 9.
- [85] F. Capasso, N. Yu, E. Cubukcu and E. Smythe. *Using plasmonics to shape light beams*. Optics & Photonics News 20 (5): 22–27 (2009). doi: [10.1364/OPN.20.5.000022](https://doi.org/10.1364/OPN.20.5.000022) – cited on page 9.
- [86] N. Yu, R. Blanchard, J. Fan, Q. J. Wang, C. Pflugl, L. Diehl, T. Edamura, S. Furuta, M. Yamanishi, H. Kan and F. Capasso. *Plasmonics for laser beam shaping*. IEEE Transactions on Nanotechnology 9 (1): 11–29 (2010). doi: [10.1109/TNANO.2009.2029099](https://doi.org/10.1109/TNANO.2009.2029099) – cited on pages 9 and 72.
- [87] R. Szedlak, C. Schwarzer, T. Zederbauer, H. Detz, A. M. Andrews, W. Schrenk and G. Strasser. *Grating-based far field modifications of ring quantum cascade lasers*. Optics Express 22 (13): 15829–15836 (2014). doi: [10.1364/OE.22.015829](https://doi.org/10.1364/OE.22.015829) – cited on page 9.
- [88] P. R. Griffiths and J. A. D. Haseth. *Fourier Transform Infrared Spectrometry*. Wiley-Interscience (2007) – cited on page 9.
- [89] A. Schliesser, N. Picque and T. W. Hansch. *Mid-infrared frequency combs*. Nature Photonics 6 (7): 440–449 (2012). doi: [10.1038/nphoton.2012.142](https://doi.org/10.1038/nphoton.2012.142) – cited on page 10.
- [90] G. Wysocki, A. A. Kosterev and F. K. Tittel. *Spectroscopic trace-gas sensor with rapidly scanned wavelengths of a pulsed quantum cascade laser for in situ NO monitoring of industrial exhaust systems*. Applied Physics B 80 (4): 617–625 (2005). doi: [10.1007/s00340-005-1764-y](https://doi.org/10.1007/s00340-005-1764-y) – cited on page 10.
- [91] S. W. Sharpe, J. F. Kelly, J. S. Hartman, C. Gmachl, F. Capasso, D. L. Sivco, J. N. Baillargeon and A. Y. Cho. *High-resolution (Doppler-limited) spectroscopy using quantum-cascade distributed-feedback lasers*. Optics Letters 23 (17): 1396–1398 (1998). doi: [10.1364/OL.23.001396](https://doi.org/10.1364/OL.23.001396) – cited on page 11.
- [92] A. G. Bell. *Upon the production of sound by radiant energy*. Philosophical Magazine 11: 510 (1881) – cited on page 11.
- [93] A. Rosencwaig. *Photoacoustic spectroscopy. new tool for investigation of solids*. Analytical Chemistry 47 (6): 592A–604a (1975). doi: [10.1021/ac60356a015](https://doi.org/10.1021/ac60356a015) – cited on page 11.



- 
- [94] A. A. Kosterev, Y. A. Bakhrkin and F. K. Tittel. *Ultrasensitive gas detection by quartz-enhanced photoacoustic spectroscopy in the fundamental molecular absorption bands region*. Applied Physics B 80 (1): 133–138 (2005). doi: [10.1007/s00340-004-1619-y](https://doi.org/10.1007/s00340-004-1619-y) – cited on page 11.
- [95] P. Patimisco, G. Scamarcio, F. K. Tittel and V. Spagnolo. *Quartz-enhanced photoacoustic spectroscopy: A review*. Sensors 14 (4): 6165 (2014). doi: [10.3390/s140406165](https://doi.org/10.3390/s140406165) – cited on page 11.
- [96] W. Ren, W. Jiang, N. P. Sanchez, P. Patimisco, V. Spagnolo, C. Zah, F. Xie, L. C. Hughes, R. J. Griffin and F. K. Tittel. *Hydrogen peroxide detection with quartz-enhanced photoacoustic spectroscopy using a distributed-feedback quantum cascade laser*. Applied Physics Letters 104 (4): 041117 (2014). doi: [10.1063/1.4863955](https://doi.org/10.1063/1.4863955) – cited on page 11.
- [97] G. Villares, A. Hugi, S. Blaser and J. Faist. *Dual-comb spectroscopy based on quantum-cascade-laser frequency combs*. Nature Communications 5: 5192 (2014). doi: [10.1038/ncomms6192](https://doi.org/10.1038/ncomms6192) – cited on pages 11 and 116.
- [98] B. Schwarz, P. Reininger, H. Detz, T. Zederbauer, A. M. Andrews, S. Kalchmair, W. Schrenk, O. Baumgartner, H. Kosina and G. Strasser. *A bi-functional quantum cascade device for same-frequency lasing and detection*. Applied Physics Letter 101 (19): 191109 (2012). doi: [10.1063/1.4767128](https://doi.org/10.1063/1.4767128) – cited on page 11.
- [99] B. Schwarz, P. Reininger, D. Ristanic, H. Detz, A. M. Andrews, W. Schrenk and G. Strasser. *Monolithically integrated mid-infrared lab-on-a-chip using plasmonics and quantum cascade structures*. Nature Communications 5 (19): 4085 (2014). doi: [10.1038/ncomms5085](https://doi.org/10.1038/ncomms5085) – cited on pages 11, 109, and 116.
- [100] J. Faist. *Quantum Cascade Lasers*. OUP Oxford (2013) – cited on pages 13, 44, and 119.
- [101] S. M. Sze and N. K. Kwok. *Physics of Semiconductor Devices*. John Wiley & Sons (2007) – cited on pages 13 and 17.
- [102] J. Singh. *Electronic and Optoelectronic Properties of Semiconductor Structures*. Cambridge University Press (2003) – cited on pages 13 and 20.
- [103] G. Bastard. *Wave mechanics applied to semiconductor heterostructures*. Monographies de physique. Les Éditions de Physique (1988) – cited on pages 13, 21, 22, and 27.

- [104] A. Andrews, M. Nobile, H. Detz, P. Klang, E. Mujagić, W. Schrenk and G. Strasser. *A new aluminum-free material system for intersubband emitters and detectors*. Journal of Physics: Conference Series 193 (1): 012065 (2009). doi: [10.1088/1742-6596/193/1/012065](https://doi.org/10.1088/1742-6596/193/1/012065) – cited on page 13.
- [105] C. Deutsch, H. Detz, T. Zederbauer, M. Krall, M. Brandstetter, A. M. Andrews, P. Klang, W. Schrenk, G. Strasser and K. Unterrainer. *InGaAs/GaAsSb/InP terahertz quantum cascade lasers*. Journal of Infrared, Millimeter, and Terahertz Waves 34 (5): 374–385 (2013). doi: [10.1007/s10762-013-9991-5](https://doi.org/10.1007/s10762-013-9991-5) – cited on page 13.
- [106] L. Vegard. *Die Konstitution der Mischkristalle und die Raumfüllung der Atome*. Zeitschrift für Physik 5 (1): 17–26 (1921). doi: [10.1007/BF01349680](https://doi.org/10.1007/BF01349680) – cited on page 15.
- [107] J. Faist, F. Capasso, D. L. Sivco, A. L. Hutchinson, S. G. Chu and A. Y. Cho. *Short wavelength ( $\lambda \approx 3.4 \mu\text{m}$ ) quantum cascade laser based on strained compensated ingaas/alinas*. Applied Physics Letters 72 (6): 680–682 (1998). doi: [10.1063/1.120843](https://doi.org/10.1063/1.120843) – cited on page 15.
- [108] C. G. Van de Walle. *Band lineups and deformation potentials in the model-solid theory*. Physical Review B 39: 1871–1883 (1989). doi: [10.1103/PhysRevB.39.1871](https://doi.org/10.1103/PhysRevB.39.1871) – cited on page 15.
- [109] T. Zederbauer. *Mixed Group V Compound Semiconductors for Intersubband Devices*. Ph.D. thesis, TU-Wien (2017) – cited on page 16.
- [110] W. Commons. *Zincblende structure.png*. Online (2012). [https://commons.wikimedia.org/wiki/File:Zincblende\\_structure.png](https://commons.wikimedia.org/wiki/File:Zincblende_structure.png), accessed: 28.09.2016 – cited on page 18.
- [111] J. C. Slater and G. F. Koster. *Simplified LCAO method for the periodic potential problem*. Physical Review 94: 1498–1524 (1954). doi: [10.1103/PhysRev.94.1498](https://doi.org/10.1103/PhysRev.94.1498) – cited on page 18.
- [112] P. Yu and M. Cardona. *Fundamentals of Semiconductors: Physics and Materials Properties*. Number Bd. 3 in Advanced texts in physics. Springer Berlin Heidelberg (2005) – cited on page 19.
- [113] L. Voon and M. Willatzen. *The  $k p$  Method: Electronic Properties of Semiconductors*. Springer Berlin Heidelberg (2009) – cited on page 20.

- 
- [114] R. Paiella. *Intersubband Transitions In Quantum Structures*. McGraw-Hill nanoscience and technology series. McGraw-Hill Education (2010) – cited on page 28.
- [115] H. C. Liu, M. Buchanan and Z. R. Wasilewski. *How good is the polarization selection rule for intersubband transitions?* Applied Physics Letters 72 (14): 1682–1684 (1998). doi: [10.1063/1.121151](https://doi.org/10.1063/1.121151) – cited on pages 30 and 58.
- [116] H. Schneider, C. Schönbein, M. Walther, K. Schwarz, J. Fleissner and P. Koidl. *Photovoltaic quantum well infrared photodetectors: The four-zone scheme*. Applied Physics Letters 71 (2): 246–248 (1997). doi: [10.1063/1.119510](https://doi.org/10.1063/1.119510) – cited on pages 31 and 119.
- [117] F. R. Giorgetta, E. Baumann, R. Thron, M. L. Pellaton, D. Hofstetter, M. Fischer and J. Faist. *Short wavelength ( $4\ \mu\text{m}$ ) quantum cascade detector based on strain compensated InGaAsInAlAs*. Applied Physics Letters 92 (12): 121101 (2008). doi: [10.1063/1.2902301](https://doi.org/10.1063/1.2902301) – cited on page 31.
- [118] A. Buffaz, M. Carras, L. Doyennette, A. Nedelcu, X. Marcadet and V. Berger. *Quantum cascade detectors for very long wave infrared detection*. Applied Physics Letters 96 (17): 172101 (2010). doi: [10.1063/1.3409139](https://doi.org/10.1063/1.3409139) – cited on page 31.
- [119] D. Hofstetter, M. Graf, T. Aellen, J. Faist, L. Hvozdar and S. Blaser. *23GHz operation of a room temperature photovoltaic quantum cascade detector at  $5.35\ \mu\text{m}$* . Applied Physics Letters 89 (6): 061119 (2006). doi: [10.1063/1.2269408](https://doi.org/10.1063/1.2269408) – cited on page 31.
- [120] S. Sakr, P. Crozat, D. Gacemi, Y. Kotsar, A. Pesach, P. Quach, N. Isac, M. Tchernycheva, L. Vivien, G. Bahir, E. Monroy and F. H. Julien. *GaN/Al-GaN waveguide quantum cascade photodetectors at  $\lambda \approx 1.55\ \mu\text{m}$  with enhanced responsivity and  $\sim 40\text{GHz}$  frequency bandwidth*. Applied Physics Letters 102 (1): 011135 (2013). doi: [10.1063/1.4775374](https://doi.org/10.1063/1.4775374) – cited on page 31.
- [121] Y. Zhou, S. Zhai, F. Wang, J. Liu, F. Liu, S. Liu, J. Zhang, N. Zhuo, L. Wang and Z. Wang. *High-speed, room-temperature quantum cascade detectors at  $4.3\ \mu\text{m}$* . AIP Advances 6 (3): 035305 (2016). doi: [10.1063/1.4943675](https://doi.org/10.1063/1.4943675) – cited on page 31.
- [122] D. Hofstetter, F. R. Giorgetta, E. Baumann, Q. Yang, C. Manz and K. Köhler. *Midinfrared quantum cascade detector with a spectrally broad response*. Applied

- Physics Letters 93 (22): 221106 (2008). doi: [10.1063/1.3036897](https://doi.org/10.1063/1.3036897) – cited on pages 31 and 100.
- [123] M. Graf, N. Hoyler, M. Giovannini, J. Faist and D. Hofstetter. *InP-based quantum cascade detectors in the mid-infrared*. Applied Physics Letters 88 (24): 241118 (2006). doi: [10.1063/1.2210088](https://doi.org/10.1063/1.2210088) – cited on page 31.
- [124] P. Reininger, T. Zederbauer, B. Schwarz, H. Detz, D. MacFarland, A. M. Andrews, W. Schrenk and G. Strasser. *InAs/AlAsSb based quantum cascade detector*. Applied Physics Letters 107 (8): 081107 (2015). doi: [10.1063/1.4929501](https://doi.org/10.1063/1.4929501) – cited on page 31.
- [125] A. P. Ravikumar, J. D. Jesus, M. C. Tamargo and C. F. Gmachl. *High performance, room temperature, broadband II-VI quantum cascade detector*. Applied Physics Letters 107 (14): 141105 (2015). doi: [10.1063/1.4932538](https://doi.org/10.1063/1.4932538) – cited on page 31.
- [126] F. Giorgetta, E. Baumann, M. Graf, Q. Yang, C. Manz, K. Kohler, H. Beere, D. Ritchie, E. Linfield, A. Davies, Y. Fedoryshyn, H. Jackel, M. Fischer, J. Faist and D. Hofstetter. *Quantum cascade detectors*. Quantum Electronics, IEEE Journal of 45 (8): 1039–1052 (2009). doi: [10.1109/JQE.2009.2017929](https://doi.org/10.1109/JQE.2009.2017929) – cited on page 34.
- [127] H. Schneider. *Quantum Well Infrared Photodetectors: Physics and Applications*. Springer (2007) – cited on pages 34, 96, 98, and 99.
- [128] F. Giorgetta. *Design, fabrication, and testing of intersubband infrared photodetectors operating at wavelengths between 2  $\mu\text{m}$  and 17  $\mu\text{m}$* . Ph.D. thesis, Université de Neuchâtel (2007) – cited on pages 34, 43, and 98.
- [129] H. C. Liu. *Noise gain and operating temperature of quantum well infrared photodetectors*. Applied Physics Letters 61 (22): 2703–2705 (1992). doi: [10.1063/1.108115](https://doi.org/10.1063/1.108115) – cited on page 39.
- [130] H. Nyquist. *Thermal agitation of electric charge in conductors*. Physical Review 32: 110–113 (1928). doi: [10.1103/PhysRev.32.110](https://doi.org/10.1103/PhysRev.32.110) – cited on page 39.
- [131] A. Delga, L. Doyennette, M. Carras, V. Trinit and P. Bois. *Johnson and shot noises in intersubband detectors*. Applied Physics Letters 102 (16): 163507 (2013). doi: [10.1063/1.4803447](https://doi.org/10.1063/1.4803447) – cited on page 40.

- 
- [132] L. Gendron, C. Koeniguer, V. Berger and X. Marcadet. *High resistance narrow band quantum cascade photodetectors*. Applied Physics Letters 86 (12): 121116 (2005). doi: [10.1063/1.1884257](https://doi.org/10.1063/1.1884257) – cited on page 40.
- [133] T. Ando. *Line width of inter-subband absorption in inversion layers: Scattering from charged ions*. Journal of the Physical Society of Japan 54 (7): 2671–2675 (1985). doi: [10.1143/JPSJ.54.2671](https://doi.org/10.1143/JPSJ.54.2671) – cited on page 41.
- [134] M. Ilegems, G. Weimann and J. Wagner. *Compound Semiconductors 2002*. Institute of Physics Conference Series. Taylor & Francis (2003) – cited on page 41.
- [135] T. Unuma, M. Yoshita, T. Noda, H. Sakaki and H. Akiyama. *Intersubband absorption linewidth in gaas quantum wells due to scattering by interface roughness, phonons, alloy disorder, and impurities*. Journal of Applied Physics 93 (3): 1586–1597 (2003). doi: [10.1063/1.1535733](https://doi.org/10.1063/1.1535733) – cited on page 42.
- [136] W. T. Masselink. *Ionized-impurity scattering of quasi-two-dimensional quantum-confined carriers*. Physical Review Letters 66: 1513–1516 (1991). doi: [10.1103/PhysRevLett.66.1513](https://doi.org/10.1103/PhysRevLett.66.1513) – cited on page 42.
- [137] P. Reininger, B. Schwarz, H. Detz, D. MacFarland, T. Zederbauer, A. M. Andrews, W. Schrenk, O. Baumgartner, H. Kosina and G. Strasser. *Diagonal-transition quantum cascade detector*. Applied Physics Letters 105 (9): 091108 (2014). doi: [10.1063/1.4894767](https://doi.org/10.1063/1.4894767) – cited on pages 44, 45, 100, and 101.
- [138] P. Reininger, B. Schwarz, R. Gansch, H. Detz, D. MacFarland, T. Zederbauer, A. M. Andrews, W. Schrenk and G. Strasser. *Quantum cascade detector utilizing the diagonal-transition scheme for high quality cavities*. Optics Express 23 (5): 6283–6291 (2015). doi: [10.1364/OE.23.006283](https://doi.org/10.1364/OE.23.006283) – cited on pages 46 and 93.
- [139] P. Reininger. *Quantum Cascade Photodetectors: Combining Optical and Electronic Engineering*. Ph.D. thesis, TU Wien (2015) – cited on pages 46 and 93.
- [140] L. S. Rothman, I. E. Gordon, Y. Babikov, A. Barbe, D. C. Benner, P. F. Bernath, M. Birk, L. Bizzocchi, V. Boudon, L. R. Brown, A. Campargue, K. Chance, E. A. Cohen, L. H. Coudert, V. M. Devi, B. J. Drouin, A. Fayt, J.-M. Flaud, R. R. Gamache, J. J. Harrison, J.-M. Hartmann, C. Hill, J. T. Hodges, D. Jacquemart, A. Jolly, J. Lamouroux, R. J. LeRoy, G. Li, D. A. Long, O. Lyulin, C. Mackie, S. T. Massie, S. Mikhailenko, H. S. M"uller,

- O. Naumenko, A. Nikitin, J. Orphal, V. I. Perevalov, A. Perrin, E. R. Polovtseva, C. Richard, M. A. H. Smith, E. Starikova, K. Sung, S. Tashkun, J. Tennyson, G. C. Toon, V. G. Tyuterev and G. Wagner. *The hitran 2012 molecular spectroscopic database*. Journal of Quantitative Spectroscopy and Radiative Transfer 130: 4–50 (2013). doi: [10.1016/j.jqsrt.2013.07.002](https://doi.org/10.1016/j.jqsrt.2013.07.002) – cited on page 48.
- [141] S. Tashkun and V. Perevalov (2012). Private communication: Line positions calculated from empirical energy levels, derived using RITZ approach – cited on page 48.
- [142] S. A. Tashkun and V. I. Perevalov (unknown year). Private communication: Line positions calculated from empirical energy levels, derived using the effective Hamiltonian – cited on page 48.
- [143] S. A. Tashkun and V. I. Perevalov (unknown year). Private communication: Intensities calculated using the effective dipole moment function – cited on page 48.
- [144] A. Harrer, B. Schwarz, S. Schuler, P. Reininger, H. D. A. Wirthmüller, D. C. MacFarland, T. Zederbauer, A. M. Andrews, M. Rothermund, H. Oppermann, W. Schrenk and G. Strasser. *4.3 $\mu$ m quantum cascade detector in pixel configuration*. Optics Express 24 (15): 17041–17049 (2016). doi: [10.1364/OE.24.017041](https://doi.org/10.1364/OE.24.017041) – cited on pages 48, 49, 50, 100, 108, 109, 110, and 111.
- [145] M. B. Esler, D. W. T. Griffith, S. R. Wilson and L. P. Steele. *Precision trace gas analysis by ft-ir spectroscopy. 2. the  $^{13}\text{C}/^{12}\text{C}$  isotope ratio of  $\text{CO}_2$* . Analytical Chemistry 72 (1): 216–221 (2000). doi: [10.1021/ac990563x](https://doi.org/10.1021/ac990563x). PMID: 10655656 – cited on page 48.
- [146] O. Baumgartner, Z. Stanojevic, K. Schnass, M. Karner and H. Kosina. *Vsp—a quantum-electronic simulation framework*. Journal of Computational Electronics 12 (4): 701–721 (2013). doi: [10.1007/s10825-013-0535-y](https://doi.org/10.1007/s10825-013-0535-y) – cited on pages 48 and 104.
- [147] B. Smith. *Fundamentals of Fourier Transform Infrared Spectroscopy*. Taylor & Francis (1995) – cited on page 51.
- [148] D. D. Coon and R. P. G. Karunasiri. *New mode of ir detection using quantum wells*. Applied Physics Letters 45 (6): 649–651 (1984). doi: [10.1063/1.95343](https://doi.org/10.1063/1.95343) – cited on page 58.

- 
- [149] T. Dougakiuchi, K. Fujita, T. Hirohata, A. Ito, M. Hitaka and T. Edamura. *High photoresponse in room temperature quantum cascade detector based on coupled quantum well design*. Applied Physics Letters 109 (26): 261107 (2016). doi: [10.1063/1.4973582](https://doi.org/10.1063/1.4973582) – cited on pages 60 and 109.
- [150] L. Lundqvist, J. Y. Andersson, Z. F. Paska, J. Borglind and D. Haga. *Efficiency of grating coupled AlGaAs/GaAs quantum well infrared detectors*. Applied Physics Letters 63 (24): 3361–3363 (1993). doi: [10.1063/1.110145](https://doi.org/10.1063/1.110145) – cited on pages 60 and 62.
- [151] H. Schneider, T. Maier, J. Fleissner, M. Walther, P. Koidl, G. Weimann, W. Cabanski, M. Finck, P. Menger, W. Rode and J. Ziegler. *Dual-band QWIP focal plane array for the second and third atmospheric windows*. Infrared Physics & Technology 47 (12): 53 – 58 (2005). doi: [10.1016/j.infrared.2005.02.028](https://doi.org/10.1016/j.infrared.2005.02.028) – cited on page 60.
- [152] J. Y. Andersson and L. Lundqvist. *Near-unity quantum efficiency of AlGaAs/-GaAs quantum well infrared detectors using a waveguide with a doubly periodic grating coupler*. Applied Physics Letters 59 (7): 857–859 (1991). doi: [10.1063/1.105259](https://doi.org/10.1063/1.105259) – cited on page 62.
- [153] A. Harrer, B. Schwarz, R. Gansch, P. Reininger, H. Detz, T. Zederbauer, A. M. Andrews, W. Schrenk and G. Strasser. *Plasmonic lens enhanced mid-infrared quantum cascade detector*. Applied Physics Letters 105 (17): 171112 (2014). doi: [10.1063/1.4901043](https://doi.org/10.1063/1.4901043) – cited on pages 62, 85, 86, 88, and 89.
- [154] L. Yin, V. K. Vlasko-Vlasov, J. Pearson, J. M. Hiller, J. Hua, U. Welp, D. E. Brown and C. W. Kimball. *Subwavelength focusing and guiding of surface plasmons*. Nano Letters 5 (7): 1399–1402 (2005). doi: [10.1021/nl050723m](https://doi.org/10.1021/nl050723m). PMID: 16178246 – cited on page 63.
- [155] D. K. Gramotnev and S. I. Bozhevolnyi. *Plasmonics beyond the diffraction limit*. Nature Photonics 4 (2): 83–91 (2010). doi: [10.1038/nphoton.2009.282](https://doi.org/10.1038/nphoton.2009.282) – cited on page 63.
- [156] A. N. Grigorenko, M. Polini and K. S. Novoselov. *Graphene plasmonics*. Nature Photonics 6 (11): 749–758 (2012). doi: [10.1038/nphoton.2012.262](https://doi.org/10.1038/nphoton.2012.262) – cited on page 63.
- [157] P. Bakshi, K. Kempa, A. Scorupsky, C. G. Du, G. Feng, R. Zobl, G. Strasser, C. Rauch, C. Pacher, K. Unterrainer and E. Gornik. *Plasmon-based terahertz*



- emission from quantum well structures*. Applied Physics Letters 75 (12): 1685–1687 (1999). doi: [10.1063/1.124791](https://doi.org/10.1063/1.124791) – cited on page 63.
- [158] M. Holzbauer, P. Klang, H. Detz, A. M. Andrews, G. Strasser, P. Bakshi and E. Gornik. *Resonant intersubband plasmon induced current in InGaAs quantum wells on GaAs*. Applied Physics Letters 104 (12): 122101 (2014). doi: [10.1063/1.4869757](https://doi.org/10.1063/1.4869757) – cited on page 63.
- [159] G. V. Naik, V. M. Shalaev and A. Boltasseva. *Alternative plasmonic materials: Beyond gold and silver*. Advanced Materials 25 (24): 3264–3294 (2013). doi: [10.1002/adma.201205076](https://doi.org/10.1002/adma.201205076) – cited on page 63.
- [160] R. H. Ritchie. *Plasma losses by fast electrons in thin films*. Physical Review 106: 874–881 (1957). doi: [10.1103/PhysRev.106.874](https://doi.org/10.1103/PhysRev.106.874) – cited on page 63.
- [161] M. L. Brongersma and P. G. Kik. *Surface Plasmon Nanophotonics*. Springer Series in Optical Sciences. Springer Netherlands (2007) – cited on page 63.
- [162] W. L. Barnes, A. Dereux and T. W. Ebbesen. *Surface plasmon subwavelength optics*. Nature 424 (6950): 824–830 (2003). doi: [10.1038/nature01937](https://doi.org/10.1038/nature01937) – cited on page 63.
- [163] S. A. Maier. *Plasmonics Fundamentals and Applications*. Springer (2007) – cited on pages 63, 65, 69, 70, and 71.
- [164] S. Enoch and N. Bonod. *Plasmonics: From Basics to Advanced Topics*. Springer Series in Optical Sciences. Springer Berlin Heidelberg (2012) – cited on page 63.
- [165] G. A. Reider. *Photonik eine Einführung in die Grundlagen*. Springer Verlag, Wien (2005) – cited on pages 63, 64, and 65.
- [166] J. Jackson. *Classical electrodynamics*. Wiley (1975) – cited on pages 63 and 64.
- [167] M. A. Ordal, L. L. Long, R. J. Bell, S. E. Bell, R. R. Bell, R. W. Alexander and C. A. Ward. *Optical properties of the metals Al, Co, Cu, Au, Fe, Pb, Ni, Pd, Pt, Ag, Ti, and W in the infrared and far infrared*. Applied Optics 22 (7): 1099–1119 (1983). doi: [10.1364/AO.22.001099](https://doi.org/10.1364/AO.22.001099) – cited on pages 66, 67, and 105.
- [168] R. L. Olmon, B. Slovick, T. W. Johnson, D. Shelton, S. H. Oh, G. D. Boreman and M. B. Raschke. *Optical dielectric function of gold*. Physical Review B 86:



- 235147 (2012). doi: [10.1103/PhysRevB.86.235147](https://doi.org/10.1103/PhysRevB.86.235147) – cited on pages 66, 67, and 74.
- [169] H. Raether. *Surface Plasmons on Smooth and Rough Surfaces and on Gratings*, 4–39. Springer Berlin Heidelberg, Berlin, Heidelberg (1988). doi: [10.1007/BFb0048319](https://doi.org/10.1007/BFb0048319) – cited on page 70.
- [170] E. Kretschmann. *The determination of the optical constants of metals by excitation of surface plasmons*. Zeitschrift für Physik A Hadrons and nuclei 241 (4): 313–324 (1971). doi: [10.1007/BF01395428](https://doi.org/10.1007/BF01395428) – cited on page 70.
- [171] T. W. Ebbesen, H. J. Lezec, H. F. Ghaemi, T. Thio and P. A. Wolff. *Extraordinary optical transmission through sub-wavelength hole arrays*. Nature 391 (6668): 667–669 (1998). doi: [10.1038/35570](https://doi.org/10.1038/35570) – cited on page 70.
- [172] L. Martín-Moreno, F. J. García-Vidal, H. J. Lezec, K. M. Pellerin, T. Thio, J. B. Pendry and T. W. Ebbesen. *Theory of extraordinary optical transmission through subwavelength hole arrays*. Physical Review Letters 86: 1114–1117 (2001). doi: [10.1103/PhysRevLett.86.1114](https://doi.org/10.1103/PhysRevLett.86.1114) – cited on page 70.
- [173] R. A. Watts, T. W. Preist and J. R. Sambles. *Sharp surface-plasmon resonances on deep diffraction gratings*. Physical Review Letters 79: 3978–3981 (1997). doi: [10.1103/PhysRevLett.79.3978](https://doi.org/10.1103/PhysRevLett.79.3978) – cited on page 71.
- [174] A. Hessel and A. A. Oliner. *A new theory of wood’s anomalies on optical gratings*. Applied Optics 4 (10): 1275–1297 (1965). doi: [10.1364/AO.4.001275](https://doi.org/10.1364/AO.4.001275) – cited on page 72.
- [175] R. W. Wood. *On a remarkable case of uneven distribution of light in a diffraction grating spectrum*. Proceedings of the Physical Society of London 18 (1): 269 (1902) – cited on page 72.
- [176] J. W. Cleary, G. Medhi, R. E. Peale and W. R. Buchwald. *Long-wave infrared surface plasmon grating coupler*. Applied Optics 49 (16): 3102–3110 (2010). doi: [10.1364/AO.49.003102](https://doi.org/10.1364/AO.49.003102) – cited on page 72.
- [177] C. Ropers, C. C. Neacsu, T. Elsaesser, M. Albrecht, M. B. Raschke and C. Lienau. *Grating-coupling of surface plasmons onto metallic tips: a nanoconfined light source*. Nano Letters 7 (9): 2784–2788 (2007). doi: [10.1021/nl071340m](https://doi.org/10.1021/nl071340m) – cited on page 72.

- [178] J. A. Shackleford, R. Grote, M. Currie, J. E. Spanier and B. Nabet. *Integrated plasmonic lens photodetector*. Applied Physics Letters 94 (8): 083501 (2009). doi: [10.1063/1.3086898](https://doi.org/10.1063/1.3086898) – cited on page 72.
- [179] T. Ishi, J. Fujikata, K. Makita, T. Baba and K. Ohashi. *Si nano-photodiode with a surface plasmon antenna*. Japanese Journal of Applied Physics 44 (3L): L364 (2005). doi: [10.1143/JJAP.44.L364](https://doi.org/10.1143/JJAP.44.L364) – cited on page 72.
- [180] L. Martín-Moreno, F. J. García-Vidal, H. J. Lezec, A. Degiron and T. W. Ebbesen. *Theory of highly directional emission from a single subwavelength aperture surrounded by surface corrugations*. Physical Review Letters 90: 167401 (2003). doi: [10.1103/PhysRevLett.90.167401](https://doi.org/10.1103/PhysRevLett.90.167401) – cited on page 72.
- [181] N. Hiramatsu, F. Kusa, K. Imasaka, I. Morichika, A. Takegami and S. Ashihara. *Propagation length of mid-infrared surface plasmon polaritons on gold: Impact of morphology change by thermal annealing*. Journal of Applied Physics 120 (17): 173103 (2016). doi: [10.1063/1.4966934](https://doi.org/10.1063/1.4966934) – cited on pages 73 and 74.
- [182] E. D. Palik. *Chapter 2 - refractive index*. E. D. Palik, editor, *Handbook of Optical Constants of Solids*, 5 – 114. Academic Press, Burlington (2002). doi: [10.1016/B978-012544415-6.50149-7](https://doi.org/10.1016/B978-012544415-6.50149-7) – cited on page 73.
- [183] J. B. Pendry, L. Martín-Moreno and F. J. Garcia-Vidal. *Mimicking surface plasmons with structured surfaces*. Science 305 (5685): 847–848 (2004). doi: [10.1126/science.1098999](https://doi.org/10.1126/science.1098999) – cited on pages 74 and 78.
- [184] A. Rusina, M. Durach and M. I. Stockman. *Theory of spoof plasmons in real metals*. Applied Physics A 100 (2): 375–378 (2010). doi: [10.1007/s00339-010-5866-y](https://doi.org/10.1007/s00339-010-5866-y) – cited on pages 74 and 75.
- [185] V. M. Shalaev. *Optical negative-index metamaterials*. Nat Photon 1 (1): 41–48 (2007). doi: [10.1038/nphoton.2006.49](https://doi.org/10.1038/nphoton.2006.49) – cited on page 92.
- [186] N. Liu, M. Mesch, T. Weiss, M. Hentschel and H. Giessen. *Infrared perfect absorber and its application as plasmonic sensor*. Nano Letters 10 (7): 2342–2348 (2010). doi: [10.1021/nl9041033](https://doi.org/10.1021/nl9041033). PMID: 20560590 – cited on page 92.
- [187] X. Liu, T. Starr, A. F. Starr and W. J. Padilla. *Infrared spatial and frequency selective metamaterial with near-unity absorbance*. Physical Review Letters 104: 207403 (2010). doi: [10.1103/PhysRevLett.104.207403](https://doi.org/10.1103/PhysRevLett.104.207403) – cited on pages 92 and 138.

- 
- [188] Z. H. Jiang, S. Yun, F. Toor, D. H. Werner and T. S. Mayer. *Conformal dual-band near-perfectly absorbing mid-infrared metamaterial coating*. ACS Nano 5 (6): 4641–4647 (2011). doi: [10.1021/nm2004603](https://doi.org/10.1021/nm2004603). PMID: 21456579 – cited on page 92.
- [189] A. Benz, M. Krall, S. Schwarz, D. Dietze, H. Detz, A. M. Andrews, W. Schrenk, G. Strasser and K. Unterrainer. *Resonant metamaterial detectors based on THz quantum-cascade structures*. Scientific Reports 4: 4269 EP – (2014). doi: [10.1038/srep04269](https://doi.org/10.1038/srep04269). Article – cited on page 92.
- [190] G. Sarusi, B. F. Levine, S. J. Pearton, K. M. S. Bandara and R. E. Leibenguth. *Improved performance of quantum well infrared photodetectors using random scattering optical coupling*. Applied Physics Letters 64 (8): 960–962 (1994). doi: [10.1063/1.110973](https://doi.org/10.1063/1.110973) – cited on page 93.
- [191] S. I. Borenstain, U. Arad, I. Lyubina, A. Segal and Y. Warschawer. *Optimized random/ordered grating for an n-type quantum well infrared photodetector*. Applied Physics Letters 75 (17): 2659–2661 (1999). doi: [10.1063/1.125110](https://doi.org/10.1063/1.125110) – cited on page 93.
- [192] A. P. Ravikumar, D. Sivco and C. F. Gmachl. *Wavelength independent normal incident quantum cascade detectors*. Optics Express 24 (22): 25269–25276 (2016). doi: [10.1364/OE.24.025269](https://doi.org/10.1364/OE.24.025269) – cited on page 93.
- [193] P. Reininger, B. Schwarz, A. Harrer, T. Zederbauer, H. Detz, A. M. Andrews, R. Gansch, W. Schrenk and G. Strasser. *Photonic crystal slab quantum cascade detector*. Applied Physics Letters 103 (24): 241103 (2013). doi: [10.1063/1.4846035](https://doi.org/10.1063/1.4846035) – cited on page 93.
- [194] C. McNab, R. Bujeiro and A. Gilliland. *German Automatic Rifles 1941–45: Gew 41, Gew 43, FG 42 and StG 44*. Weapon. Bloomsbury Publishing (2013) – cited on page 97.
- [195] A. Goldberg. *Laboratory and field performance of megapixel QWIP focal plane arrays*. Proceedings of the International Workshop on Quantum Well Infrared Photodetectors 47 (1-2): 91–105 (2005). doi: [10.1016/j.infrared.2005.02.014](https://doi.org/10.1016/j.infrared.2005.02.014) – cited on page 99.
- [196] A. Rogalski, J. Antoszewski and L. Faraone. *Third-generation infrared photodetector arrays*. Journal of Applied Physics 105 (9): 091101 (2009). doi: [10.1063/1.3099572](https://doi.org/10.1063/1.3099572) – cited on page 99.

- [197] N. Gautam, H. S. Kim, M. N. Kuty, E. Plis, L. R. Dawson and S. Krishna. *Performance improvement of longwave infrared photodetector based on type II InAs/GaSb superlattices using unipolar current blocking layers*. Applied Physics Letters 96 (23): 231107 (2010). doi: [10.1063/1.3446967](https://doi.org/10.1063/1.3446967) – cited on page 99.
- [198] H. Zimmermann. *Integrated Silicon Optoelectronics*. Springer (2010) – cited on page 99.
- [199] H. E. Bennett and J. M. Bennett. *Optical Properties and Electronic Structure of Metals and Alloys*. F. Abeles Ed. North-Holland, Amsterdam (1966) – cited on page 105.
- [200] G. Wysocki, M. McCurdy, S. So, D. Weidmann, C. Roller, R. F. Curl and F. K. Tittel. *Pulsed quantum-cascade laser-based sensor for trace-gas detection of carbonyl sulfide*. Applied Optics 43 (32): 6040–6046 (2004). doi: [10.1364/AO.43.006040](https://doi.org/10.1364/AO.43.006040) – cited on page 115.
- [201] K. Krzempek, M. Jahjah, R. Lewicki, P. Stefański, S. So, D. Thomazy and F. K. Tittel. *Cw dfb rt diode laser-based sensor for trace-gas detection of ethane using a novel compact multipass gas absorption cell*. Applied Physics B 112 (4): 461–465 (2013). doi: [10.1007/s00340-013-5544-9](https://doi.org/10.1007/s00340-013-5544-9) – cited on page 115.
- [202] D. Ristanic, B. Schwarz, P. Reininger, H. Detz, T. Zederbauer, A. M. Andrews, W. Schrenk and G. Strasser. *Monolithically integrated mid-infrared sensor using narrow mode operation and temperature feedback*. Applied Physics Letters 106 (4): 041101 (2015). doi: [10.1063/1.4906802](https://doi.org/10.1063/1.4906802) – cited on page 116.
- [203] C. Gmachl. *Recent progress in mid-infrared quantum cascade lasers. Lasers, Sources, and Related Photonic Devices*. Optical Society of America (2012). doi: [10.1364/LACSEA.2012.LM2B.2](https://doi.org/10.1364/LACSEA.2012.LM2B.2) – cited on page 119.
- [204] C. Jirauschek and T. Kubis. *Modeling techniques for quantum cascade lasers*. Applied Physics Reviews 1 (1): 011307 (2014). doi: [10.1063/1.4863665](https://doi.org/10.1063/1.4863665) – cited on page 119.
- [205] B. Schwarz, D. Ristanic, P. Reininger, T. Zederbauer, D. MacFarland, H. Detz, A. M. Andrews, W. Schrenk and G. Strasser. *High performance bi-functional quantum cascade laser and detector*. Applied Physics Letters 107 (7): 071104 (2015). doi: [10.1063/1.4927851](https://doi.org/10.1063/1.4927851) – cited on pages 120 and 136.

- 
- [206] A. Harrer, R. Szedlak, B. Schwarz, H. Moser, T. Zederbauer, D. MacFarland, H. Detz, A. M. Andrews, W. Schrenk, B. Lendl and G. Strasser. *Mid-infrared surface transmitting and detecting quantum cascade device for gas-sensing*. Scientific Reports 6: 21795 EP – (2016). doi: [10.1038/srep21795](https://doi.org/10.1038/srep21795). Article – cited on pages [120](#), [122](#), [123](#), [124](#), and [125](#).
- [207] C. Schwarzer, E. Mujagić, S. I. Ahn, A. M. Andrews, W. Schrenk, W. Charles, C. Gmachl and G. Strasser. *Grating duty-cycle induced enhancement of substrate emission from ring cavity quantum cascade lasers*. Applied Physics Letters 100 (19): 191103 (2012). doi: [10.1063/1.4712127](https://doi.org/10.1063/1.4712127) – cited on page [120](#).
- [208] R. Szedlak, C. Schwarzer, T. Zederbauer, H. Detz, A. M. Andrews, W. Schrenk and G. Strasser. *On-chip focusing in the mid-infrared: Demonstrated with ring quantum cascade lasers*. Applied Physics Letters 104 (15): 151105 (2014). doi: [10.1063/1.4871520](https://doi.org/10.1063/1.4871520) – cited on page [121](#).
- [209] E. Mujagić, M. Nobile, H. Detz, W. Schrenk, J. Chen, C. Gmachl and G. Strasser. *Ring cavity induced threshold reduction in single-mode surface emitting quantum cascade lasers*. Applied Physics Letters 96 (3): 031111 (2010). doi: [10.1063/1.3292021](https://doi.org/10.1063/1.3292021) – cited on page [121](#).
- [210] R. Szedlak, A. Harrer, M. Holzbauer, B. Schwarz, J. P. Wacławek, D. MacFarland, T. Zederbauer, H. Detz, A. M. Andrews, W. Schrenk, B. Lendl and G. Strasser. *Remote sensing with comtable monolithic laser and detector*. ACS Photonics 3 (10): 1794–1798 (2016). doi: [10.1021/acsphotonics.6b00603](https://doi.org/10.1021/acsphotonics.6b00603). PMID: 27785455 – cited on pages [124](#), [129](#), [130](#), [131](#), and [133](#).
- [211] B. Bai, X. Meng, J. Laukkanen, T. Sfez, L. Yu, W. Nakagawa, H. P. Herzig, L. Li and J. Turunen. *Asymmetrical excitation of surface plasmon polaritons on blazed gratings at normal incidence*. Physical Review B 80: 035407 (2009). doi: [10.1103/PhysRevB.80.035407](https://doi.org/10.1103/PhysRevB.80.035407) – cited on page [138](#).
- [212] H. Tao, N. I. Landy, C. M. Bingham, X. Zhang, R. D. Averitt and W. J. Padilla. *A metamaterial absorber for the terahertz regime: Design, fabrication and characterization*. Optics Express 16 (10): 7181–7188 (2008). doi: [10.1364/OE.16.007181](https://doi.org/10.1364/OE.16.007181) – cited on page [138](#).
- [213] G. Dayal and S. A. Ramakrishna. *Design of highly absorbing metamaterials for infrared frequencies*. Optics Express 20 (16): 17503–17508 (2012). doi: [10.1364/OE.20.017503](https://doi.org/10.1364/OE.20.017503) – cited on page [138](#).

- [214] N. Liu, M. Mesch, T. Weiss, M. Hentschel and H. Giessen. *Infrared perfect absorber and its application as plasmonic sensor*. Nano Letters 10 (7): 2342–2348 (2010). doi: [10.1021/nl9041033](https://doi.org/10.1021/nl9041033). PMID: 20560590 – cited on page 138.

## ABBREVIATIONS

### Abbreviations

<b>AFM</b>	atomic force microscopy
<b>ARC</b>	anti-reflection coating
<b>AZ</b>	active zone
<b>CBO</b>	conduction band offset
<b>CMOS</b>	complementary metal oxide semiconductor
<b>CVD</b>	chemical vapor deposition
<b>CW</b>	continuous wave
<b>DFB</b>	distributed feedback
<b>DTGS</b>	deuterated triglycine sulfate
<b>EOT</b>	extraordinary optical transmission
<b>FOV</b>	field of view
<b>FP</b>	Fabry-Pérot
<b>FPA</b>	focal plane array
<b>FWHM</b>	full width at half maximum
<b>FTIR</b>	Fourier transformation infrared spectrometer
<b>IB</b>	interband
<b>ICL</b>	interband cascade laser
<b>ISB</b>	intersubband
<b>IR</b>	infrared
<b>LED</b>	light emitting diode
<b>LWIR</b>	long-wave infrared
<b>MBE</b>	molecular beam epitaxy
<b>MCT</b>	mercury cadmium telluride
<b>MIR</b>	mid-infrared
<b>MOCVD</b>	metal-organic chemical vapor deposition

<b>NEP</b>	noise equivalent power
<b>NETD</b>	noise equivalent temperature difference
<b>NIR</b>	near-infrared
<b>NSD</b>	noise spectral density
<b>ROIC</b>	read out integrated circuit
<b>PAS</b>	photoacoustic spectroscopy
<b>PCB</b>	printed circuit board
<b>PECVD</b>	plasma enhanced vapor deposition
<b>PML</b>	perfectly matched layer
<b>QC</b>	quantum cascade
<b>QCD</b>	quantum cascade detector
<b>QCL</b>	quantum cascade laser
<b>QCLD</b>	quantum cascade laser detector
<b>QPAS</b>	quartz enhanced photoacoustic spectroscopy
<b>QW</b>	quantum well
<b>QWIP</b>	quantum well infrared photodetector
<b>RIE</b>	reactive ion etching
<b>ring-QCL</b>	ring quantum cascade laser
<b>SEM</b>	scanning electron microscope
<b>SL</b>	superlattice
<b>SMU</b>	source meter unit
<b>SNR</b>	signal to noise ratio
<b>SPI</b>	serial peripheral interface
<b>SPP</b>	surface plasmon polariton
<b>TE</b>	transverse-electric
<b>TEC</b>	thermoelectric cooler
<b>TIA</b>	transimpedance amplifier
<b>TM</b>	transverse-magnetic
<b>UHV</b>	ultra high vacuum
<b>VSP</b>	Vienna Schrödinger Poisson



## LIST OF PUBLICATIONS

### Journal publications

- J1** R. Szedlak\*, A. Harrer\*, M. Holzbauer, B. Schwarz, J. Waclawek, D. MacFarland, T. Zederbauer, H. Detz, A.M. Andrews, W. Schrenk, B. Lendl and G. Strasser, *Remote sensing with commutable monolithic laser and detector*, ACS Photonics (2016) doi: [10.1021/acsphotonics.6b00603](https://doi.org/10.1021/acsphotonics.6b00603)
- J2** A. Harrer, B. Schwarz, S. Schuler, P. Reininger, A. Wirthmüller, H. Detz, D. MacFarland, T. Zederbauer, A.M. Andrews, M. Rothermund, H. Oppermann, W. Schrenk and G. Strasser, *4.3  $\mu\text{m}$  quantum cascade detector in pixel configuration*, Optics Express, 24, 17041-17049 (2016), doi: [10.1364/OE.24.017041](https://doi.org/10.1364/OE.24.017041)
- J3** A. Harrer\*, R. Szedlak\*, B. Schwarz, H. Moser, T. Zederbauer, D. MacFarland, H. Detz, A.M. Andrews, W. Schrenk, B. Lendl and G. Strasser, *Mid-infrared surface transmitting and detecting quantum cascade device for gas-sensing*, Scientific Reports, 6, 21795 (2016), doi: [10.1038/srep21795](https://doi.org/10.1038/srep21795)
- J4** A. Harrer, B. Schwarz, R. Gansch, P. Reininger, H. Detz, T. Zederbauer, A.M. Andrews, W. Schrenk, and G. Strasser, *Plasmonic lens enhancing mid-infrared quantum cascade detector*, Appl. Phys. Lett., 105, 171112, (2014), doi: [10.1063/1.4901043](https://doi.org/10.1063/1.4901043)
- J5** P. Reininger, B. Schwarz, A. Harrer, T. Zederbauer, H. Detz, A.M. Andrews, R. Gansch, W. Schrenk and G. Strasser, *Photonic crystal slab quantum cascade detector*, Appl. Phys. Lett. 103, 241103 (2013), doi: [10.1063/1.4846035](https://doi.org/10.1063/1.4846035)

---

\* authors equally contributed to the publication

## Invited oral talks

- I1** R. Szedlak, A. Harrer, B. Schwarz, M. Holzbauer, J. P. Wacławek, D. MacFarland, T. Zederbauer, H. Detz, A. M. Andrews, W. Schrenk, B. Lendl and G. Strasser *Remote Gas Sensing with Quantum Cascade Systems*, Nano and Photonics, Mauterndorf, Austria, Mar 22-25, 2017
- I2** R. Szedlak, A. Harrer, B. Schwarz, M. Holzbauer, J. P. Wacławek, H. Moser, D. MacFarland, T. Zederbauer, H. Detz, A. M. Andrews, W. Schrenk, B. Lendl and G. Strasser *Compact mid-IR sensors based on bi-functional and commutable semiconductor lasers and detectors on the same chip*, 3<sup>rd</sup> Int. Workshop on Infrared Technologies, Olching, Germany, Nov 7-8, 2016
- I3** A. Harrer, B. Schwarz, P. Reininger, R. Szedlak, D. Ristanic, H. Detz, A.M. Andrews, T. Zederbauer, D. MacFarland, W. Schrenk, and G. Strasser *Quantum Cascade Devices: from discrete to integrated systems*, MIOMD 2016, Beijing, China, Sep. 18-22, 2016
- I4** G. Strasser, B. Schwarz, R. Szedlak, A. Harrer, H. Detz, A. M. Andrews, T. Zederbauer, D. MacFarland and W. Schrenk *Quantum cascade detectors and monolithically integrated sensing devices*, FLAIR 2016, Aix-les-Bains, France, Sept 12-16, 2016
- I5** R. Szedlak, A. Harrer, B. Schwarz, M. Holzbauer, J. P. Wacławek, D. MacFarland, T. Zederbauer, H. Detz, A. M. Andrews, W. Schrenk, B. Lendl and G. Strasser *Remote Gas Sensing with commutable Quantum Cascade Laser and Detector on the same Chip*, IQCLSW, Cambridge, United Kingdom, Sept 4-9, 2016
- I6** A. Harrer, B. Schwarz, P. Reininger, R. Szedlak, D. Ristanic, H. Detz, A.M. Andrews, T. Zederbauer, D. MacFarland, W. Schrenk, and G. Strasser *MIR Lab-on-a-chip: From Discrete Devices to an Integrated System*, WOCSDICE-EXEMATEC, Aveiro, Portugal, June 6-10, 2016

## Oral talks

- O1** A. Harrer, B. Schwarz, S. Schuler, P. Reininger, A. Wirthmüller, H. Detz, D. MacFarland, T. Zederbauer, A.M. Andrews, M. Rothermund, H. Oppermann, W. Schrenk and G. Strasser, *Quantum cascade detector at 4.3 $\mu$ m wavelength in*

- 
- pixel array configuration*, SPIE Photonics West, San Francisco, USA, Feb 01, 2017
- O2** B. Hinkov, B. Schwarz, A. Harrer, D. Ristanic, W. Schrenk, M. Hugues, J.-M. Chauveau and G. Strasser, *Resonant Tunneling Diodes based on ZnO for Quantum Cascade Structures*, SPIE Photonics West, San Francisco, USA, Feb 02, 2017
- O3** A. Harrer et al, *Quantum cascade structures for sensing applications: Towards more compact liquid and gas sensing devices*, Seminar Talk - Daylight Solutions, San Diego, USA, Feb 10, 2017
- O4** A. Harrer et al., *Mid-infrared bi-functional quantum cascade sensor for long interaction regions*, nanoFIS 2016, Graz, Austria, Jun 27-29, 2016
- O5** R. Szedlak, A. Harrer, B. Schwarz, M. Holzbauer, H. Moser, D. MacFarland, T. Zederbauer, H. Detz, A.M. Andrews, W. Schrenk, B. Lendl and G. Strasser, *Highly Integrated Gas Sensors based on Bi-functional Quantum Cascade Structures*, CLEO 2016 San Jose, USA, Jun 5-10, 2016
- O6** A. Harrer, B. Schwarz, R. Szedlak, M. Holzbauer, T. Zederbauer, H. Detz, A.M. Andrews, D. MacFarland, W. Schrenk, H. Moser, P. Waclawek, B. Lendl and G. Strasser, *Mid-infrared sensing based on quantum cascade structures*, NextLite Workshop, Wien, Austria, May 3-4, 2016
- O7** A. Harrer, B. Schwarz, P. Reininger, R. Szedlak, T. Zederbauer, H. Detz, D. MacFarland, A.M. Andrews, W. Schrenk and G. Strasser, *An optimized bi-functional material for integrated mid-infrared quantum cascade based sensors*, Photonics West, San Francisco, USA, Feb 13-18, 2016
- O8** W. Schrenk, R. Szedlak, D. Ristanic, B. Schwarz, P. Reininger, A. Harrer, H. Detz, D. MacFarland, A. M. Andrews and G. Strasser, *Integrated Ring Laser Systems for Spectroscopy based on Quantum Cascade Structures*, SCIX, Providence (RI), USA, Sep 27 - Oct 2, 2015
- O9** B. Schwarz, A. Harrer, D. Ristanic, P. Reininger, H. Detz, T. Zederbauer, A. M. Andrews, W. Schrenk and G. Strasser, *Bi-functional quantum cascade laser/detectors: From design to applications*, ITQW, Wien, Austria, Sep 6-11, 2015
- O10** A. Harrer, B. Schwarz, R. Szedlak, J.P. Waclawek, H. Moser, D. MacFarland, T. Zederbauer, H. Detz, A. M. Andrews, W. Schrenk, B. Lendl and G. Strasser,

- A bi-functional surface emitting and detecting mid-infrared device for sensing applications*, ÖPG & SPG Annual meeting, Wien, Austria, Sep 1-4, 2015
- O11** A. Harrer, P. Reininger, R. Gansch, B. Schwarz, D. MacFarland, T. Zederbauer, H. Detz, A. M. Andrews, W. Schrenk, O. Baumgartner, H. Kosina and G. Strasser, *Quantum Cascade Detectors for Sensing Applications*, ICAVS8, Wien, Austria Jul 12-17, 2015
- O12** A. Harrer, R. Szedlak, M. Holzbauer, B. Schwarz, H. Moser, E. Mujagic, D. MacFarland, T. Zederbauer, H. Detz, A. M. Andrews, W. Schrenk, B. Lendl and G. Strasser, *Monolithic integrated on-chip sensing utilizing plasmonics*, Next-Lite Workshop, Hirschwang an der Rax, Austria, Jun 18-19, 2015
- O13** R. Szedlak, A. Harrer, M. Holzbauer, B. Schwarz, H. Moser, E. Mujagic, C. Deutsch, D. MacFarland, T. Zederbauer, H. Detz, A. M. Andrews, W. Schrenk, K. Unterrainer, B. Lendl, G. Strasser, *Infrared and terahertz spectroscopy with ring quantum cascade lasers*, German THz Conference 2015, Dresden, Germany, Jun 8-10, 2015
- O14** P. Reininger, B. Schwarz, A. Harrer, T. Zederbauer, H. Detz, A. M. Andrews, R. Gansch, W. Schrenk, G. Strasser, *High-responsivity photovoltaic intersubband detectors*, Photonics West, San Francisco, USA, Feb 7-12, 2015
- O15** A. Harrer, P. Reininger, B. Schwarz, R. Gansch, S. Kalchmair, H. Detz, T. Zederbauer, D. MacFarland, A. M. Andrews, W. Schrenk, O. Baumgartner, H. Kosina and G. Strasser, *Advances in Quantum Cascade Detector Design*, 4th International Nanophotonics Meeting 2014, Igls, Austria Okt 23-25, 2014
- O16** B. Schwarz, D. Ristanic, P. Reininger, A. Harrer, H. Detz, A. M. Andrews, W. Schrenk and G. Strasser, *Monolithically integrated chemical sensor based on intersubband transitions and plasmonics*, IQCLSW, Policoro, Italy, Sep 7-12, 2014
- O17** P. Reininger, B. Schwarz, A. Harrer, T. Zederbauer, H. Detz, A. M. Andrews, R. Gansch, W. Schrenk and G. Strasser, *Room temperature quantum cascade detector*, IQCLSW, Policoro, Italy, Sep 7-12, 2014
- O18** A. Harrer, R. Gansch, P. Reininger, B. Schwarz, H. Detz, T. Zederbauer, A.M. Andrews, W. Schrenk, and G. Strasser, *Mid infrared intersubband detectors*, Microsymposium QCL Chemical Sensing, Vienna, Austria, Mar 10, 2014

- 
- O19** P. Reininger, B. Schwarz, A. Wirthmüller, A. Harrer, O. Baumgartner, H. Detz, T. Zederbauer, D. MacFarland, A. M. Andrews, W. Schrenk, L. Hvozďara, H. Kosina and G. Strasser, *Towards higher temperature operation of quantum cascade detectors*, ITQW, New York, USA, Sep 15-20, 2013
  - O20** A. Harrer, B. Schwarz, P. Reininger, R. Gansch, T. Zederbauer, A. M. Andrews, S. Kalchmair, W. Schrenk, O. Baumgartner, Z. Stanojević, H. Kosina and G. Strasser, *Intersubband Detectors*, 3rd International Nanophotonics Meeting, Salzburg, Austria, Sep 1-3, 2013
  - O21** B. Schwarz, P. Reininger, A. Harrer, R. Gansch, T. Zederbauer, A.M. Andrews, S. Kalchmair, W. Schrenk, O. Baumgartner, Z. Stanojević, H. Kosina, and G. Strasser, *Intersubband Detectors*, 3rd International Nanophotonics Meeting, Salzburg, Austria, Sep 1-3, 2013
  - O22** P. Reininger, B. Schwarz, A. Harrer, R. Gansch, T. Zederbauer, H. Detz, A. M. Andrews, W. Schrenk, O. Baumgartner, Z. Stanojević, H. Kosina and G. Strasser, *Towards high temperature operation of quantum cascade detectors*, ITQW, Bolton Landing, NY, USA, Sep 15-20, 2013

## Presentations

- P1** A. Harrer, B. Schwarz, R. Szedlak, S. Schuler, P. Reininger, H. Detz, A. M. Andrews, T. Zederbauer, D. MacFarland, W. Schrenk and G. Strasser, *High performance quantum cascade detector array for CO<sub>2</sub> detection*, IQCLSW, Cambridge, United Kingdom, Sept 4 - 9, 2016
- P2** R. Szedlak, A. Harrer, M. Holzbauer, B. Schwarz, J.P. Waclawek, D. MacFarland, T. Zederbauer, H. Detz, A.M. Andrews, W. Schrenk, B. Lendl and G. Strasser, *Gas sensing with bi-functional ring resonators as laser and detector*, Microelectronic Systems Symposium MESS16, Wien, Austria, Apr 28 - 29, 2016
- P3** A. Harrer, R. Szedlak, B. Schwarz, H. Moser, T. Zederbauer, H. Detz, A. M. Andrews, W. Schrenk, B. Lendl and G. Strasser, *A mid-infrared gas-sensing device based on bi-functional quantum cascade structures*, Winter-school Mauterndorf, Mauterndorf, Austria, Feb 21-26, 2016
- P4** A. Harrer, R. Szedlak, B. Schwarz, H. Moser, T. Zederbauer, H. Detz, A. M. Andrews, W. Schrenk, B. Lendl and G. Strasser, *Towards a monolithic inte-*

- grated surface emitting and detecting mid-infrared gas sensor*, ITQW, Wien, Austria, Sep 6-11, 2015
- P5** P. Reininger, B. Schwarz, A. Harrer, T. Zederbauer, H. Detz, A.M. Andrews, R. Gansch, W. Schrenk, and G. Strasser, *Room temperature quantum cascade detector*, IQCLSW, Policoro, Italy, Sep 7-12, 2014
- P6** A. Harrer, B. Schwarz, R. Gansch, P. Reininger, H. Detz, T. Zederbauer, A.M. Andrews, W. Schrenk, and G. Strasser, *Mid-infrared detectors with on-chip light collection*, IQCLSW, Policoro, Italy, Sep 7-12, 2014
- P7** P. Reininger, B. Schwarz, A. Harrer, T. Zederbauer, H. Detz, A.M. Andrews, R. Gansch, W. Schrenk, and G. Strasser, *2.5D photonic crystal quantum cascade detector*, CLEO, San Jose, CA, USA, Jun 8-13, 2014
- P8** A. Harrer, B. Schwarz, R. Gansch, P. Reininger, H. Detz, T. Zederbauer, A.M. Andrews, W. Schrenk, and G. Strasser, *Mid-infrared plasmonic lens intersubband photodetector*, Winterschool Mauterndorf, Mauterndorf, Austria, Feb 23-28, 2014
- P9** P. Reininger, B. Schwarz, A. Harrer, H. Detz, T. Zederbauer, A.M. Andrews, R. Gansch, W. Schrenk, and G. Strasser, *Photonic crystal quantum cascade detector*, Winterschool Mauterndorf, Mauterndorf, Austria, Feb 23-28, 2014
- P10** A. Harrer, R. Gansch, P. Reininger, B. Schwarz, H. Detz, T. Zederbauer, D. MacFarland, A.M. Andrews, W. Schrenk, and G. Strasser, *Tuning of resonances in photonic crystal photodetectors*, ÖPG & SPG Annual meeting, Linz, Austria, Sep 3-6, 2013

## Thesis

A. Harrer, *Resonance Tuning of Photonic Crystal Intersubband Detectors*, Institute of Solid State Electronics, Technische Universität Wien, Juni 2013

# CURRICULUM VITAE

## Personal Data

Name	Andreas Harrer
Date of Birth	January 14 <sup>th</sup> , 1987
Place of Birth	Wien, Austria
Nationality	Austrian



## Education

Since Sept 2013	PhD candidate in Electrical Engineering TU Wien, Vienna, Austria,
2010 – 2013	MSc in Microelectronics TU Wien, Vienna, Austria
2006 – 2010	BSc in Electrical Engineering, TU Wien, Vienna, Austria
1997 – 2002	Secondary technical high school for Mechatronics, HTL Wien 3 Rennweg, Austria
1993 – 1997	Secondary school, Bundesrealgymnasium Rahlgasse Wien, Austria
1989 – 1993	Primary school, Volksschule Sonnenuhrgasse Wien, Austria

## Scholarships

Feb.-Jun. 2001	CEEPUS Freemover Budapest University of Technology, Hungary
----------------	--

## Scientific Career

- Since Sept. 2013      Project assistant at Institute of Solid State Electronics,  
TU Wien, Austria
- Oct. 2012 – Jun. 2013      Master thesis at Institute of Solid State Electronics,  
"Resonance Tuning of Photonic Crystal Intersubband Detectors"  
TU Wien, Austria